University of Southampton

FACULTY OF ENGINEERING, SCIENCE AND MATHEMATICS

SCHOOL OF CHEMISTRY

SIMULTANEOUS TIME RESOLVED XAS, IR AND MASS SPECTROMETRIC CHARACTERISATION OF CATALYTIC SYSTEMS: AN INVESTIGATION INTO THE STRUCTURE-FUNCTION BEHAVIOUR OF SUPPORTED RHODIUM CATALYSTS

Bhrat Jyoti

A thesis submitted for the Degree of Doctor of Philosophy

September 2006

UNIVERSITY OF SOUTHAMPTON

ABSTRACT

FACULTY OF ENGINEERING, SCIENCE AND MATHEMATICS
SCHOOL OF CHEMISTRY

Doctor of Philosophy

SIMULTANEOUS TIME-RESOLVED XAS, IR AND MASS SPECTROMETRIC CHARACTERISATION OF CATALYTIC SYSTEMS: AN INVESTIGATION INTO THE STRUCTURE-FUNCTION BEHAVIOUR OF SUPPORTED RHODIUM CATALYSTS

By Bhrat Jyoti

The techniques of Energy Dispersive Extended X-ray Absorption Fine structure (EDE), Diffuse Reflectance Fourier Transform Infrared Spectroscopy (DRIFTS) and mass spectrometry have been successfully combined in an in situ, time resolved manner to investigate the structure function surface chemistry of γ-Al_2O_3 supported Rh catalysts. Complementary ex situ techniques which included TEM, XPS and EDX were used to fully characterise the systems with a metal loading ranging from 1-10 wt%, which were synthesised with chlorinated and unchlorinated (nitrate) precursors.

Only the in situ techniques applied allowed for the characterisation of wholly metallic Rh particles. TEM and XPS studies indicated the particles, with particle sizes in the region of 10-60 Å, were oxidised readily in air; however the formation of an oxide layer around a metallic core was the most likely morphology of the spherical nanoparticles. The chlorinated samples resulted in catalysts with smaller particle sizes than those from the nitrate precursors. Cl K-edge X-ray Absorption Near Edge Structure (XANES) indicated that during reduction, chlorine was observed to migrate from the Rh to the alumina. The rapid phase fluxionality and kinetic character of the nanoparticles under redox conditions could be closely followed with a 50ms repetition rate.

Catalysts with a low metal loading (2.5 wt%) were subject to facile disruption upon exposure to CO; the formation of discrete $Rh(CO)_2$ units was facilitated at higher temperatures. The proportion of dicarbonyl adopting this site was significantly less at higher metal loading (5 wt%), this was reflected by the IR and unchanging EXAFS data.

The formation of 'high wavenumber' $Rh(NO)^-$ and $Rh(NO)_2$ species could be correlated to the rapid, extensive oxidation of Rh at low temperatures upon exposure to NO. The reactive turnover of NO and increased rate of oxidation were observed at higher temperatures, and evidence for a highly transient form of $Rh(NO)_2$ to yield a linear $Rh(NO)^+$ 'spectator' species was derived. Re-reduction of the oxide proceeded at temperatures as low as 373K.

A stoichiometric feedstock of CO and NO oxidised the elemental Rh catalysts to $Rh(CO)_2$ at room temperature. The proportion of Rh adopting the dicarbonyl sites increased at higher temperatures. Above 450 K the species decomposed, the Rh component reclustered and subsequent catalysis ensued. Similar effects were observed for a 4wt%Rh/1wt%Pd alloy catalyst.

A gas switching regime between CO and NO showed an almost static oxidic Rh phase to exist at low temperatures; structural changes were more substantial at higher temperatures and followed the pattern of switching more closely. With NO in excess the Rh clusters oxidised rapidly to yield the $Rh(NO)^+$ species; reclustering was observed under CO, which also adopted linear and bridging sites on the metallic particles.

The poisoning of the catalysts reported SO_2 to subtly modify the structure of the Rh but did not adversely affect the reduction of NO by H_2. In contrast, complete and irreversible sulfidation of the nanoparticles rapidly curtailed catalysis upon exposure H_2S.

Contents

Chapter 7. The structure-function response of Rh and RhPd systems to CO and NO

Chapter 8. The response of Rh/Al_2O_3 catalysts to H_2S and SO_2; subsequent poisoning of NO reduction by H_2

Acknowledgements

Firstly I would like to thank my supervisor John Evans; this thesis would not have been possible without his constant guidance and support. There is also the fact that he was prepared to put up with me for so many years (!). Joking aside, his direction of the numerous projects I have undertaken over the years have let me develop my life skills as well as the scientific side of things. I thank him for letting (and trusting me!) to 'get on with it', and the gentle prods when things were not going so well (i.e. the writing up stage.....ouch). Anybody who has the privilege of knowing John knows that the title 'King' John Evans is rightly deserved!

To Moniek, well what can I say? As both a close friend and second supervisor, I cannot thank 'superwoman' enough! Her constant support, hard work, advice, laughter, helping lift 250 kg worth of solid steel table on the back of a 3.5 tonne tail-lift truck....the list would be longer than this doorstop of a thesis, so all I can offer in this space is a simple thank you, M! I think you know what I mean....

Mark, similar story for you too mate, cant even being to make a list, so a simple thank you is all I can offer. So glad you have settled in at the ESRF; looking forward to use and abuse with visits to Grenoble (have been in talks with Karl already haha!).

To the 'dream-team': Steveo for always being there, no matter what time or experiment, country, you've always been there for me mate and ill never forget that, SAVVY! Plus, you didn't see me, right?! Andy Dent, for teaching me that a work-life balance is possible and essential, plus your multitasking (and improvising!) skills are legendary. Sofia, the ex-queen of ID-24, for getting the project off the ground at the ESRF....and making me realise that shoes ARE an obsession.....Karl, for all your hard work in getting us across with such cheer!

The PhD lot: Uncle Col (you are a true legend nipper!), 'Vincent', Grays, MOJO, Nicola, His Holiness eight of Bobby (special thank you for all your computer support mate!).

A special thank you for my family; mims and pips...cant believe how lucky I am to have parents like you, this thesis is dedicated to you; there are not any words I can think of to even begin.... 'What time are you home, paj?!' Nige, Dids and of course little coppadan!

To my gorgeous wife-to-be Bijal, for all your support through the darker times of this work...again words escape me (which is a rarity, hey peanut?!).

'Strange thing, EXAFS.....' Professor Andrew Dent 3.40 AM, 22nd July 2004, ID24.

Chapter 1. Introduction

1.1 Introduction

This thesis encompasses an investigation into the structure-function surface chemistry of selected oxide-supported rhodium catalysts. The scope of this investigation specifically targets an understanding of the nature of Rh nanoparticles, and their subsequent properties under reactive environments. The experimental methodologies employed to achieve this will endeavour to not only observe the catalytic characteristics present but also concentrate on the structural effects such processes elicit. The array of techniques envisaged for this study have been carefully selected to afford complimentary information in order to gain a fundamental understanding of these nanoparticulate systems. Moreover, many of these techniques will be bought to bear on the systems in an in situ, time-resolved manner in order to track the processes effectively.

This chapter will introduce the general concepts of the field of catalysis, related existing work and the overall aims of the project. It will also introduce the catalytic processes chosen to probe the characteristics of the Rh systems.

1.2 Catalysis

The definition of a catalyst is a substance or system that alters the rate of reaction by becoming involved in the reaction sequence without becoming a product.[1] Figure 1.1 shows how catalysts speed up a reaction by providing the reactants with an alternative lower-energy pathway to the products.[2] A catalyst may therefore produce a greater proportion of the desired product, as it may selectively lower just one of the several reaction pathways that are present. Catalysts are thus extensively utilised in nature, industry and in the laboratory. An example of the importance of catalysts is evident in the estimation that they contribute to one-sixth of the value of all manufactured goods in industrialised countries,[3] and nearly 70% of all industrial chemical processes use a catalyst at some stage in their manufacture.[4]

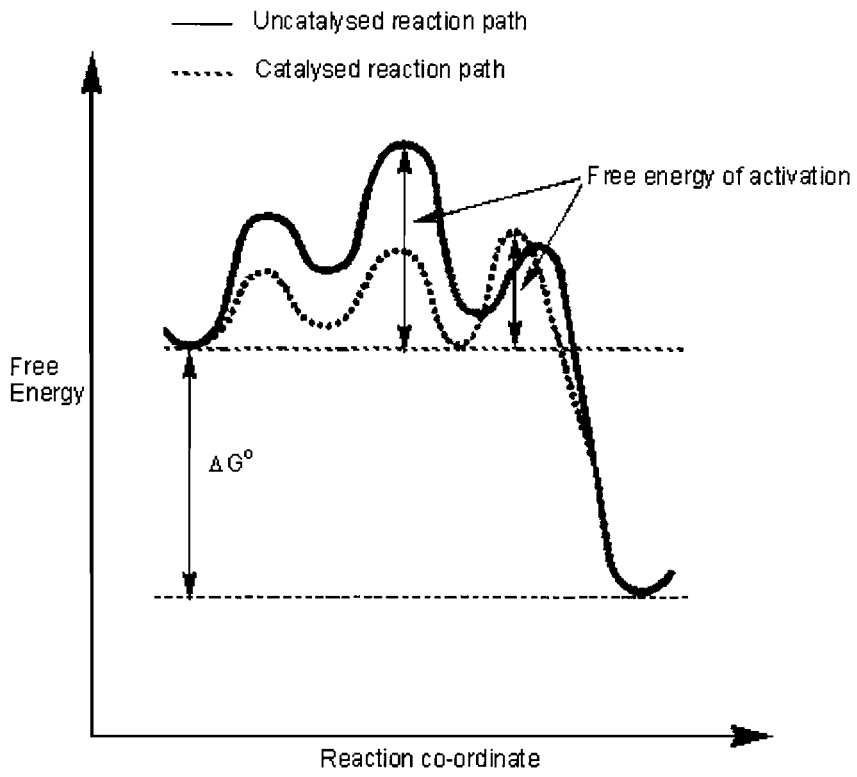

Figure 1.1: A free energy plot for a catalysed and catalysed reaction.

The subject of catalysis can be divided into two broad domains, homogeneous and heterogeneous catalysis. The differences between these two areas can be viewed effectively by looking at the properties of each catalyst type with respect to the phases present.

Homogeneous catalysis is where the catalyst is in the same phase as the reactants. Metal based homogeneous catalysts are generally well defined organometallic compounds which may be synthesised with a high degree of purity. As such, and at least initially, such systems present only one form of active site to the substrate molecules. In essence it is easier to 'fine tune' the processes involved, for example by the exchanging of ligands around the metal centre, in order to maximise the results of the catalytic reaction. Therefore homogeneous catalysts generally yield a high level of selectivity and, in general, activity than their heterogeneous analogues. Such systems are in essence also much easier to study; the reaction occurring in the solution phase can be readily characterised by using a battery of standard techniques such as infrared spectroscopy and nuclear magnetic resonance.[5,6] However, these

characterisation techniques do not yield detailed structural information and in situ experiments are often very difficult. Techniques such as UV-Vis spectroscopy have been applied in a time resolved, in situ manner in the past,[7] but the information gleaned from such experiments has been limited to the technique itself (this being specific electronic transitions in the case of UV-Vis spectroscopy).

Moreover, as the reactants, products, and the catalyst itself exist in the same phase, separation of these components and reclamation/recycling of the catalysts can be problematic. There are also issues of catalyst degradation and high development costs; hence a main use for homogeneous catalysts is in industries where small batch reactions for pure and selective products are demanded, i.e. in the pharmaceutical industry.

These problems are minimised when the catalysts, products, and reactants exist in differing phases, as is the case with a heterogeneously catalysed reaction. The main advantage here is the ease in which reaction products can be separated from the catalyst; which becomes especially pertinent when considering (for example) large-scale industrial processes.[4] Another advantage is that such catalysts generally have a higher thermal stability than their homogeneous counterparts; which can lead to improved efficiency and reaction rates. However, the use of solid catalysts leads to a greater potential for unwanted 'side' reactions and therefore decreased selectivity- the surfaces of the active phase and support material are heterogeneous in an unwanted sense.

In heterogeneous systems the concept of dispersion is used to describe the effective concentration of (potentially) active metal sites. Simply stated as the fraction of (active phase) atoms existing at the surface of the catalyst, this recognises the fact that only active phase atoms at the surface of supported particles will be available for reaction. Therefore, by using a high area dispersant, such as alumina, and nanoscale active phase particles, very large effective concentrations of the active particles exist and therefore high turnovers can be achieved. This simple notion is, however, predicted on the assumption that the reactive properties of the active phase are not adversely affected by the increasingly smaller size of the active phase particles required to obtain the greatest dispersion. The high proportion of exposed and hence potentially 'active' atoms means a definite catalytic advantage over other similar heterogeneous systems. These low dispersed systems include single crystal and thin

film analogues which, explained below, can exhibit markedly different catalytic behaviour to highly dispersed systems.

The ideal situation would then be to obtain a heterogeneous catalyst system, with as many types of catalytic site specifically contributing to the overall catalysis occurring, and very large surface areas, whilst allowing the diffusion of reactants and products through the system at a rate which does not make mass transport the rate limiting step.

To this end, considerable research has targeted the development of systems that incorporate the practical benefits of heterogeneous catalysts with the obvious advantages of homogeneous systems. [8] These 'hybrid' catalysts typically consist of transition metal compounds being supported on a surface without significant alteration of the structure of the catalyst. [9] This can lead to a catalyst system that is highly selective, reproducible and efficient. However, this is not commonly the case as anchoring of a metal to a support often leads to a change in the overall properties of that particular metal.

1.3 Transition metals as catalysts

There are many parameters that affect the overall selectivity and activity of a catalyst. The scope of these parameters are extremely diverse; factors such as type of metal used; the active site, particle morphology (i.e. size/shape), the type and porosity of the support used, the inclusion of promoters to the catalyst composition, and experimental conditions are just a few general parameters to be considered.

The examples of the effects these parameters are, not surprisingly, equally as wide ranging; catalysis can be promoted by alkali metal doping; [10] deactivated by sulfur poisoning[11,12] or influenced by the support used such as strong-metal-support interactions (SMSI) in TiO_2 supported rhodium catalysts.[13]

The parameters that distinguish transition metals (TM) from the other elements in the periodic table are due mainly to their partially filled *d* shells. Due to the specific properties this characteristic brings about, transition metals play a key role in a wide range of catalytic systems; reasons for which can be summarised under four general headings:

(i) Bonding ability

A *d*-block metal has nine valence shell orbitals available with which it is able to form sigma (σ-), and pi (π-), bonds with other ligands. This feature is simplified and effectively visualised in figure 1.2 which shows the main bonding features in a TM carbonyl complex, based on the Blyholder model.[14]

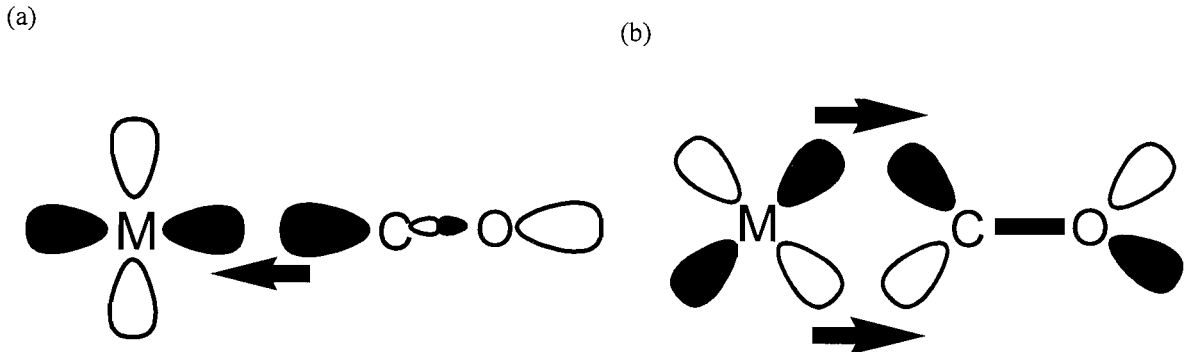

Figure 1.2: Molecular orbital schematic of a CO molecule bonded to a transition metal showing (a) the σ-component and (b) the π-component. The arrows indicate the net transfer of electrons.

The most important contribution to the bonding is the dative bond. This σ-component is formed by the interaction between a vacant metal σ-orbital and the carbon-lone pair. The π-component of this system is formed because the empty antibonding *p* π- orbitals on the carbon monoxide have the ideal symmetry to accept the electron density from the occupied metal *d* orbital.

The σ-component results in a net transfer of electron density from the ligand to the metal; the π-component in a net transfer in the opposite direction. The bonding is synergistic and results in an increase in the metal-carbon bond order and decrease in the carbon-oxygen bond order.[15] Transition metals can therefore combine with a wide range of molecules; indeed the rich coordination chemistry displayed by the systems underpins their suitability for catalysis. Such ligands can include ionic molecules such as CN^- or OH^- or neutral molecules such as H_2O and amines. Both catalytically 'active' and spectator ligands are observed to play vital roles in determining the activity and selectivity of a certain catalyst.[16]

(ii) Ligand effects

Ligands play a key role in transition metal catalysis; they can directly modify the electronic and steric environment at an active site. They also therefore have the potential to alter the properties, such as activity, of a catalyst and directly influence other factors such as controlling the overall reaction process. Generally, three models are used to predict the effect of ligands around a transition metal centre:

(a) The trans-effect. This is the labilisation of ligands trans to certain other ligands, which can be regarded as trans directing ligands. This electronic effect occurs in orbitals formed from metal-ligand bonds; an increase in orbital-orbital interaction is observed when two ligands are placed mutually trans to one another. Highly active trans-effect ligands are used in catalyst systems where the rate determining step is ligand or substrate dissociation.[17]

(b) Electron donor-acceptor properties. This concept can be explained by taking the example of CO bound to a transition metal as shown in figure 1.2. According to the Blyholder model, the electron backdonation from the metal to the empty π^* orbitals of CO takes place, resulting in a lower bond strength between C and O. This has an effect of shifting the infrared absorption band to lower wavenumbers compared to gas phase CO (ν = 2143 cm^{-1}). CO that is bound in a linear position to the metal surface has a C-O stretching frequency in the region of 2100-2000 cm^{-1}. CO coordinated in multiple, bridged positions weakens the C-O bond further, which results in the stretching frequency shifting to even lower wavenumbers.[18,19] The position of the stretching frequency can be influenced by numerous factors which in turn make this model structurally sensitive. Such factors include the adsorption site being on edges, corners or faces,[20] the overall surface coverage of the ligand (which can introduce dipole-dipole interactions),[21,22] and the amount of backdonation by the metal to name a few examples.[23,24] In summary, the coordination chemistry involving transition metals is intrinsically linked to the electron donor-acceptor properties of the ligands, changes in these properties may be probed by structurally deterministic techniques such as IR spectroscopy.

(c) Cone angle. The cone angle is used to explain certain steric influences around a metal centre; it is a crude yet effective method of the steric demands of a ligand. Basically, the wider the angle of the cone, the greater the steric influence of the ligand will be. This would result in an increase in steric hindrance for the catalytic reactants and the associated intermediates (which could have a positive or negative effect on the overall reaction). For

example, Tolman explained the steric influences arising from trivalent phosphorus ligands with this method.[25] It was found that the bulky constituents increased the cone angle, having the effect of lowering the coordination numbers of the intermediate TM complex, the formation of less sterically crowded isomers and increased rates in subsequent dissociative reactions.

(iii) Variation in oxidation state.

The ability to form complexes in a variety of oxidation states is a key characteristic of transition metals. In terms of catalysis, as transition metals can exhibit a range of oxidation states the catalyst itself has the potential to change its oxidation state during a reaction. Indeed, it is this property that plays a key role in terms of the activity and why transition metals make good catalysts.

(IV) Variation of coordination number.

The coordination number is defined as the sum of the total number of neighbours of a central atom in a compound. A key characteristic of transition metal complexes is their ability to contain a number of different ligands. For example, the coordination sphere is observed to change many times during the hydrogenation reaction catalysed by $RhCl(PPh_3)_3$.[26] In highly dispersed particulate systems, such as the ones under scrutiny in this study, the attainment of coordination information can be an extremely effective method in following the structural changes that may be occurring during a catalytic process. The variability of coordination number will therefore will be central to the current study, as it will be used extensively to characterise the systems under investigation.

1.4 The alteration of electronic and catalytic properties of noble metal particles

The concept of the electronic structure of metal particles being intrinsically linked to its cluster size has been known and studied for a long time. For example, early XPS studies by Mason showed that orbital binding energies are dependent on particle size for highly dispersed palladium, platinum and gold particles supported on carbon.[27] Further XPS studies probing the shifts in core and valence level binding energies of metallic clusters showed a trend of increasing binding energies with decreasing particle size.[27,28] However, much of this work, particularly pertaining to the origin of the shifts, is still under debate and both

initial[27,29] and final[29,30] state effects can be used to explain the trends occurring. These are just a few examples of the studies carried out in this extensively researched field.

The morphology of metal particles, i.e. the overall dimensions of particles in catalyst systems, is also well known to influence the catalytic activity and selectivity for numerous reactions in structure sensitive reactions.[31] This 'cluster size effect' is generally attributed in the literature to the number of specific catalytically active (geometric) sites that are present in a system. An effective example is reported by Oh and Eickel, where a 45-fold increase in the specific rate of the CO-NO reaction was observed as the alumina supported Rh particle size was increased from 10 to 676 Å.[32]

Other factors aside from particle size and geometry that can alter the electronic and catalytic properties of catalysts include the addition of promoters and the poisoning of such systems.[33,34] An effective example of improving catalyst selectivity is the addition of potassium metal to Fischer Tropsch rhodium catalysts,[35] which specifically increases selectivity towards higher hydrocarbons (in this case, alkenes).

The final pertinent factor to mention here is metal-support interaction leading to noble metal particle modification. The influence of the support has and continues to be an intense field of research; such interactions on noble metal catalytic activity was proposed as early as the late 1950s.[36] For example, metals supported on TiO_2 were found to have higher activities over systems supported on other oxides such as silica or alumina.[37] Moreover, some noble metal systems exhibited superior activity in catalysis when supported on an alumina-silica mix over systems supported by alumina or silica alone.[38,39] The utilisation of more ordered supports such as zeolites and mesoporous supports have reported even higher activities over their amorphous analogues.[40] It was also shown that altering the acidity of the zeolite significantly affected the catalytic behaviour, for example in numerous supported platinum and palladium systems.[41,42] The exact influence (i.e. the mechanism) the change in acidity had on the catalytic process is still under debate. In summary, attaching noble metals to a support generally improves the dispersion and catalyst stability, and can also significantly affect its catalytic behaviour.

1.5 Supported rhodium catalyst systems

Rhodium is a transition metal that is widely utilised in many catalytic processes. It differs from other platinum group metals (e.g. platinum and palladium) as it has nine electrons in its ground state ($4d^8 5s^1$) outside a closed Kr core, whereas Pt and Pd have ten outer electrons. Rh salts, often used as precursors for the catalyst systems, are easily reduced to the metallic form without any deleterious H_2 uptake; that which does adsorb can be desorbed readily.[43]

It is therefore not surprising that Rh is the subject of intense research; the literature reveals Rh to be involved in many catalytic conversions. This includes the ring opening and hydrogenolysis reactions of hydrocarbons,[44,45] CO hydrogenation to produce oxygenates and higher hydrocarbons,[46] and recently asymmetric hydrogenation chemistry.[47]

Arguably the most commercially important application of Rh is in automobile exhaust catalysis,[48] where it forms a core component in three-way catalyst (TWC) systems. This is mainly due to its superior capability to remove toxic NO_X emissions in favour of environmentally benign N_2.[49] Indeed, an effective method to visualise some of the basic properties of Rh as a catalyst is to probe its role within the TWC.

1.5.1 The three-way automotive exhaust catalyst system

The use and continual development of automotive three-way catalysts have been an active and dynamic area of chemistry and other domains, such as engineering, since their commercial introduction in the early 1980s. Prior to this, emission control catalysts were purely oxidation catalysts, and the reduction of the nitric oxides was achieved via various engine modifications, namely exhaust gas recirculation.[50]

The detrimental environmental effects of exhaust emissions have seen various worldwide exhaust emission regulations, and therefore the increased use of catalytic converters. Other stringent laws such as the Zero Emission Vehicle and emission standards have led to the perpetual development of these catalysts and all the related systems involved.[49] For example, the USA's Environmental Protection Agency (EPA) set stringent performance targets in 2004 for TWCs to reduce combined NO_X and HC emissions from 12 to 3 gram/BHP-hour or

less. A further push for technological improvement has been mandated for 2007, where a decrease to 2 gram/BHP-hour of emissions will be imposed.[51]

The TWC therefore performs three simultaneous tasks:

1). The removal of NO:

$2NO + 2CO \rightarrow 2CO_2 + N_2$ (redox reaction)

$2NO + 2H_2 \rightarrow N_2 + 2H_2O$ (Hydrogen reduction)

2). The removal of CO:

$2CO + O_2 \rightarrow 2CO_2$ (CO oxidation)

$CO + H_2O \rightarrow CO_2 + H_2$ (water gas shift)

3). The oxidation of unburned hydrocarbons (HC) to carbon dioxide and water:

$C_XH_Y + nO_2 \rightarrow XCO_2 + nH_2O$

These three reactions occur most effectively when the catalytic converter receives exhaust from an engine that is running at the 'stoichiometric point' (Lambda) (for example ca. 14.7 parts oxygen to one part fuel for petrol). Figure 1.3 highlights the problematic 'balance' a TWC must conform to, which in turn is directly linked to its overall performance as a catalyst.[52] In lean, oxidising conditions, the oxidation of CO and hydrocarbons are favoured at the expense of the reducing reaction. Conversely under fuel rich conditions the reduction of NO_X is favoured, at the expense of CO and HC oxidation. It is thus theoretically possible to attain 100% conversion efficiencies at the stoichiometric point, recently TWCs have been developed that can operate at ca. 90% efficiency.[52]

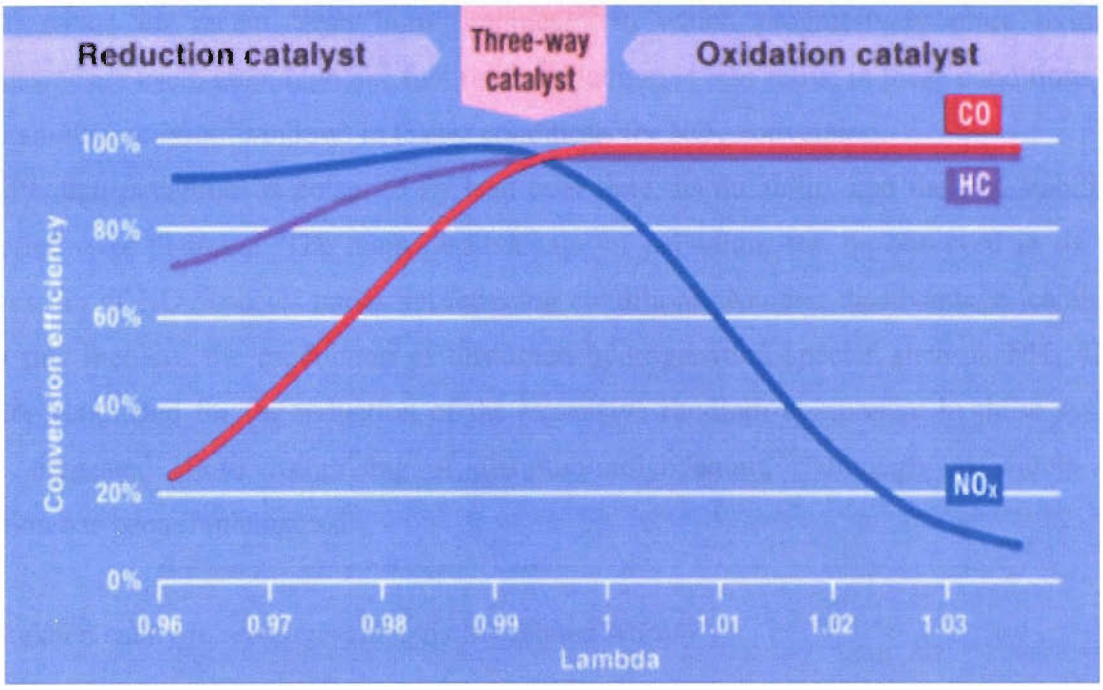

Figure 1.3: Exhaust gas conversion in the three-way catalyst.[52]

The typical 'ceramic monolith' catalytic converter is composed of cordierite ($2MgO.2Al_2O_3.5SiO_2$) in a honeycomb structure. This is covered with a layer of alumina, 30-50 μm thick, which acts as a support for all the metals. Other additives such as ceria are added to increase the durability and performance of the catalyst. The catalyst composition varies with application, but the primary metal constituents in the majority of three-way catalysts are rhodium, palladium and platinum.

The increasing use of palladium, for the effective oxidation of CO and hydrocarbons, in the bimetallic system over the use of platinum is due to the increased durability under high temperature oxidising conditions and lower light-off temperature such systems exhibit. However, the relative use of Pt and Pd in catalyst formulation fluctuates in response to the cost, and other economic factors, of these metals.

The recent interest in replacing rhodium and/or platinum with palladium due to these economic factors has lead to extensive studies into the effectiveness of the idea.[53] As mentioned before, rhodium is favoured over all three metals for the reduction of NO_X species. It also has comparatively high activity, low ammonia production and a NO_X conversion 'window' that extends to leaner or more oxidising conditions. This has significant

ramifications for recent 'lean burn' engines,[54] in which progressively more oxidising conditions are used, i.e. a high air: fuel ratio. Palladium is less active in these conditions, and has a smaller activity 'window' in leaner conditions for NO_X conversion.

Although palladium is poisoned by lead over time, its durability and thermal stability is preferred over platinum. The main disadvantage of palladium can be observed in its poor conversion of NO_X species under net reducing conditions. Another disadvantage leading on from this includes the production of unwanted hydrogenation species such as NH_3. Other studies conducted for the reduction of the expensive rhodium component in these systems have suggested alloys comprising of platinum/molybdenum,[55] although no widely used solution has been implemented.

1.6 Related catalytic reactions and existing related work

The principle catalytic reactions that occur over the surface of the catalytic converter form a basis of understanding of the processes that occur over the systems investigated in this study. The main target of engine management systems is the stoichiometric balancing of exhaust streams to yield a simultaneous reduction of NO_X products and oxidation of CO/hydrocarbons. In this sense the two principal and heavily studied reactions are the CO/NO reaction over rhodium and the reduction of NO by H_2 and hydrocarbons. Many models of the mechanism of the CO/NO reaction over Rh have been proposed in the past,[56] yet debate still lies in a unified view of the mechanism and the related kinetics of the reaction.[57] Figure 1.4 highlights a widely regarded mechanism, proposed by Hecker and Bell,[49] of the reaction between NO and CO over rhodium. This can be summarised as the decomposition of nitric oxide preceding the removal of the oxygen from the catalyst via a reaction with a reducing agent, in this case CO.

$$CO \rightarrow CO_a \quad (1)$$

$$NO \rightarrow NO_a \quad (2)$$

$$NO_a \rightarrow N_a + O_a * \quad (3)$$

$$NO_a + N_a \rightarrow N_2 + O_a * \quad (4)$$

$$2N_a \rightarrow N_2 * \quad (5)$$

$$CO_a + O_a \rightarrow CO_2 * \quad (6)$$

$$NO_a + N_a \rightarrow N_2O * \quad (7)$$

$$N_2O \rightarrow O_a + N_2 * \quad (8)$$

- * indicates irreversible reaction.
- Reaction 5 is thought to be the rate limiting step. The recombination of N_a is shown to be a function of Rh particle size, an issue addressed in this study.
- Reaction 7 is the reaction to be minimised, or eliminated in an 'ideal' catalyst.
- Subscript (a) indicates an adsorbed species.

Figure 1.4: Mechanism of the NO/CO reaction over Rh.[49]

This reaction occurring over Rh, as with all the processes, is sensitive to the changes in the surface morphology of the incipient metal, i.e. differing kinetic behaviour ensuing over single crystal and supported catalysts.[58] In relation to this study, the concept of understanding and deriving the relationships between structure and reactivity, a widespread aim in many areas of science, comes into focus. In catalysis specifically, this aim is at the centre of understanding how a catalyst functions. This in turn means that factors such as catalyst design and modification can be rationalised, and if properly understood an 'optimal' catalyst system can be designed.

The CO/NO reaction (figure 1.4) is shown as it occurs over metallic rhodium. The widespread view of the Rh component in such catalysts, and one that underpins the axiom that single metal crystals[59,60] may be utilised as reasonable models of these systems, is of an essentially static metallic phase over which the processes outlined above occur. This is despite many studies acknowledging and addressing this 'pressure gap' issue (between low and highly dispersed Rh systems) in the past.[61]

However, Rh nanoparticles are not static but labile in some environments. The corrosion of very small Rh particles under CO to yield supported $Rh^{I}(CO)_2$ species has been known

and studied since 1957.[43] The driving force for this phase transforming process has been rationalised with relatively simple thermodynamic arguments based upon the molecular heat of adsorption of CO on Rh, and estimates of Rh-Rh bond energies in such particles.[57]
That this process is generally agreed to proceed via molecular adsorption of CO, this factor also limits the range of Rh particle size that may be corroded in such fashion. Therefore where quantification has been undertaken this pathway is only significant for very small, very highly dispersed, Rh particles containing on average only ca. 10 atoms.

The contribution that this reaction path has under realistic catalytic conditions is not well known though the $Rh^{I}(CO)_2$ species has been shown to be a 'spectator' in CO oxidation catalysis.[62] However, it is also known that this species is thermally labile and susceptible to reduction by H_2.[63]

Recently a new type of adsorption driven process, that is demonstrably rapid and capable of instantaneously oxidising particles up to 20-30Å across (containing hundreds of Rh atoms), has been demonstrated.[64] Moreover this process has been shown to be deterministic in terms of both selectivity and light off in the reduction of NO by H_2 over supported Rh catalysts.[65] This process is fundamentally different to the CO induced corrosion of small Rh particles as it is driven by the dissociation of oxidants such as NO[64] and O_2.[66,67] Molecular dissociation releases much more energy than molecular adsorption and in these cases proceed very rapidly. This results in a rapid local heating of the Rh particles leading to the potential for a rapid attainment of previously inaccessible equilibrium structures. In the case of Rh this results in an instantaneous change of phase from 'metallic' to 'oxidic' at room temperature. Single crystal Rh surfaces only show significant surface oxidation under extremely lean O/CO environments and only at temperatures in excess of 500 K.[68,69,70] A metallic Rh phase is only obtained under relatively H_2 rich conditions and at temperatures where the new oxidised phase itself is unstable (ca. 470 K).[64]

These observations help to explain why, for reactions involving NO models, based upon measurements made on Rh single crystals fail to model net reaction orders and activation energies successfully.[57] Similar effects are observed in CO oxidation.[66] By their very nature such models do not allow for gross changes in reactivity as a function of Rh particle size and therefore cannot model these sorts of metaphasic processes.

1.7 Aims and motivation for this thesis

The underlying motivation for this thesis is derived from the ever increasing importance of studying gas-solid processes in an in situ manner,[71] alongside complimentary experimental techniques to gain a thorough understanding of such processes and associated systems.

Recently the literature has reported a wide range of experiments that incorporate a multi-technique approach to study the quantitative structure function relationships (QSARS) of working catalysts at both ambient and high pressures in an in situ manner.[72] The structural technique of Extended X-ray Absorption Fine Structure (EXAFS), central to achieving the aims of this thesis, has been applied in tandem with UV-Vis,[73] UV-Vis and Raman,[74] Attenuated Total Reflection (ATR) infra red spectroscopy,[75] and mass spectrometry (MS)[76] in order to achieve such aims.

This thesis will aim to expand upon these experiments by introducing a platform that utilises EXAFS (in transmission mode) and combining it with Diffuse Reflectance Infra-red Fourier Transform Spectroscopy (DRIFTS) and MS.[76] It is clear from the literature that the processes affecting the structure of catalyst systems, for example in redox cycles, can have a significant influence on their overall performance, and often occur on very short timescales.[77,78,79] The current set up was therefore envisaged to probe the structure, function and reactivity of selected processes with a time resolution previously unattainable. In doing so it is hoped new insights into this exciting and ever important (i.e. direct links to environmental factors) field of catalysis will be gleaned. Specifically, the QSARS will be probed and rationalised for various highly dispersed, alumina supported, Rh nanoparticulate systems. These 'real' catalyst systems will be observed under various catalytic conditions, which will try to emulate 'working' conditions as closely as possible. In its broadest sense, the experiments will be investigating the processes that occur over the TWC and specifically targeting how its core component, Rh, responds to environments created in automotive applications.

To summarise the direction of this thesis, the following chapter will introduce the mentioned complimentary techniques that will be used to probe the catalysts, and also to highlight their strengths and weaknesses. **Chapter 3** will be concerned with characterising the catalyst systems in order to gain a core understanding of the systems prior to the

application of catalytic conditions. The redox cycle over nanoparticulate Rh, another 'core' processes that needs to be understood for these systems, will be probed in **chapter 4**.

Chapter 5 and 6 will investigate the adsorption process of two pertinent molecules, CO and NO respectively, upon the Rh systems under various temperatures and conditions. The latter chapter will also follow how the systems respond to reductive environments after being exposed to the NO gas. The combination of these key molecules into the gas stream will be used in **chapter 7**; moreover the CO/NO experiments will be expanded upon as each molecule will be alternated in the gas stream and the response of the systems closely followed. Finally, the poisoning of the catalysts will be studied in **chapter 8**, an equally important area of study when considering the complex 'whole' of these systems.

1.8 References

[1] P.H. Emmett, P. Sabatier and E.E. Reid, 'Catalysts Then and Now', 1965, Franklin, Englewood Cliffs, New Jersey.

[2] P. Bolton, PhD Thesis, University of Southampton, 2003.

[3] D.F Shriver, P.W. Atkins, C.H. Langford, 'Inorganic Chemistry', 1997, Oxford University Press, Oxford.

[4] W. Klein, Angew. Chem. Int. Ed. Engl.,1990, **29**, 235.

[5] C. Masters, *Adv. Organomet. Chem*, 1979, **17**, 61.

[6] B.R. James, 'Homogeneous Hydration', 1973, John Wiley, New York, New York.

[7] M. Tromp, PhD thesis, University of Utrecht, 2004.

[8] For instance: Y. Iwasawa, *Adv. Catal.*, 1987, **35**, 187.

[9] R. J. Farrauto, R.M. Heck and B. K. Speronello, *Chem Eng. News*, 1992, **7**, 42.

[10] W.D.M. Ross, *Catal. Rev.-Sci. Eng.*, 1983, **25(4)**, 591.

[11] J.T. Miller, D.C. Koningsberger, *J. Catal.*, 1996, **162**, 209.

[12] M.A. Newton, B. Jyoti, A. J. Dent, S. Diaz-Moreno, S. G. Fiddy, J. Evans, *Chem. Commun.*, 2003, 1906.

[13] B.E. Hayden, A. King, M.A. Newton, N. Yoshikawa, *J. Mol. Catal. A: Chem.*, 2001, **167**, 33.

[14] G. Blyholder, *J. Phys. Chem.*, 1964, **68**, 2772.

[15] F.A. Cotton, *Inorg. Chem.*, 1964, **3**, 702.

[16] B. Bogdanovic, *Adv.Organomet. Chem.*, 1979, **17**, 105.

[17] R. Cramer, *Inorg. Chem.*, 1965, **4**, 445.

[18] J. Xu, J.T. Yates Jr., *Surf Sci.*, 1995, **193**, 327.

[19] W.K. Kuhn, J. Szanyi, D.W. Goodman, *Surf. Sci. Lett.*, 1992, **L611**, 274.

[20] R. van Hardeveld, F. Hartog, *Adv. Catal.*, 1972, **75**, 22.

[21] F. Stoop, F.J.C.M. Toolenaar, V. Ponec, *J. Catal.*, 1982, **73**, 50.

[22] J. Evans, B.E. Hayden, G. Lu, *Surf. Sci.*, 1996, **360**, 61.

[23] L.-L. Sheu, Z Karpinski, W.M.H. Sachtler, *J Phys. Chem.*, 1989, **46**, 429.

[24] R.A. van Santen, *J. Chem. Soc. Faraday Trans.*, 1987, **83**, 1915.

[25] C. A. Tolman, *J. Am. Chem. Soc.*, 1970, **92**, 2956.

[26] J.F. Young, J.A. Osborn, F.H. Jardine and G. Wilkinson, *J. Chem. Soc., Chem. Commun.*, 1965, 131.

[27] M.G. Mason, *Phys. Rev. Lett. B.*, 1983, **27**, 748.

[28] For example: W. Eberhart, P. Fayet, D.M. Cox, Z. Fu, A. Kaldor, R. Sherwood, D. Sondericker, *Phys. Rev. Lett.*, 1990, **64**, 780.

[29] V.I. Bukhtiyarov, I.P. Prosvirin, R.I. Kvon, S.N. Goncharova, B.S. Bal'zhinimaev, *J. Chem. Soc., Faraday Trans.*, 1997, **93**, 2323 and references therein.

[30] A.R. Williams, N.D. Lang, *Phys. Rev. Lett.*, 1978, **40**, 954.

[31] B.C. Gates, *Chem. Rev.*, 1995, **95**, 511.

[32] S.H. Oh, C.C. Eickel, *J. Catal.*, 1991, **128**, 526.

[33] Y.Y. Tong, G.A. Martin, J.J. van de Klink, *J. Phys. Condens. Matter*, 1994, **6**, 533.

[34] J.A.B. Bourzutschky, N. Homs, A.T. Bell, *J. Catal.*, 1990, **124**, 73.

[35] A.J. Urquhart, J.M. Keel, F.J. Williams, R.M. Lambert, *J. Phys. Chem. B*, 2003, **38**, 107.

[36] G.M. Schwab, J. Block, D. Schultze, *Angew. Chem.*, 1959, **79**, 101.

[37] G.B. McVicker, J.J. Ziemiak, *J. Catal.*, 1985, **95**, 473.

[38] P. Marecot, J.R. Mahoungou, J. Barbier, *J. Appl. Catal. A: General*, 1993, **101,** 143.

[39] D.L. Shawn, M.A. Vannice, *J. Catal.*, 1993, **143**, 539.

[40] C. Besoukhanova, J. Guidot, D. Barthomeuf, M. Breysse, J.R. Bernard, *J. Chem. Soc. Faraday Trans. I.*, 1981, **77**, 1595.

[41] G. Larson, G.L. Haller, *Catal. Lett.*, 1989, **3**, 103.

[42] B.L. Mojet, M.J. Kappers, J.C. Muijsers, J.W. Niemantsverdriet, J.T. Miller, F.S. Modica, D.C. Koningsberger, *Stud. Surf. Sci. Catal.*, 1994, **84**, 909.

[43] For instance: A. C. Yang, C. W. Garland, *J. Phys. Chem.*, 1957, **61**, 1504.

[44] For instance: G. Rupprechter, G. Seeber, H. Koller, K. Hayek, *J. Catal.*, 1999, **186**, 201.

[45] K. Hayek, H. Goller, S. Penner, G. Rupprechter, C. Zimmerman, *Catal. Letts.*, 2004, **1**, 92 (and references therein).

[46] S.S.C. Chaung, R.W. Stevens Jr., R. Khatri, *Top. Catal.*, 2005, **32**, 225.

[47] For example: O. Sonderegger, G.M.W. Ho, T. Burgi, A. Baiker, *J. Catal.*, 2005, **230**, 499.

[48] For instance: H.S. Gandhi, G.W. Graham, R.W. McCabe, *J. Catal.*, 2003, **216**, 433.

[49] For instance: K.C. Taylor, *Catal. Rev. Sci. Eng.*, 1993, **35**, 457.

[50] D.F Shriver, P.W. Atkins, C.H. Langford, 'Inorganic Chemistry', 1994, Oxford University Press, Oxford.

[51] Http://www.epa.gov/epahome/laws.htm

[52] Http://ect.jmcatalysts.com/technologies-3way.htm

[53] For example: P. Araya, V. Díaz, *J. Chem. Soc., Faraday Trans.*, 1997, **93**, 3887.

[54] P. Araya, C. Ferrada, J. Cortés, *Catal. Lett.*, 1995, **35**, 175.

[55] N.W Cant, D.E. Angove, D.C. Chambers, *Appl. Cat. B.*, 1998, **17**, 63.

[56] P. Granger, H. Praliaud, J. Billy, L. Leclercq, G. Leclercq, *Surf. Interface Anal.*, 2002, **34**, 92 (and references therein).

[57] V.P. Zhdanov, B. Kasemo, *Surf. Sci. Rep.*, 1997, **29**, 31.

[58] A. Maroto-Valiente, I. Rodríguez-Ramos, A. Guerrero-Ruiz, *Catal. Today*, 2004, **93**, 567.

[59] E.I Altman, R.J. Gorte, *J. Catal.*, 1988, **113**, 185.

[60] W.A. Brown, D.A. King, *J. Phys. Chem. B.*, 2000, **60**, 17.

[61] For example: S.H. Oh, G.B. Fisher, J.E. Carpenter, D.W. Goodman, *J. Catal.*, 1986, **100**, 360.

[62] P. Basa, D. Panyatov, J.T. Yates, *J. Phys. Chem.*, 1987, **91**, 3133.

[63] H.F.T. Van't Blik, J.B.A.D. Van Zon, T. Huizinga, J.C. Vis, D.C. Koningsberger, R. Prins, *J. Phys. Chem.*, 1983, **87**, 2264.

[64] T. Campbell, A.J. Dent, S. Diaz-Moreno, J. Evans, S.G. Fiddy, M.A. Newton, S. Turin, *Chem. Commun.*, 2002, 304.

[65] A.J. Dent, B. Jyoti, S. Diaz-Moreno, J. Evans, S.G. Fiddy, M.A. Newton, *Physica Scripta*, 2005, **T115**, 72 (and references therein).

[66] M.A. Newton, B. Jyoti, A.J. Dent, S. Diaz-Moreno, S.G. Fiddy, J. Evans, *Chem. Eur. J.*, 2006, **12**, 1975.

[67] M.A. Newton, B. Jyoti, G. Guilera, S.G. Fiddy, J. Evans, *Chem. Commun.*, 2005, 118.

[68] C.H.F. Feden, D.W. Goodman, D.S. Blair, P.J. Berlowitz, G.B. Fisher, S.H. Oh, *J. Phys. Chem.*, 1998, **92**, 1563.

[69] J. Koshy, *Thin Solid Films*, 1978, **51**, 217.

[70] G.L. Kellog, *J. Catal.*, 1985, **92**, 167.

[71] For instance: B.M. Weckhuysen, *Phys. Chem. Chem. Phys.*, 2003, **5**, 4351.

[72] G.S. Sankar, J.M. Thomas, *Top. Catal.*, 1998, **8**, 1.

[73] J.G. Mesu, A.M.J. van der Eerden, F.M.F. de Groot, B.M. Weckhuysen, *J. Phys. Chem. B.*, 2005, **109**, 4042.

[74] A.M. Beale, A.M.J. van der Eerden, K. Kervinen, M.A. Newton, B.M. Weckhuysen, *Chem. Commun.*, 2005, 3015.

[75] J.D. Grunwaldt, A. Baiker, *Phys. Chem. Chem. Phys.*, 2005, **7**, 3526.

[76] M.A. Newton, B. Jyoti, A.J. Dent, S.G. Fiddy, J. Evans, *Chem. Commun.*, 2004, 2382.

[77] C.T. Williams, E.K-Y. Chen, C.G. Takoudis, M.J. Weaver, *J. Phys. Chem. B.*, 1998, **102**, 4785.

[78] M.A. Newton, B. Jyoti, A.J. Dent, S. Diaz-Moreno, S.G. Fiddy, J. Evans, *Chem. Phys. Chem.*, 2004, **5**, 1056.

[79] A. Suzuki, Y. Inada, A. Yamaguchi, T. Chihara, M. Yuasa, M. Nomura, Y. Iwasawa, *Angew. Chem. Intl. Ed.*, 2003, **42**, 4795.

Chapter 2. Experimental

2.1 Introduction

The investigation of the structure-function characteristics of catalytic systems requires techniques that are complimentary in nature, for a 'complete' understanding of the systems and the processes associated with them. To gain such quantitative structural knowledge of these systems Extended X-ray Absorption Fine Structure (EXAFS) was chosen as the principle technique; the focus bearing on the particular form of this method, Energy Dispersive EXAFS (EDE).

The combination of EDE and mass spectrometry (MS) to study catalysts, tested in a microreactor-based environment, allows for structure and reactivity information to be gleaned from a system simultaneously, the key components in such in situ experiments. This methodology is further developed and expanded by including time resolved Diffuse Reflectance Infrared Fourier Transform Spectrometry (DRIFTS) to probe/study the speciation of IR active surface adsorbates. Therefore both methods mentioned would provide a powerful tool to achieve the aims of this thesis.

In addition to the in situ time resolved information obtained, Transmission Electron Microscopy (TEM), X-ray Photoelectron Spectroscopy (XPS), Energy Dispersive Analysis of X-rays (EDX) and Brunauer Emmett Teller (BET) measurements were applied. TEM was used to provide information on the metal particles size present on the surface of the catalysts. With XPS further information on the chemical nature of the noble metal components, i.e. the relative composition of the particles in their bulk and at their surfaces, was obtained. EDX measurements provided quantitative elemental analysis, including the total metal loading on and the amount of chlorine retained in the systems.

This chapter describes the experimental methods utilised in this study, as well as the description of the techniques applied, in both a practical and theoretical manner. The strength and limitations of the different techniques, especially in view of the catalytic systems studied, are also discussed.

2.2 Basic considerations

A number of the techniques used in this thesis involve the detection of electrons that are emitted or scattered from the sample. As such these spectroscopies share a number of common principles and characteristics. For instance, XPS and XAFS share core hole generation as the initial excitation event. All of the spectroscopies used utilise the fundamental physics of electron-matter interactions in differing ways to yield their specific information. Considering the underlying physics of these techniques leads to a clearer understanding as to why such techniques are employed in this thesis.

2.2.1 Basic Processes: Elastic and inelastic processes

2.2.1.1 Elastic Processes

Elastic processes that occur within the mentioned techniques fall under three main categories, diffraction, scattering and effects due to excitation/relaxation events involving initially unoccupied molecular orbitals (e.g. XANES, see section 2.4). The scope of this study will be primarily concerned with scattering events, although diffraction from the monochromators used in the apparatus can interfere considerably with for example EXAFS measurements. Diffraction can be a useful tool in some TEM applications,[1] for example surface 3D modelling of clusters present.[2]

2.2.1.2 Inelastic Processes

Inelastic processes in this case are scattering events that lead to a loss of energy in the electron. This energy loss effectively leads to the loss of information pertaining to the initial state from whence the electron was derived and any structural information that may only be derived from electrons that have been elastically scattered, i.e. with no concomitant loss of energy.

The presence of inelastic effects has two major ramifications. The first is the generation of an 'inelastic tail' of electrons at energies where the incident energy (i.e. from an X-ray) is

less than a particular atoms core binding energy (i.e. $E < E_B$). This tail contributes to background intensities that need to be subtracted from data obtained from such techniques as EXAFS and XPS prior to analysis; excessive scattering of this sort can therefore complicate data processing and subsequent analysis.

Secondly, and more fundamentally, inelastic scattering limits the physical distance over which elastically scattered electrons may be detected, and it therefore limits the effective range over which chemical state and structural information may be derived. Figure 2.1 shows an inelastic mean free path curve.[3]

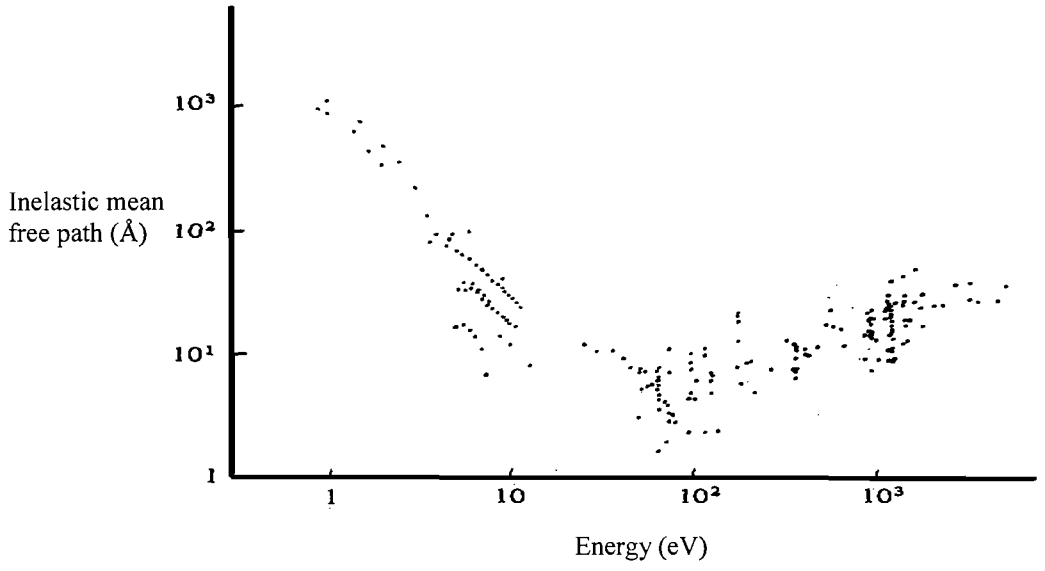

Figure 2.1: Collection of experimental determinations of inelastic scattering electron mean free paths as a function of energy above the Fermi level for many different materials.[3]

From the inelastic mean free path curve we can see that for electrons with kinetic energies typically detected in XPS (<1.5keV) that the mean free paths are relatively short (<20-30Å). It is this that gives XPS its intrinsic surface sensitivity as electrons will only escape the sample to be detected from the outer 20-30Å of the sample.

At the much higher electron energies used in TEM (ca. 100keV) it can be seen that the mean free paths of the electrons will be much greater, leading to the limiting requirement for sample thickness in TEM of ca. 1 μm.

EXAFS in transmission mode (see section 2.5.3.1) does not utilise direct detection of the elastically scattered electrons and therefore has no intrinsic surface sensitivity. In this case

however the effect of inelastic processes acts in a different way, limiting the distance over which elastically scattered electrons may travel before they experience energy loss and become non-contributory to EXAFS. As such, it is these processes that constrain the EXAFS effect to the determination of local structure information only.

2.3 X-ray Photoelectron Spectroscopy

A spectroscopy that utilises core level shifts to derive chemical state information is XPS. The technique uses a fixed (energetically) X-ray source (monochromated Al K_α, E_K=1486.6 eV, linewidth 0.35 eV for the XPS measurements carried out in this study) to eject photoelectrons from the core levels of having energy $E_B<h\nu$. These electrons are then directly detected using a hemispherical electron analyser.

Photoelectron spectroscopy is in principle a simple process. When a photon of energy $h\upsilon$ penetrates the surface of a solid and is absorbed by an electron with a binding energy E_{BE}, the electron can escape the atom with a subsequent kinetic energy E_{KE}. Equation 2.1 shows the Einstein relationship which is known as the photoelectric effect.

$$E_{KE} = h\upsilon - E_{BE} \qquad \text{eq. 2.1}$$

The distribution of the resultant photoelectron intensity with respect to its energy is therefore termed XPS. The photoionisation that occurs in fact requires a minimum of threshold photon energy for the electron to overcome the energy barrier between the vacuum and Fermi levels, which is the work function, denoted Φ.

XPS therefore involves photon excitation involving primary core level electron ejection. Following the formation of a core hole, Auger electron generation or fluorescence emission occur as secondary processes. These processes lead to separate techniques in themselves and have differing sensitivities according to the size of the emitting atom. The energy relationships in these processes are as follows:

$E_{KE} = h\upsilon - E_K - \Phi$ (XPS) Eq. 2.2

$E_A = E_K - E_{L1} - E^*_{L2,3}$ (Auger) Eq. 2.3

$h\upsilon' = E_K - E_{L2,3}$ (Fluorescence) Eq. 2.4

The L2,3 terms from the 2P energy level therefore corresponds to a Kα doublet, which is dipole allowed.

The core energy levels are measured from the Fermi energy level. The asterisk in equation 2.3 indicates the excited state after producing the core hole in level L_1. These processes can be visualised as in figure 2.2,[4] which shows an energy level diagram highlighting the fundamental XPS processes following the formation of a core hole state.

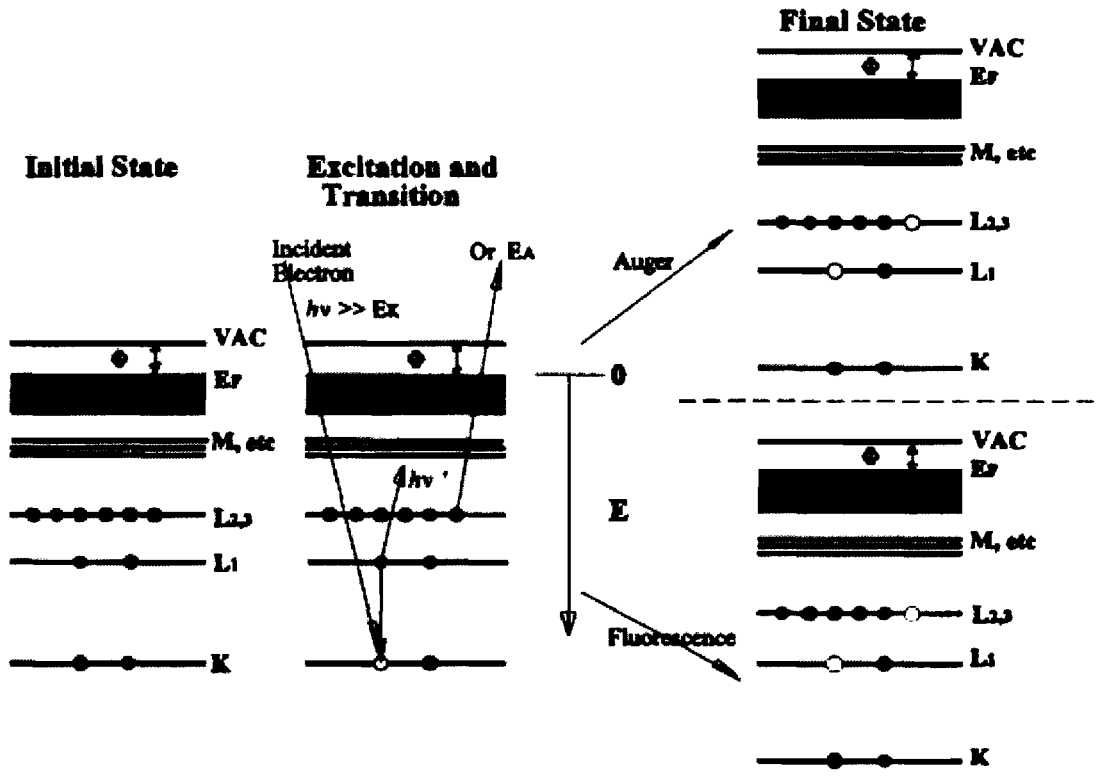

Figure 2.2: Energy level diagram showing the fundamental XPS process and Auger electron/fluorescence emission following formation of a core hole state.[4]

It is important to note here that only XPS reflects the initial state directly; Auger emission and fluorescence are the result of the final states response to the creation of a core hole.

The initial state argument here is that the E_B of the XPS electron directly reflects the effective charge felt by the initial core level electron and is therefore indicative of the chemical state of the unexcited atom. This means that core level shifts due to particle size, photoemission from surface atoms (as compared to the bulk), which do not directly reflect the initial chemical state can also complicate analysis. Therefore a relationship exists between the inherent binding energy and the chemical state of the element.

XPS measurements in the scope of this study will be used to elucidate the chemical state of the Rh elements in their 'fresh' state (i.e. systems that have been previously treated but exposed to air, see section 2.9 for full details)

2.3.1 Experimental

XPS measurements were carried out using a Scienta ESCA300 XPS analyser located at NCESS (National Centre for Electron Spectroscopy and Surface analysis), Daresbury Laboratories. An overview of the apparatus is given in figure 2.3.

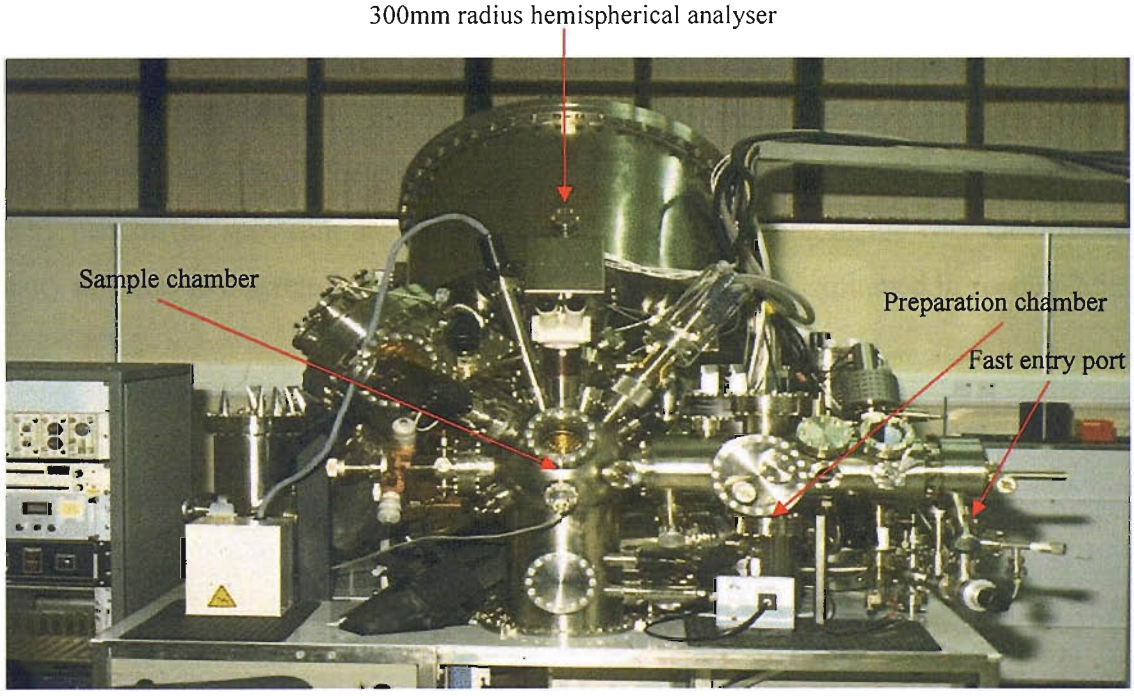

Figure 2.3: The Scienta ESCAA300 XPS analyser.

The major advantages of the machine are mainly due to the high X-ray power produced; the rotating anode has a maximum power rating of 8 kW, a factor of 13 higher than a typical power rating of 600 W for a conventional fixed anode source. A large, seven crystal, double focussing monochromator focuses the X-rays to a line image that measures 6mm by 0.5mm on the sample. The monochromated Al X-rays used yielded a net energy resolution of ca. 0.35 eV.[5]

The samples were pressed into 7 mm discs using a maximum of 1.25 tons of pressure and ca. 20 mg of sample. Samples that could not be pressed into discs were mounted onto hydrocarbon tape before analysis. The base pressure of the analysis chamber was $5x10^{-10}$ mbar, and a 'load lock' system was used for the introduction of the samples.

The compositional analysis performed on the catalyst systems utilised a different method for analysis than the discrete chemical state analysis explained above. The compositional analysis uses the total intensity measurements obtained rather than the peak positions. The analysis also relies upon the knowledge of the relative probabilities of core level excitation from each level involved.

2.4 X-ray Absorption Near Edge Structure (XANES)

Figure 2.4 shows a full XAFS spectrum, i.e. the pre-edge, XANES and EXAFS region in an absorption spectrum of a palladium foil. The XANES part of the spectrum runs from just before the edge to ~ 50 eV beyond the edge. The sharp peaks and oscillations present in this energy part of the spectrum are caused by electronic transitions of the core electron empty density of states to discrete bound valence levels, which is fully explained in section 2.5.1.

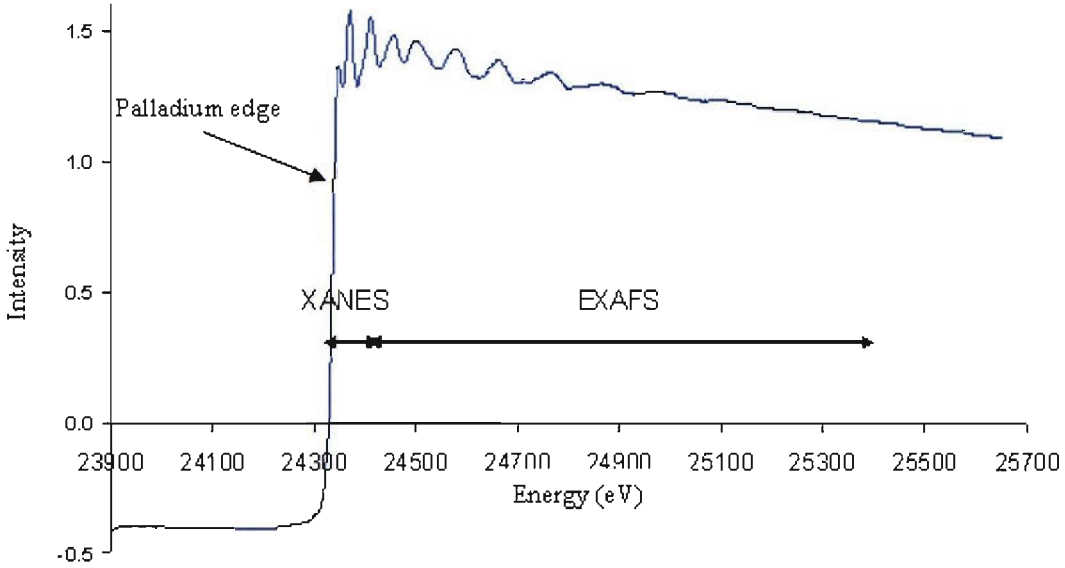

Figure 2.4: An X-ray absorption spectra of a palladium foil, highlighting the regions of interest.

XANES is therefore sensitive to the both the structural (geometry) and electronic (oxidation state) properties of the absorbing atom. Table 2.1 summarises some important characteristics associated with the XANES region, and figure 2.5 details the particular regions of interest by showing a spectrum from a Rh foil.

Region	Transitions	Information content
Pre-edge (a)	Features caused by electronic transitions to empty bound states. The transition probability is controlled by dipolar selection rules.	Reveals the local geometry around absorbing atom. Dependence on oxidation state and bonding characteristics (for example, the chemical shift of a particular element). The number and position of pre-edges gives information on the symmetry of the geometry (for example, the lowering of symmetry leads to hybridisation and orbital overlap, making more, different transitions (partially) allowed and visible in the XANES spectrum.
Edge (b)	Defines the ionisation threshold to continuum states.	General results suggest dependence on oxidation state (chemical shift); main edge shifts to higher energy with increased oxidation state. However, recent work reveals a dependence on where the final state is located,[6] i.e. either on the absorbing atom or not (causing decrease or increase in the chemical shift respectively).
XANES (c)	Features dominated by multiple scattering resonances of the photoelectrons ejected at low kinetic energy. Large scattering cross section.	Reveals atomic positions of neighbours: interatomic distances and bond angles. Multiple scattering dominates.

Table 2.1: Important characteristics associated with the XANES region.

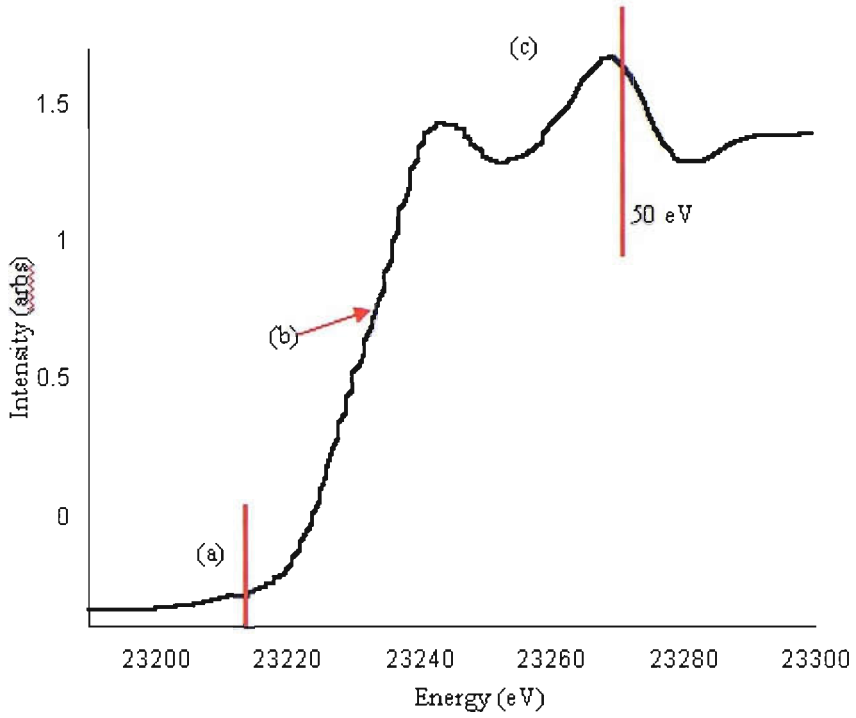

Figure 2.5: XAFS spectrum of a Rh foil detailing the; (a) pre-edge, (b) edge and (c) XANES regions as described in table 2.1.

As with XPS, to a first approximation XANES is a probe of chemical state and electronic structure, and is a direct probe of the density of states. However, as the inelastic mean free path curves of the electrons at these energies (<50 eV) are relatively short, this situation is greatly complicated by the potential for complex multiple scattering events. The EXAFS equation (described in section 2.5.1) breaks down at low k, which further complicates XANES interpretation. As such, a simple XANES equation does not exist. This means that XANES can only be described semi-quantitatively in terms of coordination chemistry, molecular orbitals, band structure and multiple scattering.

Despite the mentioned drawbacks of XANES analysis and interpretation, a number of advantageous attributes are highlighted by comparing the XANES and EXAFS techniques. In many cases XANES spectra are experimentally easier to measure than EXAFS; the features are intense and concentrated in a smaller energy region. There is a weaker temperature dependence (hence a lowered influence from Debye Waller factors, see section 2.5.2), therefore spectra are easier to obtain and interpret at reaction temperatures. XANES spectra are also faster to measure than a 'full' EXAFS spectrum; <millisecond resolution has been

demonstrated. The sensitivity to chemical information such as charge transfer and valence, and the probing of unoccupied electronic states makes it a powerful tool in this area of chemistry. Indeed, XANES is often used as a simple 'fingerprint' to identify the presence of a particular chemical species. It is therefore the notion of a compromise between time resolution and quality of data that has to be considered for experiments such as the ones in the current study. If the required information of a system can be obtained from XANES studies, then the EXAFS might be less important; there is now also a potential for the increase in time resolution.

In terms of this study, all XANES calculations and subsequent interpretations were carried out by Dr. Moniek Tromp using the FEFF8 program[7] to aid and compliment the understanding of the EXAFS results obtained.

2.5 EXAFS

2.5.1 EXAFS Theory

Extended X-Ray Absorption Fine Structure spectroscopy (EXAFS) is a technique utilised in this study to provide local structural information of the surface-supported metal species. Specifically, EXAFS is the modulation of an atom's X-ray absorption probability due to the chemical and physical state of the atom.

When an X-ray of a particular wavelength impinges upon an atom, the radiation may be absorbed. If the incident radiation is of sufficient energy, this absorption effect causes the subsequent ejection of a core electron with an energy equal to that of the incident X-ray energy minus its binding energy. This in turn results in an outgoing photoelectron wave from the absorbing atom. Modulation of this wave occurs by backscattering from the surrounding atoms. EXAFS is therefore the phenomenon of oscillations in the absorption coefficient as both the outgoing and backscattered waves interfere constructively or destructively, on the variation of the X-ray beam wavelength.

This process occurs due to the wavelength of the ejected photoelectron being dependent on its energy, and therefore the phase of the backscattered wave at the central absorbing atom will consequently change with the energy of the incoming photon.

$\mu(E)_x$ is the absorbance and can be represented by equation 2.5:

$$\mu(E)_x = [\mu(E)_s + \mu(E)_m + \mu(E)_0 + \mu(E)_{EXAFS}]_x \qquad \text{Eq. 2.5}$$

The absorbance is therefore the addition of $\mu(E)_s$, the sloping spectrometer baseline, $\mu(E)_m$ the absorption due to the matrix in which the absorbing atom is embedded, $\mu(E)_0$ the absorption observed for the corresponding free atom, and $\mu(E)_{EXAFS}$ represents the modulation in the adsorption around $\mu(E)_0$. The EXAFS intensity, represented by $\chi(E)$, is contrived by subtraction of the background components and normalisation with respect to the free atom absorption. This is represented by equation 2.6:

$$\chi(E) = \mu(E)_{EXAFS}/\mu(E)_0 = [\mu'(E)/\ \mu(E)_0] - 1 \qquad \text{Eq. 2.6}$$

A schematic view of this phenomenon is shown in figure 2.6.[8]

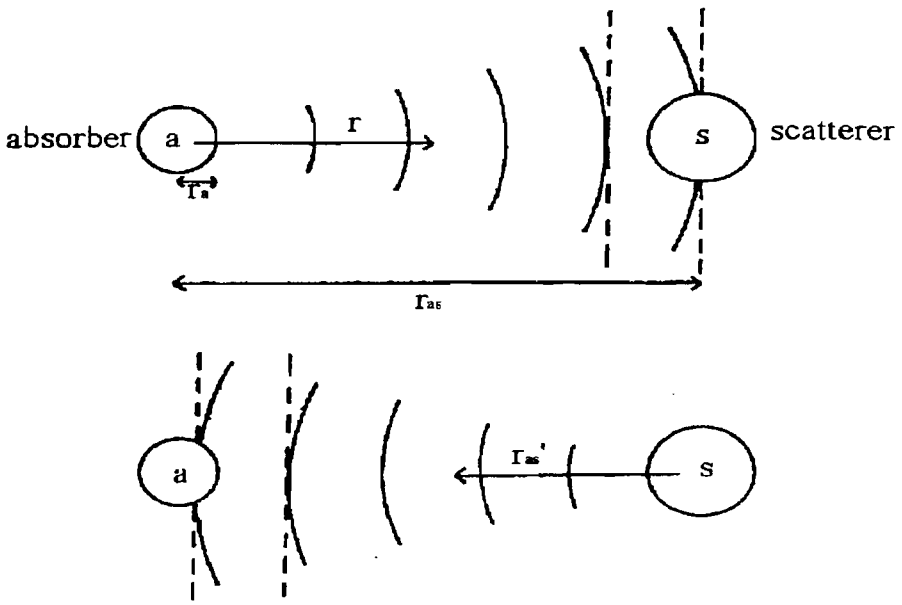

Figure 2.6: A schematic of the EXAFS scattering phenomenon.

The phenomenon of multiple scattering takes effect if an ejected photoelectron encounters more than one backscattering atom before returning to the absorbing atom. This can be a significant contributor towards the overall EXAFS.

The first consideration here is that multiple scattering effects will tend to contribute at increasing k (electron energy); this is simply a result of the increasing mean free path of the electrons. Multiple scattering is also important when considering XANES.

The multiple scattering effect will be highest for high symmetry arrangements of atoms. This is because at higher electron energies a second effect is seen. As the photoelectron energy increases, the cross section for back scattering (through ca. 360° and the principle effect used in EXAFS) diminishes. Concurrently the cross section for forward scattering (through 180°) increases. What this means is that atoms in a linear configuration, for example, and beyond the principal scatterer, will experience an enhanced flux of electrons and thus contribute to the observed EXAFS to a greater degree than they would in the absence of this effect. Figure 2.7 compares examples of the single and multiple scattering pathways.

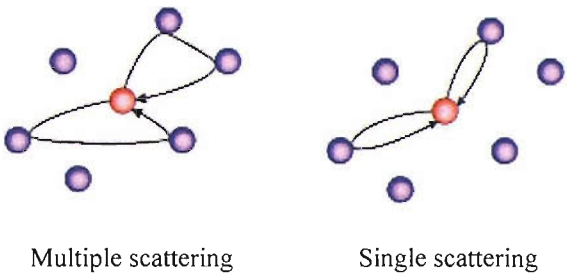

Figure 2.7: Photoelectron scattering processes.

EXAFS therefore has a significant advantage of being an analytical technique that is element specific and can be utilised regardless of the physical state of the material. Systems that are in solution, in the gas phase or amorphous solids can therefore be characterised.

2.5.2 EXAFS and Debye-Waller factors

The Debye-Waller (DW) factors associated with EXAFS are of central importance to this study due to the inherent effect it has on the EXAFS data. The Debye-Waller factor, denoted as σ^2, is consisted of two main components, caused by static and thermal disorder. An overview of the single scattering theoretical expression of the EXAFS event effectively highlights the origin of the DW factor and the relationship it has with temperature dependency in EXAFS intensities. The generally used EXAFS equation for an unoriented sample with Gaussian disorder with only one type of atom present in the *j*th coordination shell is as follows.[9,10,11,12]

$$\chi(k) = (\mu-\mu_0) / \mu_0 \qquad \text{Eq 2.7}$$

$$= \Sigma \frac{\mathbf{N_j}F_j(k)}{kR_j^2} \exp(-2k^2 \boldsymbol{\sigma_j^2}) \exp(-2R_j/\lambda) \sin[2kR_j + \phi_j(k)] \qquad \text{Eq 2.8}$$

Where $F_j(k)$ is the backscattering amplitude from each of the N_j surrounding atoms in the *j*th shell with a DW factor of $2\boldsymbol{\sigma_j^2}$ R_j away. The term $\exp(-2R_j/\lambda)$ is used to account for the inelastic losses in the scattering process with λ being the electron mean free path. The term $\boldsymbol{\sigma}$ reflects the mean squared deviation in bondlength from the average (equilibrium) bond length due to static and dynamic variations in this parameter. Equation 2.8 therefore shows the close relationship between the DW factor and the effective coordination number obtained. The static disorder stems from the fact that all the atoms within a shell are at different distances from the central atom. Additionally, the distance of an atom from the absorbing species is not constant due to thermal motion effects. Therefore atoms that are close to the central atom will move in sync, this correlation becoming weaker at larger distances. This means that shells at larger distances from the central atom will have larger DW values. Increased DW factor values will therefore be observed at higher temperatures. Increasing the DW values has a dampening effect on the EXAFS. Hence the analysis of the EXAFS data taken for this study would be affected to a large extent by the DW factors, as

temperatures of up to 673 K are used, and the determination of the correct DW factors is central to achieving the restoration of accurate spectra and hence reliable results.

In summary, the result of the EXAFS equation shows relationships that are directly related to this study, and has a direct influence on the validity of any subsequent interpretation of the data collected.

$I \alpha Ne^{(-\sigma 2)}$, therefore Eq. 2.9

$N \alpha I/[e^{(-\sigma 2)}]$. Eq. 2.10

The coordination term (N) is therefore a sensitive function of the DW factor and a small variation in the DW factor will result in a relatively large change in the value of N required to fit the measured intensity (equation 2.9). Subsequently this effect will be greater at higher k values due to the k^2 term in the exponent in equation 2.10.

An experimental methodology was developed to determine the correct Deybe-Waller factors for all the catalysts investigated in this study, which is described in detail in chapter 3.2.5.1.

2.5.3 Data Acquisition

Synchrotron radiation is highly intense, highly collimated, electromagnetic radiation which can be produced over a broad range of wavelengths, making it ideal for the acquisition of EXAFS data. The radiation is produced by the acceleration of an electron beam, by a magnetic field, to close to the speed of light in an ultra-high vacuum. The electrons are then injected into a storage ring and the electron trajectory is maintained within the storage ring by arrays of magnets that constrain and bend the path of the electrons into a circular shape. Once in the storage ring, the electrons are kept at a fixed energy until the radiation is released to the experimental stations via tangential ports. The energy of the stored electrons and the radius of curvature in which they travel determine the maximum photon energy available. Figure 2.8 shows the layout of a typical synchrotron.[13]

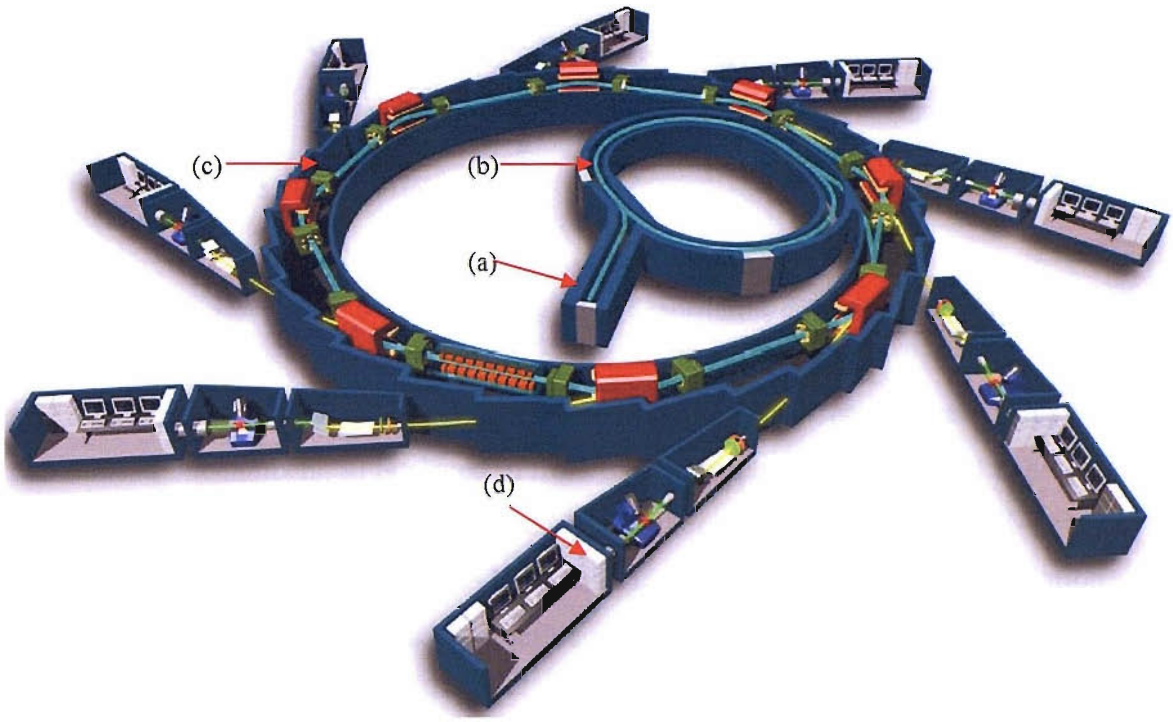

Figure 2.8: A representative layout of a synchrotron showing; (a) The linear accelerator (linac), (b) Booster synchrotron, (c) Storage ring with insertion devices and (d) experimental beamlines.[13]

EXAFS spectra were recorded at two synchrotron sources located in Grenoble, France (ESRF, beam line ID24) and in Daresbury UK (SRS, Daresbury Laboratory, Stations 3.4, 9.2 and 9.3) There are various modes that can be used to acquire data which include transmission, fluorescence and electron yield.

2.5.3.1 Transmission mode: Scanning EXAFS

In standard scanning mode, EXAFS spectra are acquired by scanning the photon energy in a step wise method. The monochromatic X-rays from the source are used to measure the absorption as a function of energy, thus producing the spectra discussed above. A schematic of a typical standard scanning EXAFS experiment is given in figure 2.9.

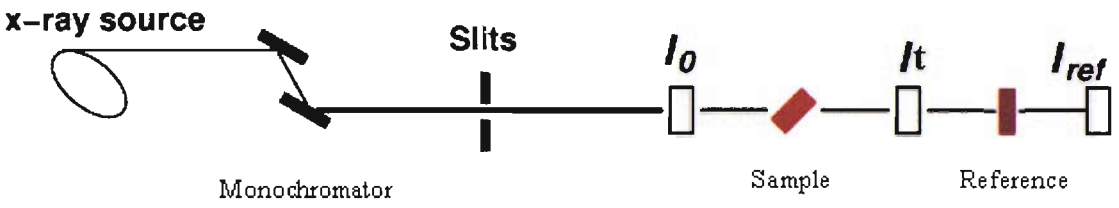

Figure 2.9: Schematic of a typical scanning EXAFS experiment, indicating the major components.

For samples in solution or as thin solid samples, EXAFS spectra are normally taken via two ionisation chambers. Io is placed in front of the sample, and I_t is placed behind in a linear arrangement. Noble gases are used in each chamber, each with differing X-ray absorption coefficients such that Io absorbs ~20%, and I_t ~80% of the incoming radiation. As the wavelength of the X-rays varies, the relative absorption is as follows (equation 2.11):

$$I_t = I_0 \exp(-\mu t) \qquad \text{Eq. 2.11}$$

[μ= absorption coefficient; t= thickness of sample.]

A reference sample such as a foil can be measured synchronously between the second and third ionisation chamber (I_{ref}) for calibration purposes.

2.5.3.2 Transmission mode: Quick-EXAFS

The technique of quick-EXAFS (QEXAFS) is a derivative of the standard scanning EXAFS experiment where by the data is obtained point by point across an energy range. The difference from conventional EXAFS lies in the continuous movement of the double crystal monochromator system across the energy range using high geared stepping motors or a dc motor with encoder. Therefore the absorption of the sample can be measured in both the forward and reverse direction. Collection times for data vary from tens of seconds to minutes, for example EXAFS spectra over a range of approximate 500 eV are now regularly collected over the timescales of seconds. Detection of the EXAFS is normally made with the standard scanning detectors as above. The QEXAFS method does have its disadvantages as the quality of data is intrinsically linked to the speed of acquisition; thus faster acquisition times will

result in lowering of data quality. However, QEXAFS still allows for all detection methods as it is still principally and practically a 'normal' scanning technique.

2.5.3.3 Transmission mode: Energy Dispersive EXAFS

As mentioned previously, EXAFS can be used for kinetic studies with regards to the often complex mechanisms involved during a chemical reaction. In addition to this, EXAFS studies can present the structures of intermediate species in catalytic systems. In order to follow the processes that may be occurring in such systems in more detail, traditional scanning EXAFS methods as described above are at a distinct disadvantage; mainly due to the inherent time scales associated with the acquisition of EXAFS spectra.

Energy Dispersive EXAFS (EDE) on the other hand is a technique that uses an elliptically bent crystal monochromator to simultaneously yield the required spectral range[14,15,16,17] which ultimately has the desired effect of drastically reducing the timescales of spectral acquisition. A typical arrangement for an EDE experiment is shown in figure 2.10. The monochromator can either be in reflection (Bragg - as shown in figure 2.10) or transmission (Laue) geometry. The bent crystal focuses the incoming X-rays onto the sample to be analysed, which is placed at the focal length of the monochromator, and a position-sensitive detector measures the intensity of the differing wavelengths present. The detectors are typically photodiode detectors or CCD cameras.[18,19] The technique has been used since 1981, where the 'multi-edge' possibility of EDE was implicitly recognised by Matsushita and Phizackerley[20] and by Couves *et al.* in 1991.[21] It is only until relatively recently however that practical applications of this unique property has been demonstrated.[22]

EDE data can only be acquired in transmission mode, and this can be a disadvantage as only concentrated samples can be subjected to the technique. Another limiting factor is the high local flux the sample experiences over a relatively small area during exposure to the 'white beam' (the focussed incident X-rays). This may lead to beam-induced changes such as local heating and degradation of the sample. It is clear from the above that whilst being a potentially powerful experimental tool, EDE experiments and sample choice can be limited and therefore careful planning (of experimental design and selection of suitable systems to be studied) must be employed.

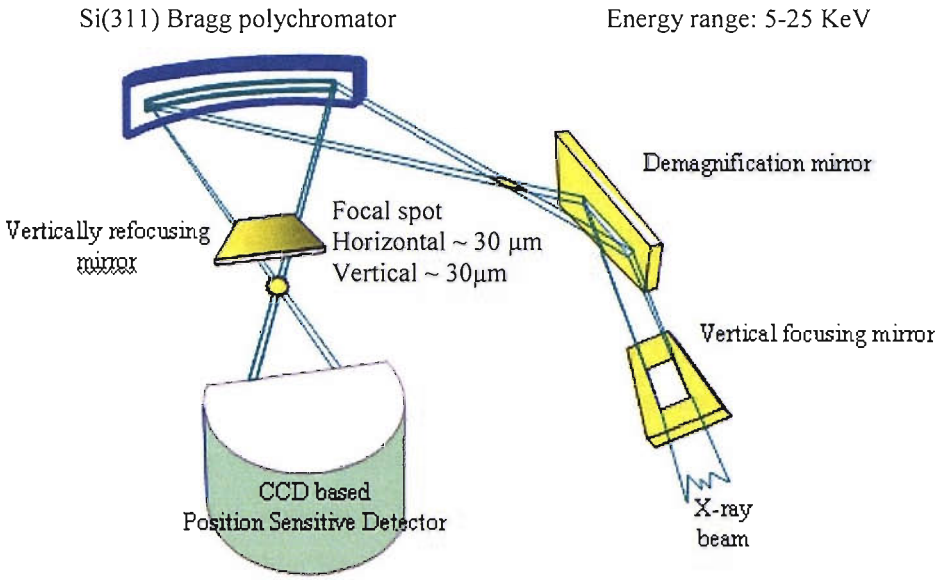

Figure 2.10: A typical arrangement for an EDE experiment, example shown shows the layout used at station ID24, ESRF.

2.5.3.4 Fluorescence mode

Fluorescence mode is used when the sample under investigation is too absorbing and cannot be diluted in any way without altering its inherent properties. It is also utilised when there is a low concentration of absorbing atoms present in the sample, i.e. in very thin or dilute samples. The fluorescence intensity is therefore the measure of absorption probability. The fluorescence yield over the background scatter is maximised (for dilute samples) by placing the sample 45° to the X-ray beam, with the detector perpendicular to the beam.

The additional technique of electron yield can also be used in these situations, and is often used to enhance the surface sensitivity of the XAFS technique.[23]

2.5.4 Experimental: Scanning EXAFS, Station 9.2, SRS

Room temperature scanning EXAFS experiments of the catalysts used in this thesis were obtained at station 9.2 at the SRS.[24]

The sample stage used was the same plugged flow microreactor set-up as described in section 2.5.7, without the heating apparatus as all spectra were taken at room temperature. In a typical experiment ca. 20 mg of a previously calcined and reduced sample was loaded into a quartz tube (ca. 3 mm id (internal diameter), wall thickness ca. 0.2 mm) and held in place using quartz wool plugs, giving a sample bed of around 5mm in length. The tube was then placed into the microreactor apparatus under a flow of He. The gases, under mass flow control at 25 ml min^{-1}, could then be introduced to the system depending on the experiment being performed.

2.5.5 Experimental: QEXAFS/MS, Station 9.3, SRS

Scanning QEXAFS measurements on the catalysts were carried out at station 9.3 using the DRIFTS cell apparatus as described in section 2.5.8. The major components experimental apparatus are outlined in figure 2.11. Measurements were made using a Si [220] double crystal monochromator. Due to unforeseen technical problems, which included insufficient space on the beamline for which to mount the experimental apparatus, DRIFTS spectra could not be recorded, but the cell did provide a viable basis for QEXAFS/MS experiments to be performed on the catalysts. This adapted technique was employed to obtain EXAFS data of higher quality and longer k range to compliment the data acquired from the time resolved EDE experiments.

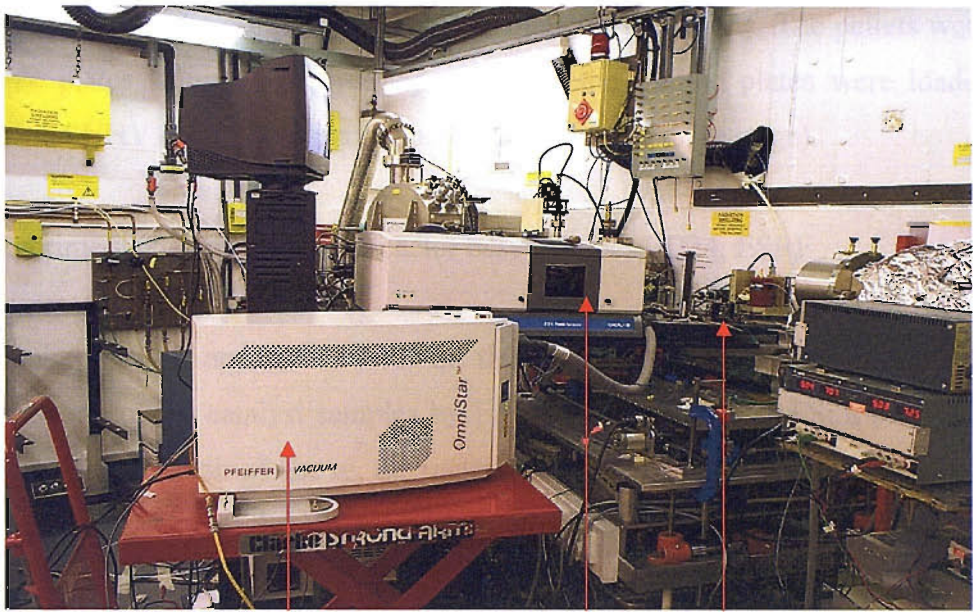

(a) (b) (c)

Figure 2.11: Photo showing the apparatus at station 9.3; (a) mass spectrometer, (b) FTIR spectrometer (not used) and (c) the sample stage (optical bench). The proximity of the hutch wall to the sample stage was one of many technical problems encountered.

A typical experiment with regards to sample presentation follows that as outlined in section 2.5.8, with the use of the DRIFTS cell and mass spectrometer only. All catalysts were pre-treated in situ prior to any experiment being performed. This entailed heating the uncalcined sample to 573 K under a flow of 5%H_2/95%He, switching to a flow of 5%O_2/He for 10 minutes, before switching back to the flow of H_2. After the required reaction temperature was reached, a flow of He was used to purge the system. After this pre-treatment of the catalyst the desired gas/gases could be introduced into the system. All of the gases used were set at a flow rate of 25 ml.min^{-1} under mass flow control.

2.5.6 Experimental: Cl K edge XAFS studies, Station 3.4, SRS

Cl K-edge X-ray Absorption Near Edge spectra (XANES) were also obtained for the systems in this study at the SRS, at beamline 3.4. A Si [111] monochromator was used and XANES spectra were obtained using total electron yield detection. Untreated and fresh samples were pressed in pellets with ~70 wt% high purity graphite. A sample amount of 10

mg was used for all the samples to be able to quantify the results. The pellets were mounted on sample plates using conductive tape. Finally, the sample plates were loaded into the experimental UHV chamber (mounted on a manipulator sample stage).

2.5.7 Experimental: EDE/MS microreactor based studies, ID24, ESRF

The microreactor apparatus used in this study is designed to allow the in situ characterisation of the catalyst samples by Energy Dispersive EXAFS; a schematic is given in figure 2.12. As explained above, the material is required to be held in a configuration that allows the transmission of the X-rays through the sample. This is achieved in this case via the use of a quartz tube as the sample holder with holes in the heater block to allow X-rays to pass through.

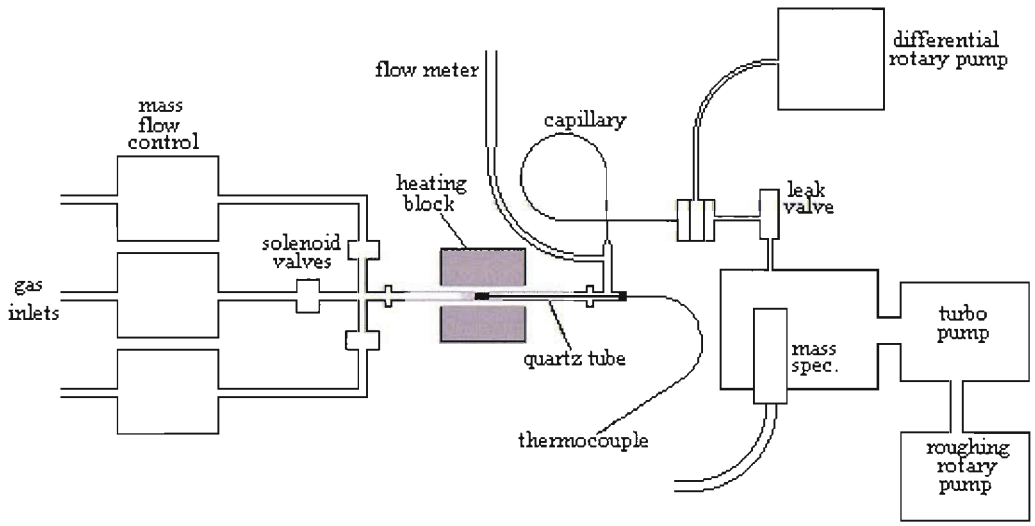

Figure 2.12: Schematic showing the microreactor set-up.

This configuration allows up to three different gases/gas mixtures to flow through the system, the flow rate of the gas controlled by UNIT 7300 mass flow controllers. The selection or mixing of the gases before they enter the catalyst bed is done via a set of solenoid valves.

Figure 2.13 shows the microreactor apparatus at ID24 in its entirety, and the heating system can also be viewed here. Figure 2.14 shows a detailed view of the sample stage. Up to

twelve 75 W cartridge heaters are inserted into a two-piece brass block, which accommodates the quartz tube. This arrangement allows the sample to be heated to ca. 673 K. For optimal temperature stability and attainment, a ceramic hood is utilised. A Eurotherm 902 series temperature controller controls the power output, and effectively the correct heating rate, to the cartridge heaters.

The mass spectrometer used in the EDE/MS studies was a Pfeiffer vacuum Omnistar mass spectrometer. Resulting ions can be detected in two ways: by the Faraday plate or an electron multiplier. Due to its sensitivity, the electron multiplier detector was used in all the EDE/MS experiments. The dynodic strip, which forms the basis of this detector, has a typical potential drop of 2 kV across it. Bombarding the cathode with ions from the analyser results in the emission of electrons. The resulting electrons are directed, by a magnetic field, back towards the dynodic strip in a cyclic path. The resulting current is increased as each impinging electron results in the emission of several more electrons. This process is then repeated at set stages along the strip towards the anode, greatly amplifying the signal.

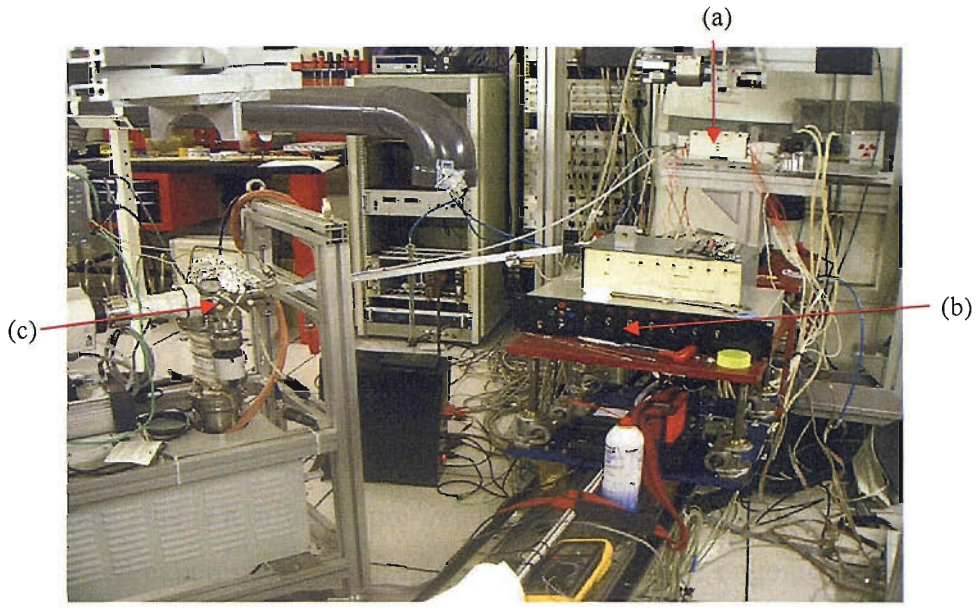

Figure 2.13: Microreactor apparatus at ID24 showing; (a) Sample stage, (b) heating equipment and (c) mass spectrometer.

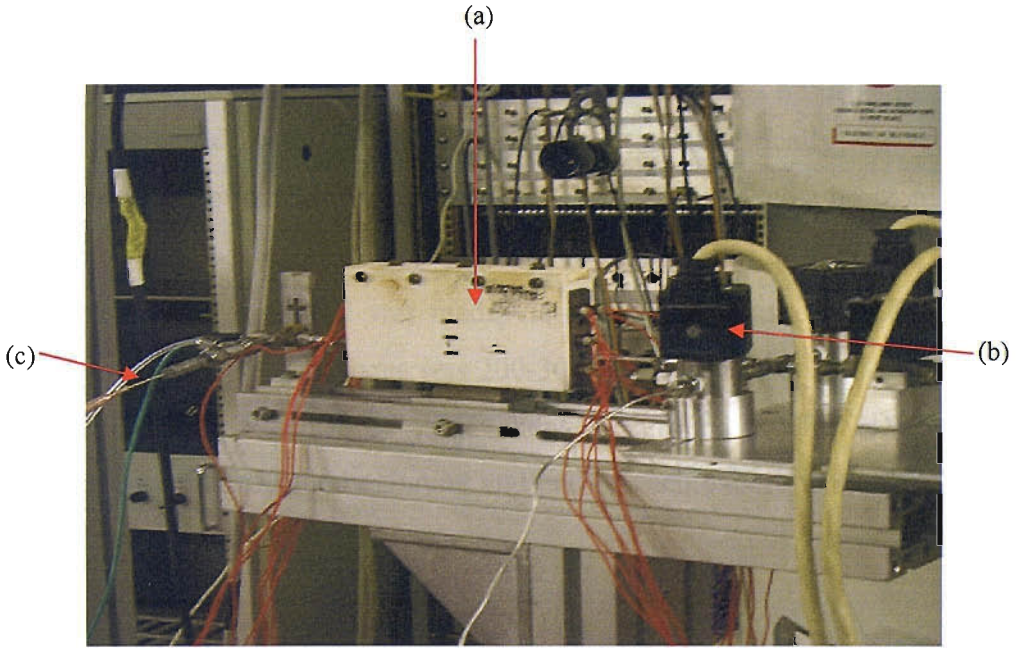

Figure 2.14: Sample stage of microreactor showing; (a) brass heating block housing the quartz tubing, (b) gas switching valves and (c) thermocouple.

A typical experimental procedure for EDE/MS data acquisition was carried out as follows. The previously calcined and reduced catalyst sample (ca. 20 mg) was loaded into a quartz tube (ca 3mm internal diameter, wall thickness ca. 0.2 mm) and held in place using quartz wool plugs, yielding a sample bed of around 5 mm in length. The tube was then placed into a microreactor and a 0.5 mm mineral insulated thermocouple was inserted directly into the catalyst bed. This allowed the sample to be heated to ca. 673 K at 10 $Kmin^{-1}$.

Each catalyst was pre-treated in situ prior to any EDE/MS experiment. This involved exposing the sample to a flow of 5%H_2/He at room temperature for ca. 30 minutes, before switching back to a flow of He, in an effort to re-reduce the sample prior to any experiment performed. (Note: This is a different pre-treatment procedure than the procedure used in the DRIFTS cell based experiments [see section 2.5.8], due to the ongoing development of the experimental method that the EDE/DRIFTS/MS entailed).

The gases under mass flow control were set to give 25 $mlmin^{-1}$ each over the sample bed. This gave gas hourly space velocities (GHSV) of ca. 10^4 hr^{-1}. The resultant composition of the gaseous products was continuously monitored via a mass spectrometer equipped with a fused silica capillary to give a constant inlet rate to the mass spectrometer. 16 relevant mass fragments were continuously monitored.

EDE measurements were performed using an asymmetrically cut (6°) Si [111] monochromator in Laue (transmission) configuration.[25] This yielded a horizontal beam focus on the sample of ca. 70-80 μm and a spread of X-ray energies of ca. 2.5 keV.[26] Detection of the subsequent EXAFS produced was made via a phosphor masked, Peltier cooled, CCD camera (Princeton). The vertical focus was 200-300 μm. The hard (>23 keV) X-ray energies passing through air was found to be an excellent background (I_0) for EDE measurements, while this was only taken at the beginning and end of each experiment to allow continuous monitoring of the sample.

2.5.8 Experimental: EDE/DRIFTS/MS DRIFTS cell based studies, ID24, ESRF

Further to the studies performed with the EDE/MS microreactor based experimental platform, the addition of DRIFTS to expand upon the spectroscopic characterisation was envisaged. The speciation of surface adsorbates by their vibrational characteristics could then be monitored simultaneously with the use of XAFS to probe the metal particles of the heterogeneous catalysts and mass spectrometry to track the gas phase composition after the catalysis bed.

Figure 2.15 shows the outline of the experimental system built for the combined EDE/DRIFTS/MS experiments. The figure shows the major components of the entire experiment, but firstly the DRIFTS cell itself must be explained in order to visualise the rest of the set up.

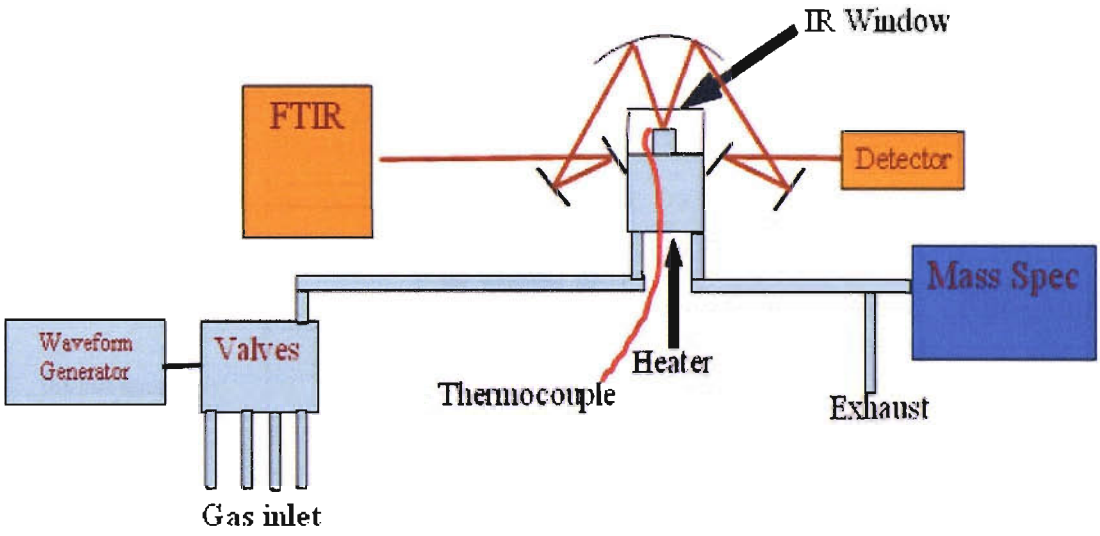

Figure 2.15: Schematic of the combined EDE/DRIFTS/MS apparatus showing all of the major components (not to scale).

The custom built EDE/DRIFTS/MS cell is based upon a commercially available optical system (Spectratech) with a modified reactor cell. An overview of the cell is given in figure 2.16.[27]

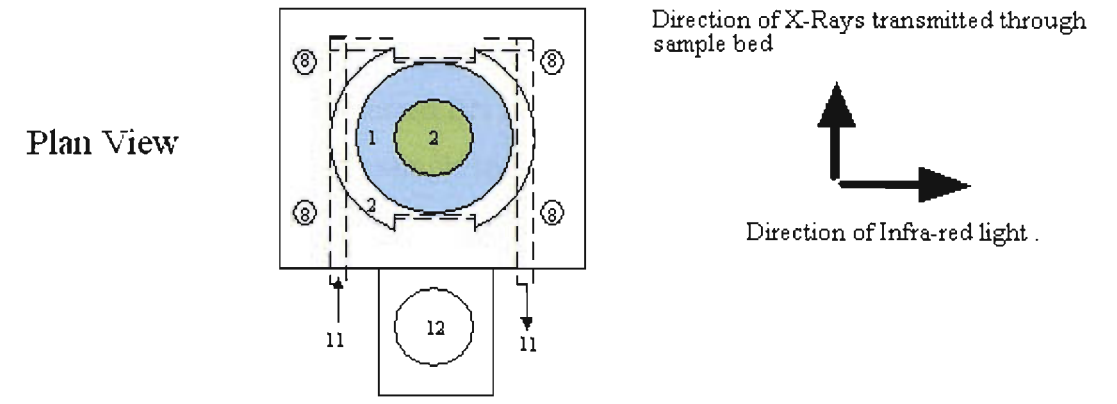

1. CaF2 window.
2. Cell with 10mm x 3mm x 0.5mm Boron Nitride windows welded/glued into sides of flange (for transmission of X-Rays; dashed box).
3. Retaining bolts for flange assembly.
4. Boron Nitride sample cup.
5. Cartridge/cable heater.
6. Pipelines for gas feed in/out,mineral insulated thermocouple for temperature measurement.
7. Stainless steel sample post.
8. Retaining bolts for cell.
9. Machineable cearamic insulation with conduits: gas feeds and thermocouples.
10. Kalrez sealing gasket.
11. Water cooling in base.
12 Mounting to micrometer drive for sample height adjustment.

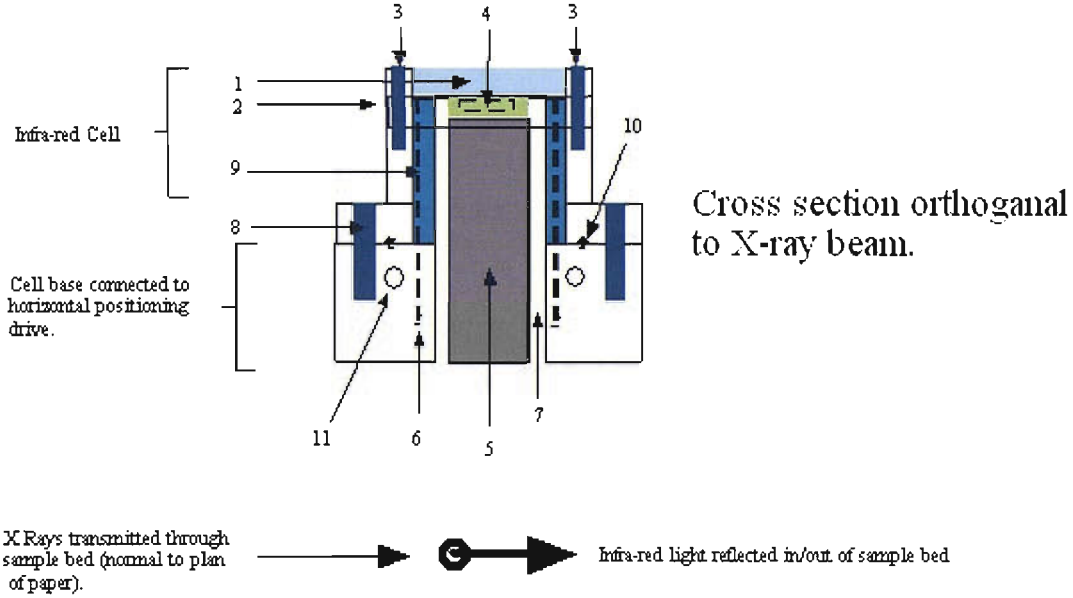

Figure 2.16: Overview of the EDE/DRIFTS/MS reactor cell.

The sample is contained within a pyrolytic boron nitride (BN) mount (5 mm id, 3 mm depth, 0.06 cm^3) to permit transmission of the X-rays through the sample. In addition the cell was X-ray windowed with hot pressed BN and IR windowed with 2mm thick CaF_2 or ZnSe. The cell allows the heating of the sample to ca. 600 K and is controlled via a Eurotherm 9300 equipped with a PC interface.

The DRIFTS cell configuration allows up to four different gases/gas mixtures to flow through the system, the flow rate of the gas controlled by UNIT 9300 mass flow controllers. The selection or mixing of the gases before they enter the catalyst bed is done via a set of four-way solenoid switching valves (VICI instruments). Downstream analysis of the gaseous feedstock was made using a Pfeiffer Quadstar 422 mass spectrometer.

The determination of the 'dead time' of the system (i.e. the time for a particular flow of gas to reach the catalyst bed) was carried out due to the planned time resolved experiments. The timescales of such experiments were in the regime where dead times could potentially have a significant impact on the results obtained. To this end, a series of 15 'dummy' experiments were performed utilising MS to accurately determine the dead time during a switch from He to 5%CO/He over previously dried Al_2O_3. The flow rates for both gases were 25 ml min^{-1}; the typical flow rate used for the experiments performed. The average of the experiments gave a value of just under 2 s (1.85 s with a range from 1.7 to 2.05 s); this has been factored into the analysis of the results in this thesis.

DRIFTS measurements were made in a geometry orthogonal to the EDE data using a Digilab FTS 7000 IR spectrometer and a linearised, high sensitivity MCT detector. The spectrometer provided satisfactory IR intensities at 64 ms per spectrum. Section 2.5.8.1 gives a brief synopsis of the DRIFTS technique.

In a typical experiment, the uncalcined catalyst sample (ca. 40-50 mg) was loaded into the DRIFTS cell under a flow of He. All catalysts were pre-treated in situ prior to any experiment being performed. This entailed heating the sample to 573 K under a flow of 5%H_2/He, switching to a flow of 5%O_2/He for 10 minutes (or until remaining carbonaceous deposits have been removed from the catalyst by observing carbon related fragments in the MS), before switching back to the flow of H_2 (all at 25 ml min^{-1}). After the required reaction temperature was reached, a flow of He was used to purge the system. After this pre-treatment of the catalyst the desired gas/gases could be introduced into the system. (Note: This is a

different pre-treatment procedure than the method used in the microreactor based experiments [see section 2.5.7], due to continuing experimental method development the DRIFTS cell based experiments entailed).

EDE measurements were made at the using either an asymmetrically cut (10°) Si [111] monochromator in Laue configuration or a Si [311] monochromator in Bragg mode. Detection was made with either the Peltier cooled, phosphor masked CCD camera (Princeton) or the fast readout FReLoN CCD camera (total acquisition time ca. 1.5 s and ca. 0.064 s per spectrum respectively). Measurements were made within the top 0.5-1 mm of the sample bed, and ideally within the first 500 microns as this is the maximum penetration of IR light onto the systems currently under study. The DRIFTS spectra were obtained synchronously to the EDE spectra, using identical repetition rates.

I_0 measurements were taken using an analogous noble metal catalyst supported on alumina placed in an identical BN mount used in the DRIFTS cell. For example, EDE measurements made for a 5wt% Rh catalyst used a 5wt% Pt catalyst as the I_0. Figure 2.17 shows Rh K edge EDE spectra taken for the 5wt% RhCl catalyst (under 5%H_2/He at room temperature) using two separate types of I_0: (A) with air (the medium used prior to this methodology) and (B) with the mentioned 'dummy' supported sample. It is clear from the figure that by using a dummy sample, far superior spectra can be obtained compared to the widely used medium of air; noted by the significantly improved the signal to noise ratio. Although not shown by the figure, the analysable data length is considerably increased (from ca. k = 12 to 14.5 $Å^{-1}$) for the same photon flux and integration time. The most likely explanation for the increase in data quality is that the dummy sample effectively mimics the homogeneity and microstructure of the sample, particularly the support material that is the main cause for detrimental scattering effects.

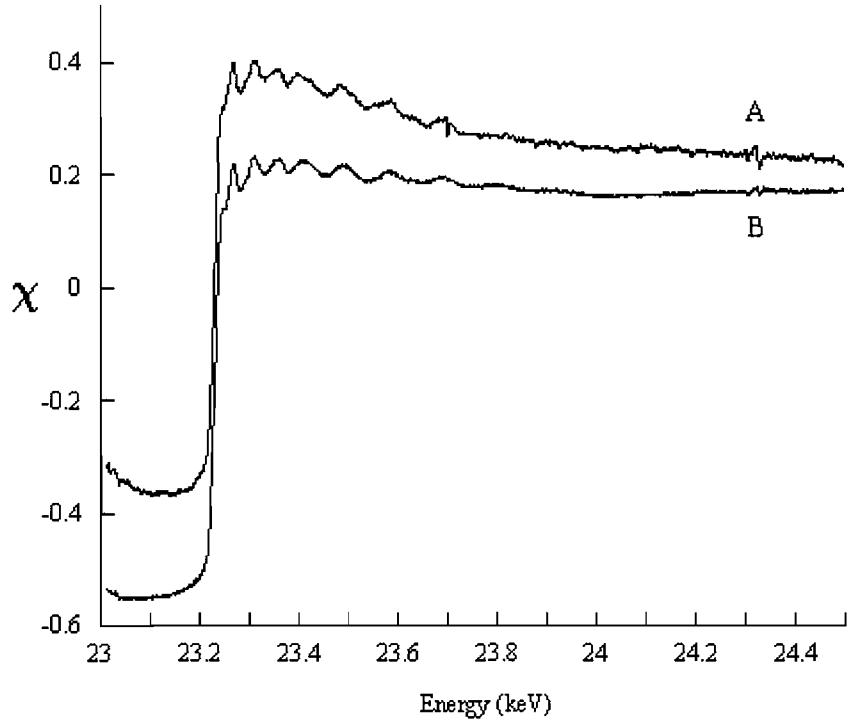

Figure 2.17: The effects of different modes of normalisation of the EDE experiment showing raw normalised Rh K edge EDE data obtained with (A) air I(o), and (B) utilising a dummy sample (see main text). The two spectra were both taken sequentially on the sample maintained under flowing 5% H_2/He at 300 K. The acquisition time for each spectrum was 60 ms.

An external trigger was used to start the experiment, which initiated the acquisition of EDE, DRIFTS and mass spectrometric data with the introduction of the reactive gas/gases under investigation all in a synchronous, time-resolved manner. The trigger could also initiate any sample heating that was required.

Figures 2.18 and 2.19 show the complete apparatus as it would be assembled in a typical experiment at ID24. Figure 2.18 shows the experiment in its entirety, whilst the DRIFTS cell apparatus is detailed in figure 2.19, showing its arrangement on the optical bench.

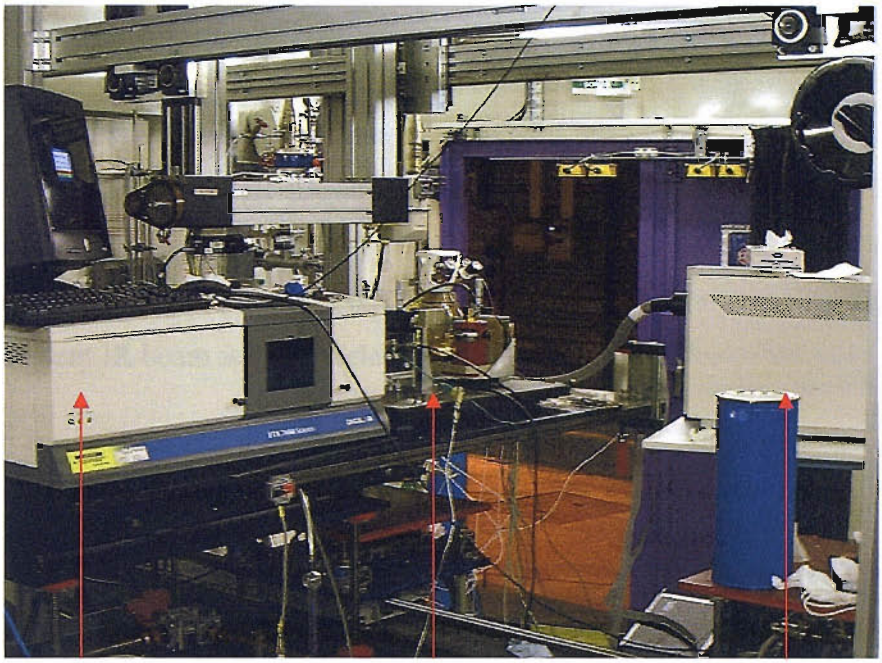

Figure 2.18: Photo showing an overview of the experiment; (a) IR spectrometer orthogonal to the X-ray beam, (b) optical bench and (c) mass spectrometer.

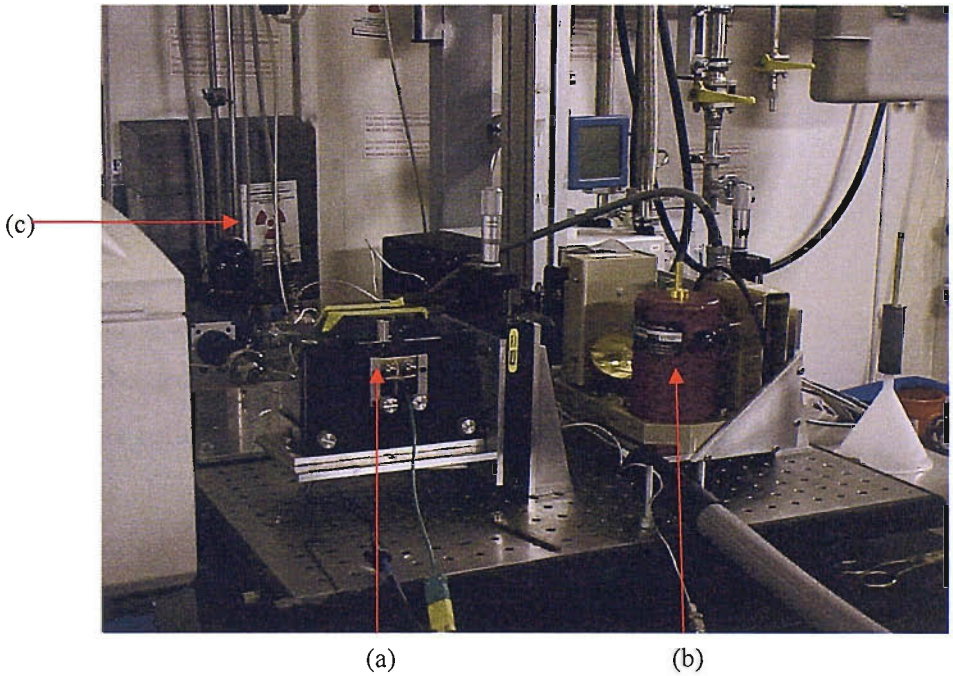

Figure 2.19: Photo showing the optical bench comprising of; (a) custom built DRIFTS cell, (b) MCT detector, (c) shutter where X-rays are admitted into the experimental hutch.

2.5.8.1 Overview of the DRIFTS technique

DRIFTS is an experimental technique that allows IR spectra of solid materials to be obtained when alternative sample preparation methods such as a pressed disc or hydrocarbon mull held between non-absorbing discs (not a 'real' representation of a catalytic bed) are not a viable option for the experiment and/or the sample itself. A schematic diagram showing the path of the incident IR beam is given below in Figure 2.20.[28]

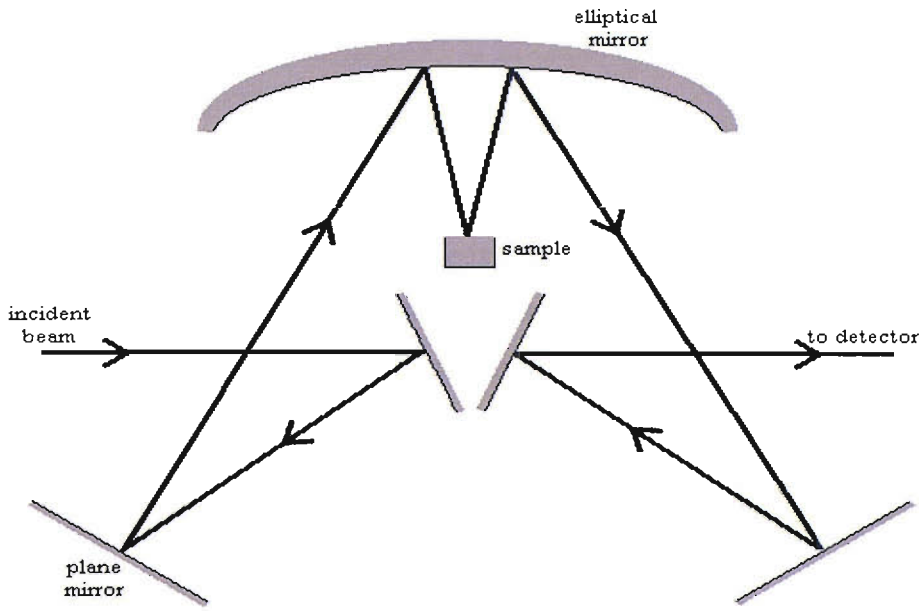

Figure 2.20: The mirror arrangement used in the DRIFTS cell

The incident beam can interact with the particles of the powdered sample in several ways. Firstly, the focussed beam can undergo mirror-like surface reflection, termed true specular reflection. This reflection occurs from the top surface of the particles only, and is a direct function of the absorptivity and refractive index of the sample. The beam can also undergo multiple reflections off numerous particle surfaces, the resulting beam emerging at random angles relative to the incident beam. This process is termed diffuse specular reflectance and is also related to the refractive index of the sample. The penetration of the incident IR beam into the particles and the subsequent scatter from the sample matrix is termed true diffuse reflectance. The resulting IR beam can emerge at any angle relative to the incident beam, but

as it has interacted with the particles it contains information of the material's absorption characteristics. Therefore it is interaction that produces the IR spectrum of the sample. However, as this process is optically indistinguishable from diffuse specular reflection, problematical data distortion can arise in certain experiments. DRIFTS data obtained in this thesis are not significantly affected by these phenomena.

2.6 EXAFS Data analysis

2.6.1 Energy Calibration

The 'raw' EXAFS data obtained was calibrated using a foil of the particular k edge being probed, for example an energy calibrated EXAFS spectrum of a bulk Rh foil was used calibrate any Rh data obtained. This procedure is explained in the following results chapters.

EXAFS data accumulated may be analysed via two stages. Firstly, the actual EXAFS spectra must be separated from the background absorption. This is called background subtraction, and is done via a computer programme by Binsted called PAXAS.[29] Another PC based program called EXCURV98 was used to fit the data.[30] The program utilises a spherical wave formalism, which fits the resulting spectrum of $\chi(k)$, the intensity, versus k, the reciprocal space.

2.6.2 PAXAS

PAXAS uses subtraction of the pre-edge background to remove the absorption due to the spectrometer. Subtraction of the post-edge background removes the absorption due to all the other elements within the system, for example any anomalous signals stemming from the monochromator. Therefore a poor post-edge subtraction can dominate the EXAFS features, resulting in the distortion of the amplitude of the EXAFS oscillations. This leads to anomalous features at R values less than 1 Å in the Fourier transform of the data. It is therefore the role of the background subtraction to minimise the effect of the peaks or features at the lower R value range. This is due in principal by setting a 'window' in R space to include only the 'real' coordination shells present. An iteration procedure is then

performed on the variables in the resulting polynomial expression and the next analytical stage is ready to be performed on the resulting data.

2.6.3 EXCURV98

EXCURV98, as explained above, utilises a spherical wave formalism which stems from the curved wave theory[31] to fit the data. The programme uses a theoretical model of the EXAFS oscillations, in conjunction with an array of algorithms, to yield structural information. The phenomenon of the ejected photoelectron wave passing through the potential of neighbouring atoms causes phaseshifts, which are calculated by *ab initio* methods.

The calculations essentially model the surrounding environment of the absorbing atom, using the nearest neighbouring atom to build the model. The following list describes the major parameters and limits to EXAFS curve fitting, and also serves as a glossary for some of the terms used throughout this thesis.

Structural parameters:

NS - The number of shells for which the model is calculated.

N_n - The number of atoms in shell n.

T_n - The type of atom in shell n.

E_{min} - The minimum energy used to calculate the theoretical spectrum.

E_{max} - The maximum energy used to calculate the theoretical spectrum.

A_n - The Debye-Waller factor for shell n, given as $2\sigma^2$, where σ is the mean square variation in interatomic distances.

E_f - The difference between the calculated Fermi level energy and the known values for the element.

AFAC - The energy independent amplitude factor that accounts for the reduction in amplitude to multiple excitations occurring at the central atom. It is different for each absorbing element, and is obtained from the analysis of model compounds.

L_{max} – The maximum angular momentum used in theory calculation.

The effectiveness of the fit can be measured by discrete values which are regarded as effective parameters and limits.

When a set of parameters is refined within EXCURVE, a minimum in the Fit Index is calculated, principally by adding the differences of the experimental and theoretical data points. Values of the Fit Index should fall between $5x10^{-4}$ and $8x10^{-4}$ to be considered a good fit.

The R-factor is used as an estimation of goodness of fit. It is calculated by the sum of all the errors between all the data points, giving the result against the experimental curve in percentage form. The R-factor should not nominally exceed 30%, but some systems such as dilute systems or the catalysts observed in this study, values of around 45% are acceptable.

DW factors are very dependent on sample and experimental conditions but as a guide the values should roughly lay between 0.004 and 0.03, the values that are used in this study do indeed fall into this range. EXAFS correlated factors such as DW and coordination values should not be refined together (or refined with caution). If such aforementioned parameters are met during analysis, the accuracy of the first shell coordination distances can be expected to be ± 0.01 Å[32] and of the coordination numbers to fall between ± 10%.[32,33] An example of the results obtained after analysis in EXCURVE is given in figure 2.21; the sample being a 7.5wt% Rh system supported on γ-Al_2O_3.

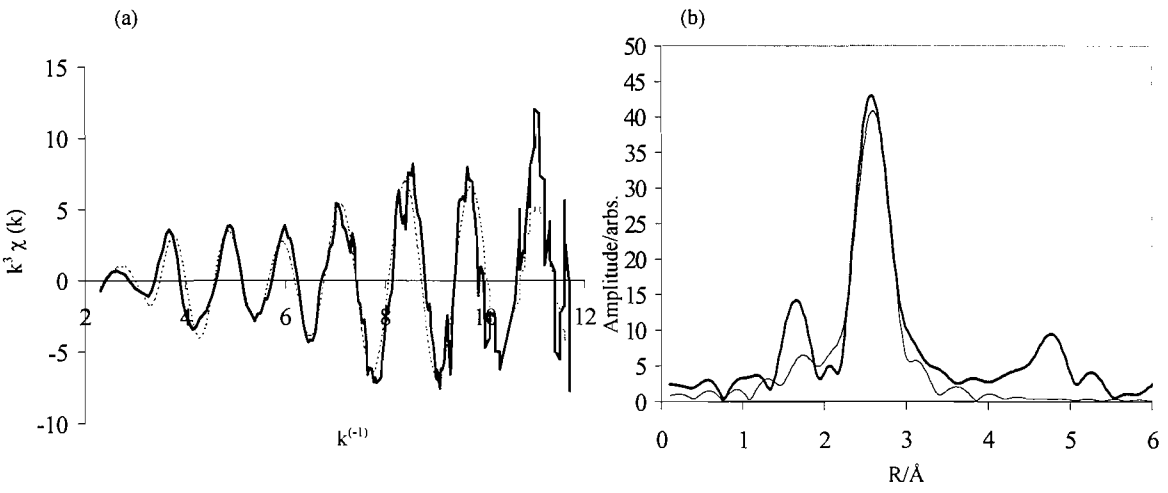

Figure 2.21: An example of the results obtained after analysis in EXCURVE (a) k^3 weighted EXAFS data, (b) radial distribution curve from Fourier transform of EXAFS, data for (a) and (b) derived from 7.5wt%Rh supported on γ-Al_2O_3 at 673 K (using the microreactor set-up as described in section 2.5.7). Dotted lines indicate theoretical fit, solid lines are from experimental data.

2.6 Transmission Electron Microscopy

An electron microscope utilises a focused, narrow beam of high-energy electrons which is directed at a specimen to be analysed. Images of the surface can then be obtained via two techniques. If the sample is thick, secondary emissions from the surface are used, called scanning electron microscopy (SEM). For thin samples, the images are formed by passing electrons through the sample, called transmission electron microscopy (TEM). The maximum obtainable resolution for an image, defined as the closest spacing between two points that can be distinguished through the microscope, is directly proportional to the wavelength of the light impinging on the sample. Electron microscopy therefore has a significant advantage over conventional light microscopy, as a beam of electrons at 100 keV has a wavelength of 0.0037 nm, compared to around 400 nm for a light microscope. Table 2.2 highlights these differences.

Type of microscopy	Resolution (nm)	Magnification	Depth of Field (μm)
Light (λ = 400 nm)	150	10^3	<1
Electron (for a 100 keV electron beam)	0.2	10^6	10

Table 2.2: Properties of light and electron microscopy

The electron beam used for TEM is generated typically between 100 and 200 keV, yielding a resolution of ~0.2 nm and a magnification $1x10^6$. TEM therefore can afford both ultrastructural and microstructural information on the specimen surface. The primary electrons that pass through the sample may be transmitted without being deflected, elastically scattered (i.e. diffracted), or inelastically scattered. Images formed in brightfield mode, for example, are the result of variable transmittance across the sample surface. This means that parts of the sample where the electron beam has passed through unhindered will appear white. Where inelastic scattering has occurred, the image appears darker. This phenomenon occurs when the mean atomic number and the thickness of sample increases, known as the mass-thickness contrast. In darkfield mode, for which the samples must be very thin (<95 nm), an image is produced by selecting a diffracted beam, and then moving the detector off the axis of the incoming electrons. The images are viewed on a scintillation screen via magnification by electromagnetic projector lenses. Figure 2.22 outlines the major components of the TEM apparatus.[34]

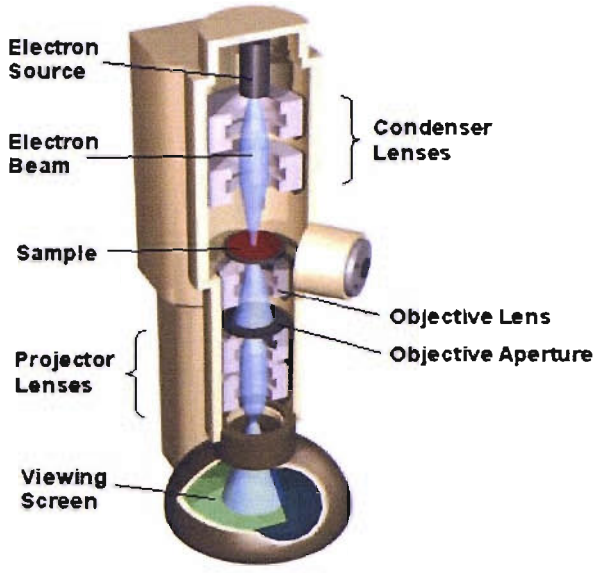

Figure 2.22: A schematic of a TEM machine outlining all of the major components.

2.6.1 Experimental: TEM

All TEM images used in this study were obtained on either a JEOL FX 2000 or JEM-3010 (the latter is shown in figure 2.23) transmission electron microscope set in brightfield mode. The samples were prepared by crushing ca 10^{-4} g of catalyst into a fine powder. Distilled water (ca. 2 ml) was then added slowly to the mortar and then ground further until a fine suspension was obtained. This mixture was then transferred to a sample vial and placed in an ultrasonic bath for at least 10mins. A small drop of the suspension was taken from the very top of the vial and placed onto a TEM copper disc with a fine carbon grid (Agar). The discs were then left to dry for 48 hours in a vacuum desiccator. Figure 2.24 shows an example of a TEM image in brightfield mode, the image has been digitally enhanced to show the particles present on the surface. Current resolution limits meant that particles under 4 Å were undetectable, which for example would have a disadvantageous effect on determining particle size distributions. The TEM machines did not have the capability for in situ experiments to be performed. i.e. the samples could not be exposed to the various reactive gases employed throughout this study. As such, all of the samples analysed with the TEM technique are 'fresh' samples, having been exposed to air.

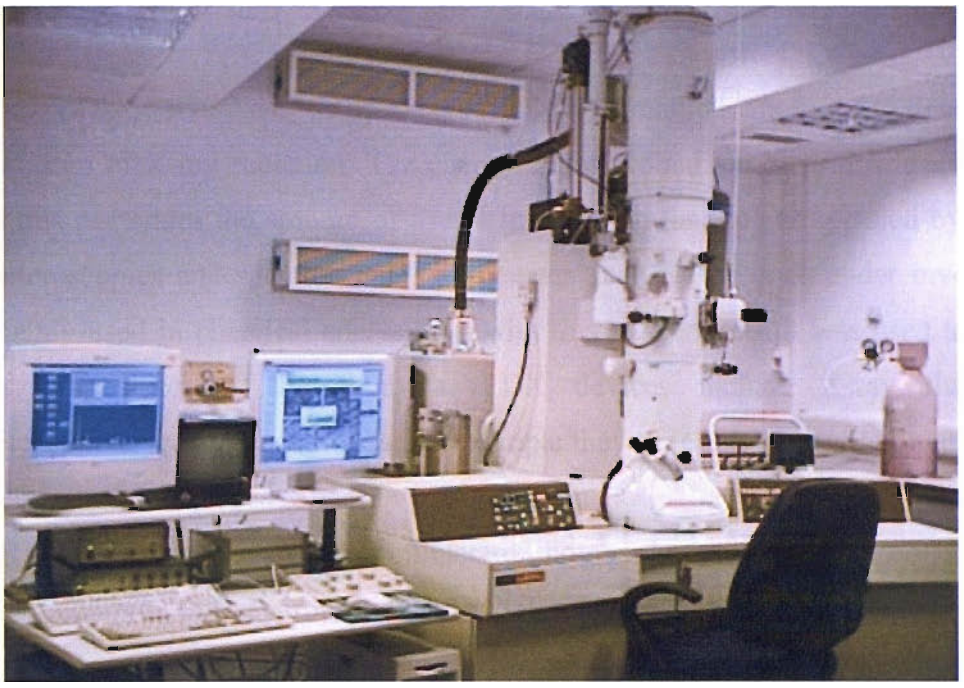

Figure 2.23: Photo of the JEM-3010 TEM apparatus used in this study.

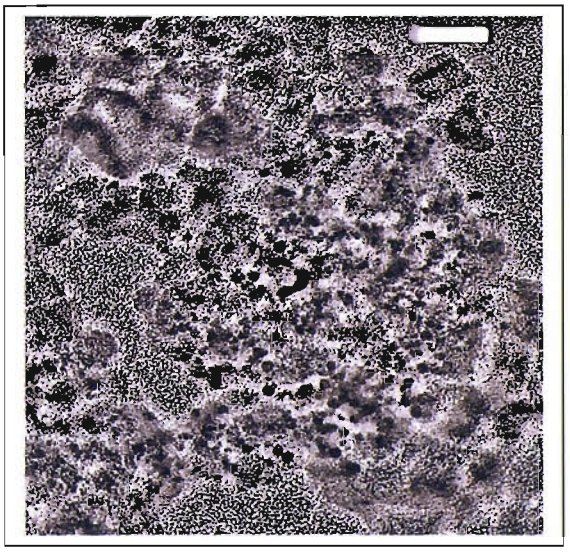

Figure 2.24: A TEM image of 5wt%Rh supported on γ-Al_2O_3, the dark areas show the Rh particles. The scale bar represents 20 nm.

2.7 Energy Dispersive Analysis of X-rays

The Energy Dispersive Analysis of X-rays (EDX) is a method employed to determine the energy spectrum of X-ray radiation. The energy edges probed are in principle the same as XAS, and this re-iterates the amount of useful information that can be gleaned by applying electron microscopies and spectroscopies to systems such as the ones under investigation. EDX is mainly used in chemical analysis, as with this study where it was used to give the elemental composition of the catalysts. EDX devices include X-ray fluorescence spectrometers and electron microprobes, for example they are contained within many modern scanning electron microscopes (SEM).

An X-Ray spectrum is generated from electron bombardment. A detector collects X-rays and produces current pulses proportional to X-Ray energy; a pulse processor acts as a matched filter to convert the signal to analogue voltage pulses. A pulse height analyser measures and records the pulse heights, and therefore the energies of the X-Rays. The information is used to create an X-ray spectrum, a plot of counts detected versus X-ray energy. The spectrum can be acquired in probe mode (stationary beam) or in scanning mode (moving beam).

2.7.1 Experimental: EDX

EDX data was taken for the catalyst samples using a JEOL JSM-6500F SEM machine equipped with an Oxford Instruments 300 for EDX data acquisition, shown in figure 2.25.

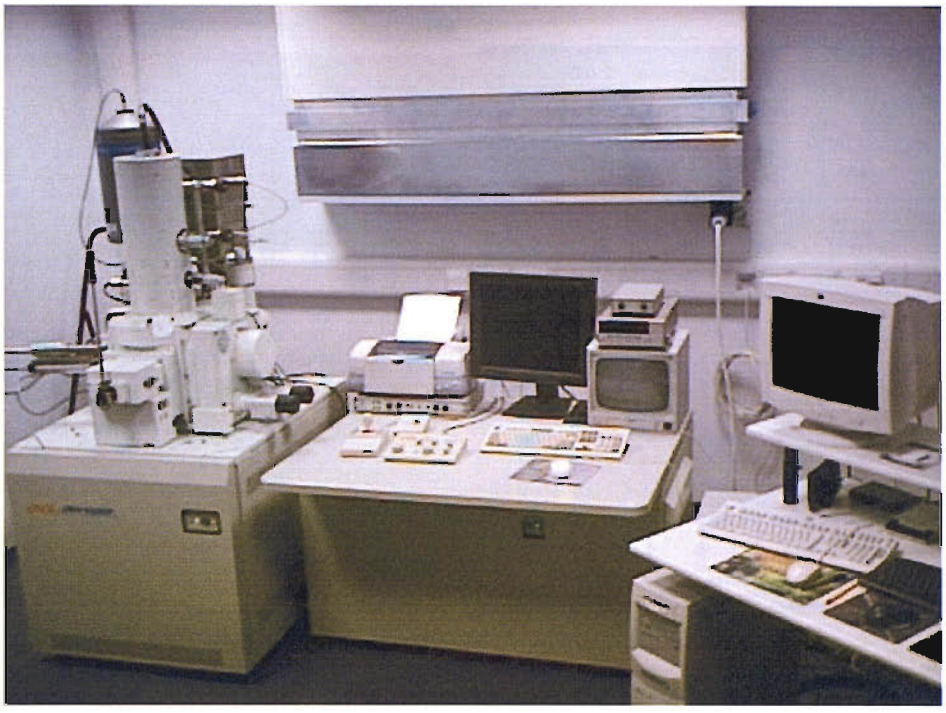

Figure 2.25: Photo showing the JSM-6500F SEM machine and data stations.

In terms of sample presentation, the system to be studied was dispersed in ethanol, and then deposited on a perforated carbon foil supported on a copper grid (Agar). The Rh L edge was probed for each sample as the upper limit of the EDX machine used in this study was ca. 20 keV. The resolution of the machine was sufficient to distinguish between the Rh L and Cl K edges. In a typical experiment, three scans sampling ca. 1.5 mm^2 of a catalyst were performed with EDX; the average weight and atomic percentages are reported along with the Rh:Cl ratio in chapter 3. An example SEM image and corresponding EDX spectrum is given in figure 2.26; the data obtained from the 5wt% Rh example is given in table 2.3.

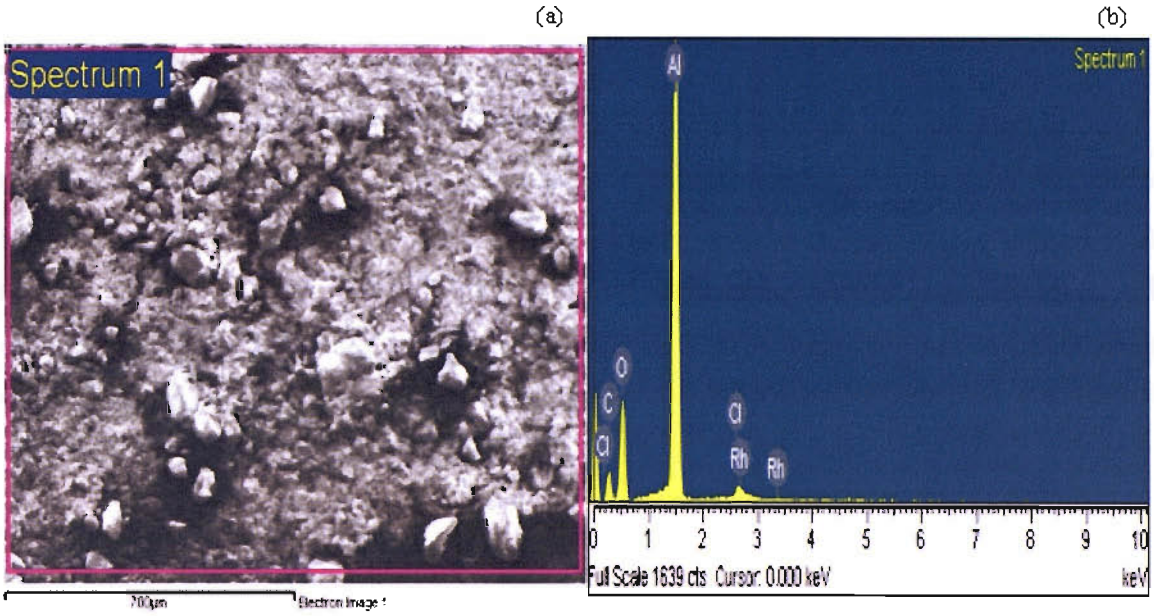

Figure 2.26: EDX data collection showing; (a) SEM image and (b) corresponding EDX spectrum of a 5wt% Rh/γ-Al_2O_3 sample.

Element	Weight%	Atomic%
O K	38.94 (± 0.75)	53.65
Al K	53.99 (± 0.77)	44.11
Cl K	1.78 (± 0.21)	1.11
Rh L	5.29 (± 0.39)	1.13
Totals	100.00	100.00

Table 2.3: Elemental data acquired from EDX data shown in figure 2.26 for a 5wt% Rh/γ-Al_2O_3 sample. Error estimation for the atomic% data was not available.

2.8 Isothermal Nitrogen Adsorption Analysis

The phenomena of nitrogen adsorption on an oxide surface can be observed to occur in two stages. At low pressures of the adsorbate, an initial monolayer is formed. The second stage is observed upon further adsorption at higher pressures where multilayers of the substrate are formed. The isotherm that is utilised for these processes is known as the BET isotherm, created by Brunauer, Emmett and Teller in 1938,[35] and is utilised to determine the total surface area of the oxide support in this study:

$$\frac{V}{V_{mon}} = \frac{cz}{(1-z)\{1-(1-c)z\}} \quad \text{where } z = \frac{p}{p^*} \qquad \text{Eq. 2.12}$$

Equation 2.12 highlights p^* as the vapour pressure above a layer of nitrogen that is more than one molecule thick, essentially thought of as a pure bulk liquid. V_{mon} is the volume of the monolayer, and c is a constant which corresponds to the following expression (equation 2.13):

$$c \approx e^{(\Delta_{des}H^\circ - \Delta_{vap}H^\circ)/RT} \qquad \text{Eq. 2.13}$$

when this coefficient is large (c>>1), the isotherm simplifies to the following expression:

$$\frac{V}{V_{mon}} = \frac{1}{1-z} \qquad \text{Eq. 2.14}$$

Equation 2.14 is therefore most applicable to the systems used in this study, as $\Delta_{des}H^\circ$ is essentially much greater than $\Delta_{vap}H^\circ$. From this, the calculated volume can be related to the number of moles of gas adsorbed, and hence the surface area in m^2. A value of m^2g^{-1} can be found if the mass of material is known. BET data can therefore yield information on the physical properties of the catalysts in question, such as total surface area, porosity and poresize distributions. BET measurements were made using a Quantachrome Nova 3000 series BET machine.

2.9 Synthesis and Pre-treatment of Catalysts

The following catalysts were made with varying metal loading. The support used was γAl_2O_3 (aluminium oxide c from Degussa):

- 10wt%Rh, 7.5wt%Rh, 5wt%Rh; 2.5wt%Rh, 2wt%Rh and 1wt%Rh.

The choice of γ-Al_2O_3 as the oxide support used for the catalysts was based on it being a prototypical material in this field of study (i.e. its use as a support in the TWC). Of the two forms of anhydrous alumina, the other being α-Al_2O_3, γ-Al_2O_3 exhibits a 'defect' spinel structure, with a deficit of cations.

γ-Al_2O_3 combines a relatively high surface area (ca. 100 m^2g^{-1}) with advantageous physical properties such as thermal stability, making it a potentially useful dispersant for active metal species. Al_2O_3 also possesses both Brønsted (OH groups) and Lewis acid (oxygen deficient Al sites) character. However, whilst these properties are exploited in a variety of areas in catalysis, they will not be considered in detail in the current study.

A chlorinated and chlorine-free set of samples were made at each metal loading. This was due to the planned investigation into the role of chlorine in the catalytic systems. The corresponding precursors for each set were as follows:

- $RhCl_3.3H_2O$ (Strem) for the chlorinated set, denoted RhCl systems
- $Rh(NO_3)_3$ (Alfa-Aesar) for chlorine-free set, denoted RhN systems.

In addition to these samples, a 4wt%Rh/1wt%Pd alloy system was synthesised using chlorinated precursors only; the Pd component was sourced from $PdCl_2$ (Aldrich).

2.9.1 Method

The precursors were weighed out according to the amount of alumina support used (2g) and dissolved in ca. 5 ml of distilled water. The alumina was placed into a beaker with a magnetic stirrer and the solution was added under constant stirring until a homogeneous substance was obtained. The sample was then dried overnight in an oven set at 303 K. The samples were then sieved to a 90μm fraction using molecular sieves.

Each of the sample batches was split, 1g to be calcined only and 1g to be calcined and reduced, for future in-situ reduction experiments.

- Calcination conditions: Under flowing 5%O_2/He (25 $mlmin^{-1}$) at 673 K for 5 hours.
- Reduction conditions: Under flowing 5%H_2/He (25$mlmin^{-1}$) at 573 K for 6 hours.

Each sample was purged under the gas for 1 hour prior to the particular pre-treatment. The cooled sample was then transferred to sealed sample jars. No attempt was made to stop the samples being exposed to air.

The synthesis of the 4wt%Rh/1wt%Pd alloy system entailed dissolving the Rh component as above; the Pd component was dissolved in acidified water (pH 1.5). The two solutions were then added simultaneously to the alumina under constant stirring to yield a slurry that was then subjected to the same preparative method as the Rh-only systems.

Samples that were not subjected to any treatment (i.e. dried from the slurry) will be further denote as 'untreated' samples; calcined and reduced samples as 'fresh'; and samples reduced in situ (within the experimental set-up, before characterisation takes place) will be designated 'reduced' samples.

2.10 References

[1] M. Harada, K. Asakura, Y. Ueki, N. Toshima, *J. Phys. Chem. B.*, 1993, **97**, 10742.

[2] A.I. Frenkel, C.W. Hills, R.G. Nuzzo, *J. Phys. Chem. B.*, 2001, **121**, 16.

[3] D.P. Woodruff, T.A. Delcher, 'Modern techniques of surface science', 1989, Cambridge University Press, Cambridge.

[4] J.C. Riviére, 'Surface analytical techniques', 1990, Clarendon Press, Oxford.

[5] G. Beamson, D. Briggs, 'High resolution XPS of organic molecules- the Scienta ESCA 3000 data book, 1992, John Wiley and Sons, Cambridge.

[6] M. Tromp, J. A. van Bokhoven, G. P. F. van Strijdonck, P. W. N. M. van Leeuwen, D. C. Koningsberger, D. E. Ramaker, *J. Am. Chem. Soc.*, 2005, **127**, 777.

[7] A. L. Ankudonov, B. Ravel, J. J. Rehr, S. D. Conradson, *Phys. Rev. B.*, 1998, **58**, 7565.

[8] D. Burnaby, PhD Thesis, University of Southampton, 2000.

[9] D.E. Sayers, E.A. Stern, F.W. Lytle, *Phys. Rev. Lett.*, 1971, **27**, 1204.

[10] E.A. Stern, *Phys. Rev. Lett. B.*, 1974, **10**, 3027.

[11] D.C. Koningsberger, R. Prins Eds., 'Theory of EXAFS: principles, applications and techniques of EXAFS, SEXAFS and XANES, 1988, John Wiley and Sons.

[12] G. Lu, M. Chen, L. Ma, *Acta. Chimica. Sinica.*, 1989, **47**, 37.

[13] Http://www.synchrotron-soleil.fr

[14] R.B. Gregor, F.W. Lytle, *J. Catal.*, 1980, **63**, 476.

[15] S.J. Gurman, *J. Phys.Chem.*, 1983, **16,** 2987.

[16] M. Hagelstein, C. Ferrero, U. Hatje, T. Ressler, W. Metz, *J. Synchrotron Rad.*, 1995, **2**, 174.

[17] M. Hagelstein, C. Ferrero, M. Sanchez del Rio, U. Hatje, T. Ressler, W. Metz, *Physica B.*, 1995, **208**, 223.

[18] T. Ressler, M. Hagelstein, U. Hatje, W. Metz, *J. Phys. Chem.*, 1997, **101**, 6680.

[19] G.E. Derbyshire, W.I. Helsby, A.J. Dent, S.A. Wright, R.C. Farrow, G.N. Greaves, C. Morrell, G.I. Baker, *Daresbury Laboratory technical Memorandum,* DL/SCI/P723E.

[20] T. Matsushita, R.P. Phizackerley, *Jpn. J. Appl. Phys.*, 1981, **20**, 2223.

[21] J.W. Couves, J.M. Thomas, D. Waller, R.H. Jones, A.J. Dent, G.E. Derbyshire, G.N. Greaves, *Nature*, 1991, **354**, 465.

[22] For instance: (a) S.G. Fiddy, M.A. Newton, T. Campbell, J.M. Corker, A.J. Dent, I. Harvey, G. Salvini, S. Turin, J. Evans, *Chem. Commun.*, 2001, 445; (b) A.Suzuki, Y. Inada, A. Yamaguchi, T. Chihara, M. Yuasa, M. Nomura and Y. Iwasawa, *Angew. Chem. Int. Ed.*, 2003, **42**, 4795.

[23] M. Tromp, PhD Thesis, University of Utrecht, 2004.

[24] M. Tromp, B. Jyoti, A.J. Dent, S. Diaz-Moreno, M.A. Newton, S.G. Fiddy, J. Evans, in preparation.

[25] M. Hagelstein, C. Ferraro, U. Hatje, T. Ressler, W. Metz, *J. Synchrotron Radiat.*, 1998, **5**, 1396.

[26] M.A. Newton, A.J. Dent, J. Evans, *J. Chem. Soc. Rev.*, 2002, **31**, 83.

[27] M. A. Newton, B. Jyoti A. J. Dent, S. Diaz-Moreno, S. G. Fiddy, J. Evans, *Angew. Chem. Int. Ed.* 2002, **41**, 2587.

[28] T. Campbell, PhD Thesis, University of Southampton, 2002.

[29] N. Binsted, PAXAS: Program for the Analysis of X-ray Absorption Spectra, University of Southampton.

[30] N. Binsted, EXCURV98, CCLRC Daresbury Laboratory computer program, 1998.

[31] S.J. Gurman, *J. Phys. C.*, 1988, **21**, 3699.

[32] J.M. Corker, J. Evans, H. Leach, W. Levason, *Chem. Commun.*, 1989, 181.

[33] B.K. Teo, 'EXAFS: Basic principles and data analysis', 1986, Springer Verlag, Berlin.

[34] Http://www.barrettresearch.ca/teaching/nanotechnology/nano02.htm

[35] D. Dollimore, G.R. Heal, *J. Appl. Chem.*, 1964, 101.

Chapter 3. A detailed structural characterisation of Rh/Al_2O_3 catalysts

3.1 Introduction

Structure – performance relationships of heterogeneous catalysts are fundamentally important to optimise both the catalyst composition and the catalysis process conditions. The application of in situ, time-resolved techniques are increasingly applied to characterise real, 'working' catalysts under process conditions during a particular reaction, in contrast to model systems investigated in relevant gas environments.

Rhodium supported catalysts have been the subject of study for many years as a result of its applications in industry, especially as a component of the three way automotive exhaust catalyst (see chapter 1). For example, its surface properties have been probed extensively by CO adsorption using Infra Red (IR) spectroscopy, [1] X-ray Absorption Fine Structure Spectroscopy (XAFS) [2] and energy dispersive XAFS (EDE) [3] all showing dissociative adsorption resulting in $Rh(CO)_2$ units. Characterisation of these heterogeneous catalysts during three way catalytic processes such as CO oxidation to CO_2,[4] NO reduction by H_2[5] and NO reduction by CO[6] have been studied in the past; indeed such processes form an integral part of the current study. Previous studies have provided complementary information about the nature of the metal sites and serve to highlight that the activity and the formation of specific (active) sites are closely related to the process conditions applied.

Although the structure of the catalyst during process conditions is vital to elucidate their catalytic intermediates and fundamental reaction mechanisms, the detailed structure of the 'starting' catalysts must firstly be established. By characterising the initial state of the catalysts used in this study, more detailed insights into their transformations upon application of different process conditions like gas environment and temperature can be obtained and their reactivity better understood. As mentioned, supported rhodium nanoparticles systems are very sensitive to the conditions applied. To this end, a series of Rh nanoparticle systems on γ-alumina were synthesised and studied via the diverse range of complementary in situ and ex situ techniques introduced in the previous chapter as function of precursor, treatment and rhodium metal loading.

3.2 Experimental

The following experimental section serves only as a brief synopsis of the techniques used; a more detailed account is given in chapter 2.

3.2.1 Catalyst preparation

Supported Rh samples, with loadings of 1-10 wt% Rh, were synthesised via wet impregnation of alumina (γ-Al_2O_3, Degussa AluC, surface area ~100 m^2g^{-1}), under constant stirring, with aqueous solutions of $RhCl_3.3H_2O$ or $Rh(NO_3)_3$ (see chapter 2.9). These samples will be further denoted as the 'untreated' samples.

Calcined/reduced samples are further denoted as 'fresh' samples. The systems prepared from the chloride precursors are denoted as RhCl, the nitrate derived systems as RhN.

Some samples were required to be reduced in situ (within the experimental platform, before any characterisation took place). This entailed heating the sample to 573 K under a flow of 5%H_2/He, switching to a flow of 5%O_2/He for 10 minutes (or until remaining carbonaceous deposits have been removed from the catalyst by observing carbon related fragments in the MS), before switching back to the flow of H_2 (gases all at 25 ml min^{-1}). These samples are denoted as 'reduced'.

3.2.2 Transmission Electron Microscopy (TEM) and Energy Dispersive Analysis of X-rays (EDX)

TEM measurements (see chapter 2.6) were carried out on JEOL FX 2000 and JEM-3010 microscopes in brightfield mode. EDX measurements (see chapter 2.7) were carried out using a JEOL JSM-6500F SEM machine equipped with an Oxford Instruments 300 for EDX data acquisition. The 'fresh' Rh supported samples were dispersed in ethanol, and deposited on a perforated carbon foil supported on a copper grid. Three area scans of 1.5 mm^2 were performed with EDX; the average weight percentages for all elements are determined and reported here.

3.2.3 X-ray Photo-electron Spectroscopy (XPS)

XPS measurements (see chapter 2.3) were carried out using a Scienta ESCA300 XPS analyser. 'Fresh' samples were analysed using monochromated Al K_α X-ray radiation and sample charge compensation. A 150 mm radius Scienta hemispherical analyser operating with pass energy of 150 eV and a 0.8 mm entrance slit yielded a nominal resolution of 0.35 eV. Samples were pressed into self supporting disk (under 2 tonnes $inch^{-2}$ of pressure), or used in powder form (on adhesive tape), and mounted onto a stub. The stub was loaded into the XPS system via a load-lock and evacuated before transfer to the analysis chamber, which was maintained at a base pressure of ca. 5×10^{-9} mbar.

3.2.4 X-ray Absorption Fine Structure Spectroscopy (XAFS)

3.2.4.1 Rh K-edge XAFS

Rh K-edge XAFS spectra were measured at beamline 9.3 of the Daresbury Synchrotron Radiation Source (SRS, see chapter 2.5.5). A Si [220] double crystal monochromator was detuned to 50% intensity in order to minimize the presence of higher harmonics. A horizontal plane Pd-coated mirror was used to provide harmonic rejection as well as vertical collimation and focusing. The measurements were performed in transmission mode using optimized ionization chambers as detectors. The spectra are energy calibrated by aligning the 1st peak of the 1st derivative of the Rh foil to 23220 eV.

The combined Energy Dispersive EXAFS (EDE) / Diffuse Reflectance Infrared Fourier Transform spectroscopy (DRIFTS) / Mass Spectrometry (MS) set-up was used to perform the in situ sample treatments and provide the appropriate gas environments while measuring the XAFS data. The sample holder was packed with ~20 mg of fresh sample. The sample was then mounted in the DRIFTS cell to allow gas and temperature treatments.

Due to space limitations at beamline 9.3, we were unfortunately not able to set up the complete EDE/DRIFTS/MS equipment and therefore no simultaneous DRIFTS experiments have been performed in this chapter.

3.2.4.2 Cl K-edge XAFS

Cl K-edge X-ray Absorption Near Edge spectra (XANES) were also obtained at the SRS, at beamline 3.4 (see chapter 2.5.6). A Si [111] monochromator was used and XANES spectra were obtained using total electron yield detection. Untreated and fresh samples were pressed in pellets with ~70 wt% high purity graphite. A sample charge of 10 mg was used for all samples to be able to quantify the results. The pellets were mounted on sample plates using conductive tape. Finally, the sample plates were loaded into the experimental UHV chamber (mounted on a manipulator sample stage).

3.2.5 XAFS analysis

3.2.5.1 Rh K-edge EXAFS analysis and the determination of Debye-Waller (DW) factors in variable temperature EDE studies

EXAFS data reduction and analysis was carried out using the PAXAS[7] and EXCURVE98 programs (see chapter 2.6).[8]

As mentioned in chapter 2, the inherent relationship between static and dynamic disorder (as analytically accounted for by using DW factors) and coordination numbers in EXAFS means that for the restoration of accurate coordination numbers to be undertaken correct estimates of the DW factors need to be made. This is particularly true in variable temperature studies of the type undertaken throughout this study. Figure 3.1 illustrates this for typical foil spectra taken at 298 K and 673 K, the raw EXAFS highlighting the attenuation of EXAFS signal at higher temperature.

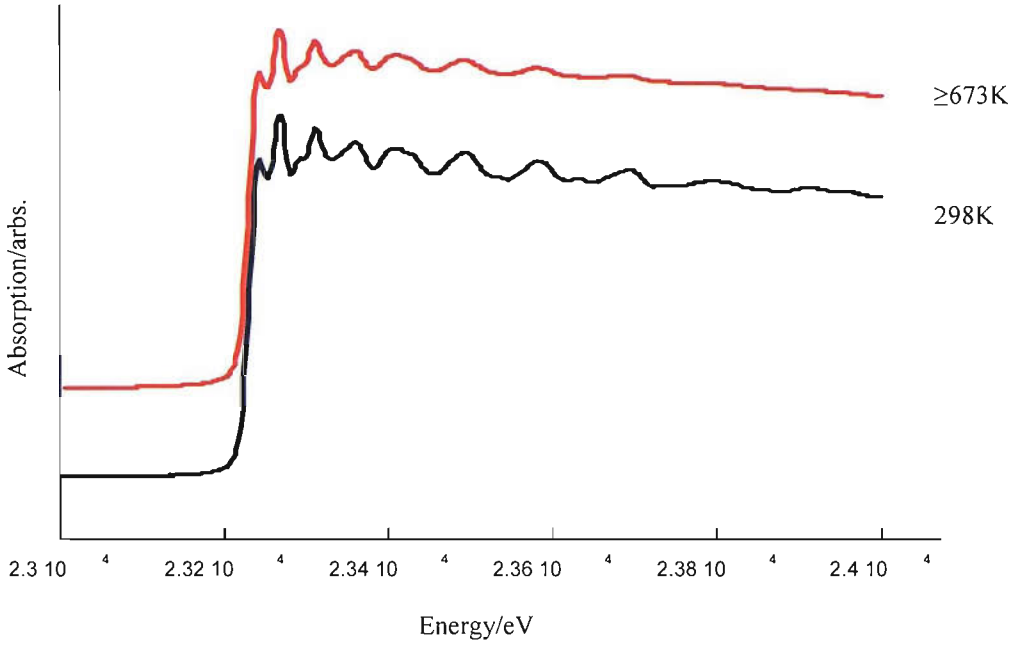

Figure 3.1: EXAFS signature showing a Rh foil at the temperatures indicated. A difference in EXAFS intensity is observed with increasing temperature.

As the face centred cubic (fcc) structure of the foil remains invariant between these two cases, the apparent difference in EXAFS signal with increasing temperature therefore cannot be due to differences in coordination number. If these or any spectra with a variance in temperature were to be analysed with the same DW factors, a severe underestimation of the occupation of the Rh shells for spectra at high temperatures would result. As such a method of correctly determining the DW factors as the temperature is increased is needed for the accurate analysis of spectra.

As this study deals with nanoparticulate systems, containing a range of particle sizes, the use of a foil is not necessarily the most effective method to determine the DW factors. This is principally because it cannot be assumed that the static and dynamic components of the DW factors and their variation with temperature will be the same in the nanoparticulate case as in the bulk foil.

In an attempt to address this problem, a 5wt% Rh sample was re-reduced in situ in a flow of $5\%H_2$/He to 673 K. EDE measurements were then performed on the sample as it cooled. This procedure assumes that no changes occur in either metal particle size distribution or

morphology when the sample is in the cooling cycle from 673 K; meaning changes in EXAFS are only attributed to changes in sample temperature. The resulting spectra were analysed and refined for the first shell metal co-ordination number (N_1^{metal}), metal-metal bond length and Fermi level (E_f) values. The spectra were analysed over a constant spectral width (k = 2-13 $Å^{-1}$), holding the DW factor constant. At each temperature a range of DW factors (0.004-0.036) was analysed and the R factors determined. The minimum in the subsequent plot of R factor versus DW factor yielded the correct DW factor for the given temperature. This method can be effectively visualised in figure 3.2, which shows the DW factors obtained via the minima of the subsequent R factor at a given temperature. The figure also highlights the inherent errors involved in determining DW factors, as the minima in the R versus DW curves are broad. Hence the accuracy of the DW factors used has an error of ca. ± 10% involved, giving the potential for error in subsequent coordination numbers as 10-20%. Extrapolation of the linear relation between DW and R factor provides the correct DW factors to be applied at different temperature, as is displayed in figure 3.3.

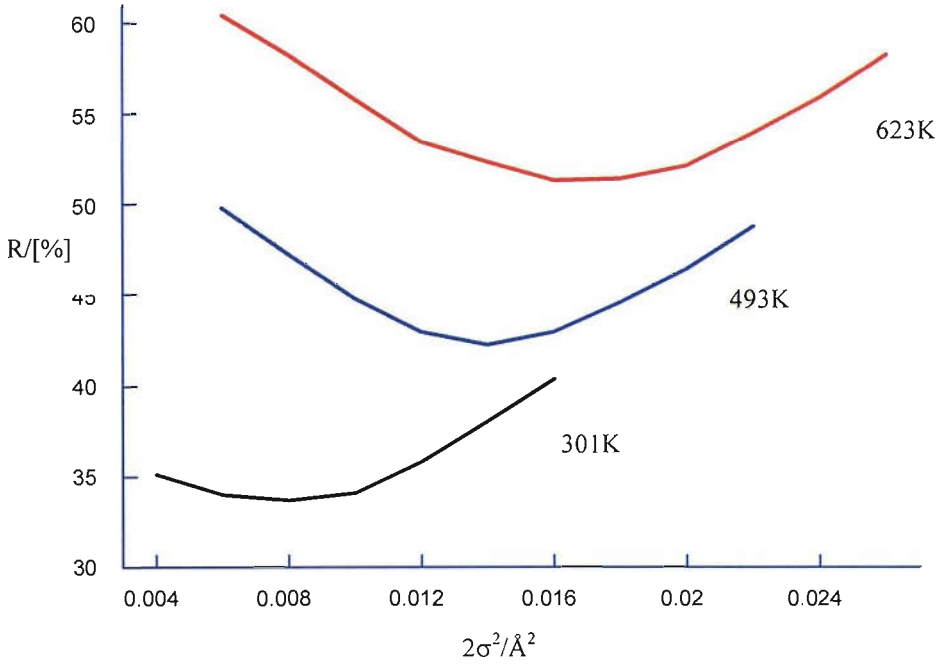

Figure 3.2: Plot of R factor versus DW factor ($2\sigma^2/Å^2$) highlighting the method used for correct DW factor determination.

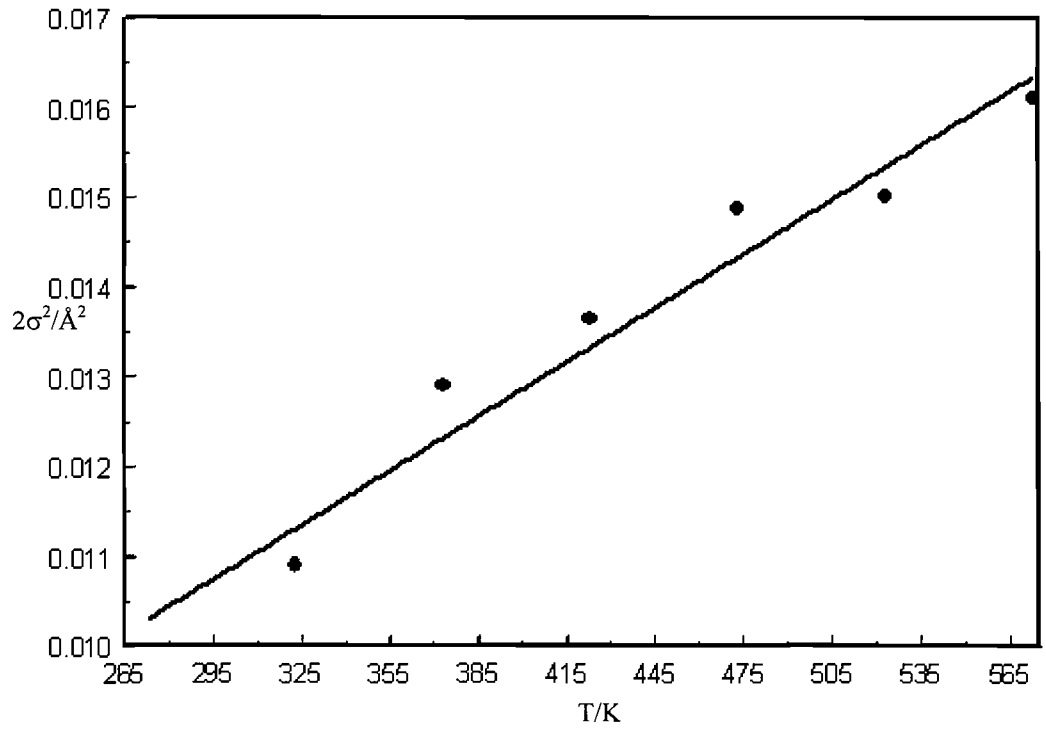

Figure 3.3: DW factor versus Temperature dependence as determined for a 5wt% RhCl sample.

3.2.5.2 1st Derivative Rh K-edge XANES data

NB All XANES data analysis and subsequent interpretation reported in this chapter was carried out by Dr. Moniek Tromp, University of Southampton, UK.

To highlight the different features in the Rh K-edge XANES data more clearly, the 1st derivative of the normalised absorption data is taken by using the Savitsky-Golay smoothing and differentiation procedure. The first and second derivatives of the XANES data have been used by others[9] and prove to provide valuable information on the density of states of the samples under investigation, and also for broad high energy edges.[9a] The 1st derivative is calculated on an energy grid of 500 points separated by 0.5 eV using a smoothing order of 9, which is the number of surrounding points to be used in the computing of the smoothed 1st derivative. This results in a 1st derivative energy window of 4.5 eV.

3.2.5.3 FEFF8 calculations

The FEFF8 code[10] was used to perform ab-initio self-consistent field (SCF), real space, full multiple scattering (FMS) calculations. A core hole is included in order to mimic the final state of the photon absorption process. An experimental resolution correction of 3 eV has been applied. No E_0 corrections have been applied.

To study the influence of the metal particle size on the Rh K-edge XANES data obtained, a series of metal clusters with different sizes was generated and the XANES simulated. All metal clusters were based on the bulk structure of Rh, which consists of a fcc lattice with a unit cell size of 3.797 Å[11] (resulting in a Rh-Rh distance of 2.68 Å). A series of spherical clusters was generated using the program 'ATOMS', by stepwise increasing the 'maximum radial distance' of the clusters. The smallest particle simulated as such is consequently an Rh_{13} particle. In addition, a triangular Rh_3 and a Rh_6 'Janin' particle,[12,13] as shown in Figure 3.4, possessing both a fcc and hexagonal closed packed (hcp) adsorption site, have been calculated. An overview of the series of clusters is given in table 3.1, including the estimated first shell coordination number (CN) with an error of 10%.[14]

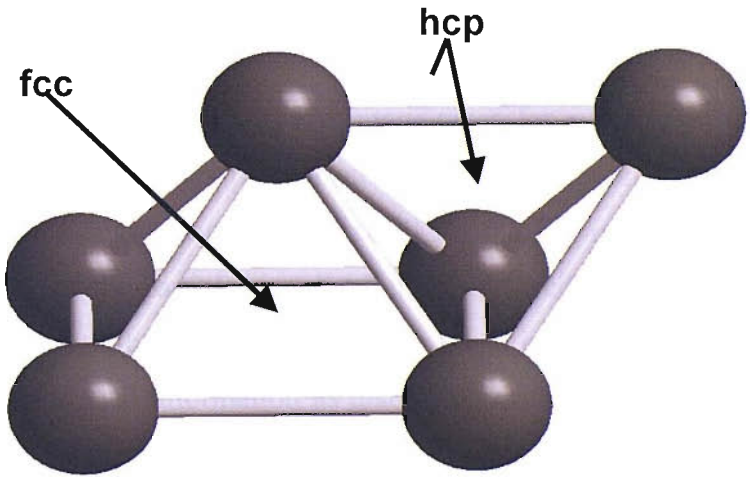

Figure 3.4: The 'Janin' Rh_6 cluster showing both fcc and hcp sites.[12]

Cluster shape	Number of atoms	Radius/Å	Diameter/Å	CN first shell (Rh-Rh)
'Janin'	6	Rh-Rh = 2.68	2.68 (effective diameter)	3.7
Spherical	13	2.68	5.36	5.2
Spherical	19	3.79	7.58	6.0
Spherical	43	4.64	9.28	7.4
Spherical	55	5.36	10.72	7.7
Spherical	79	5.99	11.98	8.2
Spherical	87	6.56	13.12	8.3

Table 3.1: The Size and shape of model clusters as simulated with FEFF8 (CN = coordination number).

3.3 Results

3.3.1 TEM and EDX

Figure 3.5 shows a representative TEM image taken for a fresh 5wt% RhCl sample. The dark areas show the Rh particles present on the γ-Al_2O_3 support and display the spherical morphology. Similar images have been obtained for the full range of fresh RhCl and RhN samples. A collation of the particle size distributions derived from these images is displayed in figures 3.6 and 3.7, with the relevant statistics given in table 3.2. It should be noted that the figures quoted for such information as dispersion originate from the averages extracted from the PSD, i.e. they are not directly measured. Furthermore only particles from the size of 4 Å and larger are observed in these TEM measurements due to the resolution limits of the machines utilised. Assuming spherical particles with an fcc structure are present, TEM will only sample metal particles consisting of a minimum of ~43 atoms (see table 3.1).

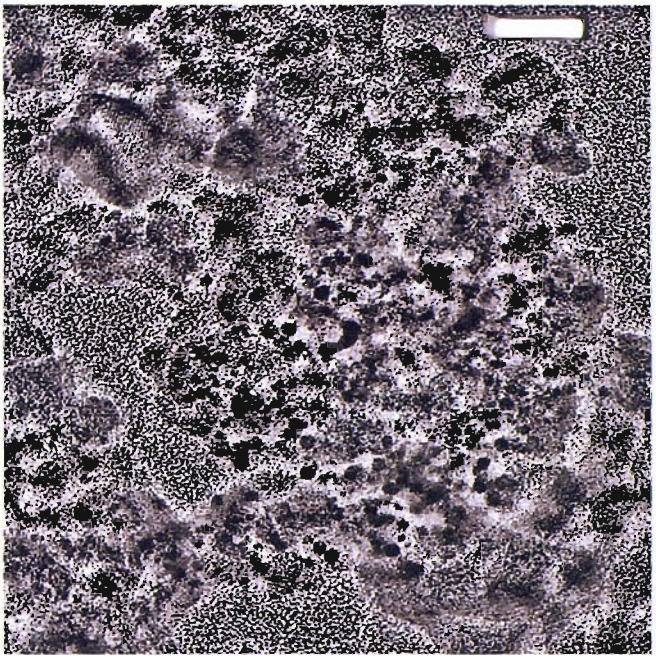

Figure 3.5: TEM image of a fresh 5wt% RhCl sample. The scale bar represents 20 nm.

Figures 3.6/3.7 and table 3.2 show that the Rh systems prepared in this study are characterised by an average particle size in the range of 10 – 60 Å. An increase of Rh metal loading leads to an increase in average particle diameter as well as a broadening in particles size distribution. Moreover, with increasing total Rh loading an increased difference between the particle size distributions for the two precursors is observed.

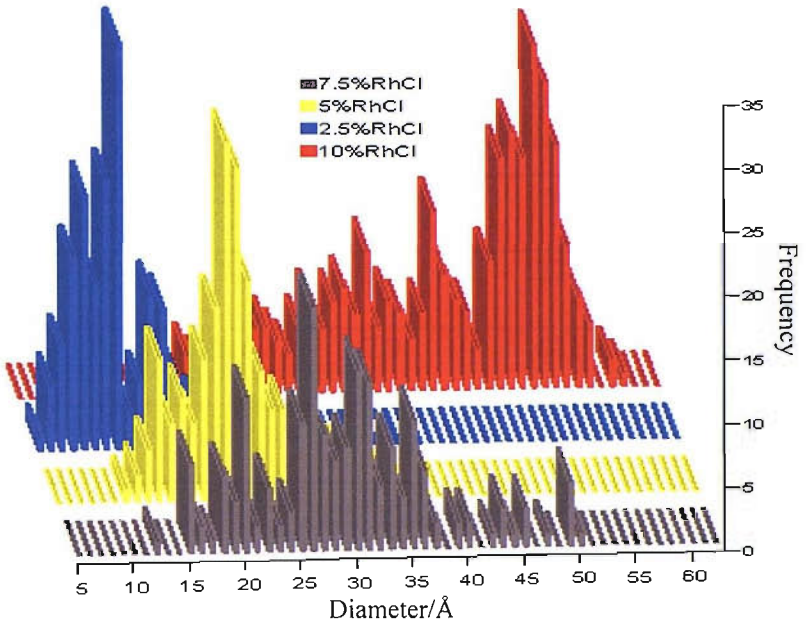

Figure 3.6: Particle size distribution derived from TEM for a series of fresh RhCl samples.

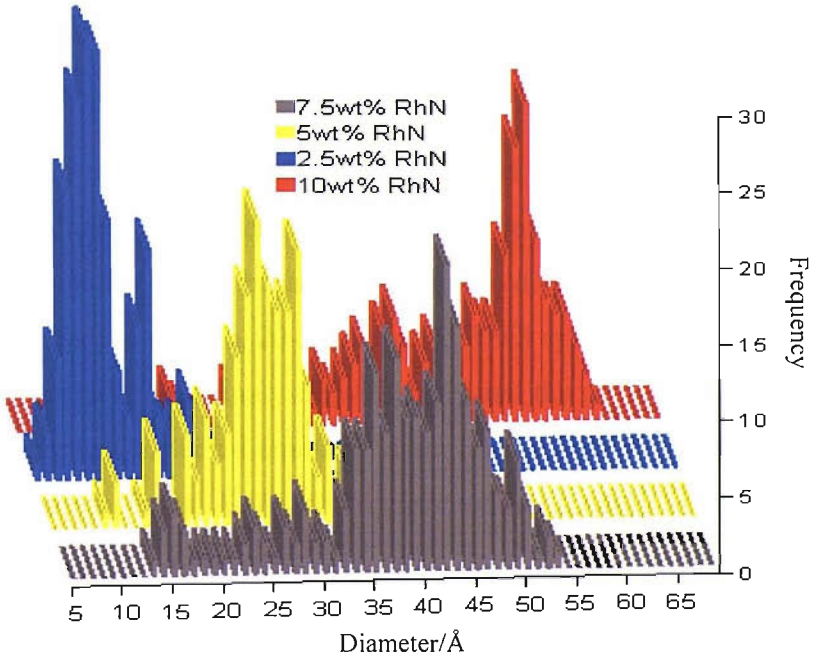

Figure 3.7: Particle size distribution derived from TEM for a series of fresh RhN samples.

Sample	Points	Average Particle Size (Å)	Standard Deviation	Mean number Atoms in Particle (N_t)	Mean number Surface Atoms (N_s)	Dispersion (N_s/N_t)
2.5wt% RhCl	169	12.4	4.4	50	43	0.86
5.0wt% RhCl	189	21.5	5.1	225	117	0.52
7.5wt% RhCl	179	28.6	7.9	612	228	0.37
10wt% RhCl	213	53.9	6.4	1155	430	0.38
2.5wt% RhN	197	13.3	4.7	62	50	0.8
5.0wt% RhN	182	26	6.8	460	188	0.41
7.5wt% RhN	222	42.1	6.7	901	335	0.37
10wt% RhN	197	56.2	8.3	1203	448	0.37

Table 3.2: Rhodium particle size distributions for the series of RhCl and RhN samples as determined with TEM.

At 2.5 wt% Rh metal loading both chlorinated and non-chlorinated samples yield very similar particle size distributions, between ca. 5-27 Å; both display an average particle size of ca. 13 Å. At the 10wt% Rh level a broader particle size distribution of ca. 20-62 Å is seen for the RhN system, compared with ca. 20-56 Å for the RhCl system.

The RhCl samples have been analysed with EDX and the results are displayed in table 3.3, along with the theoretical expected amounts, assuming no loss of material occurs during the calcination/reduction processes. A slightly higher rhodium loading as well as oxygen amount, versus a lower amount of aluminium and chlorine (for samples 2.5 to 10 wt% Rh) is observed. The discrepancies with theoretical values could be due to the fact that a considerable amount of chlorine seems to be removed from the sample in the calcination/reduction process. Moreover, the amount of oxygen is difficult to determine with EDX because of its low atomic weight and consequent low binding energy (the EDX technique accurately determines elements from sodium onwards). Differences in chlorine and inaccuracies in oxygen amounts will result in different weight percentages relative to the

theory for all atoms present in the sample. Another likely explanation is experimental error during the synthesis of the catalysts.

Sample	Theory[1]			EDX			Cl XAS
	Atom	Wt%	Atom %	Wt%[2]	Atom%	Rh:Cl	Wt%
Untreated							
1 wt% RhCl	Cl	1.0					1.2
2.5wt% RhCl	Cl	2.5					2.9
5 wt% RhCl	Cl	5.0					5.4
7.5wt% RhCl	Cl	7.5					n.d.[3]
10wt% RhCl	Cl	10.0					13.3
Fresh							
1wt% RhCl	O	46.1	59.5	40.4	54.3		
	Al	51.9	39.7	56.8	44.6		
	Cl	1.0	0.6	1.1	0.7		1.1
	Rh	1.0	0.2	1.2	0.3	0.4	
2.5wt% RhCl	O	44.7	58.8	40.3	54.8		
	Al	50.3	39.2	55.6	44.4		
	Cl	2.5	1.5	1.1	0.7		2.5
	Rh	2.5	0.5	2.8	0.6	0.9	
5wt% RhCl	O	42.4	57.5	39.4	54.3		
	Al	47.6	38.4	53.1	43.4		
	Cl	5	3.0	1.6	1.0		2.5
	Rh	5	1.1	5.9	1.3	1.3	
7.5wt% RhCl	O	40.0	56.2	39.0	54.5		
	Al	45.0	37.5	51.7	42.8		
	Cl	7.5	4.7	1.5	1.0		n.d.[3]
	Rh	7.5	1.6	7.8	1.7	1.7	
10wt% RhCl	O	37.7	54.7	37.3	55.9		
	Al	42.3	36.5	50.1	41.5		
	Cl	10.0	6.5	2.3	0.6		2.2
	Rh	10.0	2.3	10.3	2.0	3.3	

[1] Theory assumes no contributions are removed from the sample during the calcination/reduction procedure.
[2] EDX results are an average of three area scans. The error is estimated at ± 1wt% for all.
[3] n.d. = experimentally not determined.

Table 3.3: Rh and Cl EDX and Cl XAS results for the series of fresh RhCl samples as indicated.

An almost linear correlation between the amount of rhodium determined with EDX and the expected amount is observed. However, the amount of chlorine is lower for all samples from 2.5wt% Rh onwards indicating loss of chlorine during the calcination/reduction processes (as mentioned above). Although the weight and corresponding atom percentages obtained for these samples with EDX have significant error factors associated with them (up to 15%), the overall trends observed can be deemed reliable. As both Rh and Cl can be determined relatively accurately, the Rh:Cl ratio can also be reliably acknowledged; the data reports an almost linear increase of Rh:Cl ratio as a function of metal loading.

3.3.2 XPS

Figure 3.8 shows the Rh $3d_{5/2}$ and $3d_{3/2}$ XPS spectra for a Rh foil and a Rh_2O_3 reference, and representative spectra for a series of fresh RhCl and RhN samples with different metal loadings. The positions of the two bands clearly show that the Rh oxidation state in the fresh RhCl samples, reduced and exposed to air, is very similar to Rh_2O_3 ($3d_{5/2}$ binding energy ca. 308.5 eV). When compared to the chlorinated Rh samples, the RhN systems appear to be less oxidised with a $3d_{5/2}$ binding energy of ca. 307.7 eV. This effect is most pronounced for the 5wt% RhN sample, the $3d_{5/2}$ binding energy being ca. 307.4 eV.

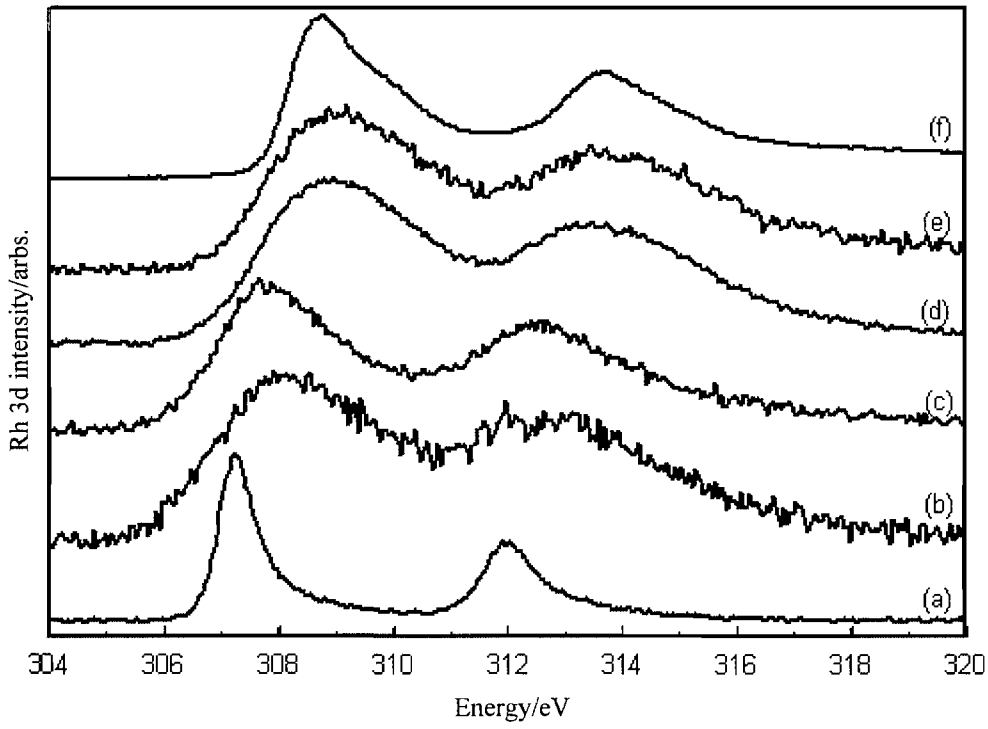

Figure 3.8: Rh 3d XPS spectra obtained for; (a) Rh foil, (b) fresh 2.5wt% RhN, (c) fresh 5wt% RhN, (d) fresh 10wt% RhCl, (e) fresh 5wt%RhCl and (f) bulk Rh_2O_3.

The Cl 2p XPS spectra were also obtained in addition to the Rh 3d spectra for the series of fresh RhCl samples. Figure 3.9 shows that a clear relation between the binding energy of the Cl 2p and the Rh metal loading exists. As the Rh metal loading is increased, the Cl 2p binding energy decreases following an almost linear relationship. The Rh 3d binding energy only differs for the 2.5 wt% sample; all other RhCl samples display the same Rh 3d binding energies ($3d_{5/2}$ as shown in figure 3.8). Unfortunately, no XPS data on the 1wt% RhCl system or the RhN samples have been obtained.

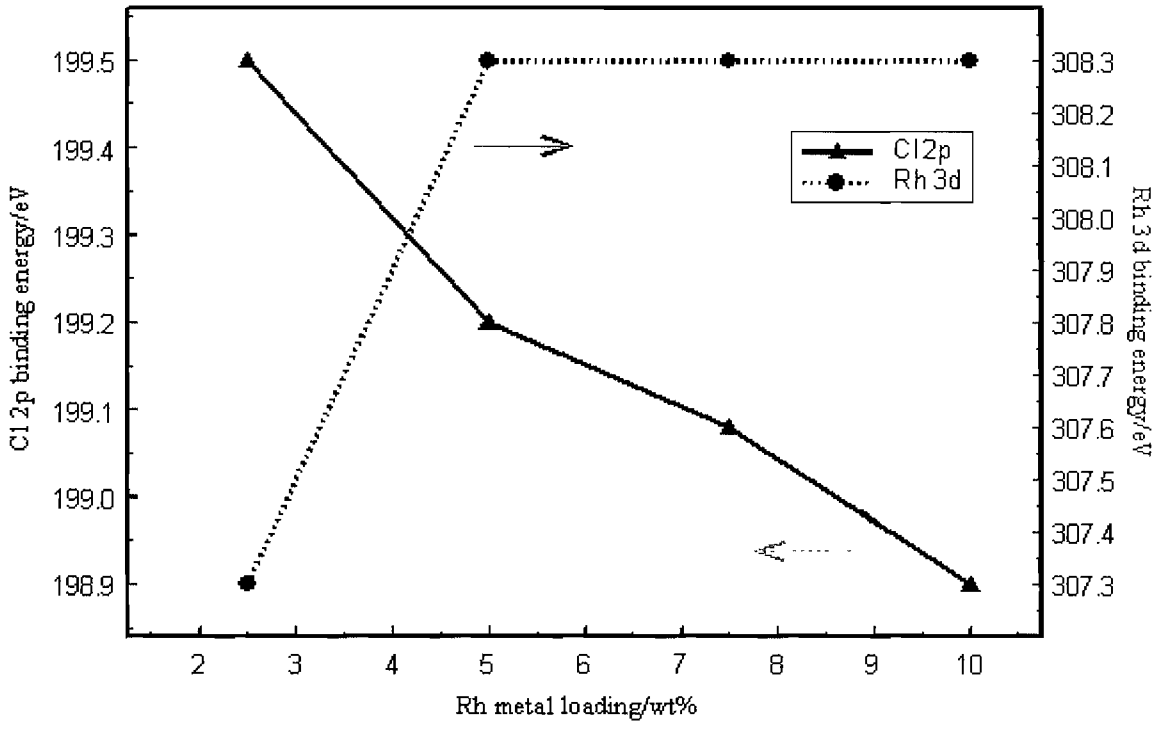

Figure 3.9: Cl 2p and Rh 3d binding energies as a function of Rh metal loading for a series of fresh RhCl samples.

Although both Rh 3d and Cl 2p XPS spectra have been obtained and thus the photoelectron lines of each contribution can be integrated and compared, a reliable quantification of individual atomic contributions cannot be extracted for the following reason. For the Cl 2p bands empirical values are available for the sensitivity factors obtained by standard compounds, hence they include a photoionisation cross section spectrometer transmission function and escape depth. However, the sensitivity factors for Rh are theoretical values based on the photoionisation cross section only, thus making quantitative correlations unreliable.

Representative Rh 3d XPS spectra comparing fresh 2.5wt% and 10wt% RhCl catalysts in both powder and pressed disc form are presented in figure 3.10. It is clear from the figure that the Rh component in the pressed discs is less oxidised than the powdered samples. The re-exposure of the disc to air, after pressing, for transfer into the spectrometer has therefore not resulted in the full (re)oxidation of the overall Rh component. This suggests that by pressing the samples into pellets has resulted in a system which is comparatively resistant to

the facile, room temperature oxidation observed in the powdered analogue. This is evidenced by a colour change; the pale fresh system turns into a black powder characteristic of a reduced system. A possible explanation of this effect could be that the act of pressing a disc results in creating voids in the pellet,[15] thus resulting in the apparent reduction of the Rh component. Previous studies have shown the act of disc pressing to modify surfaces and structures,[16] seemingly occurring in the current case. An alternative explanation for the reduction could be due to the fact that the powdered samples are known to be partially oxidised, as they are stored in air prior to pressing a disc. It may therefore simply be the act of pressing that aids the reduction of the Rh metal; once in a disc oxygen diffusion would be restricted and consequent re-oxidation would be slower. Further investigation, with the possible inclusion of such techniques as XAFS, is needed to probe the disc systems.

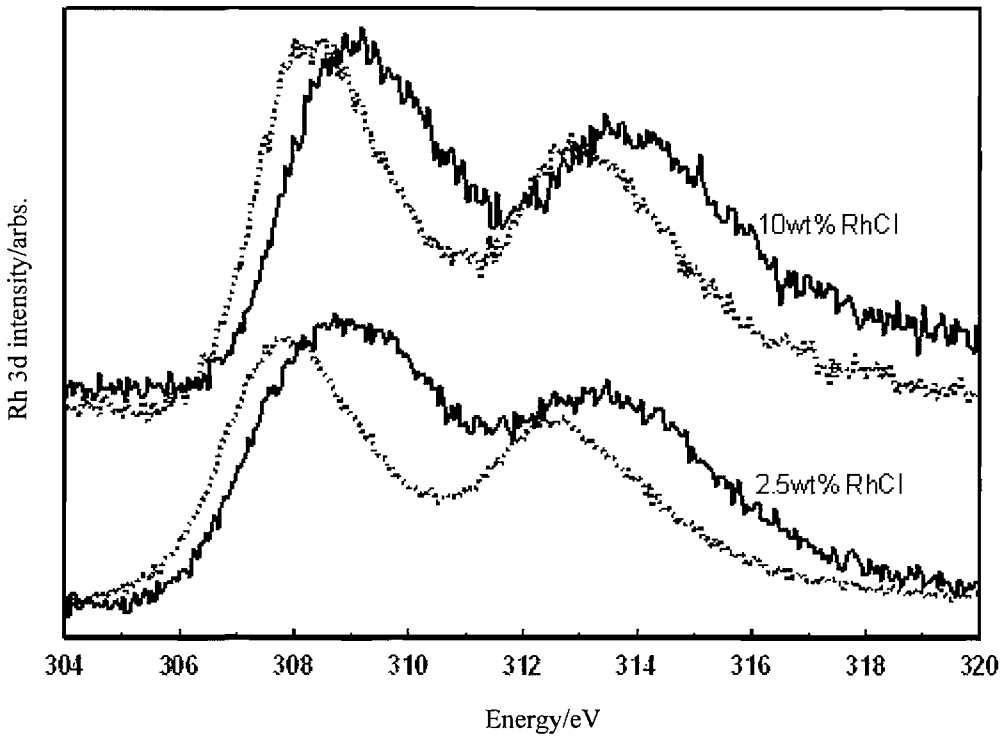

Figure 3.10: Rh 3d XPS spectra obtained for indicated fresh RhCl systems; solid line = powder signal; dotted line = pressed disc signal.

3.3.3 Cl K-Edge XANES

Figures 3.11 and 3.12 show the Cl K-edge XANES data for the RhCl samples as indicated, for both the untreated and the fresh samples respectively. Cl EXAFS data could not be obtained due to the Rh L_3-edge being located only 182 eV above the Cl K-edge (3004 and 2822 eV respectively) and would therefore interfere with any recorded spectra.

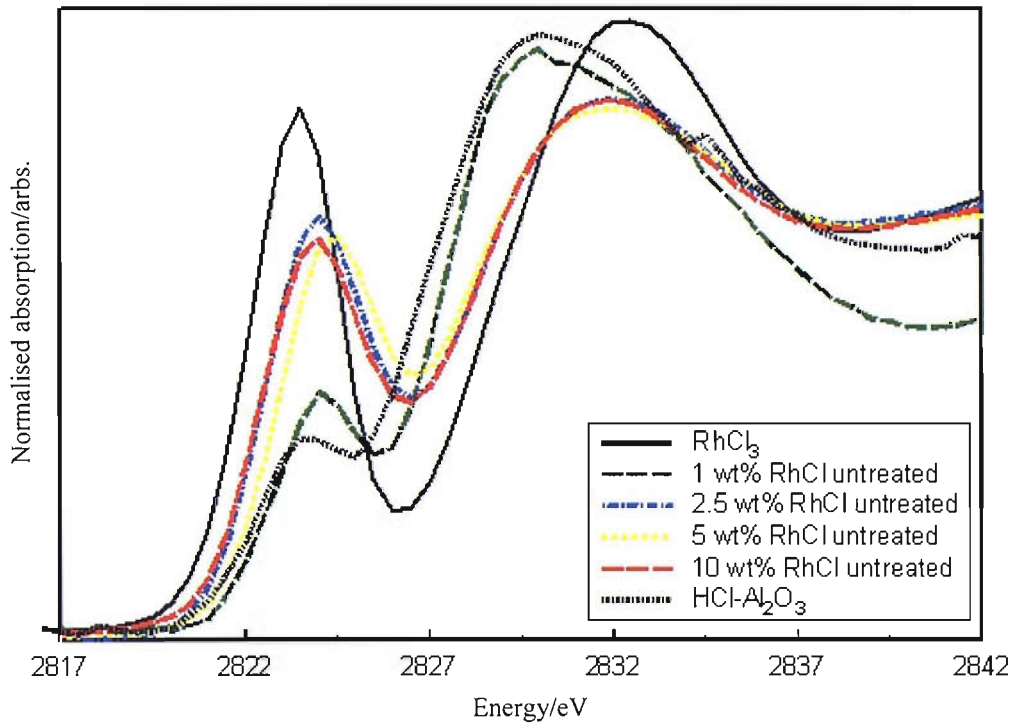

Figure 3.11: Normalised Cl K-edge XANES data for a series of untreated RhCl samples measured under vacuum at room temperature.

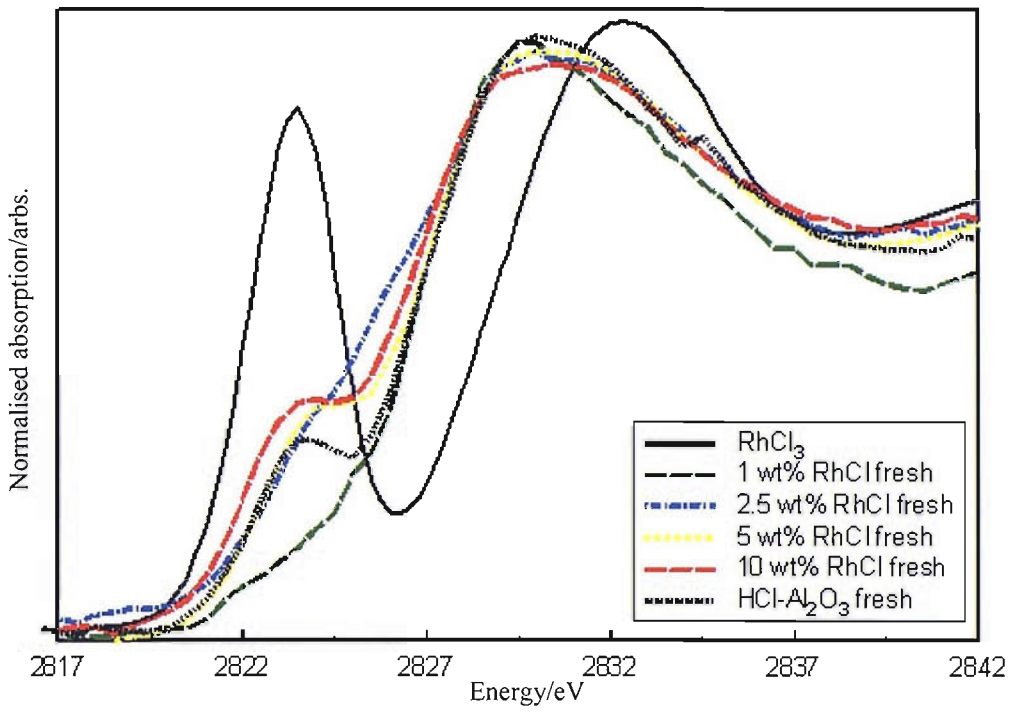

Figure 3.12: Normalised Cl K edge XANES data for a series of fresh RhCl samples measured under vacuum at room temperature.

To be able to interpret the Cl K edge XANES data, two relevant reference spectra have been obtained; the $RhCl_3$ starting (precursor) complex and a chlorinated γ-Al_2O_3 support (prepared by impregnating γ-Al_2O_3 with an HCl solution). The $RhCl_3$ is representative for Cl directly associated with Rh, whereas the HCl-Al_2O_3 mimics the Cl attached to or associated with the support. It can be seen in Figures 3.11 and 3.12 that the edge position of the HCl-Al_2O_3 is ~5 eV lower in energy than the $RhCl_3$ Cl K edge. Moreover, the pre-edge observed for the $RhCl_3$ sample is much more pronounced than for the HCl-Al_2O_3, while its position is shifted to a lower energy.

The pre-edge observed in this Cl K-edge XANES data is previously observed for ligands bound to 3d transition metals.[17] The observations made in the literature can be directly transferred to the 4d transition metal system studied here. The chlorine 3p orbital is directly involved in bonding with transition metal complexes. Because the electric dipole allowed transitions for the K-edges are 1s → *n*p, ligand metal K XAS provides a direct probe for these metal – ligand bonding interactions. The lowest energy available for Cl 1s K edge is the

unoccupied 4s and 4p orbitals levels. The 1s → 4p transition is dipole allowed and thus primarily responsible for the edge transition at 2827-2829 eV (depending on sample), see figures 3.11/3.12. The Rh(III) in $RhCl_3$ is a d^6 ion and has a hole in two of its 4d orbitals. The pre-edge observed here thus corresponds to a Cl 1s → Rh 4d transition. For this transition to occur (i.e. for it to obtain intensity), this 4d orbital should interact with a Cl p orbital. The presence of this pre-edge implies that covalent Rh–Cl bonding exists and its intensity indicates the covalent character between metal and ligand. The $RhCl_3$ Cl K-edge XANES spectrum is simulated by FEFF8.0, displayed in figure 3.12(a) along with its calculated DOS. The pre-edge as observed in the experiment is simulated well by such calculations. The origin of the pre-edge is displayed in the density of states and, as expected, due to a transition to Rh d and Cl p (and Rh p) overlapping molecular orbitals. The further shape of the XANES between theory and experiment does differ; this is due to the fact that in the experiment a hydrate has been measured, whereas the theory assumed a pure, dry, rhodium trichlorate.

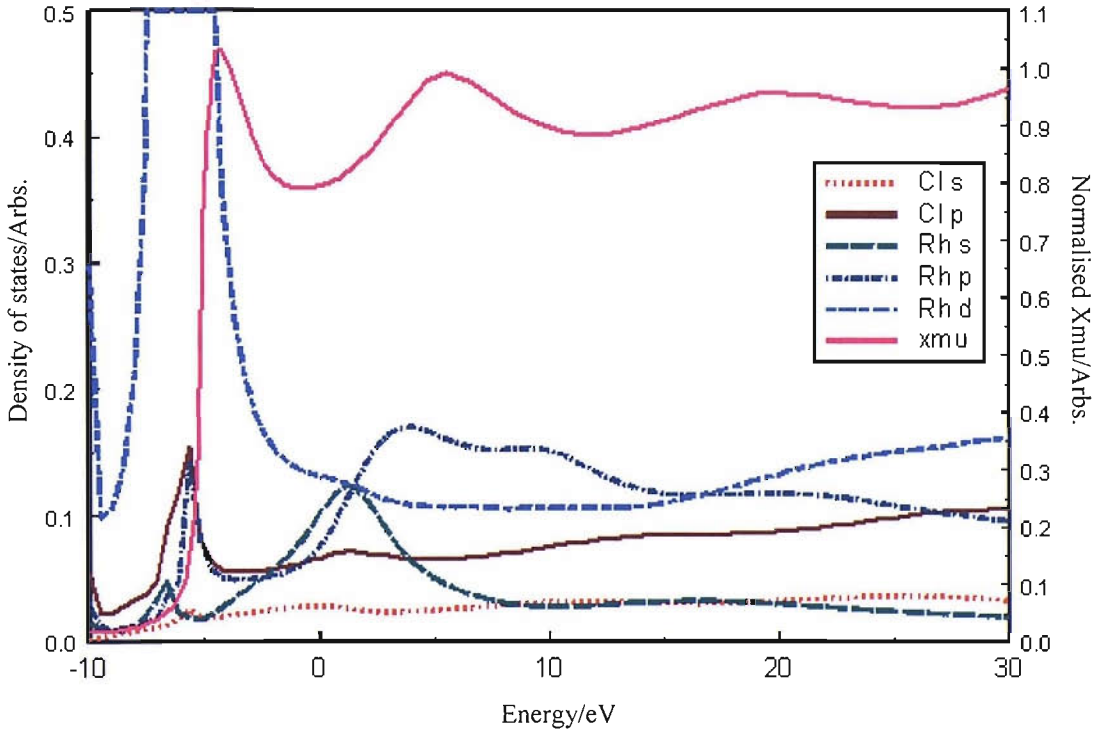

Figure 3.12 (a): Simulated normalised Cl K-edge XANES and DOS (FEFF8.0) for the $RhCl_3$ reference. The energy is displayed relative to the edge (which is situated at 0eV).

The Cl K-edge position for the $HCl\text{-}Al_2O_3$ sample is situated lower in energy than for the $RhCl_3$ sample, and displays only a small pre-edge. For the $HCl\text{-}Al_2O_3$ sample the chlorine is coordinated to the alumina surface and will most likely interact with acid sites on the alumina or with the aluminium directly. The effective bonding will be much less in comparison to the aforementioned Rh–Cl bond, leading to less charge transfer and thus a lower XAS edge energy position.

The alumina support is an insulator with a considerable band gap between filled and empty molecular orbitals. Introduction of chlorine ions on or into the support creates an empty molecular orbital in this band gap, in which the photo-electron can be excited and as such creating a pre-edge feature in the Cl K-edge XANES. FEFF8.0 calculations have not been successful in this instance primarily due to the simulation of the $\gamma\text{-}Al_2O_3$ support structure. The $\gamma\text{-}Al_2O_3$ structure is complicated; it has been quoted as being 'a mystery', and has not been fully solved so far.[18] A minimum of five different hydroxyl groups have been recognised and various defect sites are also known to be present;[19] all of which are sites on which chlorine could potentially adsorb. Studies in the literature[20] suggest that the intensity of the pre-edge reflects the position of the chlorine atom in or on the alumina. For chlorine adsorbed on the alumina support, a small pre-edge is observed, whereas chlorine present in the support structure (simulated by replacing oxygen for a chlorine ion) results in an increased pre-edge feature observed.

^{27}Al-NMR results for unsupported, untreated and fresh samples are identical, displaying only the tetrahedral Td and octahedral Oh Al sites. Although Al-NMR should potentially detect these low concentrations of chlorine (*vide infra*), no AlClx or AlOCl type sites can be identified in this instance. This is likely due to the large variety of possible adsorption sites as discussed before, resulting in weak and very broad bands. The Al-NMR experimental data were gratefully received from Prof. Jeroen A. van Bokhoven, ETH, Zurich, Switzerland.

The untreated RhCl samples shown in figure 3.11 highlight the 2.5 to 10 wt% samples to closely resemble the $RhCl_3$ in pre edge intensity, position and edge position, indicating the Cl is still closely associated with the Rh. The small differences with the $RhCl_3$ precursor are expected since the complex is associated to the Al_2O_3 support, thereby changing its geometry. The small changes in geometry will lead to changes in ligand-metal covalency and thus a change in pre-edge intensity. The Cl on the 1wt% sample closely resembles the $HCl\text{-}Al_2O_3$

which suggests it is coordinated to the support; thus (partial) dissociation of the $RhCl_3$ has taken place.

The fresh RhCl samples (i.e. after reduction in hydrogen) in figure 3.12 show a close resemblance to the $HCl\text{-}Al_2O_3$ spectrum. Their edge positions are observed to have shifted down considerably compared to the untreated analogue samples. They now correspond closely to the $HCl\text{-}Al_2O_3$ sample, and only a small pre-edge is observed. The calcination and ex situ reduction processes seem to have resulted in a dissociation of the $RhCl_3$ precursor, resulting in loss of Cl from the sample and the remaining Cl is bound to the support. Indeed, no significant coordination to the Rh is observed. Whereas the XANES data for the untreated samples (2.5, 5 and 10 wt%) are essentially invariant, small differences in pre-edge intensities and edge positions are observed for the fresh samples. With increased Rh metal loading, an increase in the pre-edge feature is observed. As discussed above, this feature is most likely related to the position of the Cl in or on the alumina support.[20]

The amount of Cl present in the different samples has been quantified using the edge step calibrated to the reference samples, the results are given in table 3.3. The accuracy of the quoted figures is estimated to be ~ ±20%; 10% in amount of sample weighted in (experimental error) and 10% in the edge step determination. For the untreated samples slightly higher amounts of Cl are observed, suggesting slightly higher amounts of $RhCl_3$ precursor have been used in the synthesis of the supported complexes than the theory indicates. Inspection of the amounts of Cl observed in the fresh samples, reveals that for the 2.5 wt % to 10 wt% RhCl samples a similar amount of Cl is retained on the support (while the rest is removed from the sample in the calcination and reduction processes). An expected lower amount of ~1 wt% is observed for the 1 wt% RhCl, since not more than 1.2 wt% Cl (see table 3) has been deposited on this sample.

3.3.4 Rh K-edge XANES and EXAFS

The fresh and in situ reduced 2.5 wt% and 5 wt% RhCl samples have been characterised with Rh K-edge XAFS; figure 3.13 displays the normalised X-ray absorption data for the 5 wt% RhCl sample as an example of the data obtained.

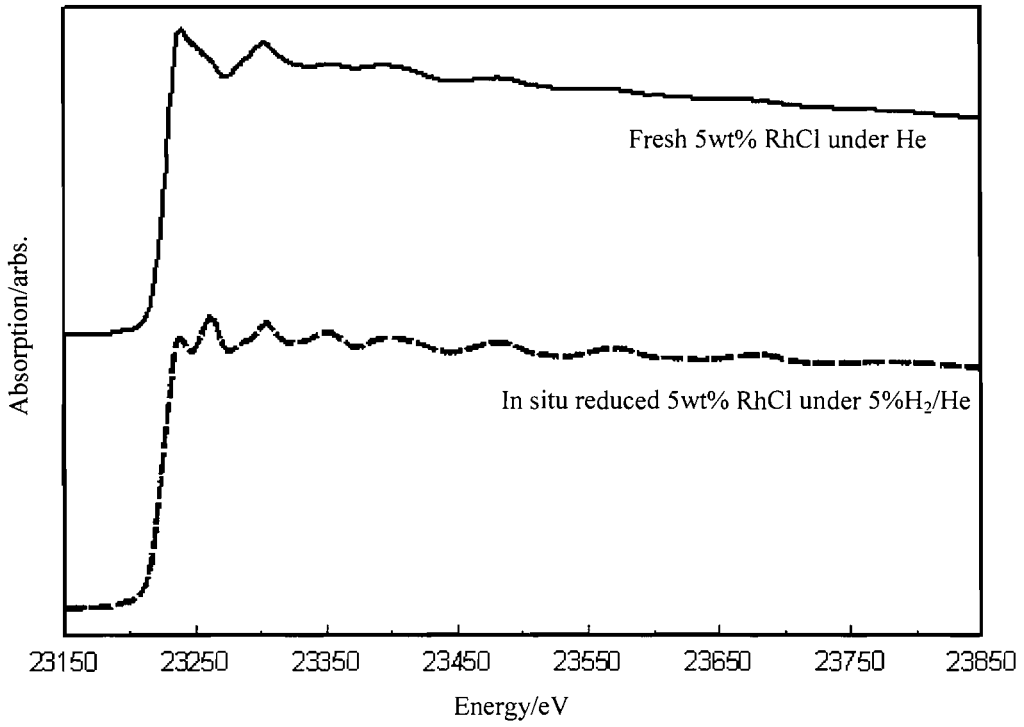

Figure 3.13: Rh K-edge scanning XAFS data of 5wt% RhCl; fresh in He (solid line) and in situ reduced in $5\%H_2/He$ (striped line). Both spectra were obtained at room temperature.

The XANES and EXAFS signatures of the two spectra are clearly different; the fresh sample resembles rhodium oxide whereas the in situ reduced sample displays a metallic structure. The k^3-weighted EXAFS data and their corresponding Fourier transforms of the experimental data and their theoretical fits are reported in figures 3.14 and 3.15 respectively. The structural and statistical data relating to these figures is given in table 3.4. For the fresh 5wt% RhCl sample a predominant Rh–O contribution at a distance of 2.03 Å is found, indicating that rhodium oxide is present; the Rh–O bond length in Rh_2O_3 is indeed ~2.03 Å.[21] The Rh-O bond lengths of Rh metal particles to the Al_2O_3 support are in the range of 2.7 Å.[22] Pure Rh_2O_3 would give a 1st shell Rh-O contribution with a coordination number of 6, a 2nd shell Rh-Rh contribution with a coordination number of 4 and Rh-Rh bond distance of 2.98 Å.[2] All of this data suggests that the Rh nanoparticles in the 5wt% chloride system are partially oxidised. However, the most likely morphology is of a metallic core surrounded by an oxide layer; this would explain the metallic Rh-Rh bond distance of 2.69 Å as observed by EXAFS being much smaller than for Rh_2O_3.

The in situ reduction in $5\%H_2/He$ results in the 1st shell Rh-Rh coordination number increasing to a value of ca. 7 and the presence of oxygen in close proximity is not observed, indicating metallic particles have formed. A similar trend in results is observed for the 2.5 wt% RhCl sample. However, EXAFS reports smaller metal particles to have formed (N_1^{Rh} = ca. 2.6 and 4.2 for the fresh and in situ reduced system respectively); an expected result based on the TEM results obtained for both of the systems in question.

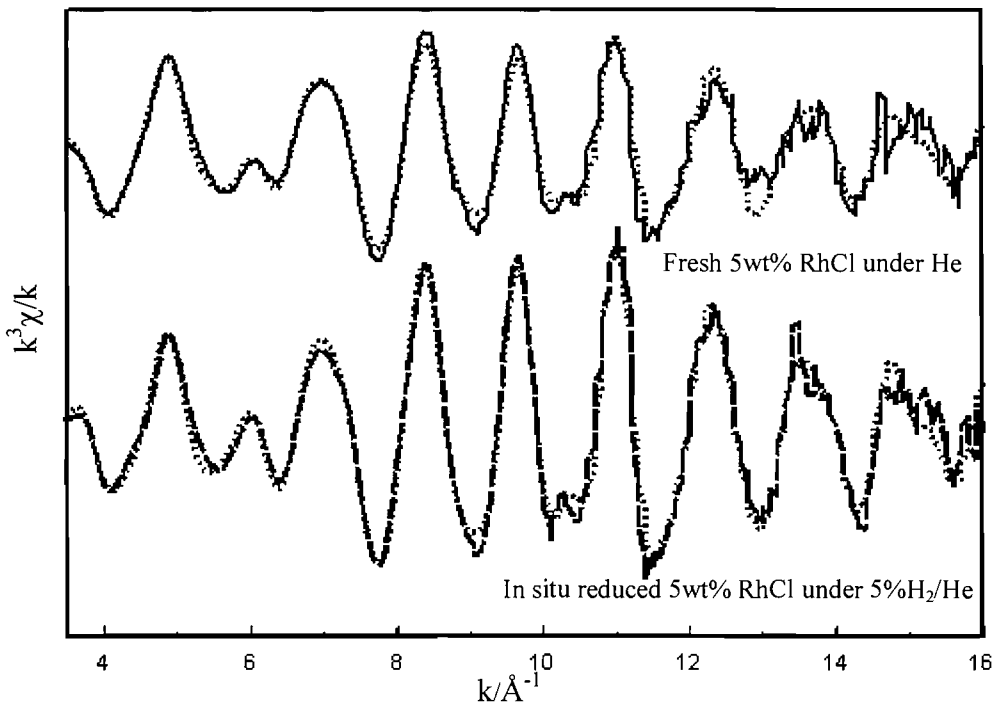

Figure 3.14: k^3 weighted scanning EXAFS data of fresh 5wt%RhCl in He and in situ reduced in $5\%H_2/He$. Both spectra are obtained at room temperature. The solid lines show experimental data, dotted lines show theoretical data.

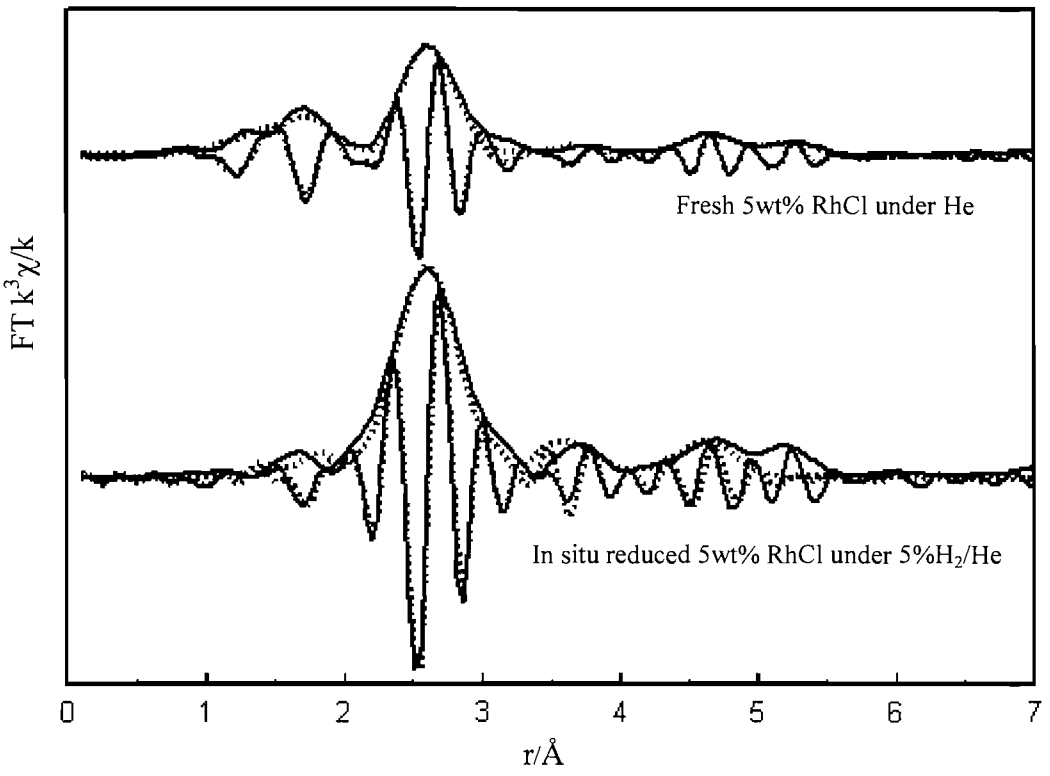

Figure 3.15: k^3 weighted Fourier transforms showing the fresh 5wt% RhCl under He and in situ reduced under 5%H_2/He. Both spectra are obtained at room temperature. The solid lines show the experimental data, dotted lines show the theoretical data.

Sample (Conditions)	Scatterer	CN	R/Å	$\Delta\sigma^2/Å^2$	E_f/eV	R/%
Fresh 5wt% RhCl	O	3.4 (± 0.3)	2.03	0.014		
(He, room temperature)	Rh	3.6 (± 0.3)	2.68	0.011		
	Rh	2.8 (± 0.3)	3.79	0.024		
	Rh	2.7 (± 0.2)	4.66	0.009	-6.39	20
In situ reduced 5wt% RhCl	Rh	7.0 (± 0.6)	2.67	0.011		
(5%H_2/He, room temperature)	Rh	1.3 (± 0.1)	3.76	0.011		
	Rh	4.2 (± 0.3)	4.65	0.010	-7.06	32
Fresh 2.5wt% RhCl	Rh	2.6 (± 0.2)	2.69	0.011	-3.21	53
(He, room temperature)						
In situ reduced 2.5wt% RhCl	Rh	4.2 (± 0.4)	2.67	0.011	-6.25	36
(5%H_2/He, room temperature)						

Table 3.4: Structural and statistical data derived from the Rh K-edge EXAFS analysis of the fresh and in situ reduced 2.5 and 5wt% RhCl systems. Other parameters: k = 3-16 $Å^{-1}$, k^3-weighted fit. Errors in DW factors deemed to be ± 0.001 and ± 0.02 in bondlength determination. Data for the 2.5wt% system was not of sufficient quality to permit analysis of a second shell.

The Rh K-edge XANES spectra are investigated in more detail by taking the 1st derivative of the normalised data, shown in figures 3.16 and 3.17 for the 5 wt% and 2.5 wt% RhCl samples respectively. A clear difference is observed between the fresh and reduced samples on simple inspection of the room temperature data, both in energy position and in peak shapes (also apparent in figure 3.13). The peak position of the fresh sample is positioned at a higher energy, indicating a higher Rh oxidation state for the fresh sample when compared to the reduced sample. The reduced samples seem to consist of at least two contributions and their intensity (ratio) also differs.

Figure 3.17 also displays data obtained from the in situ reduced 2.5 wt% RhCl sample at 573 K, which serves to highlight that a significant structural change occurs during the reduction process. This phenomenon is outside the scope of this study, and is currently the subject of further investigation.[23]

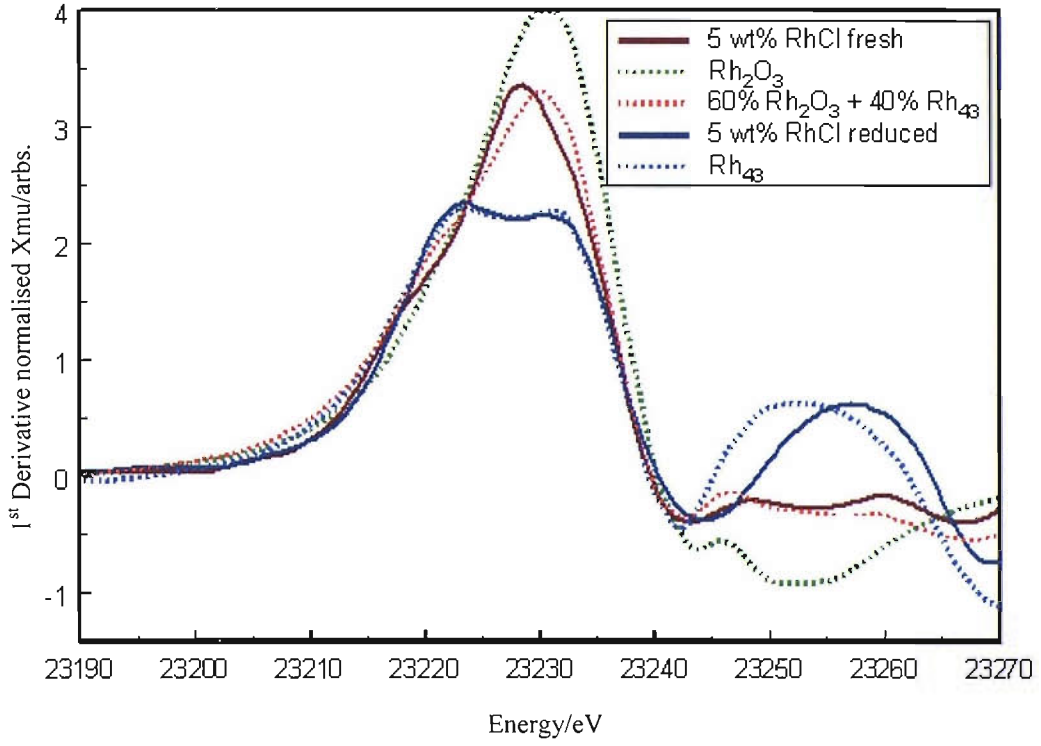

Figure 3.16: 1st Derivative of the normalised Rh K-edge XANES data for a fresh 5 wt% RhCl (red) and an in situ reduced 5 wt% RhCl sample (blue) at room temperature, showing the experimental data (solid lines) and FEFF8.0 simulations (dotted lines).

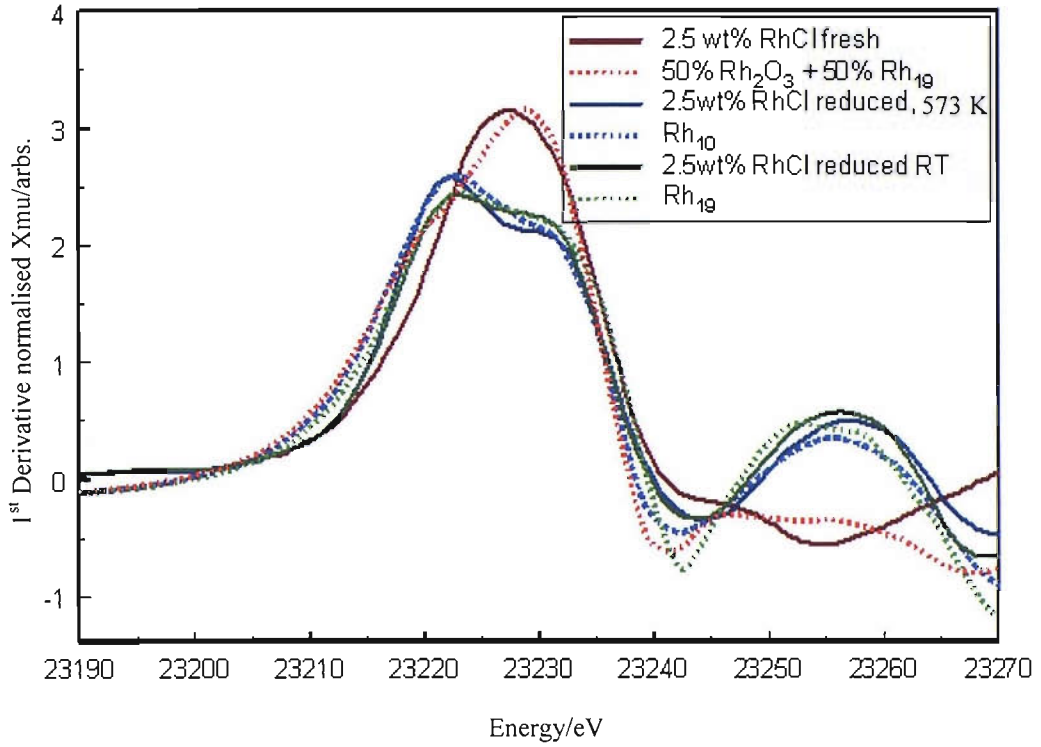

Figure 3.17: 1st Derivative of the normalised Rh K-edge XANES data for a fresh 2.5wt% RhCl (red) and an in situ reduced 2.5 wt% RhCl sample at 573 K (blue) and at room temperature (green), showing the experimental data (solid lines) and FEFF8.0 simulations (dotted lines).

FEFF8.0 calculations have been performed in order to obtain detailed insights into the origin of the edge features and possibly fit these contributions. A broad series of Rh fcc particles were simulated; the XANES and their corresponding 1st derivatives are plotted in figures 3.18 and 3.19 respectively. It is clear from figure 3.18 that although the Rh K-edge displays a broad and non-descript edge, a trend in edge shape and position with metal particle size is observed. This trend can be clarified by taking the first derivative of these XANES spectra (as shown in figure 3.19). Simulations starting from small Rh_3 clusters show that the edge consists of one main peak and higher XANES features are low in intensity. A second feature appears when the particle size is increased, broadening the edge and eventually the first peak decreases in intensity. Concurrently the higher XANES features around 23255 eV increase in intensity and shift to a slightly lower energy. No significant changes in XANES features are observed for particles consisting of $\geq$55 atoms.

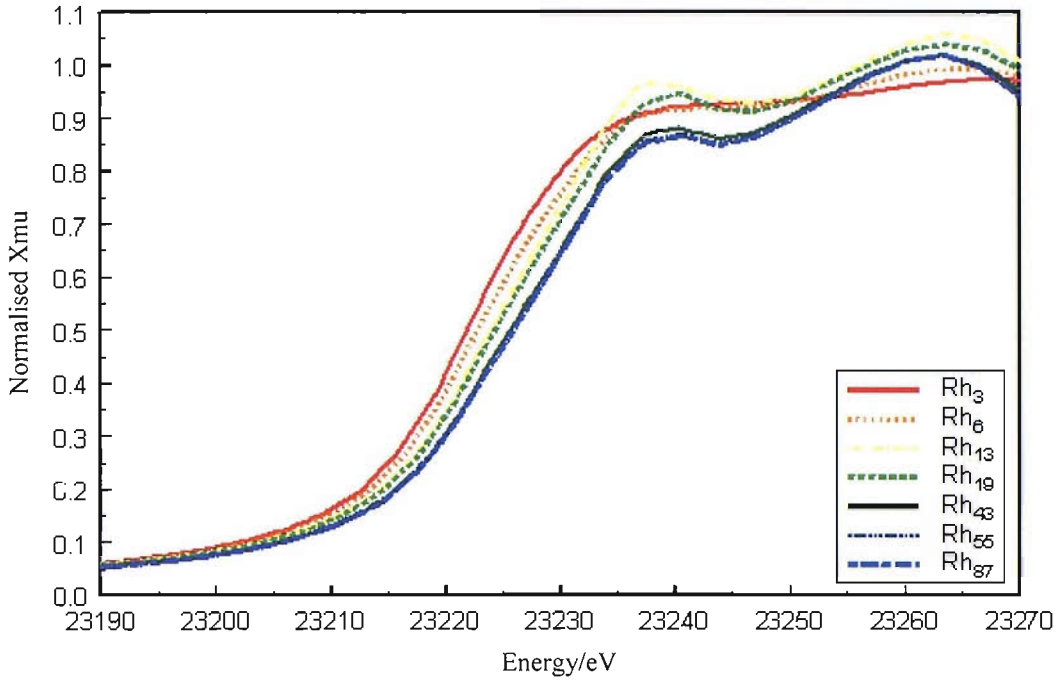

Figure 3.18:Rh K-edge XANES particle size dependence as simulated with FEFF8.0, for spherical particles with an fcc structure.

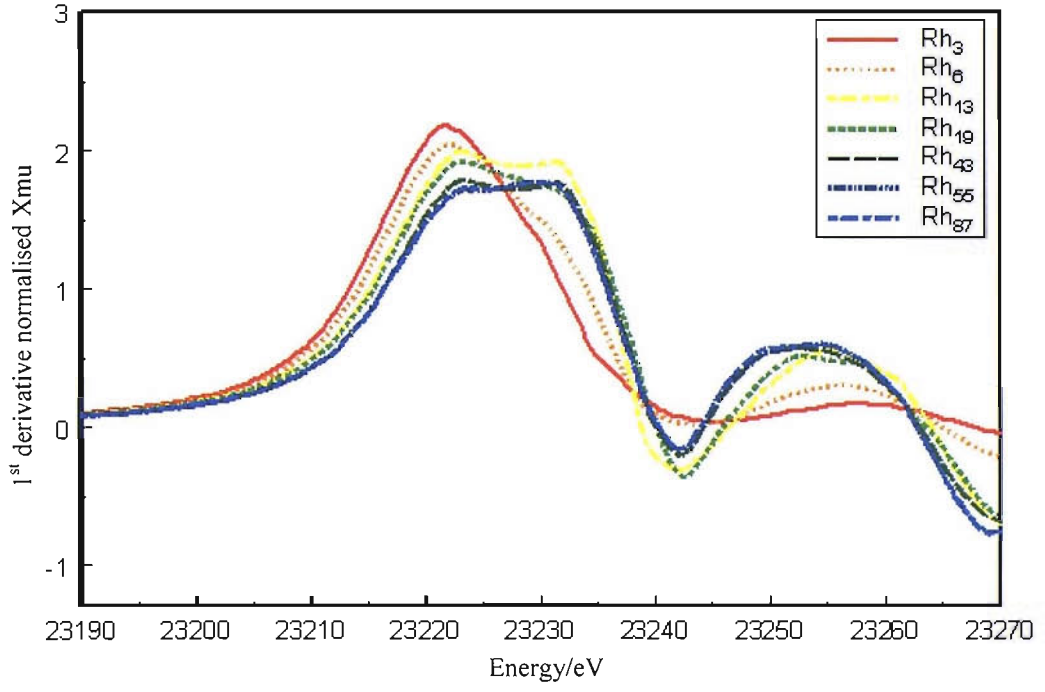

Figure 3.19: 1st derivative of normalised Rh K-edge XANES as a function of particle size as simulated with FEFF8.0, for spherical particles with an fcc structure.

As the Rh nanoparticles are supported on Al_2O_3 the effect of support contributions, i.e. from oxygen, on the Rh K-edge XANES is expected; this is especially the case when considering smaller particles. In order to mimic such support effects, O contributions with a Rh-O distance of 2.03 Å in a tetrahedral position were added to the metal particles for the simulations. For the Rh_3 particle up to 3 oxygen atoms were added; up to 4 for the Rh_6 particle (depending on the site of the particle attached to the support).

The effect of adding these contributions on the Rh K-edge XANES is displayed in figure 4.20. A broadening of the main XANES feature is observed, however, the first feature remains highest in intensity (a trend that is in contrast to increasing the particle size alone). Moreover, it is clear that the addition of oxygen to the rhodium particles leads to the suppression of the XANES intensity around 23255 eV. As expected, both effects discussed here are more significant for the smallest Rh_3 particle. Indeed, no significant influence of oxygen contributions for bigger particles (i.e. more than 6 atoms) is observed.

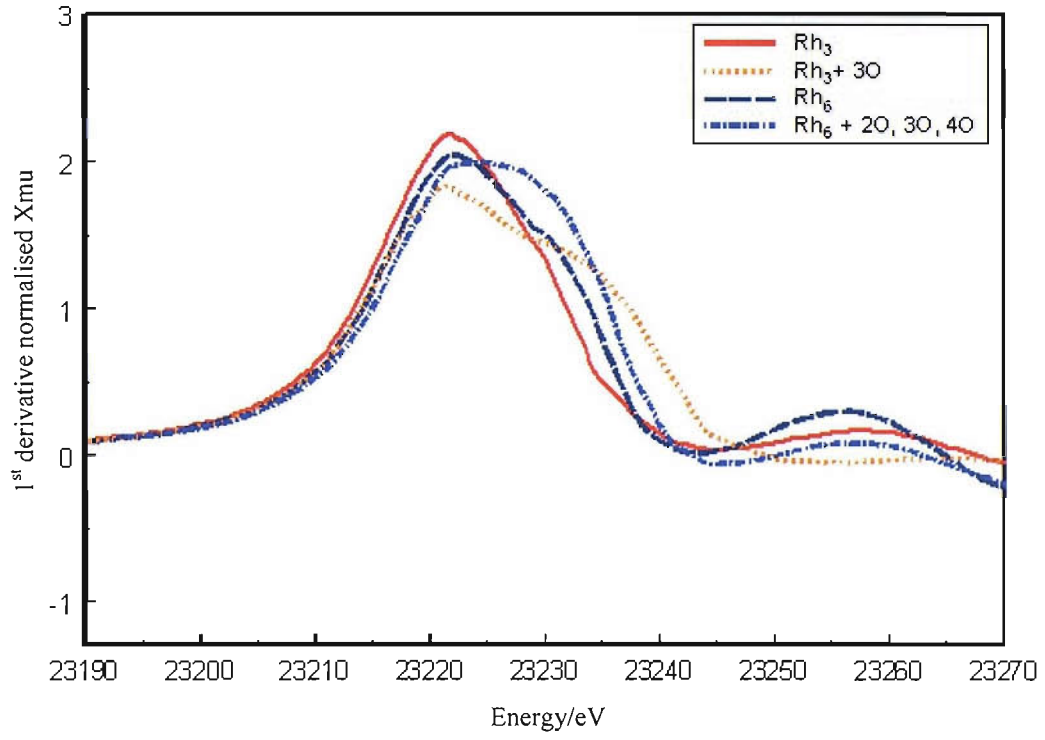

Figure 3.20: 1st derivative of normalised Rh K-edge XANES for Rh_3 and Rh_6 particles, with and without support oxygen, as simulated with FEFF8.0.

In order to obtain a clearer understanding of the origin of the XANES features reported by figures 3.18-3.20, the density of states (DOS) have been simultaneously simulated with FEFF8.0. The Rh s, Rh p and Rh d DOS for a Rh_3 and Rh_{87} cluster are plotted in figures 3.21 and 3.22 respectively. The calculated Fermi levels are shown as a vertical line at -6.99 eV and -9.33 eV respectively. The 1st derivative of the normalised XANES has been added for comparative reasons.

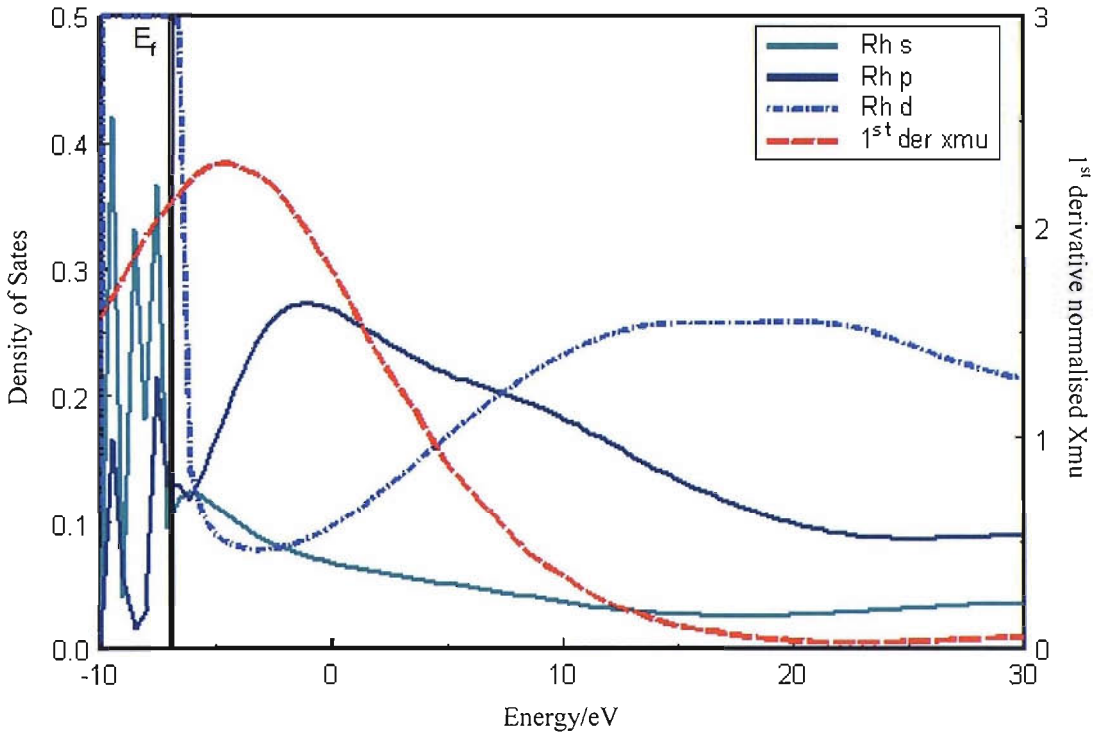

Figure 3.21: Density of states for an Rh_3 cluster, calculated using FEFF8.0. The 1st derivative of the normalised XMU is added as a striped red line. The vertical black line shows the position of the Fermi level.

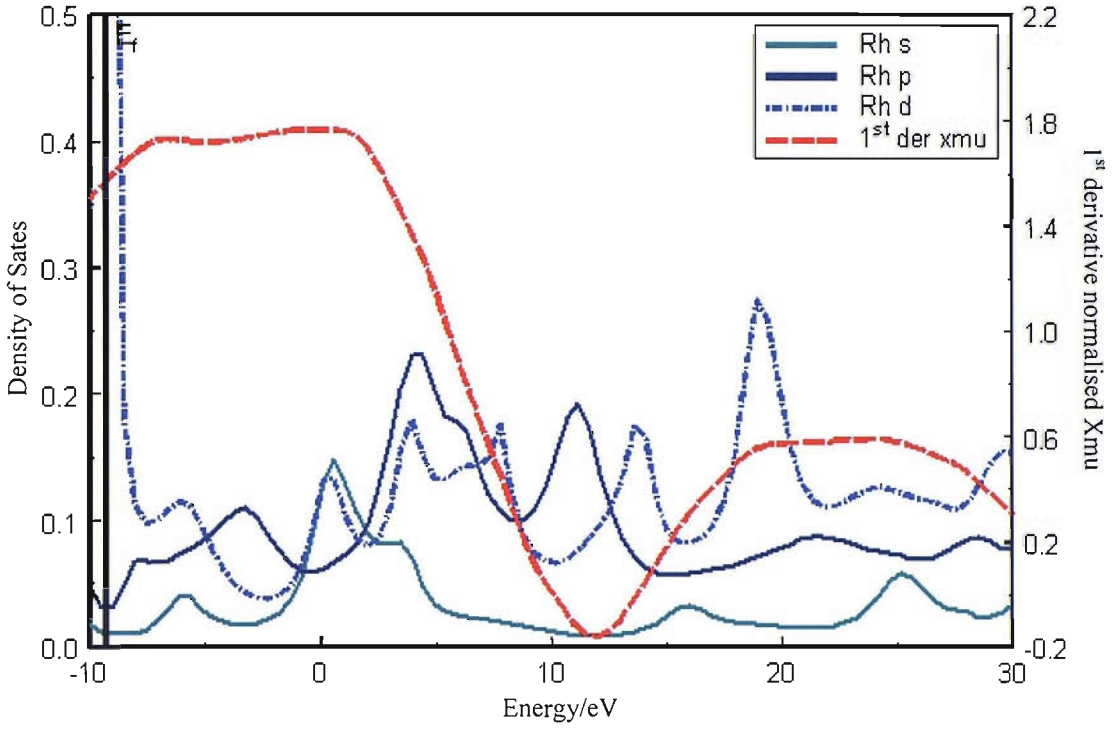

Figure 3.22: Density of states for an Rh_{87} cluster, calculated using FEFF8.0. The 1st derivative of the normalised XMU is added as a striped red line. The vertical black line shows the position of the Fermi level.

The unoccupied molecular orbitals (empty DOS) above the Fermi level are probed with Rh XANES. The main transition probed with Rh K-edge XAS is the Rh 1s→5p (shown as the solid blue lines in figures 3.21/3.22).

For the Rh_3 cluster one main p band is observed, without any overlap with s or p orbitals. The Rh p unoccupied level is observed by Rh K-edge XANES, the other contributions being forbidden.

The Rh_{87} cluster given in figure 3.22 reports the Rh p band to consist of quite different contributions. The Rh p orbital now clearly overlaps with Rh d contributions at around 5 eV, making them partially allowed and thus visible in the K-edge XANES. Therefore DOS analysis assigns the two main contributions observed in XANES to a 'pure' Rh p and a mixed Rh p / Rh d DOS respectively. The observed differential between small and larger particles can be explained by the fact that the DOS for small particles closely resemble atomic orbitals, while for bigger particles the orbitals become broader as increasing amounts

of orbitals overlap and hybridise. This leads to more of these levels to be detected with XANES (increasing the width of the band and the intensity of the second feature).

To summarise the results in this section, the metal particle simulations serve to fit the XANES data obtained for the in situ reduced RhCl samples shown in figures 3.16/3.17. The 5wt% sample can be matched well with a Rh_{43} metal particle; which corresponds to an EXAFS 1st shell Rh-Rh coordination number of 7.4 (± 10 %) (see table 3.1). As expected, the particle size derived from XANES analysis closely corresponds to the EXAFS analysis results obtained for this sample which indexes an N_1^{Rh} value of ca. 7. It has to be noted here that the position of the XANES peak ~23255 eV is not entirely accurate; however the overall intensity is still well represented.

The 2.5 wt% sample has been analysed at two temperatures. The XAS spectrum obtained at 573 K in $5\%H_2$/He is fitted with an average particle size of 10 Rh atoms ($\{Rh_6 + Rh_{13}\}/2$), whereas an Rh_{19} particle correlates well to the XANES spectrum obtained at room temperature. Again these results closely match the values obtained via EXAFS analysis (see table 3.4); the N_1^{Rh} values at 573 K and room temperature being ca. 4.2 and 6 respectively.

The fresh Rh supported samples were simulated by using a combination of a Rh_2O_3 structure[21] and a metal particle (see figures 3.16/3.17), based on inspection of the raw data and the EXAFS analysis results (see figure 3.13 and table 3.4). The XANES pattern for a pure Rh_2O_3 structure is added for comparison reasons (the difference between a Rh_2O_3 simulation for an oxide particle with a radius of ~3 and of ~7 Å is negligible; therefore the data is not shown here). The intensity of the Rh edge band feature in the 1st derivative is much more pronounced for the oxide as for the metal. An oxide percentage of 60% and 50% for the 5 and 2.5 wt% RhCl samples respectively was necessary to effectively simulate the intensity of the peak and the contributions at higher energy (Rh_2O_3 only gives a negative contribution around 23255 eV, metal particles give a positive contribution).

3.5 Discussion

The impregnation of γ-Al_2O_3 with rhodium nitrate and chloride precursors to yield metal loadings between 1 and 10 wt% Rh results in the formation of highly dispersed supported nanoparticulate systems. The TEM results indicate particle sizes with a distribution of 5 to 60 Å for the 2.5 to 10 wt% samples. However, the in situ EXAFS and XANES obtained for these reduced samples indicate that the metallic Rh particle size in these systems is considerably smaller: 7.5 vs. 12 Å (EXAFS vs. TEM) for the 2.5wt% sample and 9 vs. 21 Å for the 5wt% sample. Rh EXAFS, XANES and XPS results on the fresh samples indicate the supported rhodium particles to be oxidic rather than metallic.

The resolution of the TEM measurements therefore precludes an identification of the Rh phase present. Moreover, TEM only detects particles with a minimum diameter of 5 Å, whereas EXAFS determines an average of all particle sizes (including atomic Rh). Assuming spherical particles are formed on the γ-Al_2O_3 support; TEM will only detect particles in the regime of ca. 13 atoms or greater, i.e. with an EXAFS coordination number of 5 and higher. Based on the particle size distributions given in figures 3.6/3.7 this discrepancy is especially applicable for the 2.5 wt% samples. Both the un-chlorinated and chlorinated 2.5 wt% samples show particle sizes from the limit of 5 Å in TEM, and the particle size distribution suggests significant amounts of smaller particles are indeed present. Systems with a higher metal loading, however, exhibit a larger average PSD and suggest this resolution limit to exert an attenuated influence on the results.

The XANES analysis of the Rh K-edge data for the in situ reduced samples resulted in similar particle sizes as determined by the EXAFS analysis, confirming the validity of the two methods. These metal particles are simulated well using spherical fcc particles, indicating this to be a good approximation for the particle shape present in these systems. Jentys[14] presented a method to estimate metal particle shapes based on multiple shell EXAFS analysis. By observing the 1^{st} or 2^{nd} shell coordination number and comparing this with higher shell (3^{rd}, 4^{th}) coordination numbers, information on the size and shape of the clusters is obtained. By comparing the results of the 5wt% sample (see table 3.4) with the model presented in reference 14, spherical cluster shapes do indeed apply (as opposed to distorted cubic or slab (hemispherical) shapes). Unfortunately, the EXAFS data obtained for the 2.5

wt% sample only allowed for a single shell fit, therefore a determination of the particle shape cannot be made.

The advantage of using XANES analysis procedures to obtain particles sizes over EXAFS analysis is that only a small part of the spectrum needs to be obtained. This is especially relevant in the case of time-resolved experiments. For example, in order to monitor catalytic reactions such as the experiments performed in this study, a trade-off between time-resolution and signal to noise ratio needs to be made.[24] Data with a long energy range (~1000 eV) and a good signal to noise ratio needs to be obtained to allow reliable EXAFS analysis. For XANES analysis this energy range can be up to ~15 times smaller, potentially increasing the time-resolution of data-acquisition proportionally. Moreover, XANES analysis can serve to act as an initial 'indicator', providing essential information prior to any detailed EXAFS analysis. Figure 3.18 shows that, in the current case, this procedure is only applicable for small Rh metal particles of up to ~55 atoms (equating to an N_1^{Rh} value of ca. 7.7, see table 3.1).

For particles of 55 atoms and more, the dispersion of (surface atoms/total atoms) falls to below 0.9 (for 55 atoms i.e. ~0.8). This means that more than 10% of the metal particles are present in a 'wholly' metallic environment. Since these atoms will give rise to heavy metal - metal multiple scattering pathways they will also significantly affect the subsequent XANES data.

Consideration of the results accumulated in this study indicates the fresh samples to be oxidised; it is only after the in situ reduction that metallic particles are detected. The facile oxidation of Rh supported samples after exposure to air at room temperature has been previously reported by both time-resolved[6] and scanning EXAFS data.[25,26] Time-resolved EXAFS monitoring the oxidation of a sieve fraction of a reduced 5 wt% RhCl sample in a microreactor at room temperature in $4\%O_2/He$, showed a decrease in the N_1^{Rh} value from ca. 7 to 4.5 in less than 5 seconds with the formation of a short (2.04 Å) 1st shell Rh-O coordination (CN = 2).[4] A Rh-Rh EXAFS coordination number of ca. 2.6 and 3.6 is observed for the fresh 2.5 and 5wt% Rh samples respectively in this study (table 3.4), with a Rh-O coordination number of ca. 4 for the 5wt% sample (data not available for the 2.5wt% Rh sample). Since a bulk Rh_2O_3 will give a 1st shell Rh-O coordination number of 6,[21] the 5wt% sample is ~66 % oxidised. EXAFS results report there to be a metallic core present (which is

surrounded by an oxide layer) as the Rh-Rh bond distance is of metallic Rh, i.e. considerably shorter than in Rh_2O_3.

Similar percentages have been obtained in the XANES analyses for these fresh samples (60 % for 5wt% vs. 50 % for 2.5wt%, figures 3.16 and 3.17 respectively). The increased amount of oxidation of the 5wt% samples vs. the 2.5wt% was confirmed with XPS in which a lower Rh 3d binding energy was observed for the 2.5 wt% in comparison to the higher loaded samples (figure 3.9).

To interpret the EXAFS results, the XANES simulations used a combination of fully oxidised Rh_2O_3 and fully metallic Rh particles with a coordination number similar to the reduced system. Small discrepancies between the XANES simulations and the experimental data for the fresh samples (especially the 2.5wt%) are observed, which are likely intrinsic to the simulation method used. This is due to the aforementioned oxidic shell around a metallic Rh core that is likely to have formed in the 'real' case.[25,26] The XANES simulations (and hence any EXAFS interpretation) should thus take into account the decrease of an Rh_2O_3 shell and the increase of the metal particle size; a viable simulation model has not been found so far. As the XANES features are not significantly affected by varying the size of the Rh_2O_3 particles, the influence of the thickness of the oxidic core is also expected to be small.

A combination of different metal particle sizes has also been used to simulate the fresh XANES data. The combination of Rh_2O_3 with Rh_{19} and Rh_{43} for the 2.5 and 5 wt% samples respectively gave the best result. This correlates well with all the available data as the 2.5wt% system is expected to be more extensively oxidised than its higher loaded analogue. Moreover, as TEM particle size distributions predicted, a large amount of particles present on the 2.5 wt% sample are not detectable and thus not taken into account.

TEM measurements also reported the average mean particle size in the RhN systems to be higher when compared to the RhCl samples; with XPS indicating the particles to be less extensively oxidised. This means that by using a RhN precursor results in larger Rh supported particles which are less readily oxidised, assuming no significant redistribution of rhodium particles takes place during the in situ reduction process. The difference in oxidation however suggests that an oxidic shell of similar size (thickness) around a metal particle is present for both the RhN and RhCl systems, since the particle size decreases for systems with increasing rhodium metal oxidation. In summary, a thin oxidic layer is rapidly formed around

a metallic particle upon exposure to oxygen, which subsequently acts as a barrier to prevent any further oxidation of the particle. Unfortunately no further in situ characterisation of the RhN samples is available; however they are currently under further investigation.

The array of ex situ experiments report the fresh samples to be partially oxidised, which has two important ramifications. Firstly, any assumption that Rh particles observed only by TEM (under current resolution limits) are in fact metallic is likely to be incorrect. Such an assumption can lead to an over-estimation of the metallic nuclearity for a given particle and considerable underestimation of the real dispersion of the reduced catalyst. Secondly these measurements indicate that oxidation and reduction, which has been shown to be very rapid and exothermic even at room temperature,[4] is not accompanied by a major spatial reorganisation of Rh and spherical metallic particles are obtained.

Further, our XPS measurements comparing spectra derived from powder and pressed disc samples show that in supported metal systems pellets and powders do not necessarily demonstrate the same chemical properties; therefore such results cannot always be directly correlated.

XPS and Cl XANES show that Cl is retained in the RhCl systems after the initial calcination / reduction processes, i.e. in the fresh RhCl samples. The Cl XANES results show that after impregnation and before any treatment the chlorine is, as expected, associated with the rhodium. After the calcination / reduction procedure no significant Rh – Cl interaction is observed and the majority of the chlorine is associated to the alumina support. This is further confirmed by Rh EXAFS and XANES in which no significant chloride contribution is observed.

Interestingly, the results indicate that a similar amount of chlorine is retained on all the chlorinated samples (with the exception of the 1 wt% sample onto which a smaller starting amount of Rh is deposited). Any further excess of chlorine is removed from the support during the subsequent calcinations and reduction treatments. The exact location of the chlorine on the support cannot be determined based on the current data and due to the complex nature of the support as discussed above.

However, the results do indicate that differences in behaviour between supported Rh systems originating from chlorinated versus un-chlorinated precursors[27] most likely does not originate from chlorine associated to the metal particle, but from changes to the acidity of the

support. Further investigation into the role of chlorine in these systems is needed in order to support such postulations.

3.6 Conclusions

The employment of an array of complimentary techniques has allowed for a detailed characterisation of the supported Rh systems used throughout the current study. Moreover, it has highlighted the advantages/disadvantages of each technique (and more importantly, subsequent limitations) which will be taken into account for analysis of results in the following chapters.

The results indicate that only the in situ techniques applied allowed for the characterisation of wholly metallic Rh particles. It was found that even brief exposure to air at room temperature results in the facile partial oxidation of the samples. This study therefore stresses that caution must be applied when comparing the results of different characterisation techniques, especially between techniques applied in situ versus ex situ.

There are clear differences in particle size distribution as a function of catalytic precursor. Un-chlorinated precursors (in this case nitrate) resulted in larger particles which are more difficult to oxidise than the chlorinated precursor analogue systems. For the chlorinated systems, no significant association of chlorine to the rhodium particles is observed with any of the techniques applied. For all loadings however a similar amount of chlorine was retained on the support after the calcination and reduction processes, suggesting a maximum amount of chlorine attachment/association sites are available on the γ-Al_2O_3 support.

The XAFS measurements provided in situ information on the samples under investigation. In addition to EXAFS, a Rh K-edge XANES analysis procedure has been applied. The XANES study has shown to be a reliable technique to characterise the average metal particle sizes for small particles up to 55 atoms. EXAFS and XANES both demonstrated the likely particle shape size to be spherical. Moreover, XANES analysis aided the interpretation of the EXAFS results obtained. The advantages of using XANES over more time demanding EXAFS (in the current case) in time-resolved measurements have also been discussed.

3.7 References

[1] A.C. Yang, C.W. Garland, *J. Phys. Chem.*, 1957, **61**, 1505.

[2] H.F.J. van 't Blik, J.B.A.D. van Zon, T. Huizinga, J.C. Vis, D.C. Koningsberger, R. Prins, *J. Am. Chem. Soc.*, 1985, **107**, 3139.

[3] A. Suzuki, Y. Inada, A. Yamaguchi, T. Chihara, M. Yuasa, M. Nomura, Y. Iwasawa, *Angew. Chem. Int. Ed.*, 2003, **42**, 4759.

[4] M.A. Newton, B. Jyoti, A.J. Dent, S. Diaz-Moreno, S.G. Fiddy, J. Evans, *Chem. Eur. J.*, 2006, **12**, 1975.

[5] M.A. Newton, B. Jyoti, A.J. Dent, S. Diaz-Moreno, S.G. Fiddy, J. Evans, *Angew. Chem. Int. Ed.*, 2002, **41**, 2587.

[6] M.A. Newton, B. Jyoti, A.J. Dent, S.G. Fiddy, J. Evans, *Chem. Comm.*, 2004, 2382.

[7] N. Binsted, PAXAS: Program for the analysis of X-ray absorption spectra, University of Southampton, 1988.

[8] N. Binsted, EXCURV98, CCLRC Daresbury Laboratory computer program, 1998.

[9] For example: **Pd K-edge XANES** (a) M. Tromp, J.A. van Bokhoven, G.P.F. van Strijdonck, P.W.N.M. van Leeuwen, D.C. Koningsberger, D.E. Ramaker, *J. Am. Chem. Soc.*, 2005, **127**, 777, **V K-edge XANES** (b) P. Frank, K.O. Hodgson, *Inorg. Chem.*, 2000, **39**, 6018, (c) J. Wong, F.W. Lytle, R.P. Messmer, D.H. Maylotte, *Phys. Rev. B.*, 1984, **3**, 5596, **Cu K-edge XANES** (d) S. DeBeer, D.W. Randall, A.M. Nerissian, J. Selverstone Valentine, B. Hedman, K.O. Hodgson, E.I. Solomon, *J. Phys. Chem. B.*, 2000, **104**, 10814, (e) J.L. DuBois, P. Mukherjee, T.D.P. Stack, B. Hedmann, E.I. Solomon, K.O. Hodgson, *J. Am. Chem. Soc.*, 2000, **122**, 5775, **Fe K-edge XANES** (f) W.E. Westre, P. Kennepohl, J.G. DeWitt, B. Hedman, K.O. Hodgson, E.I. Solomon, *J. Am. Chem. Soc.*, 1997, **119**, 6297.

[10] A.L. Ankudonov, B. Ravel, J.J. Rehr, S.D. Conradson, *Phys. Rev. B.*, 1998, **58**, 7565.

[11] D.R. Lide, 'Handbook of Chemistry and Physics', 1994, CRC Press Inc., Florida.

[12] E. Janin, H. van Schenck, M. Gothelid. U.O. Karlsson, *Phys. Rev. B.*, 2000, **61**, 144.

[13] M. Teliska, W.E. O'Grady, D.E. Ramaker, *J. Phys. Chem. B.*, 2004, **108**, 2333.

[14] A. Jentys, *Phys. Chem. Chem. Phys.*, 1999, **1**, 4059.

[15] W.C. Conner, E.L. Weist, T. Ito and J. Fraissard, *J. Phys Chem.*, 1989, **93**, 4138.

[16] For instance: V.Y. Gusev, X. Feng, Z. Bu, G.L. Haller and J.A. O'Brien, , *J. Phys Chem.*, 1996, **100**, 1985.

[17] For instance: E.I. Solomon, B. Hedman, K.O. Hodgson, A. Dey, R. Szilagyi, *Coord. Chem. Rev.*, 2005, **249**, 97 (including references therein).

[18] V.E. Heinrich, P.A. Cox, 'The Surface Science of Metal Oxides', 1994, Cambridge University Press, Cambridge, 64.

[19] H. Knödzinger, 'Surface Organometallic Chemistry: Molecular Approaches to Surface Catalysis', 1998, **231**, 45. Nato ASI Series C, Kluwer, The Netherlands.

[20] a) X. Qian, H. Sambe, D.E. Ramaker, *Phys. Rev.*, 1995, **B52**, 15115; (b) P.M. Natishan, W.E. O'Grady, E. McCafferty, D.E. Ramaker, K.I. Pandya, A.E. Russell, *J. Electrochem. Soc.*, 1999, **146**, 1737; (c) P.M. Natishan, S.Y. Yu, W.E. O'Grady, D.E. Ramaker, *Electrochim. Acta*, 2002, **47**, 3131.

[21] J.M.D. Coey, *Acta Crystall. B.*, 1970, **26**, 1876.

[22] D.C. Koningsberger, J.B.A.D. van Zon, H.F.J. van 't Blik, G.J. Visser, R. Prins, A.N. Mansour, D.E. Sayers, D.R. Short, J.R. Katzer, *J. Phys. Chem. B.*, 1985, **89**, 4075.

[23] M.A. Newton, B. Jyoti, A.J. Dent, S.G. Fiddy, M.Tromp, J. Evans, in preparation.

[24] For example: M.A. Newton, A.J. Dent, J. Evans, *Chem. Soc. Rev.*, 2002, **31**, 83.

[25] J.H.A. Martens, R. Prins, D.C. Koningsberger, *J. Phys. Chem.*, 1988, **92**, 1903.

[26] J.H.A. Martens, R. Prins, D.C. Koningsberger, *J. Phys. Chem.*, 1989, **93**, 3179.

[27] For example: P. Johnston, R.W. Joyner, *J. Chem. Soc. Faraday Trans.*, 1993, **89**, 863.

Chapter 4. The oxidation/reduction kinetics of supported Rh and Rh_2O_3 nanoparticles: An EDE and XANES study

4 The Oxidation/Reduction kinetics of supported Rh and Rh_2O_3 nanoparticles: An EDE and XANES study.

4.1 Introduction

Recent studies concerning the behaviour of supported metal catalysts,[1,2,3,4] and even single crystal surfaces under catalytic conditions involving facile dissociable oxidants such as O_2 and NO, have shown that changes in phase (from metallic to oxidic) of the metal component has a direct influence on the catalytic behaviour of the system. This influence includes determining the selectivity,[5,6] rates of catalytic oxidation, and even the overall performance of the catalyst in 'working' situations. A complete understanding and quantification of these redox processes that occur over supported Rh need to be attained before these systems can be probed further for their catalytic properties.

The oxidation of large metal particles (in the regime of much above 1 μm),[7] single crystals[8] and foils[9] have been measured experimentally for some time. However, a shortage of measurements performed on 'real', highly dispersed supported catalysts exists within the literature. This highlights the difficulty the experimentalist faces in quantifying such processes, the main factor being temporal limitations. An effective example to highlight these limitations concerns the reduction of 2-6 ML Rh_2O_3 films, made from electrochemically depositing aqueous $RhCl_3$ onto roughened Au, utilising Surface Enhanced Raman Spectroscopy (SERS).[10] The report observed an 'immeasurably fast reduction' of Rh_2O_3 above 473 K, ultimately limited by the 1 Hz sampling rate of the SERS experiment.

EDE is well known to afford both kinetic and structural data for reactions occurring on supported metal catalysts in the time frame of a few seconds.[11] This section, as well the study as a whole, aims to improve on this time resolution, to progress into the time regime of milliseconds. The extra information gleaned from such experiments will then be compared to existing studies to emphasize their importance in this field of study.

4.2 Experimental

A typical experimental procedure for EDE/MS data acquisition was carried out as follows. The EDE//MS microreactor experimental apparatus was used as outlined fully in chapter 2.5.7. The 5 wt% catalyst studied in this chapter was prepared using the chlorinated precursor as explained in chapter 2.9. The previously calcined catalyst sample (ca. 20 mg) was loaded into a quartz tube, which was then placed into the microreactor apparatus.

Each catalyst was pre-treated in-situ prior to any EDE/MS experiment. The samples were reduced in situ to 573 K under a flow of 5%H_2/He (20 ml min^{-1}) for approximately 15 minutes. After the required temperature had been attained, EDE/MS measurements were made in synchrony to the switch from the flow of 5%H_2/He to 20 ml min^{-1} 5%O_2/He (or vice versa depending on which redox experiment was being performed).

EDE measurements were performed using an asymmetrically cut (6°) Si[111] monochromator in Laue (transmission) configuration. Detection of the EXAFS was made with the phosphor masked, FReLoN CCD camera, which gave a typical total acquisition time of 50 ms. Air was used as the I_0 for the EDE measurements. Downstream analysis of the gas flow was made with a quadropole mass spectrometer (Pfeiffer).

4.3 Results and Discussion

NB Elements of the data analysis and subsequent interpretation in this chapter have been jointly carried out with Dr. Mark Newton, a PDRA at the time of performing these experiments.

Figure 4.1 shows raw Rh K edge EDE data taken at 473 K (for example) for both a fully reduced and oxidised 5 wt% RhCl sample, with an acquisition time of 50 ms. The characteristic EXAFS signatures the Rh affords in differing oxidation states is clear by simple inspection of the spectra; with metallic Rh (oxidation state = 0, red line) and oxidised Rh (oxidation state = +3, black line). Such differences are detailed in the inset of the figure, which expands upon the XANES region of the spectra. The blue arrow is used to indicate the point where major changes in the XANES pattern occur between the different phases of Rh;

therefore it is this point (23.25 keV) that is used to follow the oxidation/reduction cycles studied in this chapter. Although this is not a quantitative method of charting changes in phase, the 'white line' method can still be viewed as a viable means to chart the major structural changes occurring over the catalyst system.

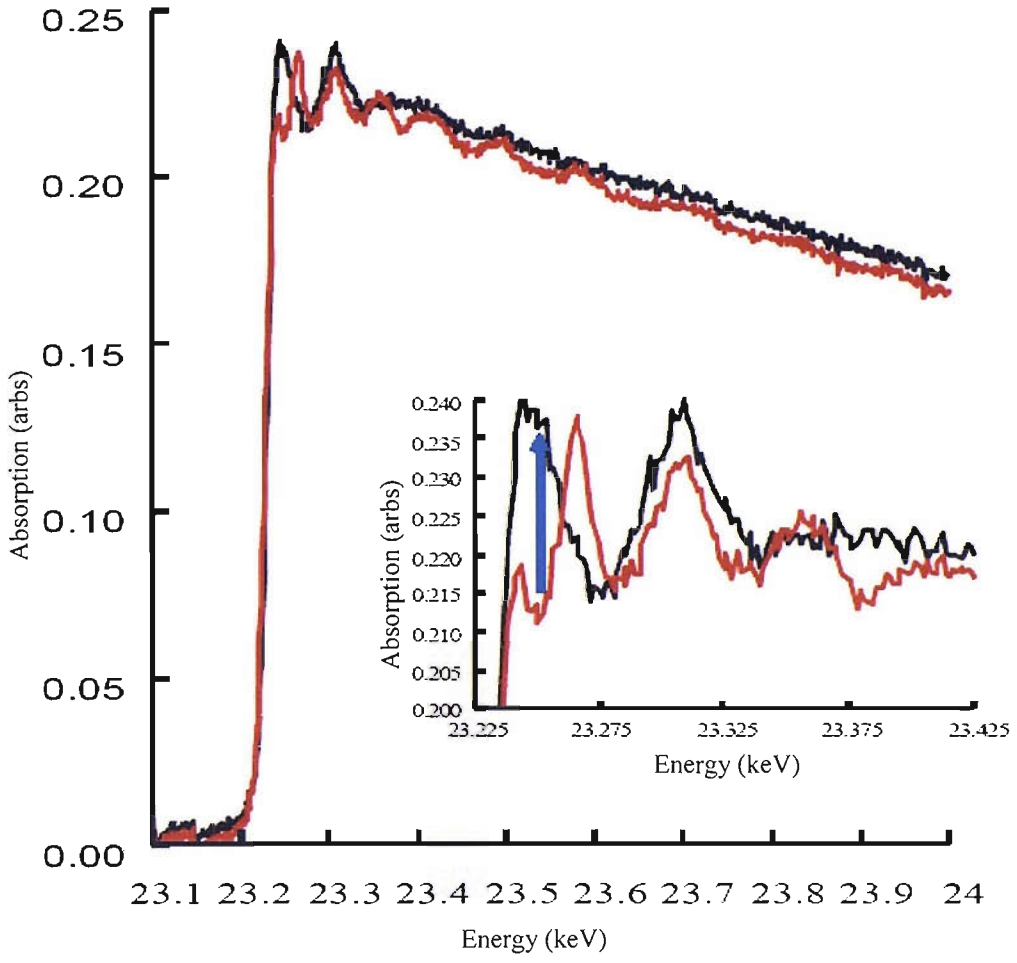

Figure 4.1: Raw EDE adsorption data derived from fully reduced (red line) and oxidised (black line) Rh nanoparticles at 473 K. The blue arrow in the inset highlights the region in XANES that is used to follow the redox cycles (23.23 keV in this case).

To quantify the spectra shown in figure 4.1, figure 4.2 shows the pertinent k^3 weighted Rh K edge EDE data, alongside the corresponding Fourier Transforms. The structural and statistical data obtained from analysis in EXCURVE98 is given in table 4.1.

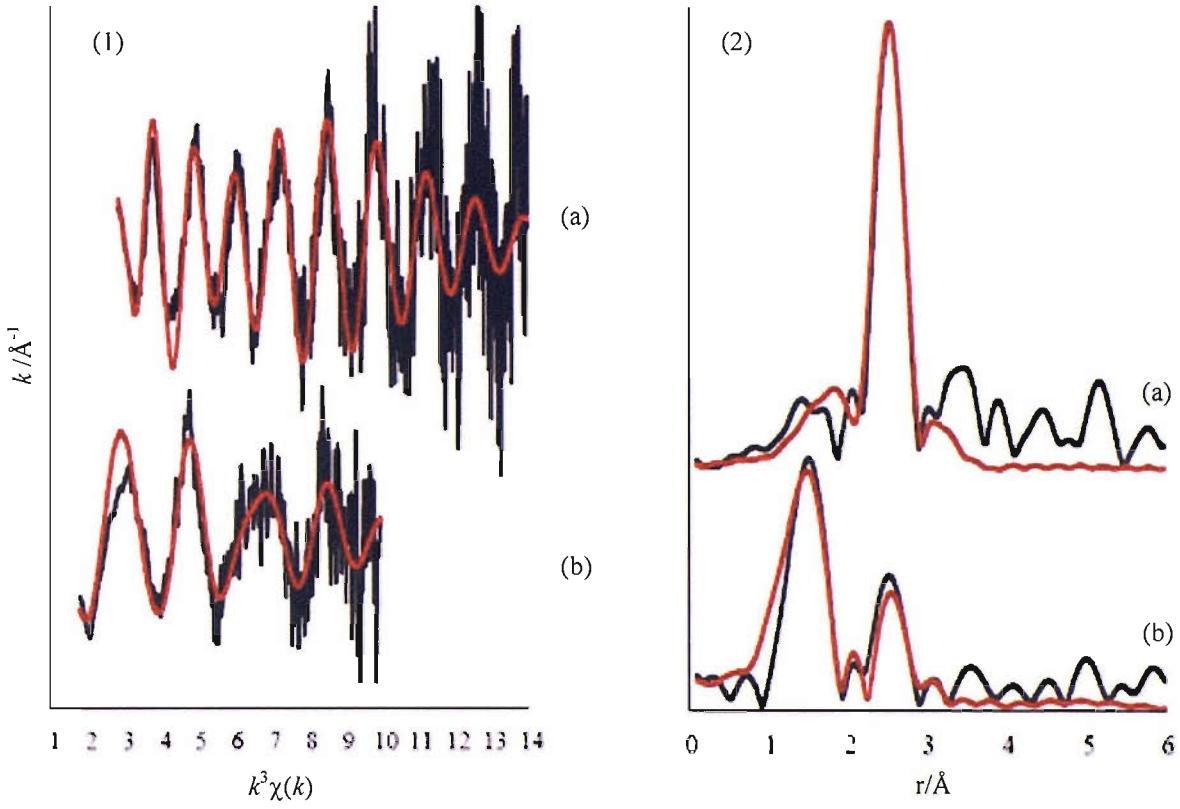

Figure 4.2: (1) k^3 weighted Rh K edge EDE spectra from (a) reduced 5 wt% RhCl and (a) oxidised 5wt% RhCl; (2) (a) and (b) show the corresponding Fourier Transforms. The black line displays the experimental data, the red line the theoretical data.

Spectrum	Scatterer(s)	CN	r/Å	$2\sigma^2/Å^2$	E_F	R (%)
(a) Post H_2 exposure at 473K	Rh	7.1 (± 0.6)	2.65 (± 0.02)	0.014 (± 0.001)	-4.82	67
(b) Oxidised Rh at 473K	Rh	1.4(± 0.2)	2.66 (± 0.02)	0.014 (± 0.001)	-2.52	66
	O	2.7 (± 0.3)	2.05 (± 0.02)	0.008 (± 0.001)	-2.52	66

Table 4.1: Data derived from the analysis of EDE spectra in figure 4.2. Other parameters: (a) k = 3-14 $Å^{-1}$ and (b) k = 3-10 $Å^{-1}$.

The Rh-Rh coordination values observed of ca. 7 and 3 for the reduced and oxidised Rh nanoparticles respectively are an expected result based on previous EXAFS studies on identical systems (also see chapter 3).[2,12,13]

These data also show that they can be favourably compared to previously acquired EXAFS data, taken with the Princeton CCD camera[14] and an asymmetrically cut Si [111] monochromator in a Laue configuration (see chapter 2.5.7) The maximal repetition rate for data acquisition with the Princeton camera was ca. 2 Hz. A comparison of the spectra taken from both the FReLoN and Princeton CCD cameras is overlaid in figure 4.3. The figure highlights that the FReLoN camera permits the high repetition rates (ca. 20 Hz) needed for these experiments without any significant degradation to the data quality of the spectra obtained. With no apparent detriment to the data quality, the planned experiments to improve on the time resolution of existing studies (such as the mentioned SERS experiment)[10] could proceed.

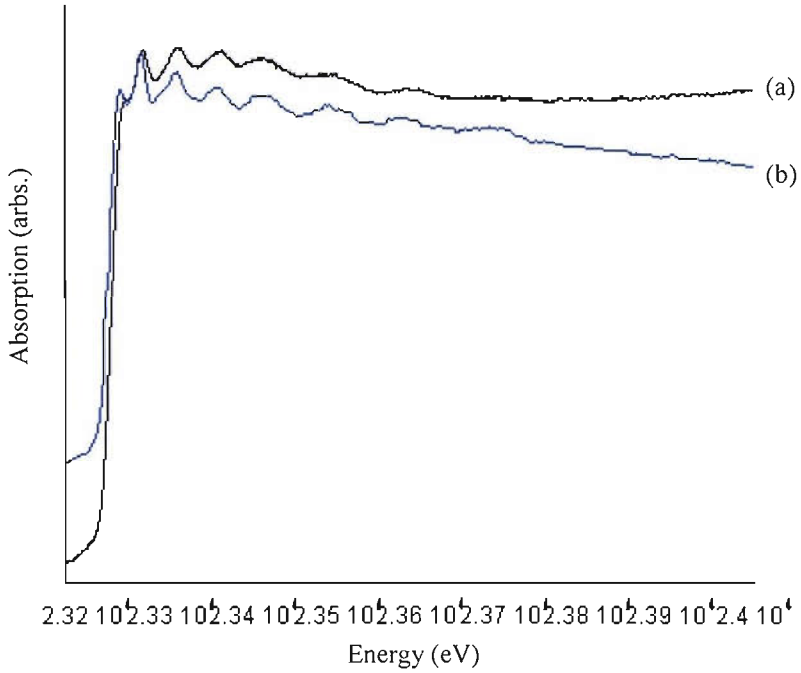

Figure 4.3: Raw Rh EDE adsorption data derived from a fully reduced 5wt%RhCl system at room temperature obtained by; (a) Princeton CCD (taken at 700 ms total readout time) and (b) FReLoN CCD camera (taken at 50 ms total readout time).

Figures 4.4 and 4.5 chart the temporal variation in XANES derived from the in situ experiments, at temperatures ranging from 373-573 K. This was achieved by using the 'white line' method to follow the changes in the XANES region as shown in figure 4.1, and plotted as a function of time. Figure 4.4 shows the data obtained for the reduction of fully oxidised Rh nanoparticles, essentially in the form of Rh_2O_3. The reversal of this process is shown in figure 4.5, which charts the oxidation of metallic Rh. In the case of the reduction reaction in figure 4.4, zero seconds refers to the time when the gas switch is made. For the oxidation in figure 4.5, zero seconds refers to the time when a measurable reaction could be recorded.

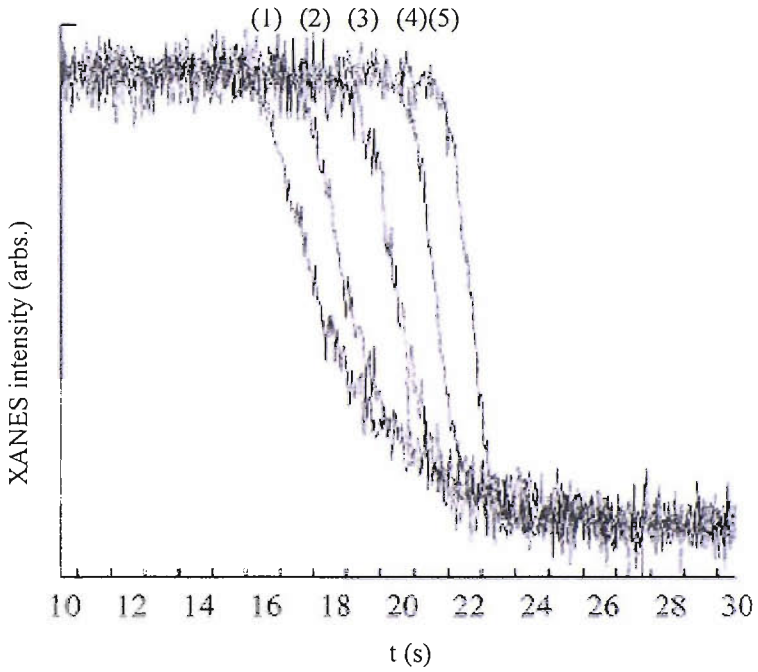

Figure 4.4: Changes in Rh K edge XANES during the reduction of 5wt%RhCl at; (1) 373 K; (2) 423 K; (3) 473 K; (4) 523 K and (5) 573 K. The flow of 5% H_2/He was introduced at t = 0 seconds (from a flow of He).

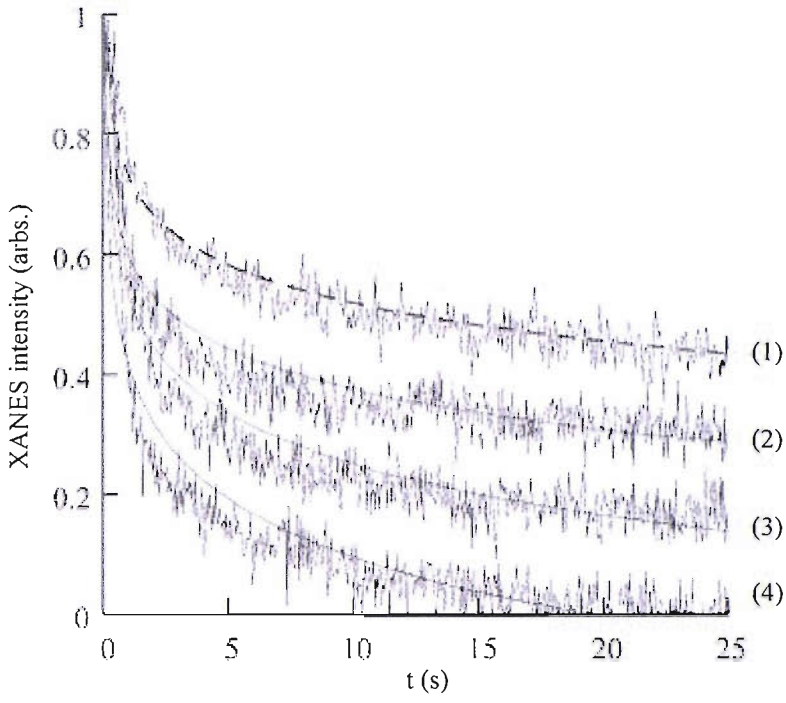

Figure 4.5: Changes in Rh K edge XANES during the oxidation of 5wt%RhCl at; (1) 298 K; (2) 373 K; (3) 458 K and (4) 573 K. The changes in the spectra have been inverted to show the differences more clearly.

These results show that the oxidation and reduction processes occurring over nanoparticulate Rh are significantly different in their character. An initial 'induction' period is observed when an oxidised Rh sample is exposed to the flow of 5%H_2/He. This length of this period appears is be closely correlated to the temperature employed; with an increased period being indexed at increasing temperatures. The following reduction process occurs in a single kinetically limiting step, which at 573 K is complete within 1 second.

Conversely, the oxidation process occurs in two distinct stages; a rapid first step which is complete in under 2 seconds and is followed by a much slower step in which the complete oxidation of Rh occurs. This effect is increasingly evident at lower temperatures. Chapter 3 reported upon the nature of the 'fresh' 5wt% RhCl system (i.e. sample had been calcined and reduced, but left exposed to air). The study found that the most likely morphology of these systems to be a metallic core surrounded by a layer of oxide, which forms rapidly and protects the remainder of the particle from further (facile) oxidation. The following analysis acknowledges the findings from chapter 3. Figure 4.6 depicts a linear correlation between the

measured O_2 uptake and the changes observed in the XANES spectra of these systems; the results indicate that at 373 K a net stoichiometry of RhO is observed by the end of the experiment. By 473 K this has changed to $RhO_{1.5}$, evidence that essentially nanosized Rh_2O_3 has been formed on the surface. As indicated in figure 4.6, the stoichiometry of the oxidised system is higher than would be expected for the formation of Rh_2O_3; it reaches a maximal value of ca. $RhO_{1.85}$ at 573 K. The data collated at these higher temperatures present no evidence of oxidised Rh (i.e. with an oxidation sate of +3) being formed. It is therefore most likely that this 'excess stoichiometry' occurs due to the oxidation of carbon containing residues present on the surface of the catalyst. These residues could conceivably be present even after the in situ reduction prior to any experiment, and in significant quantities as to contribute to the overall oxygen uptake above 473 K. Future work plans to investigate whether any CO or CO_2 is present in the gas streams.

In summary, the rates of the redox processes that occur over the Rh systems under investigation are extremely temperature dependent, when observed within the time frame of these experiments.

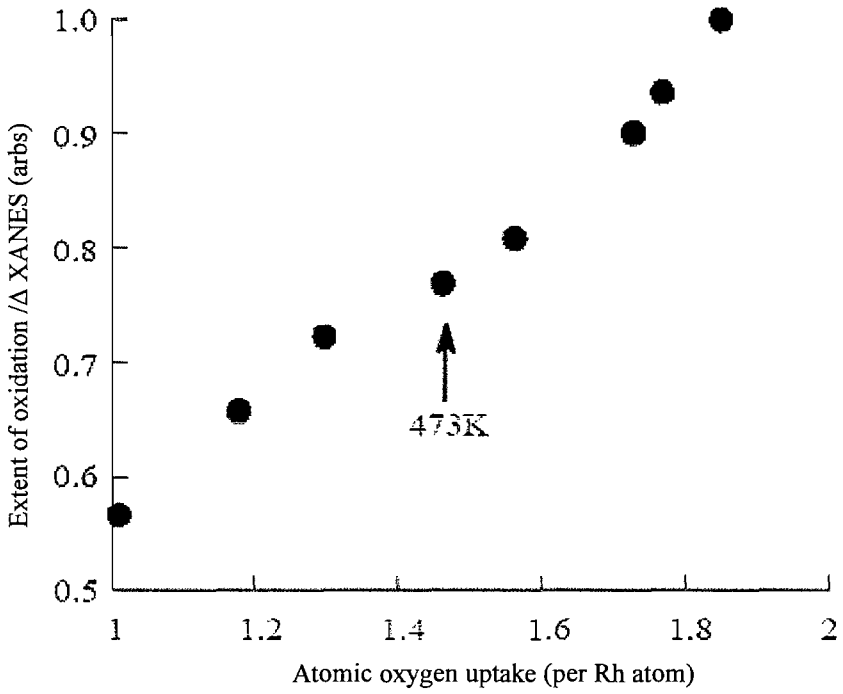

Figure 4.6: The extent of oxidation as a function of atomic oxygen uptake over a 5wt% RhCl system. Initial oxidation (ca. 60 s) leads to a stoichiometry of RhO, at 473 K this has reached a figure expected for Rh_2O_3.

Figure 4.7 shows temperature dependent Arrhenius plots derived from the data in figures 4.4 and 4.5, from which estimates of the kinetic parameters of the redox processes can be made. The Rh reduction process is seen to follow a pseudo first order rate expression for all of the temperatures investigated. The oxidation process was analysed using two methods; the first involved the evaluation of the initial rate within the first second of an observable reaction; the second endeared to fit the entire oxidation using logarithmic rate law.[8,9] A summary of the results obtained from this study and from the literature (the reduction of Rh oxide films[10] and the oxidation of Rh surfaces[8]) are given in table 4.2.

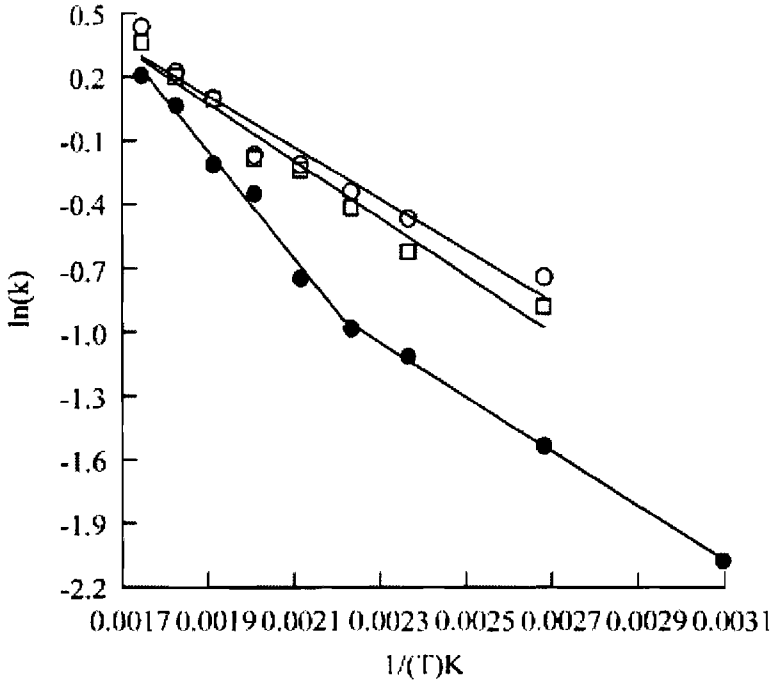

Figure 4.7: Arrhenius plots for the reduction (solid circles) and oxidation (open circles) of 5wt% RhCl. The results from logarithmic fitting are shown as open squares.

Process	E_{act}/kJmol^{-1}	υ/s^{-1}
(a) Reduction (<450K)	11 (± 2)	7
(a) Reduction (>450K)	21 (± 4)	100
(a) Reduction (average of all temperatures)	14 (± 2)	20
(a) Oxidation (initial rate)	9 (± 2)	10
(a) Oxidation (logarithmic)	12 (± 2)	40
(b) Rh(110)/Rh foil (from reference 8)	4 to 9 (± 2)	
(b) Reduction of oxide films (from reference 10)	13 (± 4)	30

Table 4.2: Kinetic data derived from (a) this study and (b) various sources (as indicated) for the reduction and oxidation of Rh.

Inspection of the reduction process indicates that a change in the kinetics occurs at temperatures above 450 K. It is above this temperature that E_{act} is seen to almost double; from ca. 10.6 to 21 kJ mol^{-1}. However this effect is compensated by an increase in υ by an order of magnitude. The value for E_{act} at temperatures below 450 K is consistent with values obtained from previous SERS experiments on oxide films,[10] which is 12.5 (±4) kJ mol^{-1}. The average value of E_{act} from this experiment (14.1 kJ mol^{-1}) correlates well with this figure, derived by fitting a single line across the data range. Such correlations should however be viewed with caution, as the SERS experiment used Rh oxide films, rather than the highly dispersed particulate Rh systems being probed by this study.

Figure 4.7 shows the oxidation process can be fitted using a logarithmic rate law, although this expression is less applicable at higher temperatures. This trend is consistent with existing models for the oxidation of a Rh foil in the temperature regime of 873 K to 973 K,[9] and also for Rh[100] in the regime of 400 K<T<600 K.[8] The activation energy for the oxidation process over the nanoparticulate Rh systems in this study lies in the range of $9.2<E_{act}<11.8$ kJ mol^{-1}.

Both the reduction by H_2 and initial oxidation by O_2 over nanoparticulate Rh can therefore be viewed as facile processes. This in turn suggests that the structure of the supported particles may be highly fluxional in feedstocks that fluctuate between oxidising and reducing conditions. The kinetic determinations made below 450 K correlate well with the data from the SERS experiment currently being compared. However, this study has a distinct advantage of increased time resolution; the more detailed data sets allow for determinations to be made

more accurately. Another clear advantage of this rapid sampling rate becomes apparent at temperatures above 450 K, where the processes were too fast to measure by SERS. Moreover, it is above this temperature regime that evidence for a change in the kinetics in the reduction process is found, further highlighting the need for such experiments to be performed.

Both the SERS and this experiment report an 'induction' time, which suggests a nucleation-growth mechanism is most likely occurring for these processes. However, the SERS data reports the induction time for reduction decreases with increasing temperature, whereas this study reports the opposite behaviour. This proposes that in the case of the oxide supported catalyst, the probability of nucleation decreases with increasing temperature.

The oxidation of the supported Rh nanoparticles is a self poisoning process, a result also observed for extended Rh surfaces.[8] It has a logarithmic dependence upon time; the rapid formation of an oxide layer decreases the amount of O_2 dissociation. This means that any subsequent oxidation becomes rate limited by diffusion of atomic oxygen into, or Rh atoms out of, the remaining metallic core. The activation energies for this process over extended Rh surfaces and the supported catalysts studied here are very similar considering they each represent the opposite extremes of atomic dispersion.[8]

4.4 Summary

In summary this initial investigation into the structural dynamics of supported Rh nanoparticles has shown that the EDE experiment, which can be made to operate on a time scale of tens of milliseconds, is an effective in situ probe. The ability to probe the structural-reactivity behaviour of these systems (in this case the redox characteristics of the 5wt% RhCl system) within these time scales will form a basis for the majority of the experiments in this study, under realistic conditions and catalytic environments.

4.5 References

[1] Y. Nishihata, H. Tanaka, J. Mizuki, T. Akao, M. Uenishi, M. Kimura, T. Okamoto and N. Hamada, *Nature*, 2002, **418**, 164.

[2] M.A. Newton, B. Jyoti, A.J. Dent, S. Diaz-Moreno, S.G. Fiddy, J. Evans, *Chem. Eur. J.* 2006, **12**, 1975.

[3] T. Campbell, A.J. Dent, S. Diaz-Moreno, J. Evans, S.G. Fiddy, M.A. Newton, S. Turin, *Chem. Commun.*, 2002, 304.

[4] M.A. Newton, A.J. Dent, S. Diaz-Moreno, S.G. Fiddy, J. Evans, *Angew. Chem., Int. Ed.*, 2002, **41**, 2587.

[5] B.L.M. Hendriksen, S.C. Bobaru, J.M.W. Frenken, *Surf. Sci.*, 2004, **552**, 229.

[6] B.L.M. Hendriksen, J.M.W. Frenken, *Phys. Rev. Lett.*, 2002, **89**, 6101.

[7] For instance, R.E. Carter, *J. Chem. Phys.*, 1961, **34**, 2010.

[8] A.N. Salanov, V.I. Savchenko, *Kinet. Catal.*, 1994, **35**, 722.

[9] L.A. Carol, G.S. Mann, *Oxid. Met.*, 1990, **34**, 1.

[10] C.T. Williams, E.K.-Y. Chen, C.G. Takoudis, M.J. Weaver, *J. Phys. Chem. B*, 1998, **102**, 4785.

[11] For instance, A. Suzuki, Y. Inada, A. Yamaguchi, T. Chihara, M. Yuasa, M. Nomura, Y. Iwasawa, *Angew. Chem., Int. Ed.*, 2003, **42**, 4795.

[12] M.A. Newton, A. J. Dent, S. Diaz-Moreno, S. G. Fiddy, B. Jyoti, J. Evans, *Chem. Phys. Chem.*, 2004, **5**, 1056.

[13] B. Jyoti, MPhil Thesis, University of Southampton, 2002.

[14] A. Koch, M. Hagelstein, A. San Miguel, A. Fontaine, T. Ressler, *Proc. SPIE 85*, 1996, 2416.

Chapter 5. The structure-function response of Rh/Al_2O_3 systems to CO

5.1 Introduction

Processes such as the formation, rearrangement and possible disintegration of catalyst structure can occur over such short timescales that many pertinent analytical techniques simply do not have the capacity to afford truly useful, time resolved data. Therefore any experiment probing for such information would require similar time resolution, or at the very least be able to track the major stages of such processes as a function of time.

EXAFS has thus far been shown to be an invaluable tool to follow such processes on an atomic basis.[1,2,3] The structural determination of the molecules themselves that absorb onto the supported metal sites is another important factor in understanding the complex entirety of a catalyst system. In situ IR spectroscopy of IR active species adsorbed on catalyst surfaces has long been an effective method to obtain such information, and is widely used to characterise supported metal particles.[1,4,5,6,7] However, studies to date have been limited by the difficulty in separating the active from the inactive species in a catalytic reaction.[8,9] Therefore, the combination of EXAFS, DRIFTS and downstream analysis of the reactive feedstock via mass spectrometry on a catalyst in a synchronous, time resolved manner should afford an array of complementary data on the supported Rh systems used in this study.

CO was chosen as an archetypal adsorbing molecule for this chapter primarily due to the extensive catalytic work that has been performed on both highly and low dispersed metal systems using this gas.[10,11,12] This is especially the case for related infrared studies, where $CO_{(g)}$ is commonly used to characterise the catalyst system. Other techniques employed to investigate the surface phenomena in these studies include STM [13] and EXAFS.[2, 14, 15] However, such studies generally fail to delineate the complex 'overall' properties of the system, as the results and conclusions are often based on data derived from a single, primary technique.

This chapter will therefore utilise the EDE/DRIFTS/MS battery of techniques to follow the adsorption of CO over nanoparticulate Rh at varying temperatures and metal loading. The rapid acquisition of time resolved data will provide detailed, fundamental behavioural data regarding the structural-reactivity of the systems. Other inherent factors such as the elucidation of reaction mechanisms will be scrutinised under realistic working conditions.

5.2 Experimental

A full description of the EDE/DRIFTS/MS experimental apparatus used is given in chapter 2.5.8.

Briefly, in a typical experiment the catalyst (ca. 45 mg) was pre-treated by heating under a flow of 5% H_2/He to 573 K. The system was then subjected to a flow of 5% O_2/He for ca. 5 minutes before switching back to the flow of 5% H_2/He and cooled to room temperature. After purging under a flow of He, a flow of 5% CO/He at 25 $mlmin^{-1}$ was introduced synchronously with the start of the EDE/DRIFTS/MS experiment. EXAFS detection was made via the FReLoN CCD camera with a total acquisition time of ca. 60 ms. The DRIFTS and mass spectrometric data obtained matched the repetition rate of the EDE.

5.3 The structure-function response and adsorption properties of rhodium systems to CO: a variable temperature study

NB Due to extensive software problems that could not be resolved after the experiments had been performed, the synchronously obtained MS data was unavailable for analysis and is therefore excluded from any further discussion in this chapter.

5.3.1 Results: 2.5 wt% RhCl System

Figure 5.1 shows k^3 weighted EDE spectra for 2.5wt% RhCl before and after exposure to 5%CO/He at room temperature, along with the corresponding Fourier transforms. The structural and statistical information derived from these spectra are given in table 5.1. For ease of spectral analysis and visual clarity, figure 5.1(b) is an average of 10 spectra, taken over the final second of the experiment (i.e. t = 29 s).

The static EDE spectra reveal significant structural changes to have occurred to the catalyst upon exposure to a flow of 5%CO/He at room temperature. Part (a) reveals the system to have an average Rh-Rh coordination number of ca. 3 under $H_{2\,(g)}$ prior to the start of the experiment; a value consistent with previous EXAFS studies on this system.[16] After 30

seconds of being exposed to the flow of gaseous CO part (b) shows the EXAFS to no longer evidence any significant Rh-Rh bonding.

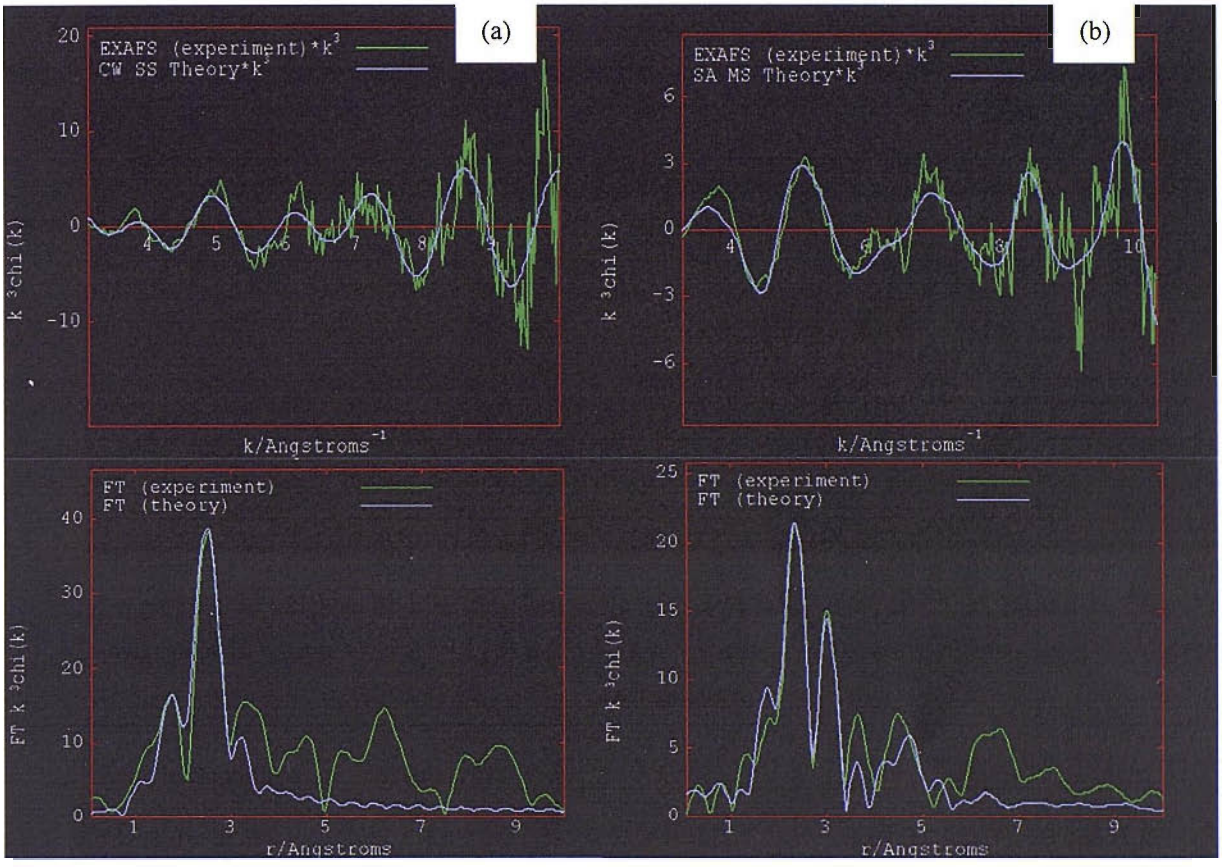

Figure 5.1: k^3 weighted Rh EDE data derived from 2.5 wt% RhCl under; (a) 5% H_2/He and (b) 5% CO/He (average of 10 spectra taken at t = 29 s) at 298 K. The corresponding Fourier transforms are given underneath each spectrum.

Sample/Conditions	Scatterer (s)	CN	r/Å	$2\sigma^2/Å^2$
(a) 2.5 wt% RhCl in 5% H_2/He at 298 K	Rh	3.3 (± 0.5)	2.63 (±0.02)	0.011 (±0.001)
	O	1.2 (± 0.1)	2.06 (±0.02)	0.012 (±0.001)
(b) 2.5 wt% RhCl in 5% CO/He at 298 K	C1 (carbonyl)	1	1.99 (±0.01)	0.010 (±0.001)
	C2 (carbonyl)	1	1.99 (±0.01)	0.010 (±0.001)
	O1 (carbonyl)	1	2.98 (±0.02)	0.023 (±0.002)
	O2 (carbonyl)	1	2.98 (±0.02)	0.023 (±0.002)

Table 5.1: Structural and statistical data derived from the analysis of spectra given in figure 5.1. Other parameters; (a) Ef = -1.34 eV, R = 60%, k = 3-10 $Å^{-1}$ and (b) Ef = -8.37 eV, R = 52%, k = 3-10 $Å^{-1}$.

Various models were used to try and delineate the structure of the catalyst after being exposed to 5% CO/He, derived from previous studies of CO exposure on similar Rh systems.[17,18] This included three different types of Rh sites on the alumina support; with CO bound on terminal (atop) sites, bridging (2 fold) and a geminal dicarbonyl entity (see figure 5.2).

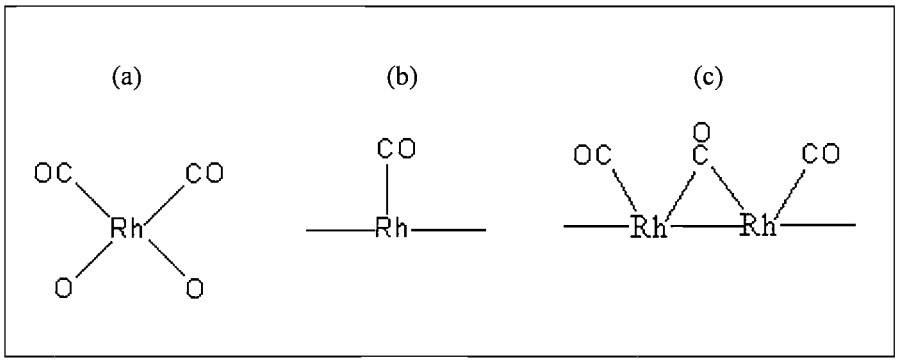

Figure 5.2: Structures of possible CO species evolved after exposure of 5% CO/He to 2.5 wt% RhCl; (a) geminal dicarbonyl species $Rh(CO)_2$, (b) linear CO (η-CO) and (c) bridge bound CO (μ-CO). Structures are given for illustrative purposes only (see main text).

The linear and bridge bonded CO species are known to be associated with extended, metallic Rh surfaces, which would be the Rh nanoparticles that exist on the catalyst in this case.[18] The $Rh(CO)_2$ unit is thought to exist as isolated units bound directly to the alumina support as a four[3,19] or even a five coordinate species.[2,20] These structures were all taken into consideration on analysing the EDE data. As expected by previous studies by our group[21,22] the 'best fit', or lowest R factor obtained in EXAFS analysis as shown in figure 4.1(b), was achieved by using a model based on the geminal dicarbonyl unit, $[Rh^1(CO)_2]$ (in a four coordinate geometry). Figure 5.3 displays the structure of this unit in three dimensional space, as modelled within the EXCURVE program.

Refinement constraints were employed for the analysis; refinement of the two carbonyl ligands was done simultaneously by fixing their Debye-Waller and bondlengths together. A full explanation for the techniques used in EXAFS analysis can be found in chapter 2, section 2.6.3. Although there is an apparent dominance of the EXAFS signal by this geminal species, the presence of any other carbonyl containing species formed upon the Rh surface cannot be discounted.

The EDE data presented here would therefore indicate that significant disruption of the surface Rh nanoparticles has occurred within 30 seconds at room temperature.

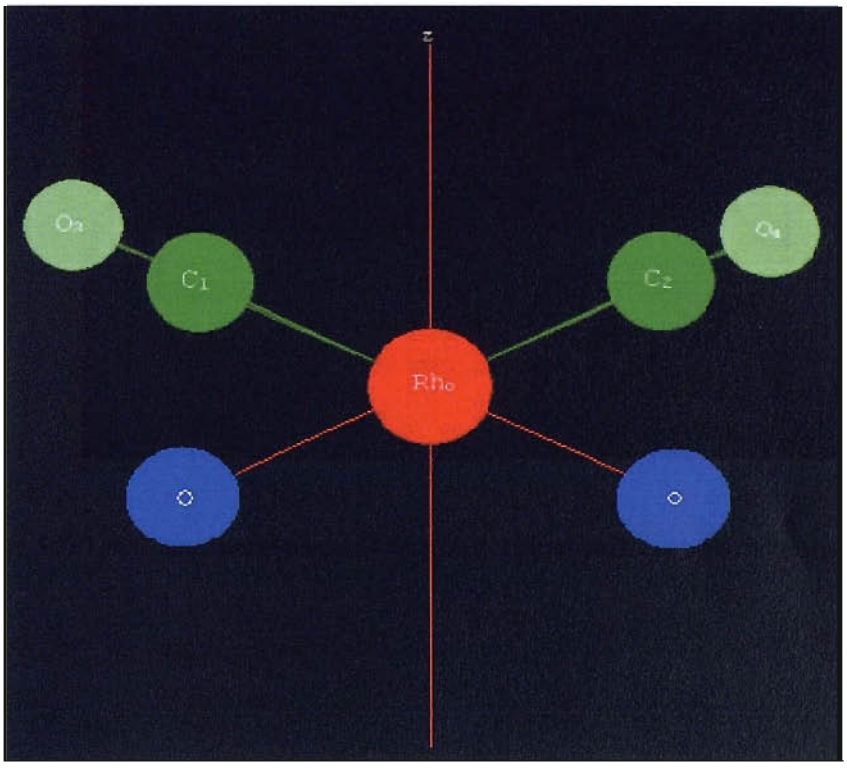

Figure 5.3: Three dimensional model of the geminal dicarbonyl unit used for analysis in EXCURVE.

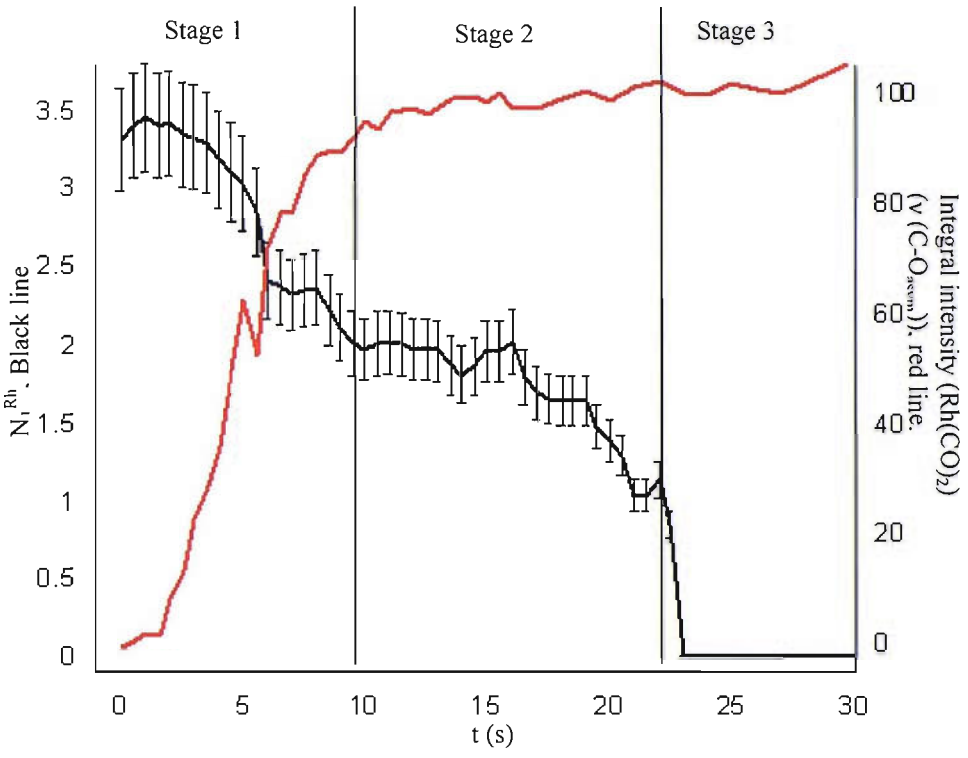

Figure 5.4: Rh-Rh coordination number (black line) and integral of the asymmetric stretch of the CO ligand (red line) as a function of time during time resolved 5% CO/He exposure to 2.5 wt% RhCl at RT. Error bars given for the coordination data are derived from the corresponding standard deviations.

Figure 5.4 charts the N_1^{Rh} (Rh) data alongside a representative integral of a species formed during the time resolved exposure of 2.5 wt% RhCl to 5%CO/He at room temperature, in this case the asymmetric stretch of a CO ligand (see below). The quality of the EDE spectra, taken every ca. 60 ms, was sufficient to permit the structural analysis given in figure 5.4 and throughout this section.

First inspection of the structural profile of the catalyst during the experiment clearly shows that by ca. 23 seconds an apparent 'complete' disruption of the Rh particles has occurred. By this time the N_1^{Rh} (Rh) indexes a value of 0 and the EXAFS spectra obtained closely resembles the spectrum shown in figure 5.1(b). There appears to be three distinct stages to the overall process occurring during the experiment when considering the EDE data alone; the N_1^{Rh} (Rh) number initially falls from ca. 3.5 to ca. 2 within the first 10 seconds (stage 1), which is followed by a slower degradation in Rh-Rh bonding (stage 2) until ca. 22

seconds at which point there is no significant Rh-Rh bonding and the $[Rh^{I}(CO)_2]$ unit structure begins to dominate the EXAFS signal (stage 3).

The evolution of this discrete species, represented by the absorbance DRIFTS integral of the asymmetric stretch of the gem-dicarbonyl species in figure 5.4, can also be correlated to the disruption of the Rh nanoparticles. Taking place over two distinct stages (not shown in figure 5.4), the integral signal can be seen to rise proportionally to the decrease in coordination number over the three stages. The reasons for displaying this DRIFTS signal will be discussed in section 5.4.

Figure 5.5 shows the Rh-Rh coordination data for similar time resolved CO experiments, performed on 2.5 wt% RhCl systems at various temperatures to 423 K. Interestingly, 'stage 1' is essentially invariant for all of the temperatures investigated; the N_1^{Rh} is seen to decrease from ca. 4 to 2 within the first 8 seconds independent of the temperature employed during $CO_{(g)}$ exposure. However, the duration of 'stage 2' is dependent on the temperature; which indexes a shorter timescale as the temperature is increased. By 423 K, the Rh-Rh bonding falls to negligible values by ca. 10 seconds.

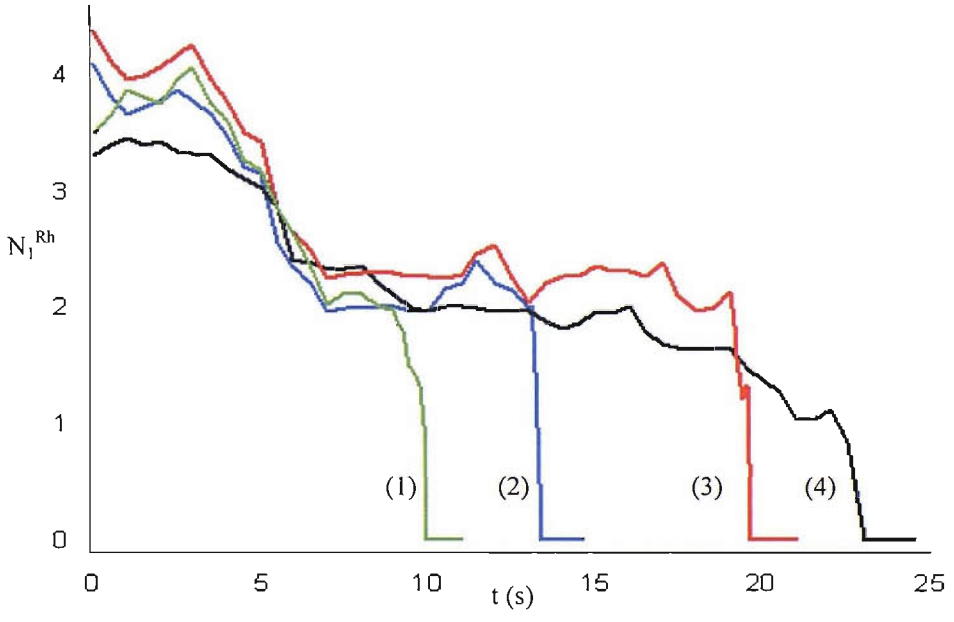

Figure 5.5: Rh-Rh coordination number as a function of time during time resolved 5% CO/He exposure to 2.5 wt% RhCl at; (1) 423 K; (2) 373 K; (3) 323 K and (4) 298 K. For accuracy, at least one EXAFS spectrum every 0.5s was analysed for each time resolved experiment.

Figure 5.6 shows that although clear correlations exist between temperature and the extensive disruption of surface particles, the DRIFTS data suggests that the evolution of carbonyl containing surface species is, within error, independent of the temperature used. The carbonyl containing entities are seen to evolve and stabilise by ca. 10 seconds, which is approximately the time taken for 'stage 1' to elapse. The figure also highlights the relative decrease in the amount of the geminal species present on the Rh surface at increased temperatures.

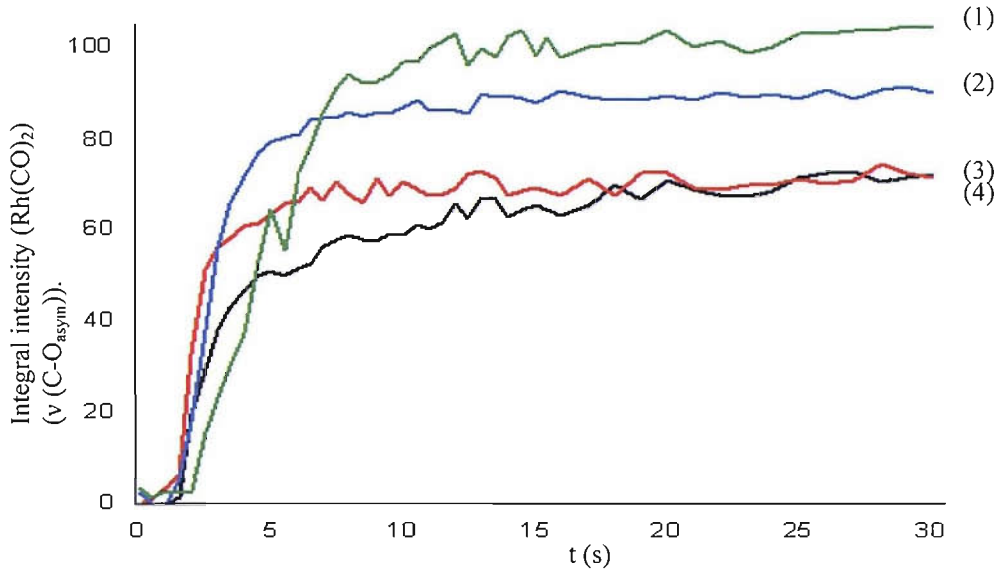

Figure 5.6: Representative figure showing the evolution of the asymmetric stretch of the carbonyl group in $Rh^{I}(CO)_2$ at; (1) 298 K; (2) 323 K; (3) 373 K and (4) 423 K for 2.5wt% RhCl.

Closer inspection of the absorbance DRIFTS data from the time resolved, variable temperature experiments in figure 5.7 reveals the full range of IR active species present on the Rh surface after ca. 30 seconds of 5% CO/He exposure. The geminal dicarbonyl species is characterised by two peaks; a symmetric and an asymmetric C-O stretch ($\nu \sim 2100$ cm^{-1} and 2030 cm^{-1} respectively). The bridged CO species (CO_B) gives a broad peak ($\nu \sim$ 1855-1865 cm^{-1}), and the linear CO (CO_L) species can be resolved between the geminal peaks ($\nu \sim$ 2060-2070 cm^{-1}).

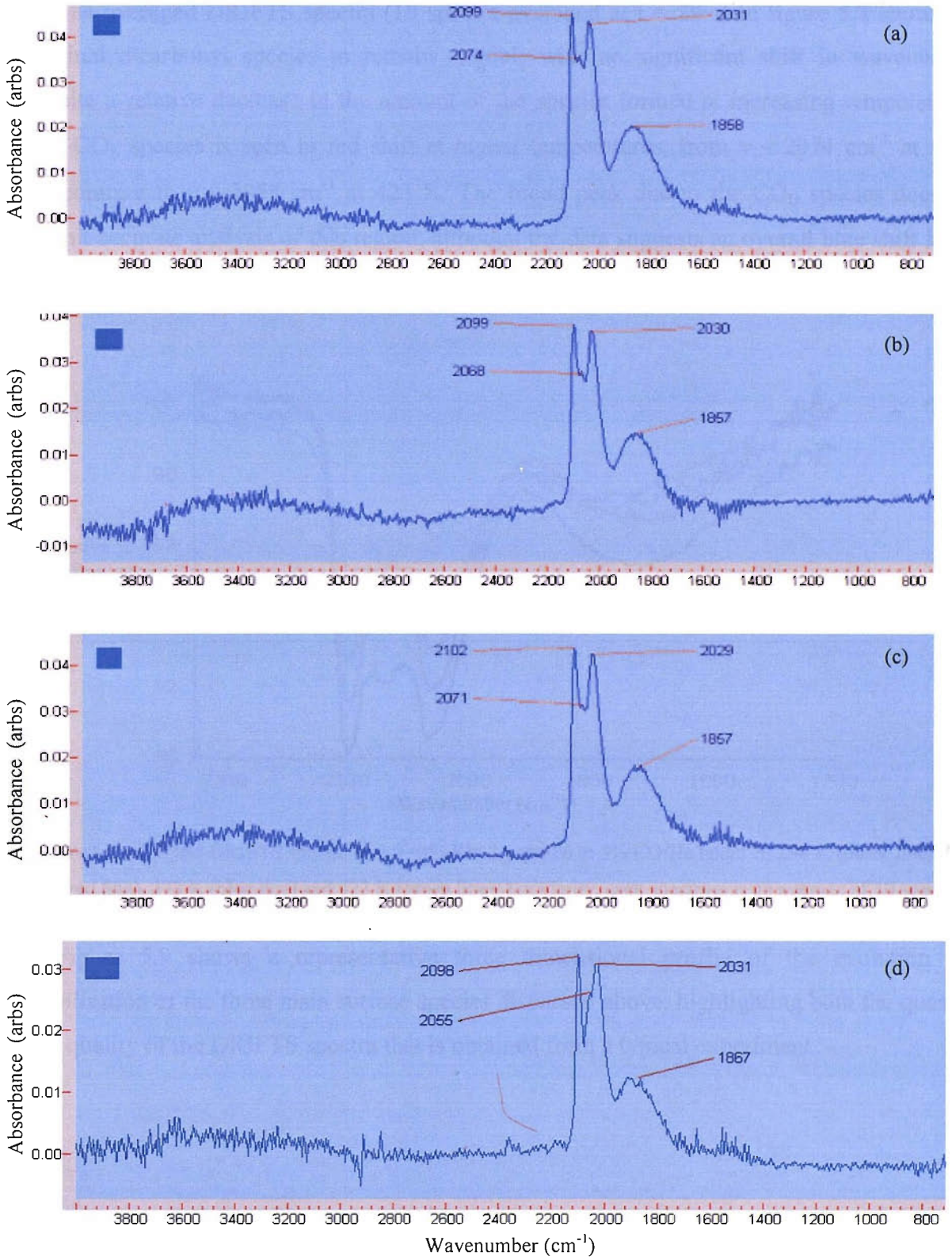

Figure 5.7: DRIFTS spectra taken from 2.5wt% RhCl after 30s exposure to5%CO/He at; (a) RT, (b) 323 K, (c) 373 K and (d) 423 K. The acquisition time for each spectrum was 64ms.

The averaged DRIFTS spectra (10 spectra averaged at t = 29 s) in figure 5.8 shows the geminal dicarbonyl species to remain 'static'; with no significant shift in wavenumber despite a relative decrease in the amount of the species formed at increasing temperatures. The CO_L species is seen to red shift at higher temperatures, from $\nu \sim 2074$ cm^{-1} at room temperature to $\nu \sim 2058$ cm^{-1} at 423 K. The broad peak due to the CO_B species does not permit accurate analysis of this region, although the data suggests an overall blue shift in the peak position, from $\nu \sim 1857$ cm^{-1} at room temperature to $\nu \sim 1865$ cm^{-1} at 423 K.

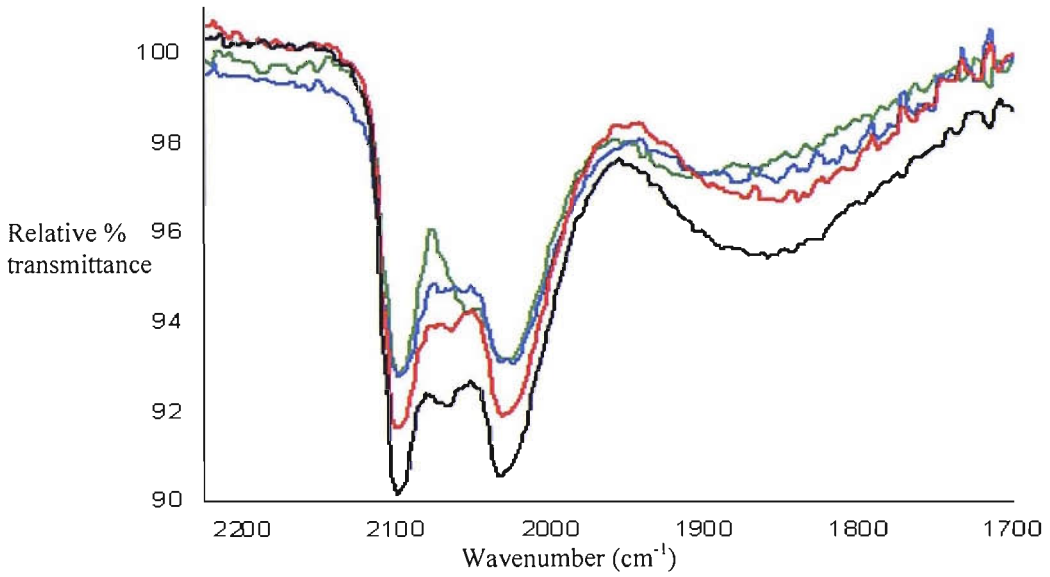

Figure 5.8: Overlaid DRIFTS spectra of 2.5 wt% RhCl exposed to 5% CO/He taken at; 298 K (black line), 323 K (red line), 373 K (blue line) and 423 K (green line). For clarity, each spectrum is an average of 10 spectra.

Figure 5.9 shows a representative three dimensional profile of the evolution and stabilisation of the three main surface species discussed above, highlighting both the quantity and quality of the DRIFTS spectra that is obtained from a typical experiment.

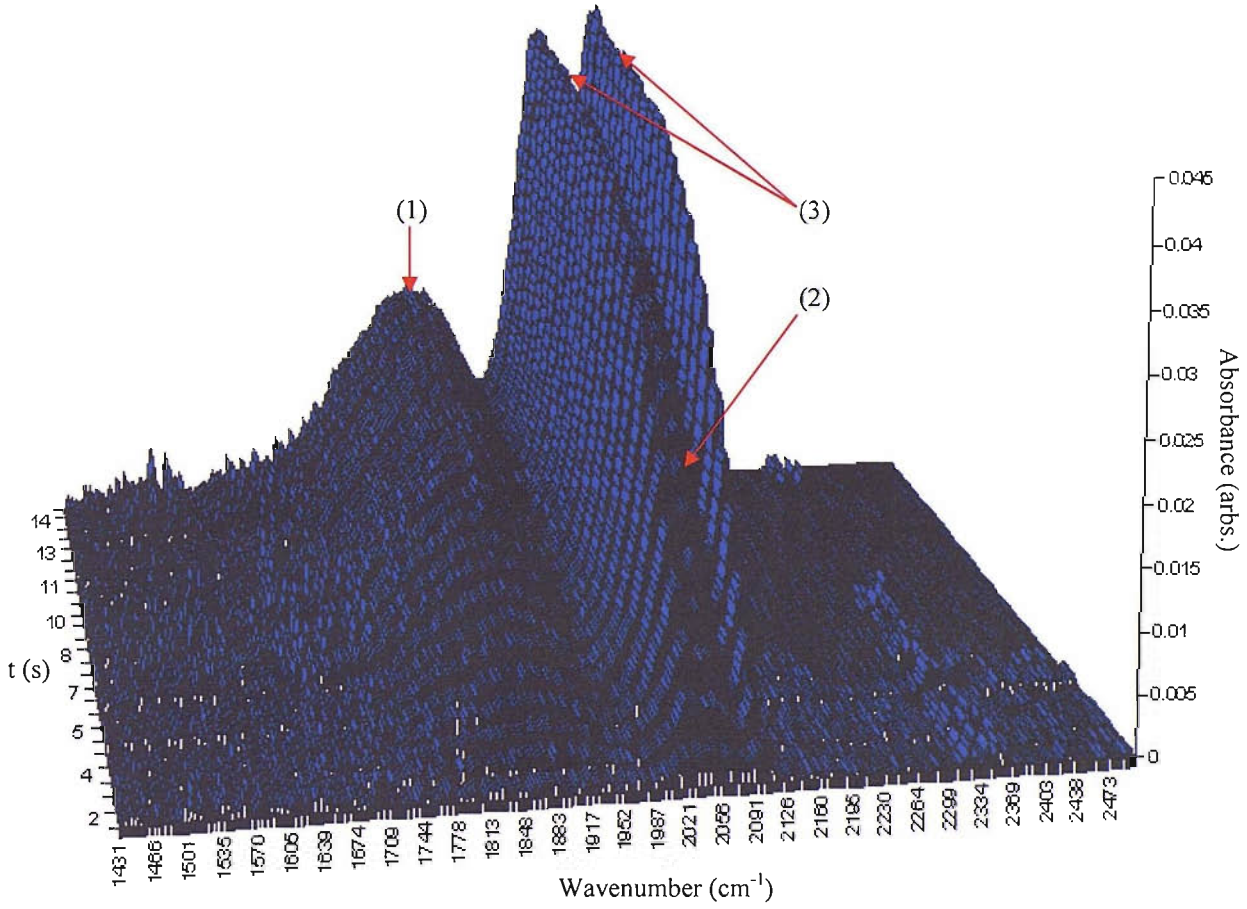

Figure 5.9: DRIFTS spectra (2485-1430cm^{-1}; 4cm^{-1} resolution) as a function of time after room temperature exposure to 5% CO/He showing the; (1) CO_B (μ-CO) ; (2) CO_L (η-CO) and (3) [$Rh^I(CO)_2$] peaks for 2.5 wt% RhCl. For clarity one spectrum every 2s is shown.

5.3.2 Results: 5 wt% RhCl System

Figure 5.10 shows k^3 weighted EDE spectra for 5wt% RhCl before and after exposure to CO at room temperature, along with the corresponding Fourier transforms. The structural and statistical information obtained from these spectra are given in table 5.2. The figure shows that, within the timescales of this experiment, EXAFS does not detect any significant structural changes occurring over the Rh particles upon exposure to 5% CO/He. The absolute N_1^{Rh} value decreases from ca. 7 under H_2 to ca. 6.5 after 36 seconds of exposure, which is not significant at the 10% error level associated with this data. The Rh-Rh bondlength supports

this observation, as it remains unchanged throughout exposure at ca. 2.68 Å. These structural parameters remain constant until the end of the experiment at 60 seconds.

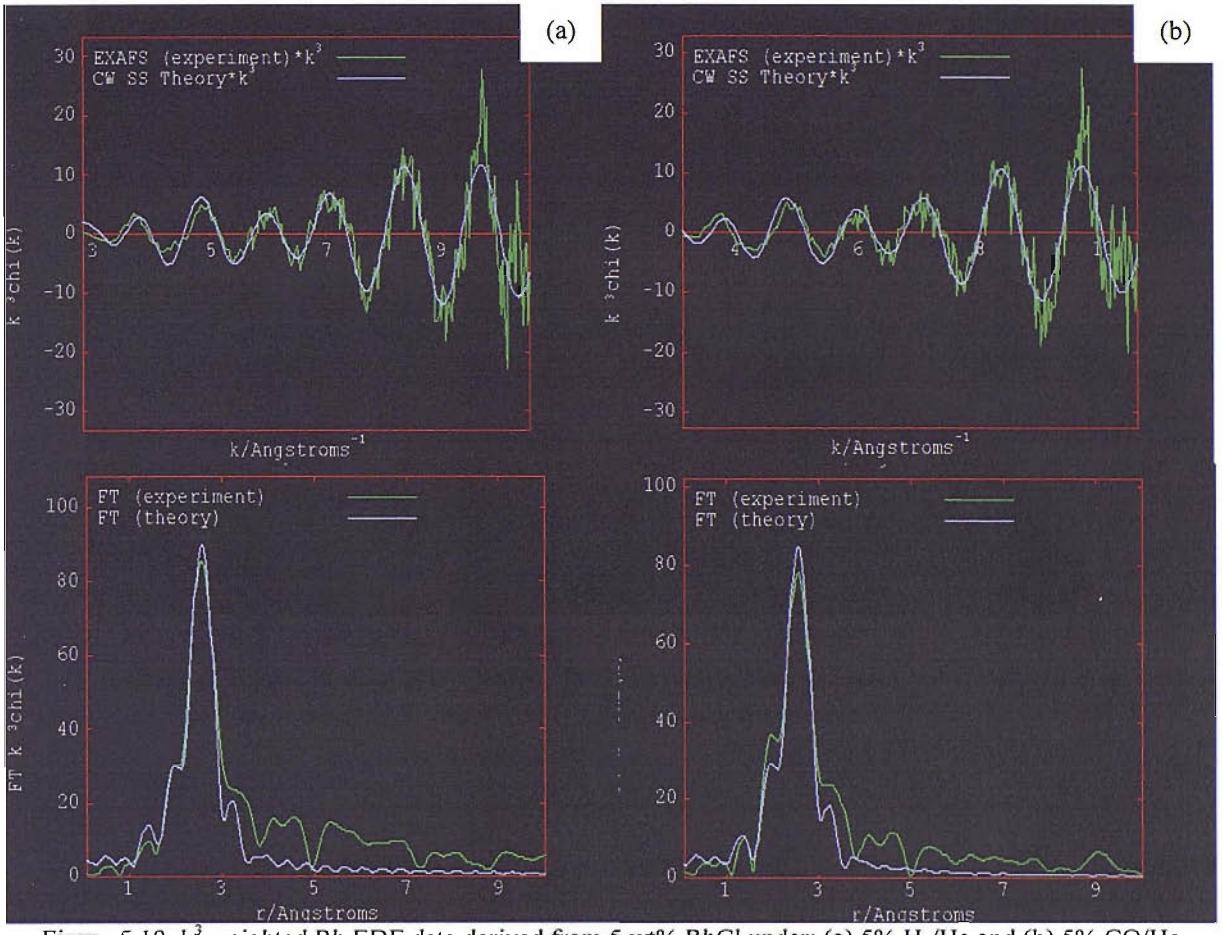

Figure 5.10: k^3 weighted Rh EDE data derived from 5 wt% RhCl under; (a) 5% H_2/He and (b) 5% CO/He (average of 10 spectra taken at t = 29 s) at 298 K. The corresponding Fourier transforms are given underneath each spectrum.

Sample/Conditions	Scatterer	CN	r/Å	E_F	R (%)
(a) 5wt% RhCl in 5%H_2/He at 298 K	Rh	7.1 (± 0.8)	2.68 (±0.02)	-5.02	49
(b) 5wt% RhCl in 5%CO/He at 298 K	Rh	6.5 (± 0.6)	2.69 (±0.02)	-4.01	53

Table 5.2: Structural and statistical data derived from the analysis of spectra given in figure 5.10. Other parameters; k = 2 – 10.5 Å, $2\sigma^2/Å^2$ = 0.011(±0.001).

A similar result to the above is seen at increased temperatures; even at 423 K there is no significant change in the EXAFS after 60 seconds of CO exposure (indexing an N_1^{Rh} value of ca. 6.5 from an initial value of 6.9). A summary of the data obtained at these temperatures is given in table 5.3. As before, an average of 10 EDE spectra (taken at t = 29 s) was used to analyse the system under $CO_{(g)}$.

Sample/Conditions	Scatterer	CN	r/Å	$2\sigma^2/Å^2$	E_F	R (%)
5 wt% RhCl in 5% H_2/He at 323 K	Rh	6.9 (± 0.5)	2.68 (±0.02)	0.011 (±0.001)	-2.63	50
5 wt% RhCl in 5% CO/He at 323 K	Rh	6.6 (± 0.5)	2.68 (±0.02)	0.011 (±0.001)	-3.25	52
5 wt% RhCl in 5% H_2/He at 373 K	Rh	7.1 (± 0.7)	2.68 (±0.02)	0.013 (±0.001)	-5.01	48
5 wt% RhCl in 5% CO/He at 373 K	Rh	6.7 (± 0.6)	2.68 (±0.02)	0.013 (±0.001)	-6.03	51
5 wt% RhCl in 5% H_2/He at 423 K	Rh	6.9 (± 0.6)	2.68 (±0.02)	0.014 (±0.001)	-2.15	48
5 wt% RhCl in 5%CO/He at 423 K	Rh	6.6 (± 0.6)	2.68 (±0.02)	0.014 (±0.001)	-3.02	51

Table 5.3: Structural and statistical data derived from EXAFS analysis of 5wt% RhCl at temperatures and conditions indicated. Data range used was 2 – 10.5 k.

Although the EXAFS reports very little structural change occurring over the Rh systems loaded at the 5 wt% level, the synchronously obtained DRIFTS data indicates that some surface processes are in effect despite this. Figures 5.11 and 5.12 show the same three carbonyl containing species are formed than in the 2.5 wt% case, i.e. CO_L, CO_B and the gem-dicarbonyl species. In contrast to the 2.5 wt% system, figure 5.12 shows that the evolution of these species has a notable temperature dependency. The time for the evolution and stabilisation of these species increases with increasing temperature (from ca. 13 seconds at room temperature to ca. 20 seconds at 423 K). Figure 5.13 shows that by 423 K both the linear and bridged species have attenuated to negligible levels, and even the $[Rh^I(CO)_2]$ species- relatively stable in the 2.5 wt% case- has been significantly reduced by this temperature.

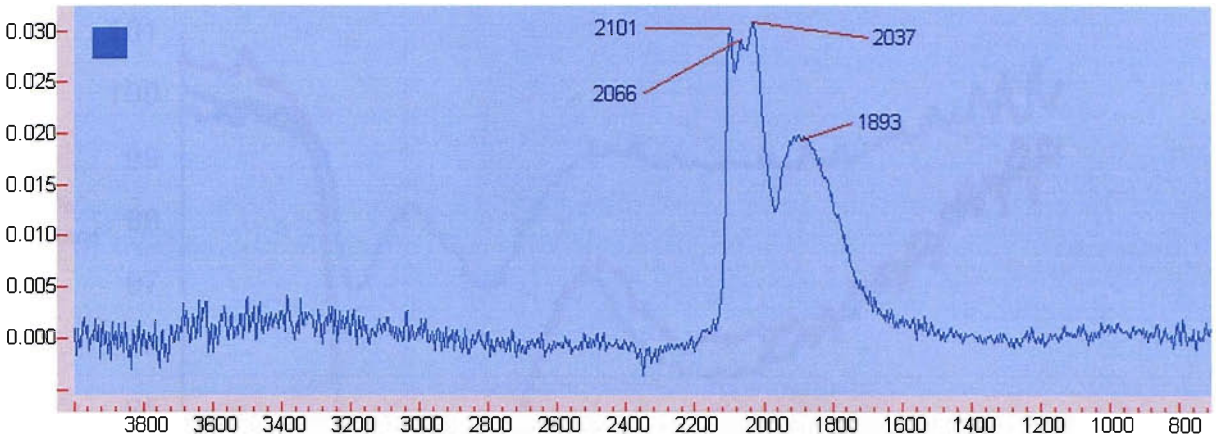

Figure 5.11: Absorbance DRIFTS data derived from time resolved CO exposure to 5 wt% RhCl at room temperature identifying the IR active surface species. The acquisition time for the spectrum was 64ms.

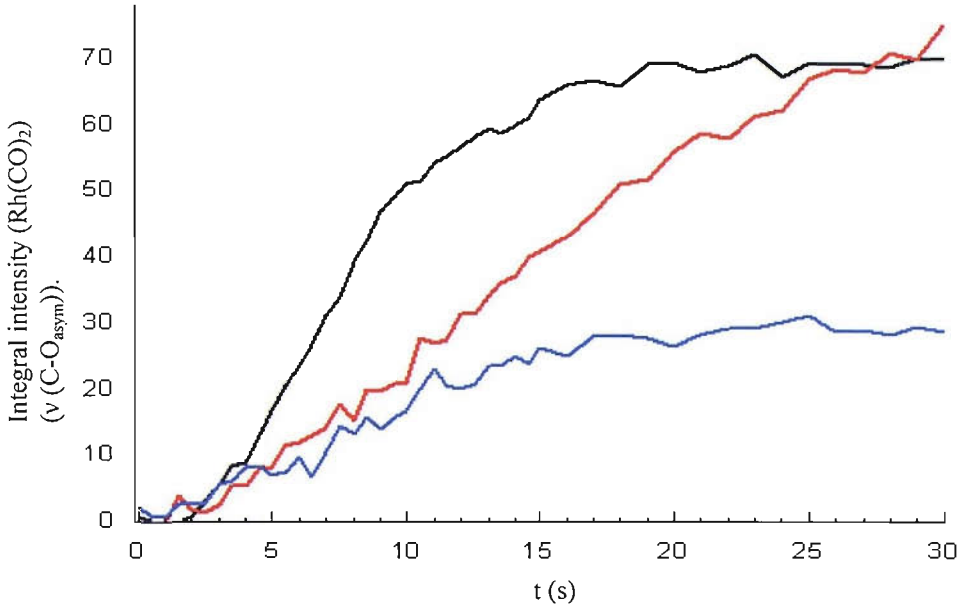

Figure 5.12: Representative figure showing the evolution of the asymmetric stretch of the carbonyl group in $Rh^{I}(CO)_2$ at; 298 K (black line), 373 K (red line) and 423 K (blue line) for 5 wt% RhCl during the time resolved experiments.

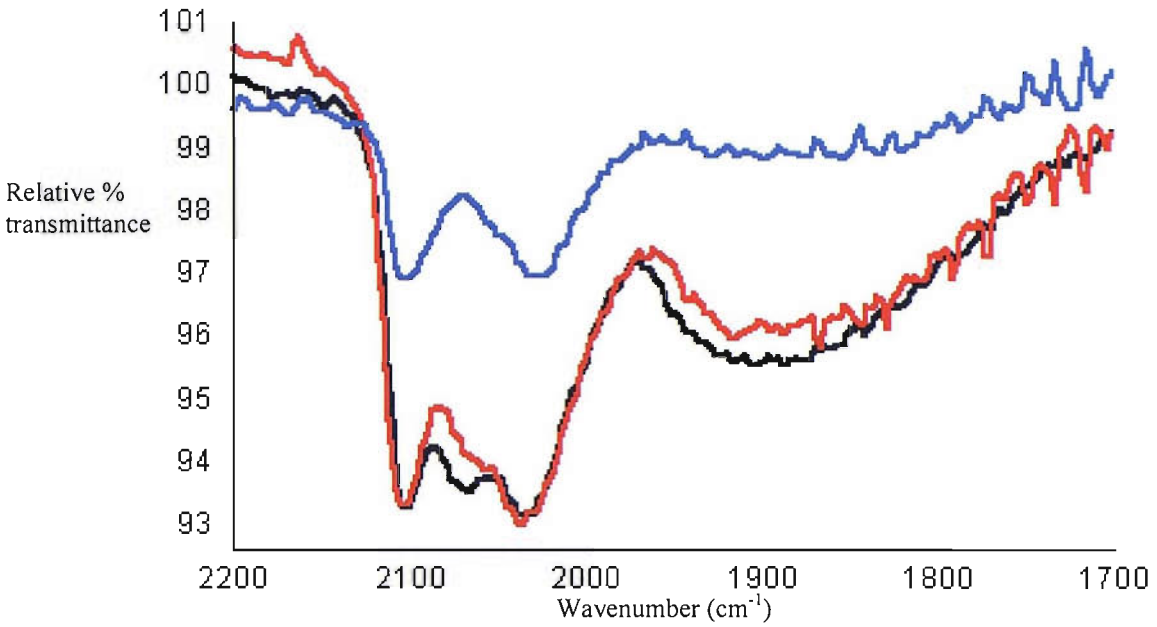

Figure 5.13: Overlaid transmission DRIFTS spectra of 5wt% RhCl exposed to 5%CO/He, taken at; 298 K (black line), 323 K (red line), and 423 K (blue line). For clarity, each spectrum is an average of 10 spectra taken at t = 29 s.

Figure 5.14 shows a representative three dimensional DRIFTS plot showing the evolution and stabilisation of surface species over the 5wt% RhCl system which, despite the structural differences reported by EDE, is remarkably similar to the 3D plot for the 2.5 wt% RhCl system in figure 5.9.

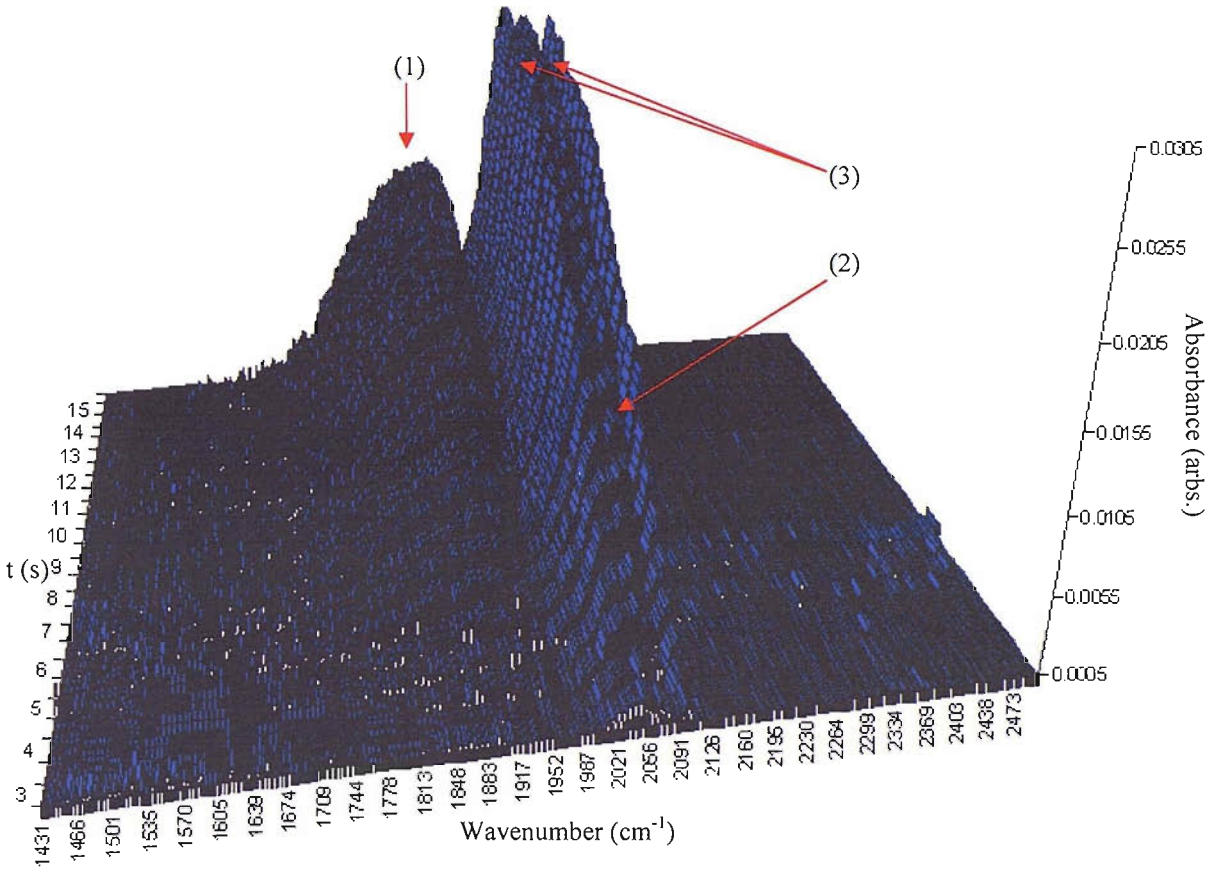

Figure 5.14: DRIFTS spectra (2485-1430cm^{-1}; 4cm^{-1} resolution) as a function of time after exposure to 5% CO/95%He showing the; (1) Bridged CO; (2) linear CO and (3) $Rh^{I}(CO)_2$ peaks for 5 wt% RhCl. For clarity one spectrum every 2s is shown.

5.4 Discussion: 2.5 wt% RhCl

Analysis of the exposure of 5%CO/He to 2.5 wt% RhCl at room temperature effectively illustrates the processes that occur over these systems. There are three distinct stages in which the reaction proceeds within the time scales of these experiments (when viewed from the perspective of the EDE data). First inspection of the static data can be simply charted as the adsorption of CO and subsequent disruption of the Rh nanoparticles that exist on the alumina, a process that is well known and has been studied in great detail in the past; for example the oxidative disruption of Rh particles by CO has been known for nearly fifty years.[23] A closer analysis of this disruption that the current time resolved, multi technique method allows for reveals the adsorption of $CO_{(g)}$ on Rh/Al_2O_3 to be far from straightforward,

with factors such as particle morphology and temperature playing key roles in the behaviour of this system.

The CN of ca. 3.4 and Rh-Rh bond distance (2.68 Å) is in good agreement with those determined by conventional EXAFS for identical 2.5 wt% RhCl catalysts under a flow of H_2 (see chapter 3). From a 'cluster model' perspective this corresponds to an average Rh particle containing ca. 6 - 19 Rh atoms. A detailed analysis outlining the main characteristics of the systems investigated in this chapter can be found in chapter 3. All further discussion assumes prior knowledge of the catalysts, obtainable from the aforementioned chapter.

As in chapter 3, assuming the Rh particles exist as discrete spherical particles on the alumina support, then the number of surface Rh atoms susceptible for CO adsorption can be calculated. Rh particles containing 6 Rh atoms or less can be regarded as essentially existing as atomic surface species; therefore for the 2.5 wt% system all of the Rh atoms are 'accessible', or at least susceptible to CO adsorption at the start of the experiment. This information will be used in later discussion when comparing the relative properties of the 2.5wt% and 5wt% catalysts.

Exposing the 2.5wt% catalyst to 5% CO/He induces a rapid and facile structural change of the system. The EDE and IR data obtained both report that the majority of the carbonyl species formed by the end of the experiment exist as discrete units of $Rh^I(CO)_2$. This result correlates well with previous findings of the disruptive capacity of CO on similar Rh systems,[3,23,24,25,26,27,28,29] where the corrosion of Rh nanoparticles has been long associated with the formation of gem-dicarbonyl units. The evolution of carbonyl containing entities can therefore be directly correlated to the formation of $Rh^I(CO)_2$. The synchronous formation of the CO_L and CO_B species as indicated by DRIFTS will be discussed later in this section.

It must be stated here that the following discussion uses a combination of the Rh-Rh coordination analysis by EDE, the subsequent interpretation of the XANES (as performed by Dr. Moniek Tromp) and the integral data extracted from the absorbance DRIFTS in order to explain the results obtained. The use of the integral derived from the asymmetric stretch of the $Rh(CO)_2$ species was deemed the most effective tool in trying the 'bridge' the obvious trends in the results between the DRIFTS and EDE techniques. This was primarily due to the fact that the $Rh(CO)_2$ entity is known to exist as a discrete surface unit; therefore an integral value of 100% would roughly indicate an atomic dispersion of the Rh component. The

method also assumes that each experiment performed to be perfectly reproducible, thus further adding to the large errors involved. Although this semi-quantitative approach should only be considered as a guide, it is nevertheless a useful technique in trying to explain the results obtained.

Inspection of the DRIFTS data shows within the first ca. 8 seconds of CO exposure, there is rapid formation of the $Rh^I(CO)_2$ species up to an integral of ca. 85. After this time the integral increases to a final value of 100, which corresponds to an apparent complete disruption of Rh nanoparticles by ca. 12 seconds of exposure to CO. Simultaneously, the Rh-Rh coordination number derived from the EDE data is seen to decrease over three distinct stages (as described in the results section above).

To explain the trends observed across the two sets of data, the conclusions from chapter 3 have to be reemphasised. This means that any given coordination number observed by EDE is in fact an average of all the particles present on the catalyst surface, which is highlighted effectively in the diverse particle size distribution for the catalyst by TEM. In terms of the corrosion of the 2.5 wt% catalyst, this means that even with an observed coordination number of 0, 3-4% of the total Rh content in the sample (i.e. 0.08wt% Rh) can still exist as relatively large particles with a coordination number of 12, but is subsequently undetectable by EXAFS. This value represents an extreme case wherein a series of other possibilities exist such as 0.1wt% Rh in particles of N_1^{Rh}=8, 0.12 wt% Rh in particles of N_1^{Rh}=6 or 0.2 wt% Rh in particles of N_1^{Rh}=4, and so on. Based on the TEM results, a mixture of these possibilities would be most likely after complete disruption has occurred.

In the first stage of $CO_{(g)}$ adsorption the CO integral derived from DRIFTS rapidly attains a value of ca. 85, which indicates that 85% of the Rh atoms (equivalent to ca. 1.7 wt% Rh) is present on the support as the isolated $Rh^I(CO)_2$ species. Simultaneously, the corresponding N_1^{Rh} value is seen to decrease to ca. 2. As the N_1^{Rh} value of the $Rh^I(CO)_2$ species is formally 0, this result would point to 15% of the Rh atoms being present in larger particles with an average coordination number of (up to) ca.12. This in turn reiterates previous conclusions that although the initial N_1^{Rh} value is 3.7 corresponding to particle size of 6-19 Rh atoms, there is most likely a spread of Rh particles with a much wider size distribution. Moreover, the presence of CO_L and CO_B in the IR data implies that some Rh-Rh bonding is still present, thus disruption of the nanoparticles cannot be 'complete'.

The onset of the 'second stage' (from the EDE viewpoint) sees the Rh-Rh coordination number decrease at a relatively slower rate to a value of ca. 1, with a mirrored increase in the CO integral to a value of 95-100%. This trend suggests that the larger, non-atomic Rh particles remaining at the end of stage 1 are corroded by $CO_{(g)}$ at a significantly slower rate. Both the rapid initial formation of $Rh^I(CO)_2$ and the slower disruption observed in stage 2 suggests that the overall mechanism proceeds 'Rh by Rh' atom. The significant amounts (up to 85%) of atomically dispersed Rh particles initially present on the catalyst are therefore rapidly disrupted upon exposure to $CO_{(g)}$, without any significant energy barrier. The remaining 15% (0.3 wt% Rh) is stripped from what is most likely larger particles resembling extended Rh surfaces, resulting in a decrease in disruption rate. If this corrosion of the residual Rh is considered to be atomic, then the process will not have any significant effect on the average EXAFS coordination number and the total amount of CO adsorbed, which is reflected in the results.

The final stage suggests that the remainder of the Rh particles have been corroded to a size regime where complete disruption can occur. Again this represents only a small fraction of the total Rh content; therefore the negligible changes in the CO integral and coordination number are reflected by this (and again, the IR data suggests some Rh-Rh bonding to still be present due to the species associated to Rh metal).

The CO adsorption process on Rh systems has been extensively studied upon low dispersed systems such as single crystals[28] or thin films.[26] The general principles and conclusions from this work can be applied to the processes occurring over nanoparticulate Rh. Moreover, a section of the literature[1,3,5,9,18,23,30] has investigated CO adsorption upon similar, highly dispersed Rh/Al_2O_3 systems primarily due to its importance in the field of heterogeneous catalysis (i.e. automotive catalyst systems). However, the majority of the literature to date fails to give an overall account to the many processes occurring over these structurally complex and catalytically active systems. The following statements will therefore be made by taking into account the conclusions and theories of existing studies and combining them with the observations made thus far in this chapter.

The presence of hydroxyl groups upon the alumina surface is well known to be intimately associated with the CO adsorption process, outlined in figure 5.15 and reaction 5.1 (figure adapted from reference [1]).

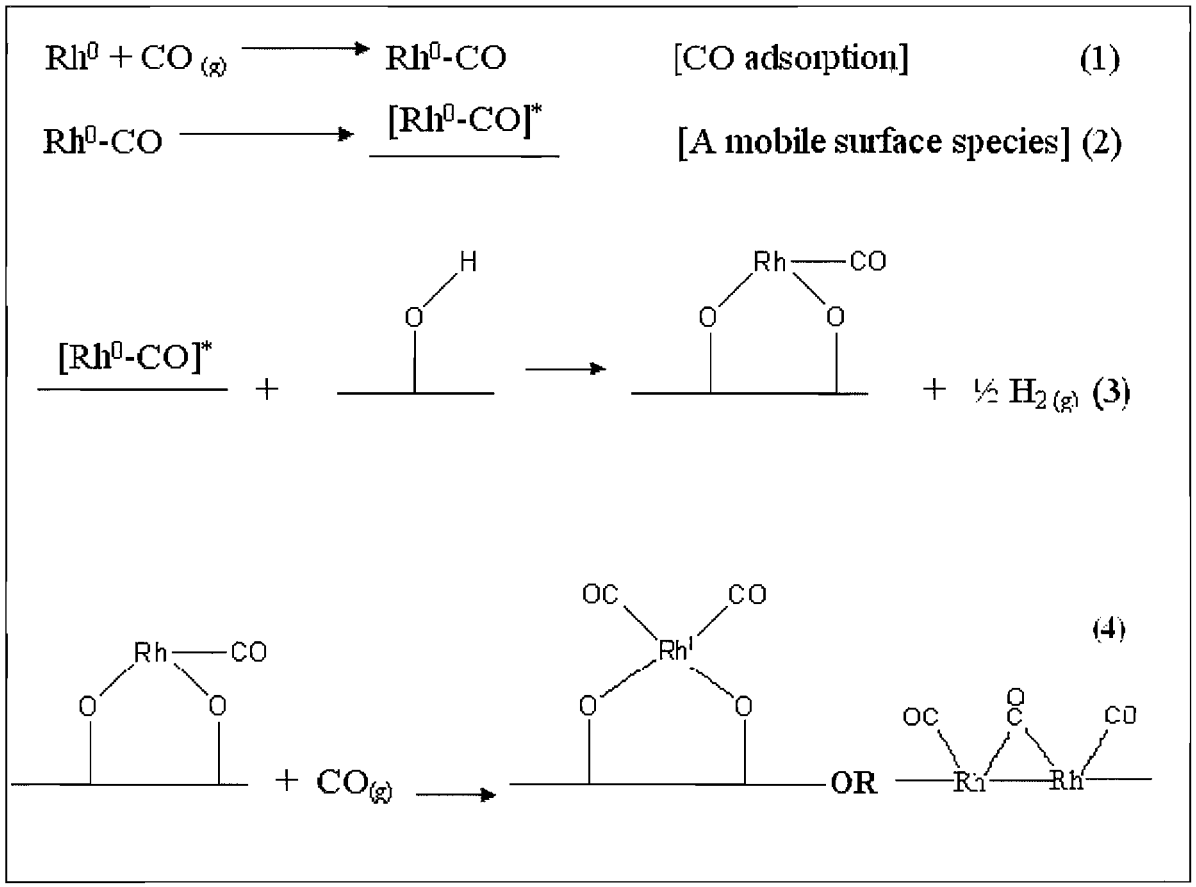

Figure 5.15: Proposed mechanism for the formation of $Rh^I(CO)_2$ species on γ-Al_2O_3. The stoichiometry of the $[Rh^0\text{-}CO]^*$ intermediate is not known. Rh^0 = Metallic Rh site in Rh^0_x crystallite. Structures of Rh entities are for illustrative purposes only.

$$(1/X)\ Rh^0_x + OH_{(a)} + 2CO_{(g)} \leftrightarrow Rh^I(CO)_{2\,(a)} + \tfrac{1}{2}\ H_{2\,(g)} \qquad \text{Reaction 5.1}$$

The proposed mechanism in figure 5.15 outlines the possible steps that occur when Rh^0 crystallites are treated with $CO_{(g)}$. After the initial molecular adsorption of $CO_{(g)}$, step 2 involves the weakening of Rh-Rh bonds by the adsorption process upon Rh^0 surface sites. This weakening within favourable sites leads to the formation of a mobile $[Rh^I\text{-}CO]^*$ species that can migrate across the oxide surface to isolated hydroxyl groups (step 3).

These groups have long been associated with the production of $Rh^I(CO)_2$, which is largely due to infra red and kinetic studies revealing the concomitant formation of $Rh^I(CO)_2$ can be directly correlated to the depletion of isolated OH groups.[1] Qualitative results have shown that only a small fraction of OH groups are involved in the process.[1,31,32] This is expected as there are $\sim 10^{19}$ OH groups per gram (figure estimated from reference [1]) present compared to $\sim 10^{18}$ Rh sites in a 2.5 wt% RhCl catalyst. It has also been shown that associated OH groups (typically hydrogen bonded and physisorbed upon alumina) are not involved in the adsorption/disruption process. The specific activity of the isolated OH groups can therefore be rationalised via two points (taken from reference [1]):

(a) Isolated OH groups are more sterically accessible than OH groups that are involved with hydrogen bonding with neighbouring groups and can therefore accommodate large surface complexes such as $Rh^I(CO)_2$.

(b) Diverse geometrical configurations of OH upon the surface lead to different net charges and therefore differing reactivity towards the oxidation of Rh^0 to Rh^I.

The quality of the DRIFTS data was not sufficient to characterise the hydroxyl groups present, or to follow their subsequent consumption/regeneration on the alumina surface.

Step 4 shows the possible products formed upon further CO adsorption; the gem-dicarbonyl and CO_B species. The exact stoichiometry of the mobile intermediate cannot be identified as it is possible that the fragmented Rh from the crystallite consists of more than one Rh atom. There is also the possibility of more than one CO ligand being bound to each Rh atom. The DRIFTS data from this study detect the presence of the gem-dicarbonyl and bridged species, as well as what is most likely to be CO_L bound upon 'residual' metallic Rh.

The overall process occurring over metallic Rh is shown in reaction 5.1, which is found to be reversible due to the subsequent $H_{2\,(g)}$ the reaction produces.[33] The production of $H_{2\,(g)}$ also indicates that the reaction proceeds under self catalytic promotion.

The results from this study correlate well with the proposed mechanism, which can be summarised as the continual atomic dispersion of Rh and production of $Rh^I(CO)_2$ in a competitive equilibrium with the regeneration of hydroxyl groups and subsequent aggregation of atomically dispersed Rh^I sites. As stated previously, although a range of particle sizes exist on the 2.5 wt% RhCl system it is largely dominated by atomically dispersed Rh (up to 85% of the total Rh content). These smaller particles have a greater

potential to form the $Rh^I(CO)_2$ species due to both steric factors and their closer proximity to isolated hydroxyl groups. It is therefore the remaining 15% of the Rh content associated with larger particles that this mechanism can be effectively applied to. These particles are also important when considering the continual presence of linear and bridged species throughout the catalytic experiment, which immediately suggests metallic Rh to be present on the surface. The hydrogen induced reversibility of reaction 5.1 most likely involves $H_{2(g)}$ dissociation to $2H_{(a)}$ at the metallic Rh sites provided by the larger particles. Following dissociative adsorption, H atoms could spillover and migrate across the support surface, ultimately encountering an anchored $Rh^I(CO)_2$ site. The H atom would donate an electron to Rh^I, reducing it to Rh^0 and existing on its surface as a proton. The basic environment of Al_2O_3 would accept the proton and regenerate OH at the surface and the $Rh^0[CO]_x$ species could then migrate across the surface, encounter Rh^0_x 'nucleation' sites (again initially provided by the larger Rh particles present) and expand its coordination number to reform larger metallic crystallites.

Although relatively insignificant in terms of total Rh content, the larger particles that are initially present on the Rh surface play a significant role in the overall catalytic process, acting as a source of H atoms and nucleation sites for the continual agglomeration of Rh particles. The particles can therefore be directly attributed to the presence of linear and bridge bound CO species throughout the experiment. Moreover, they explain their continual existence in the DRIFTS data even after EXAFS indicates that complete disruption of the Rh particles has occurred.

Exposing the 2.5 wt% RhCl catalyst to 5% CO/He at increasing temperatures reveals distinct trends in the reaction profile, and in turn expands upon the characterisation of these systems. Firstly, it is clear that the initial structural and reactive behaviour of the catalyst is independent of the temperature employed, i.e. 'stage 1' is essentially invariant across the temperature range. It is within this stage that the majority of the Rh content, which exists as essentially atomic Rh particles, is converted to the $Rh^I(CO)_2$ species.

It is also evident that the duration of 'stage 2/3', in which complete disruption of the remaining Rh particles takes place, is directly correlated to the temperature used in these experiments. The rate at which the disruption process occurs over is observed to be approximately twice as fast at 423 K than at room temperature. Moreover, at 423 K the entire

disruption process takes place within 'stage 1' indicating that this stage is the rate limiting step under the conditions employed for this study. Increasing the reaction temperature facilitates the disruption of the larger particles present on the surface, previously calculated to be particles with a coordination number of up to 12.

However, the corresponding DRIFTS data shows that the total amount of adsorbed CO species decreases with increasing temperature. Although the data is only semi-quantitative, it reports that there is up to 40% less CO species (adsorbed as $Rh^I(CO)_2$) adsorbed at 423 K than at room temperature upon the Rh catalyst. These results indicate that although Rh particles are corroded at an increased rate at higher temperatures, the onset of 'complete' disruption yields fewer, larger particles remaining on the surface at the end of the experiment. However, it is most likely that an agglomeration effect is enhanced by particle sintering at higher temperatures, creating much larger particles when compared to those at room temperature. Such particle sintering also explains the overall decrease in the number of Rh particles present at the end of the experiment. It should be noted that although this explanation is qualitative speculation, it correlates well with previous findings on the CO adsorption process.[34,35] It is also entirely possible that the agglomerated/sintered particles could corrode further, but the relatively short timescales and experimental limitations (DRIFTS/EXAFS resolution) meant that this was unobservable.

The findings of Ballinger et al.[5] offer an alternative explanation; it states that the heating of similar Rh/Al_2O_3 systems (from 400 K), initiates the removal of 'isolated' Al-OH groups that 'decrease the tendency of Rh_x^0 species to form $Rh^I(CO)_2$'. The removal of OH groups at higher temperatures would therefore inhibit the disruption process and larger, metallic Rh particles would be more likely to be present on the surface. As none of the mentioned processes can be quantified, by comparing the results of similar studies it is most likely that they all partake in the disruption process to some degree.

The two other species formed during the CO adsorption process, CO_L and CO_B, display behaviour that correlates well with the observations made above. Firstly, the stretching frequencies for CO_L and CO_B obtained via DRIFTS are in excellent agreement with previous infra red studies of CO upon Rh [111] surfaces, which in turn highlights that these species

exist upon metallic Rh. Also, the rate at which all the species are formed during exposure is, within error, identical across the temperature range. As with the geminal-CO species, there is a significant reduction in the amount of CO_L and CO_B adsorbed at higher temperatures. Although the quality of the DRIFTS data does not permit accurate analysis of the broad CO_B region, the shifts in the CO_L peak at varying temperatures indicates important structural information on the Rh catalysts.

Numerous previous IR studies probing the characteristics of CO on supported noble metal catalysts[36] have bolstered the concept that an overall red shift in the wavenumber of such species as the CO_L should be observed at lower surface coverage (in this case a linear bound CO on Pd supported upon TiO_2). The DRIFTS results obtained in this study correlate well with this trend; increasing the temperature (and thus decreasing surface coverage of the CO species) produces an overall red shift. This effect is significant as a shift of ca. 16 cm^{-1} is observed going from room temperature to 423 K.

These results imply that coverage dependence can be closely linked to the changes observed during these experiments. However, associated structural factors cannot be ruled out; further study using higher resolution DRIFTS spectra and possibly combining this with scanning EXAFS data would have to be employed to confirm such arguments.

5.5 Discussion: 5 wt% RhCl

Analogous experiments performed upon a higher loaded catalyst, 5wt% RhCl, show the catalyst to be structurally different to the 2.5wt% system but the adsorption characteristics and overall processes involved to be very similar. On first inspection of the data taken at room temperature, the exposure to 5%CO/He does not significantly alter the structural characteristics of the catalyst within the time frame used. However, the essentially unvarying EXAFS data reveals some important features of the system when combined with the DRIFTS data. Moreover, detailed analysis of the EXAFS data of the 5wt% system is seen to solidify the arguments and conclusions made for the 2.5wt% system.

As with the discussion of the 2.5wt% RhCl system, the initial state of the 5 wt% system has to be considered prior to any further catalytic discussion. A full analysis of the 5 wt% RhCl characteristics using techniques such as EXAFS, TEM and XPS can be found in

chapter 3. In summary, the EXAFS of the reduced 5 wt% system reports N_1^{Rh} of ca. 8, corresponding to an average of ca. 55-87 atoms per particle.

The EXAFS data acquired during the exposure at room temperature does not report any significant corrosion taking place; with N_1^{Rh} dropping from 8 to 7.5 the particles essentially remain intact during the experiment. The majority of the Rh atoms in the 5wt% system will therefore exist in relatively large particles on the surface, to some extent resembling extended metallic surfaces. The 2.5wt% system was found to be dominated by atomically dispersed Rh, which lead to the rapid formation of $Rh^I(CO)_2$ species upon exposure to CO. The larger metallic particles within the 5 wt% system mean that CO_L and CO_B species will be preferentially formed upon CO exposure, rather than the $Rh^I(CO)_2$. This is due to both steric and electronic limitations of extended Rh surfaces under these conditions,[18,23] where CO can only bind to Rh in a atop/ linear or bridge bound (2 fold) position. The presence of smaller, and indeed atomically dispersed, Rh particles cannot be discounted and therefore the potential for particle disruption and subsequent formation of $Rh(CO)_2$ still exist.

Detailed analysis of the DRIFTS data reveals information that would most likely be disregarded by analysis of EXAFS alone. Semi-quantitative results (derived from the method using the absorbance DRIFTS integral data described earlier in this chapter) indicate that ca. 40%, equating to 2.2 wt%, of the Rh content is either atomically dispersed or present in small particles with N_1^{Rh} <12 at the start of the experiment. The DRIFTS also shows that all three IR active CO species are formed during $CO_{(g)}$ exposure as with the 2wt% Rh case; CO_L, CO_B $Rh^I(CO)_2$ but with differing proportions as predicted. When compared to the 2.5 wt% system, proportionally less $Rh^I(CO)_2$ is formed but a marked increase in both CO_L and CO_B species is seen. This is a consequence of the 5 wt% system having a larger average PSD, which is discussed below. The formation of the $Rh^I(CO)_2$ species (and hence the disruption of Rh particles) is a prolonged process in comparison to the 2.5 wt% systems, as is the formation of CO_L and CO_B. This result is expected as the initial average Rh particle size is significantly larger than for the 2.5 wt% systems. The amount of atomically dispersed or sufficiently small Rh particles will therefore be proportionally less, resulting in the 'time consuming' stripping of larger, metallic Rh particles. This result is portrayed effectively by the DRIFTS data, in which ca. 40% of the Rh is corroded to the gem-dicarbonyl species with $N_1^{Rh} = 0$, leaving ca. 60% of the Rh present in particles of N_1^{Rh} = ca. 12. This remaining Rh correlates to an

average coordination number of ca. 7.2, which is in good agreement with the EXAFS obtained. These correlations do not take the errors involved into consideration; with errors considered the exposure of $CO_{(g)}$ does not impose any significant changes to the 5wt% system.

The use of higher temperatures during the experiment, which facilitated the disruption in the 2 wt% case, does not have any significant effect in the 5 wt% experiments. The evolution of CO species is also essentially invariant across the temperature range employed, indicating that more extreme conditions are needed to invoke the complete disruption of the Rh particles. It is therefore most likely that only an initial stage of the disruption process has been sampled within the time frame of these experiments. This supports the previously stated theory that the corrosion of Rh nanoparticles takes place 'atom by atom'; longer timescales and/or higher temperatures would be needed to probe the complete process.

The conclusions drawn from analysing the 2.5 wt% RhCl system can also be successfully applied to the 5 wt% system, solidifying the arguments posed and ultimately providing an overall perspective of the CO adsorption process on Rh nanoparticles.

The mechanism outlined in figure 5.15 and reaction 5.1 can be applied with even more relevance than with the 2.5 wt% system, as ca. 60% of the Rh content exists as 'metallic Rh^0_x' compared to just ca. 15% in the 2.5 wt% system. The evolution of linear bound CO on Rh as a dominant species would also have to be added to step (4) of the mechanism. This in turn suggests that the 'competitive equilibrium' (in which agglomeration of particles is possible) discussed for the 2.5 wt% system also exerts a significant influence on the 5 wt% catalyst behaviour. The continual agglomeration of Rh particles would effectively explain the apparent static nature of the disruption process occurring over the 5 wt% system. Therefore some form of equilibrium between the corrosive erosion of these metallic Rh particles and the subsequent agglomeration process is the most likely explanation to the processes being observed here.

The removal of the isolated OH groups at higher temperatures, leading to the decrease in the tendency of metallic Rh to form $Rh^I(CO)_2$, can also be considered for the 5 wt% catalyst. As with the proposed reaction mechanism, the OH removal has greater relevance and potentially a greater impact upon the process itself due to the significant amount of metallic Rh present. This effect, when combined with the continual agglomeration of Rh particles

discussed above, is the most likely explanation to the ongoing 'static' structural behaviour of Rh nanoparticles at higher temperatures. The possibility of particle sintering at higher temperatures to facilitate the production of metallic Rh particles is also another factor to help explain why extensive particle disruption is not observed upon 5 wt% Rh, within the time frames and catalytic conditions employed. The significant reduction of adsorbed CO species (most notably the $Rh^{I}(CO)_2$ species) at higher temperatures could also be due in part to sintering. This is because fewer, more massive Rh particles would form at higher temperatures leading to greatly reduced formation of gem-dicarbonyl. The increased lability of the CO species at elevated temperatures to desorb from the Rh surface can also be attributed to the observed decrease.

5.6 Summary

In summary, the time resolved, multi-technique experiments reveal that exposing a relatively low loaded RhCl catalyst (2.5wt%) to a flow of gaseous 5%CO/He induces a rapid disruption of the particles that results in the dominant formation of discrete $Rh(CO)_2$ species. The use of higher exposure temperatures facilitates the rate of this disruption. DRIFTS and previous evidence suggests that complete disruption does not occur; particulate Rh still plays a key role in the processes involved. Several models involving particle sintering/agglomeration and the role of hydroxyl groups from the alumina surface have been discussed in trying to explain the continual presence of particles resembling extended Rh surfaces that are undetectable by techniques such as EXAFS (although the current experiments take place over a much shorter timescale than previous work, which also has to be taken into account). This idea of an equilibrium between particle disruption and agglomeration becomes clearer when considering a RhCl catalyst loaded at the 5 wt% level; the catalyst structure is not significantly affected at any temperature employed. The almost identical DRIFTS data to the lower loaded system however confirms that a range of processes are most likely to be in effect here, and all of the available data needs to be considered when analysing the complex 'whole' of these supported systems.

5.7 References

[1] P. Basu, D. Panayotov, J.T. Yates Jr., *J. Am. Chem. Soc.*, 1988, **110**, 2074.

[2] H.F.J. Van't Blik, J.B.A.D. Van Zon, T. Huizinga, J.C. Vis, D.C. Koningsberger, R. Prins., *J. Am. Chem. Soc.*, 1985, **107**, 3139.

[3] A.Suzuki, Y. Inada, A.Yamaguchi, T.Chihara, M.Yuasa, M. Nomura, Y. Iwasawa, *Angew. Chem., Int. Ed.*, 2003, **42**, 4795.

[4] A. Maroto-Valiente, I. Rodriguez-Ramos, A. Guerrero-Ruiz, *Catal. Today*, 2004, **93-95**, 567.

[5] T. H. Ballinger, J.T. Yates Jr., *J. Phys. Chem.*, 1991, **95**, 1694.

[6] F. Solymosi, M. Pasztor, *J. Phys. Chem.*, 1985, **89**, 4789.

[7] P. Basu, D. Panayotov, J.T. Yates Jr., *J. Phys. Chem.*, 1987, **91**, 3133.

[8] W.N. Delglass, G.L. Haller, R. Kellerman, J.H. Lunsford, *'Spectroscopy in Heterogeneous Catalysis'*, 1979, Academic Press, New York.

[9] M. Cavers, J.M. Davidson, I.R. Harkness, L.V.C. Rees, G.S. McDougall, *J. Catal.*, 1999, **188**, 426.

[10]A.A. Tolia, R.J. Smiley, W.N. Delglass, C.G. Takoudis, M.J. Weaver *J. Catal.*,1994, **150,** 56.

[11] M. Bowker, Q. Guo, Y. Li, R.W. Joyner, *Catal. Letts*. 1993, **18**, 119.

[12] M.J.P. Hopstaken, J.W. Niemantsverdriet, *J. Chem. Phys.*, 2000, **113**, 5457.

[13] A. Berko, F. Solymosi, *J. Catal.*, 1999, **183**, 91.

[14] A. Berko, G. Menesi, F. Solymosi, *J. Phys. Chem.*, 1996, **100**, 1773.

[15] J.H. Sinfelt, G.H. Via, F.W. Lytle, *Catal. Rev. Sci. Eng.*, 1984, **26**, 81.

[16] B. Jyoti, MPhil Thesis, University of Southampton, 2002.

[17] A.C. Yang, C.W. Garland, *J. Phys. Chem.*, 1957, **61**, 1504.

[18] C.A. Rice, S.D. Worley, C.W. Curtis, J.A. Guin, A.R. Tarrer, *J. Chem. Phys.*, 1981, **74**, 6487.

[19] M.A. Newton, D.G. Burnaby, A.J. Dent, S. Diaz-Moreno, J. Evans, S.G. Fiddy, T. Neisius, S. Pascarelli, S. Turin, *J. Phys. Chem. A.*, 2001, **105**, 5965.

[20] H.F.J. Van't Blik, J.B.A.D. Van Zon, T. Huizinga, J.C. Vis, D.C. Koningsberger, R. Prins., *J. Phys. Chem.*, 1983, **87**, 2264.

[21]M.A. Newton, B. Jyoti, S.G. Fiddy, J. Evans, *Chem. Comm.* 2004, 2382.

[22] M.A. Newton, A.J. Dent, S. Diaz-Moreno, S.G. Fiddy, B. Jyoti, J. Evans, *Chem. Eur. J.*, 2006, **12**, 1975.

[23] A.C. Yang, C.W. Garland, *J. Phys. Chem.*, 1957, **61**, 1504.

[24] J. Evans, B. E. Hayden, M. A. Newton, *Surf. Sci.*, 2000, **462**, 169.

[25] J.A. Anderson, *J. Chem. Soc. Faraday Trans.*, 1991, **87**, 3907.

[26] For instance: J. Evans, B.E. Hayden, F. Mosselmans, A. Murray, *Surf. Sci. Lett.*, 1992, **279**, L159 and *Surf. Sci*, 1993, **301**, 61.

[27] For instance: B.E.Hayden, A. King, M.A. Newton, *Surf. Sci.*, 1998, **397**, 306.

[28] B.G. Frederick, G. Apai, T.N. Rhodin, *J. Am. Chem. Soc.*, 1987, **109**, 4797.

[29] P. Johnston, R. W. Joyner, *J. Chem. Soc. Faraday Trans.*, 1993, **89**, 863.

[30] G. Lafaye, C. Mihut, C. Especel, P. Marécot, M.D. Amiridis, *Langmuir*, 2004, **20**, 10612.

[31] H. Könzinger, P. Ratnasamy, *Catal. Rev.-Sci. Eng.*, 1978, **17**, 31.

[32] J.B. Peri, *J. Phys. Chem.*, 1965, **69**, 220.

[33] A. Brenner, D.A. Hucul, *J. Catal.*, 1980, **61**, 216.

[34] E.W. Thornton, H. Knözinger, B. Tesche, J.J. Rafalko, B. Gates, *J. Catal.*, 1980, **62**, 117.

[35] G.S. McNulty, K. Cannon, J. Schwartz, *Inorg. Chem.*, 1986, **25**, 2919.

[36] For instance: J. Evans, B.E. Hayden, G. Lu, *Surf. Sci.*, 1996, **360**, 61.

Chapter 6. The response of Rh/Al_2O_3 systems to NO and subsequent reductive behaviour

6.1 Introduction

The previous chapter investigated the interaction of CO with Rh nanoparticles using the complementary data afforded by the EXAFS/DRIFTS/MS experiment. The data taken from systems with different metal loadings and across various temperatures successfully delivered an understanding of the disruptive processes occurring over the Rh. To this effect this chapter will aim at understanding the adsorption process of another key molecule, NO.

As discussed in the introduction, NO has the tendency to undergo both molecular and dissociative reactions on Rh; numerous species such as $(NO)_{2\,(ads)}$, $N_2O_{(ads)}$, $NO_{(ads)}$, $N_{(ads)}$ and $O_{(ads)}$ are possible products. This is due to the lower dissociation energy of NO (630 kJ mol^{-1}) compared to CO (1076 kJ mol^{-1}),[1] therefore the study of NO adsorption is interesting purely from a scientific point of view. Combined with its technological importance (e.g. its interaction with the three-way catalyst)[2] and potential deleterious effects in the environment[3] it is clear to see why a thorough understanding of the basic adsorption process is needed.

By performing similar experiments to those performed in the previous chapter, the structural response of Rh nanoparticles to NO will be probed. In addition to this, IR active species formed upon the surface as well as any gaseous species produced will be identified. Trends across the vast array of data will then be identified, and models will be postulated where possible.

6.2 Experimental

The EDE/DRIFTS/MS experimental apparatus was used as outlined in chapter 2.5.8

In a typical experiment the Rh catalyst (ca. 45 mg) was pre-treated by heating under a flow of 5% H_2/He to 573 K. The system was then subjected to a flow of 5% O_2/He for ca. 5 minutes before switching back to the flow of 5% H_2/He and held at the required temperature. After purging under a flow of He, 5% NO/He at 25 $mlmin^{-1}$ was introduced synchronously with the start of the EDE/DRIFTS/MS experiment. EXAFS detection was made via the FReLoN CCD camera with a total acquisition time of ca. 60 ms.

6.3 The response and adsorption properties of rhodium systems to NO: a variable temperature study

NB: The quality of the EXAFS data obtained for the 2.5 wt% RhCl systems was not sufficient to permit reliable analysis. This was despite repeating the experiment numerous times, and repeated attempts at trying to extract useful data from the experiments.

6.3.1 NO exposure at room temperature

By analysing the EXAFS data at the beginning and end of the time resolved exposure experiment, performed at room temperature, an initial idea of the structural variances occurring can be obtained.

Figure 6.1 shows k^3 weighted Rh K-edge EDE spectra for 5 wt% RhCl before and after exposure to 5% NO/He at room temperature, along with the corresponding Fourier transforms. The structural and statistical information derived from these spectra are given in table 6.1.

The static EDE data in figure 6.1 part (a) shows the pre-treated, reduced 5 wt% RhCl catalyst to index an expected N_1^{Rh} of ca. 7, consistent with previous findings.[4,5] Upon exposing the system to a flow of 5% NO/He for 30 seconds, the EXAFS signal indicates significant structural changes to have occurred, with the coordination number falling to a value of ca. 4 (part (b)). Unfortunately, the data was not of sufficient quality to permit the modelling of any adsorbed nitrosyl species (this applies for all the temperatures investigated), but the oxygen (or nitrogen) shell at 2.03 Å does indicate oxidation of the Rh component to have occurred.

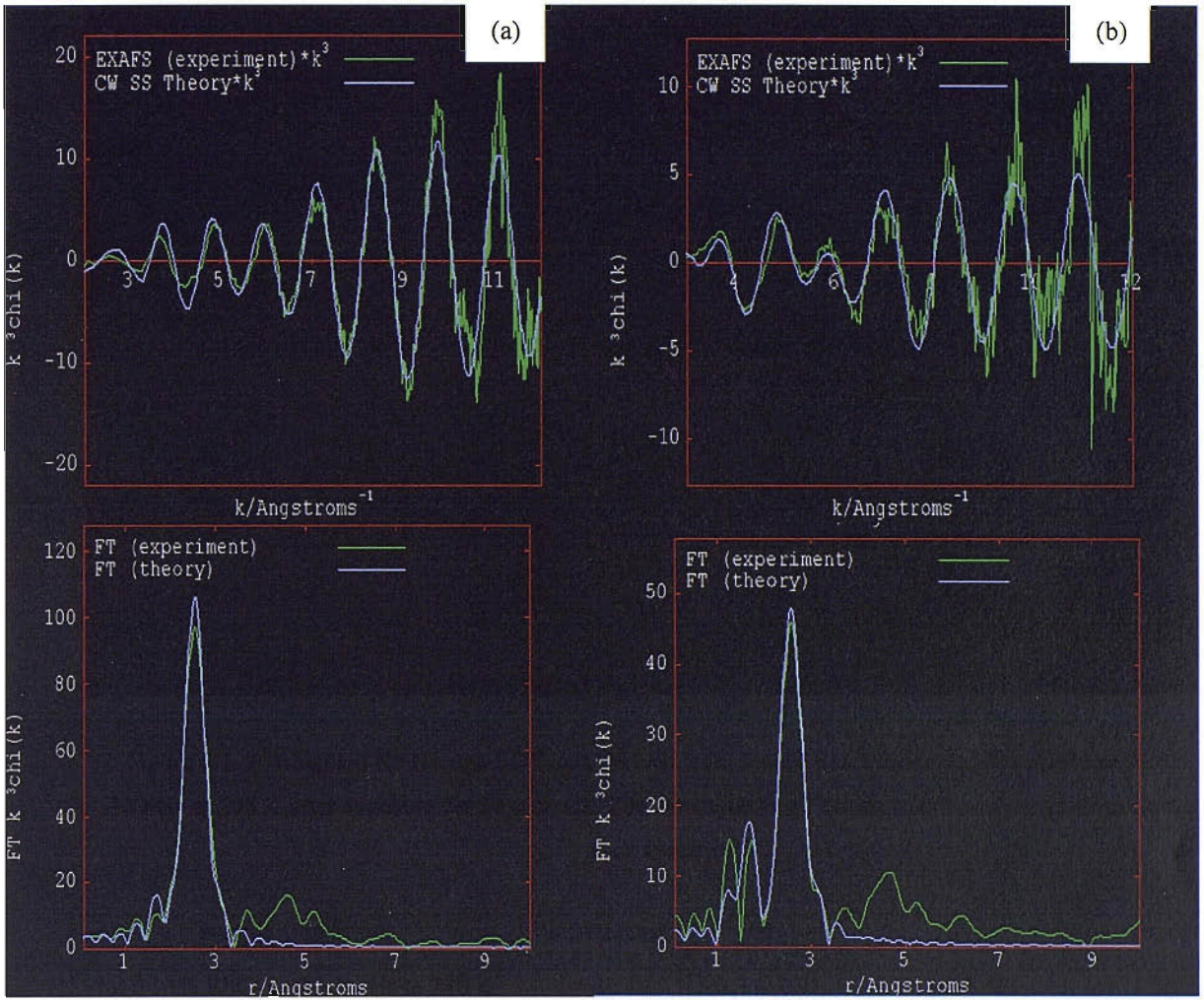

Figure 6.1: k^3 weighted Rh K-edge EDE data derived from 5 wt% RhCl under; (a) 5% H_2/He and (b) 5% NO/He at 298 K after exposure for 30 seconds. The corresponding Fourier transforms are given underneath each spectrum.

Sample/Conditions	Scatterer (s)	CN	r/Å	$2\sigma^2/Å^2$
(a) 5 wt% RhCl in 5% H_2/He at 298 K	Rh	6.9 (±0.6)	2.66 (±0.02)	0.011 (±0.001)
(b) 5 wt% RhCl in 5% NO/He at 298 K after 30 seconds exposure	Rh	3.8 (±0.3)	2.68 (±0.02)	0.011 (±0.001)
	O/N	0.7 (±0.1)	2.03 (±0.01)	0.006 (±0.001)

Table 6.1: Structural and statistical data derived from the analysis of spectra given in figure 6.1. Other parameters: (a) Ef = -2.39 eV, R = 32%, k = 2-12$Å^{-1}$, (b) Ef = -1.01eV, R = 50%, k = 2-12$Å^{-1}$.

Figure 6.2 shows the N_1^{Rh} (Rh) data alongside a representative integral of a species formed during the time resolved exposure of 5 wt% RhCl to 5% NO/He at room temperature, in this case the evolution of the $Rh(NO)^-$ species is followed (full DRIFTS results are given below). The quality of the EDE spectra, taken every ca. 60ms, was sufficient to permit the structural analysis given in figure 6.2 and throughout this chapter.

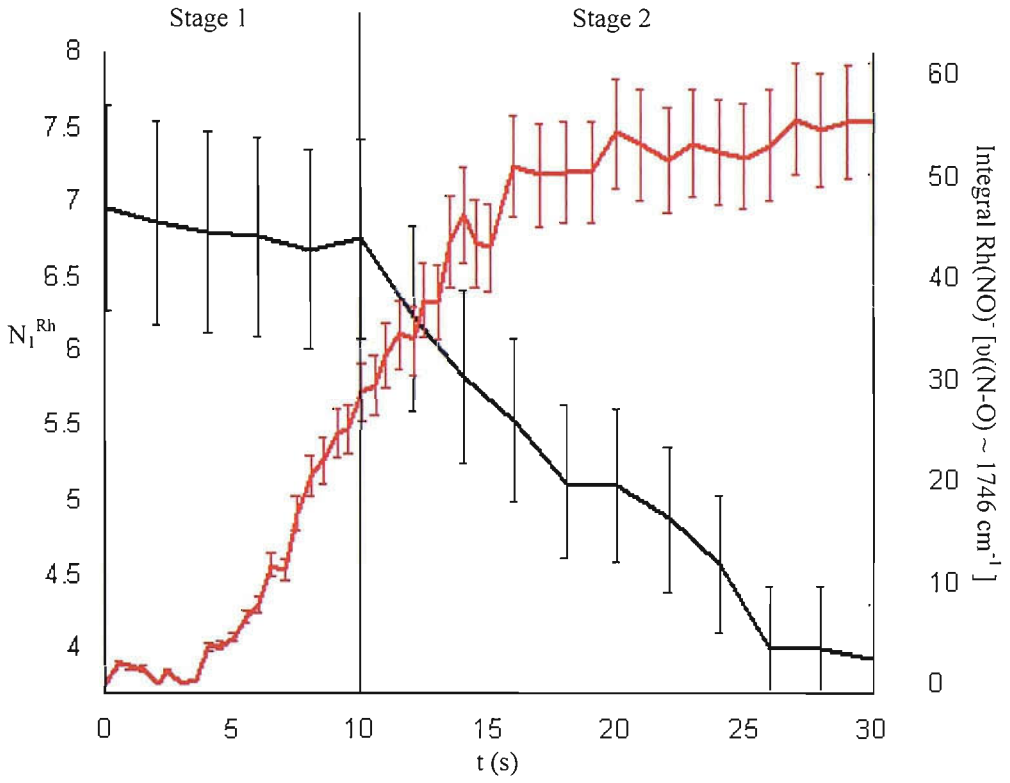

Figure 6.2: Rh-Rh coordination number (black line) and integral of the (N-O) stretch ($\nu \sim 1746\ cm^{-1}$) of the Rh-NO^- ligand (red line) as a function of time during time resolved 5% NO/He exposure to 5 wt% RhCl at room temperature. EDE data derived from every 2.5 seconds of the time resolved experiment is plotted, with DRIFTS data indexed every 0.5 seconds. Errors are derived from the corresponding standard deviations.

The time resolved data in figure 6.2 displays the aforementioned decrease in Rh-Rh coordination over time, which on first inspection can be viewed as the progressive oxidation of the Rh catalyst. However, a closer examination of the structural profile via the EDE data reveals the disruptive process can be divided into two distinct stages (as indicated within the figure). Stage 1 sees the coordination number to essentially remain at a static value of 7 for the first ca. 10 seconds. The results can be viewed as experimentally viable as the relatively

short dead time of the system of (at most) 2 seconds would not have a significant impact on the observations made over the period of 30 seconds (see chapter 2.5.8 regarding dead time issues) After this apparent 'induction' period, stage 2 charts the coordination decreasing consistently to a value of ca 4 by 25 seconds. Further oxidation of the Rh is not evident after this time, as the coordination number stabilises at a value of ca. 4. Moreover, any facile changes appear to have reached completion as this value does not change significantly even after 60 seconds of $NO_{(g)}$ exposure (data not shown for clarity reasons), with the final N_1^{Rh} reporting a value of 3.83 (± 0.3).

The representative DRIFTS integral showing the evolution of the Rh-NO^- ($\nu \sim 1746\ cm^{-1}$) species in figure 6.2 can be correlated to the disruptive process occurring over Rh, and can also be divided into two stages (not shown in figure). As with the EXAFS data, there is an initial 'induction' period of ca. 5 seconds before any significant amount of species is detected. The dead time of the system would account for the majority of this period, but again does not bear a significant impact on the results when viewed over the experiment as a whole. The second stage from 5 - 30 seconds charts the formation and stabilisation of the $Rh(NO)^-$ species.

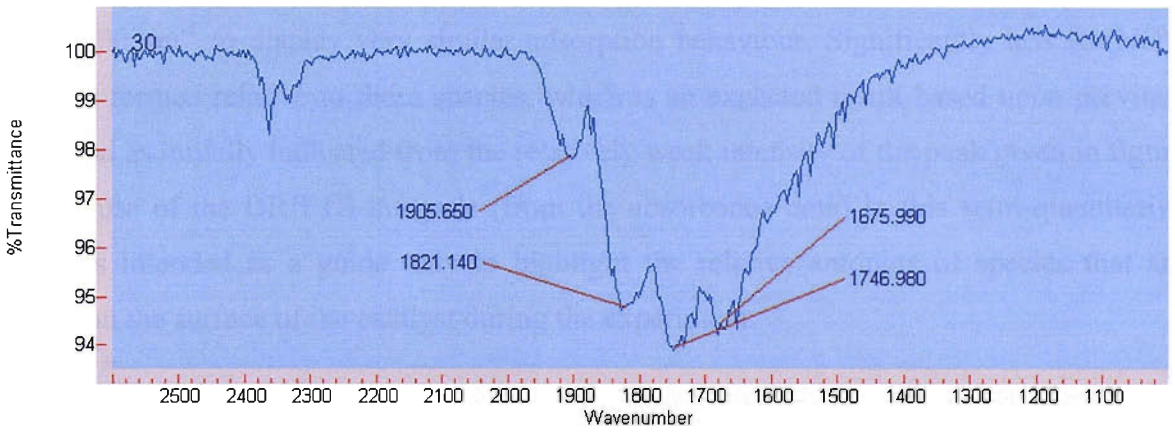

Figure 6.3: DRIFTS spectra taken from 5 wt% RhCl after 30s exposure to 5% NO/He at room temperature. The acquisition time for the spectrum was 64 ms.

A closer examination of the DRIFTS spectrum taken from the room temperature time resolved experiment in figure 6.3 reveals the range of IR active species present on the Rh surface after ca. 30 seconds of $NO_{(g)}$ exposure. The spectrum correlates well to numerous

existing studies on the interaction of $NO_{(g)}$ with Rh catalyst systems,[6] therefore the peaks can be assigned as follows. The weak signal at 1905 cm^{-1} can be assigned to the linear $Rh(NO)^+$ species.[7,8,9] The broad, yet intense peak centred on 1746 cm^{-1} is difficult to assign as a band in this region has previously been assigned to the bent, 'high wavenumber' $Rh(NO)^-$ species[10,11,12] and the ν_{asym} (N-O) of the geminal dinitrosyl species $Rh(NO)_2$.[13] The presence of the corresponding band ν_{sym} (N-O) at 1821 cm^{-1} confirms that the dinitrosyl species does form on the catalyst surface. It is therefore most likely that the peak at 1746 cm^{-1} has contributions from both the $Rh(NO)^-$ species and the ν_{asym} (N-O) of $Rh(NO)_2$. Based on previous work, the broad peak centred at 1675 cm^{-1} could be assigned to a number of species. These include nitrates adsorbed upon the alumina surface,[7-9,12-14] a proposed 'low wavenumber' $Rh(NO)^-$ species[7-9,12-14] and molecular NO adsorbed in two or threefold sites on metallic Rh clusters.[15,16] As all of these species could conceivably be present on the surface, they will be referred to as 'species below 1700 cm^{-1}' in the forthcoming discussion.

Figures 6.4 and 6.5 reveal the temporal adsorption characteristics of the 5 wt% catalyst as it is exposed to a flow of 5 %NO/He at room temperature. The integrals shown in figure 6.4 highlight the rate of evolution for each of the nitrosyl species, as well as the relative amounts that are formed during the exposure. The figure reveals the $Rh(NO)_2$, $Rh(NO)^-$ and species below 1700 cm^{-1} to display very similar adsorption behaviour. Significantly less $Rh(NO)^+$ species is formed relative to these species, which is an expected result based upon previous work[17] and as initially indicated from the relatively weak intensity of the peak given in figure 6.3. The use of the DRIFTS integrals (from the absorbance data) in this semi-quantitative manner is intended as a guide only to highlight the relative amounts of species that are forming on the surface of the catalyst during the experiment.

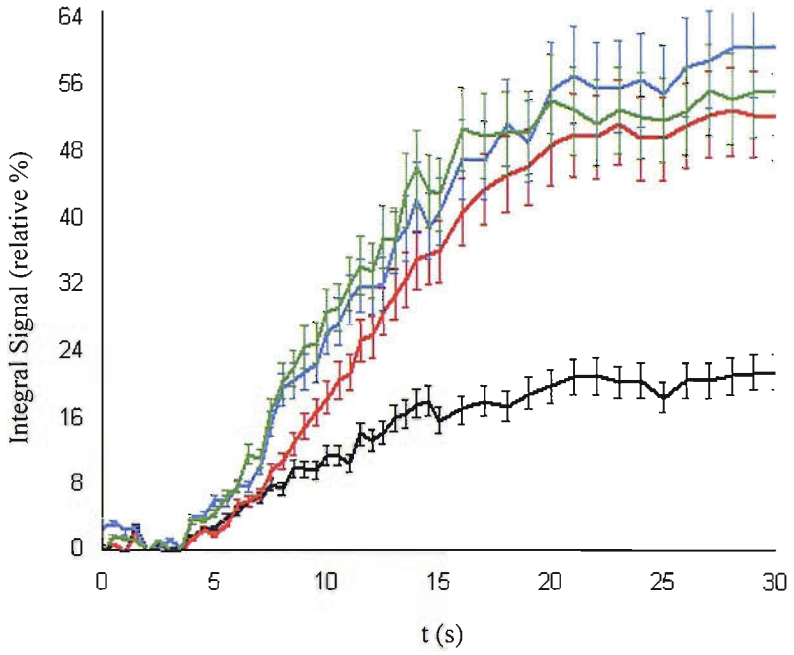

Figure 6.4: Integrals charting the evolution of IR active species on 5 wt% RhCl on exposure to 5% NO/He at room temperature; 'species below $1700cm^{-1}$' (green line), $Rh(NO)_2$ ν_{asym} (N-O) / $Rh(NO)^-$ (blue line), $Rh(NO)_2$ ν_{sym} (N-O) (red line) and $Rh(NO)^+$ (black line). Errors are derived from the corresponding standard deviations.

Figure 6.5 shows a three dimensional profile of the evolution and stabilisation of the main nitrosyl surface species discussed above, highlighting both the quantity and quality of the DRIFTS spectra that is obtained from a typical experiment.

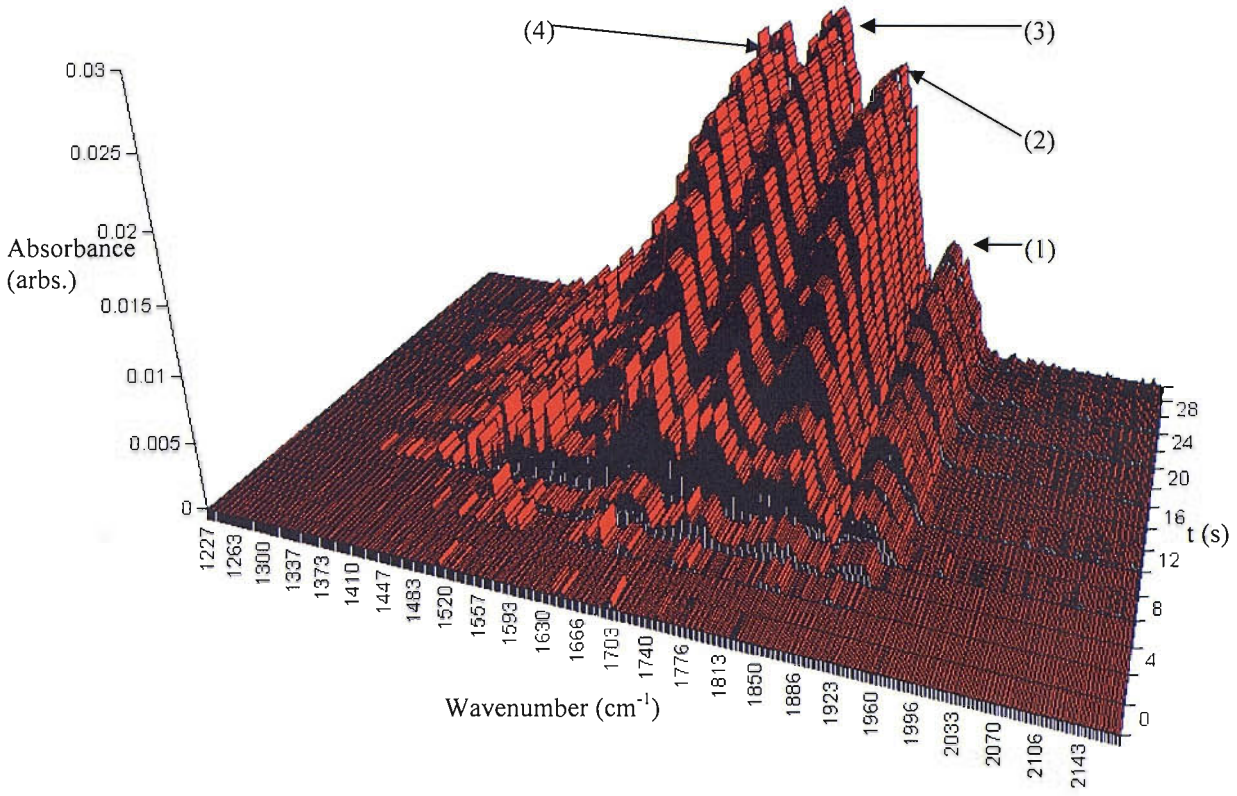

Figure 5.5: DRIFTS spectra (2176-1225 cm^{-1}; 4 cm^{-1} resolution) as a function of time after room temperature exposure to 5% NO/He showing the; (1) $Rh(NO)^+$; (2) $Rh(NO)_2$ [ν_{sym} (N-O)]; (3) $Rh(NO)^-$/ $Rh(NO)_2$ [ν_{asym} (N-O)] and (4) 'species below 1700 cm^{-1}' (see main text) peaks for 5 wt% RhCl. For clarity one spectrum every 2s is shown.

The characteristics of the 5 wt% RhCl system were then probed further by performing identical time resolved experiments at increasing temperatures. Although these experiments were performed every 50 K up to 573 K, only data from experiments performed at 423 and 573 K returned fully analysable data (i.e. from both EDE and DRIFTS data sets). These experiments do still provide a suitable range of temperatures in which to probe these systems, as they are applicable to the working regime of such systems as the TWC.

6.3.2 NO exposure at 423 K

Figure 6.6 shows k^3 weighted Rh K-edge EDE spectra for 5 wt% RhCl before and after exposure to 5% NO/He at 423 K, along with the corresponding Fourier transforms. The structural and statistical information derived from these spectra are given in table 6.2.

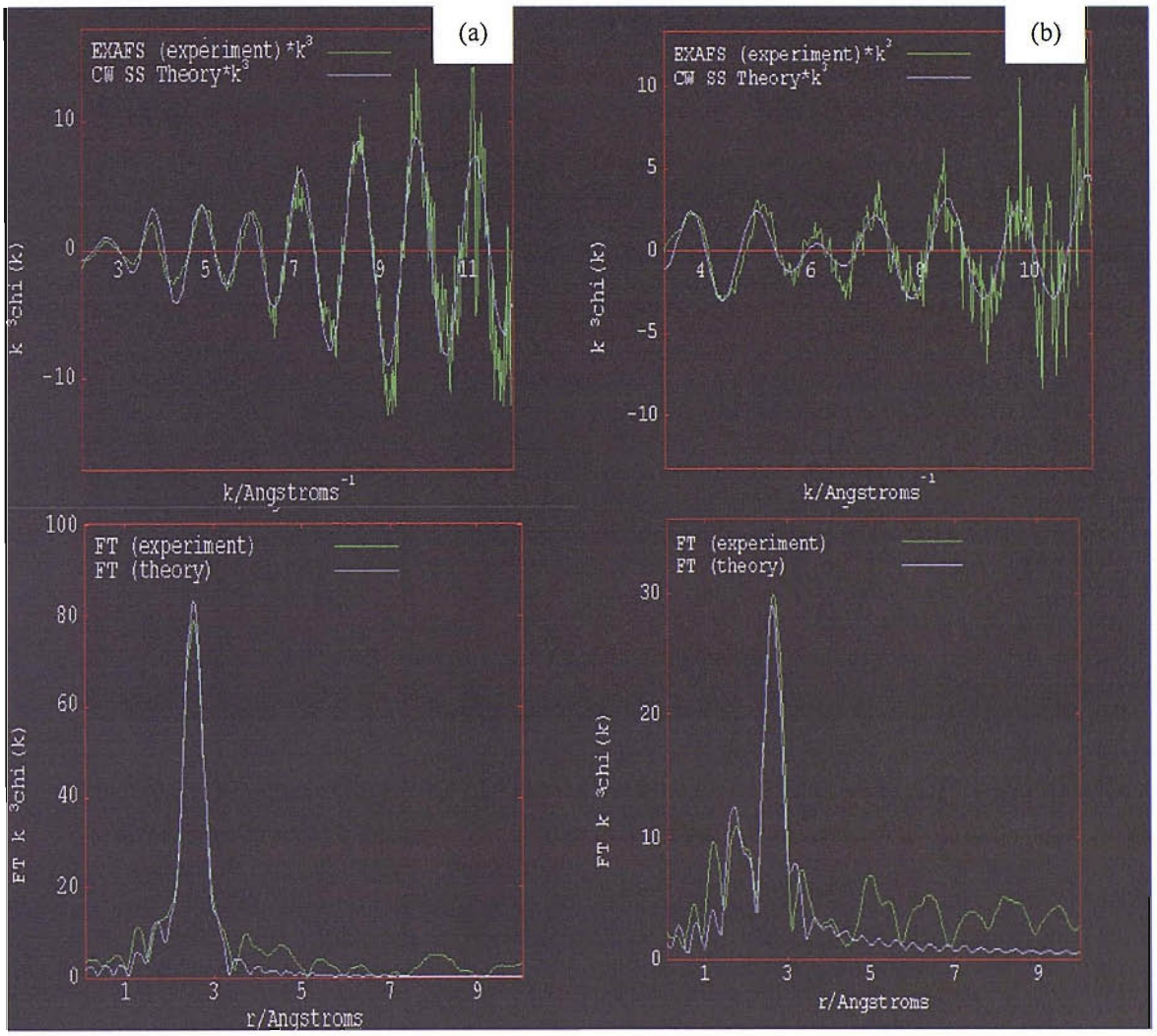

Figure 6.6: k^3 weighted Rh K-edge EDE data derived from 5 wt% RhCl under; (a) 5% H_2/He and (b) 5 NO/He at 423 K after 30 seconds exposure. The corresponding Fourier transforms are given underneath each spectrum.

Sample/Conditions	Scatterer (s)	CN	r/Å	$2\sigma^2/Å^2$
(a) 5wt% RhCl in 5%H_2/He at 423 K	Rh	6.1 (±0.5)	2.65 (±0.02)	0.014 (±0.001)
(b) 5wt% RhCl in 5%NO/He at 423 K after 30 seconds exposure	Rh	2.9 (±0.3)	2.70 (±0.02)	0.014 (±0.001)
	O/N	0.91 (±0.1)	2.04 (±0.01)	0.015 (±0.002)

Table 6.2: Structural and statistical data derived from the analysis of spectra given in figure 6.6. Other parameters; (a) Ef = -0.14 eV, R = 40%, k = 2-12Å^{1}, (b) Ef = 0.09 eV, R = 55%, k = 2-11 Å^{-1}.

Figure 6.7 charts the Rh-Rh coordination data during the time resolved exposure of 5 wt% RhCl to 5% NO/He at 423 K, and as in the room temperature case it is plotted alongside the corresponding DRIFTS integral of the $Rh(NO)^-$ species.

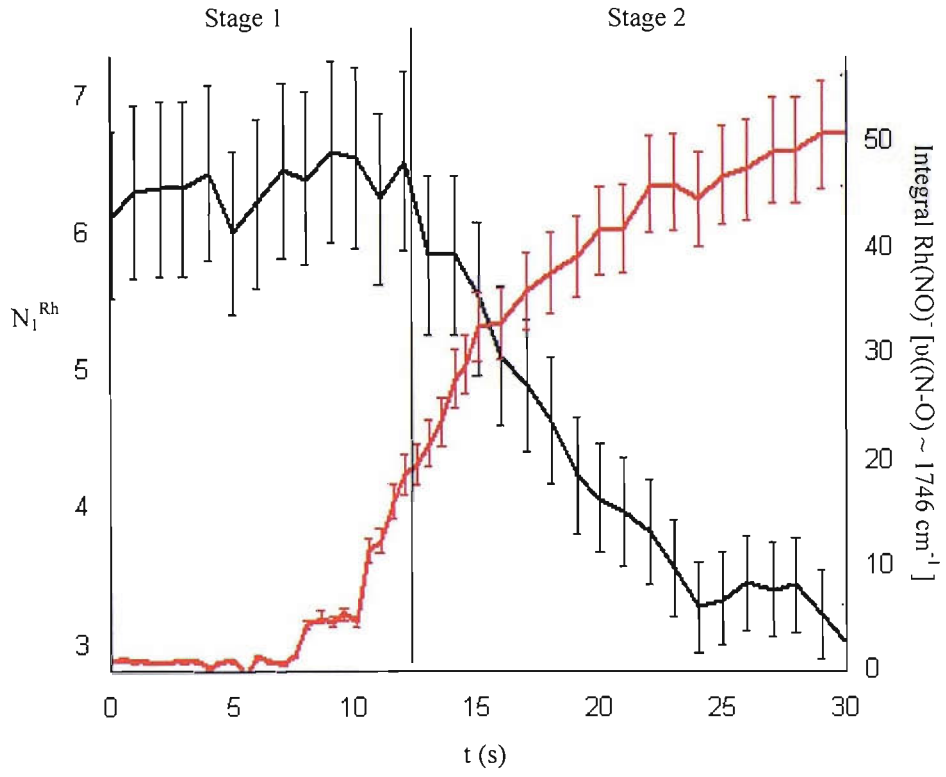

Figure 6.7: Rh-Rh coordination number (black line) and integral of the (N-O) stretch (v ~ 1746 cm^{-1}) of the Rh-NO^- ligand (red line) as a function of time during time resolved 5%NO/He exposure to 5wt% RhCl at 423 K. EDE and DRIFTS data from every second of the time resolved experiment is plotted. Errors are derived from the corresponding standard deviations.

The EDE data shown in figures 6.6 and 6.7 confirms the 5 wt% Rh system to exhibit similar characteristics at 423 K when compared to the room temperature case. The time resolved profile can still be viewed as occurring over two stages when considering the EDE data alone, the initial stage indicating an 'induction' period of ca. 12 seconds (as seen at room temperature) where the N_1^{Rh} value remains static. The second stage therefore also occurs over the same time period as at room temperature; however the disruption of the Rh component is more extensive with the N_1^{Rh} value falling from ca. 6 to ca. 3 at t = 30 seconds. There is no further significant oxidation seen within the timescale of the whole experiment: at t = 60 seconds the N_1^{Rh} indexes a value of 2.84 (±0.3) (data not shown for clarity reasons).

The DRIFTS results reveal the $Rh(NO)^-$ species to also evolve over two stages (not shown on figure), which is closely correlated to the stages charted by EXAFS. The induction period lasts until ca. 10 seconds, after which the nitrosyl species is seen to evolve and stabilise upon the Rh surface.

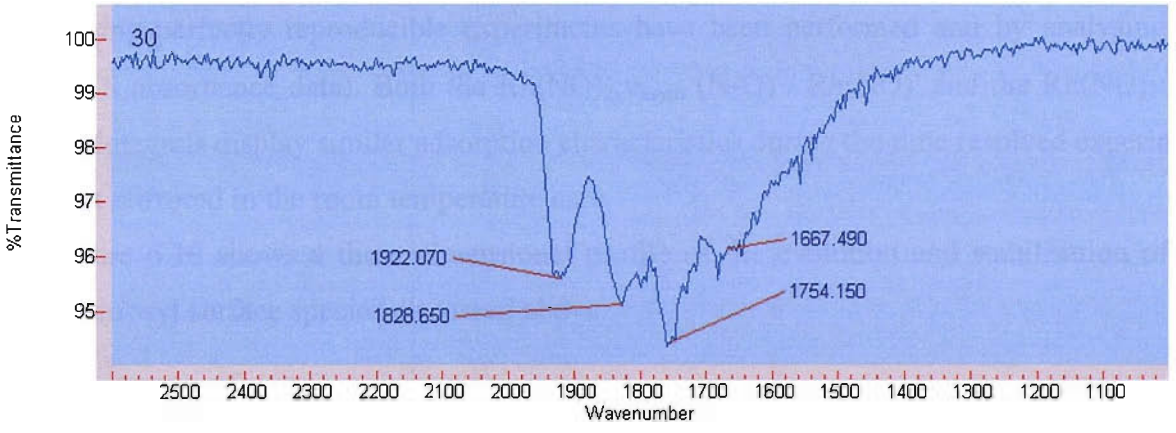

Figure 6.8: DRIFTS spectra taken from 5 wt% RhCl after 30 s exposure to 5% NO/He at 423 K. The acquisition time for the spectrum was 64 ms.

The DRIFTS spectrum in figure 6.8 taken from the time resolved experiment at 423 K shows the range of nitrosyl species formed on the Rh surface after ca. 30 seconds of 5% NO/He exposure. Although visually similar to the spectrum obtained at RT, a few notable differences are observable; the peak assigned to the $Rh(NO)^+$ displays a blue shift to 1922 cm^{-1} (from 1905 cm^{-1} at room temperature) and the peak itself is ca. twice as intense as the signal obtained at RT. This is a significant increase in the relative amount of $Rh(NO)^+$

present, even after the consideration of possible errors involved. These errors include experimental variances between each time resolved experiment, for example the sample alignment/height may not be identical in each case, leading to possible errors. Other sources of error would include the assignment of peak positions. The IR bands centred on 1828 cm^{-1} and 1754 cm^{-1} assigned to the $Rh(NO)_2$ species display a blue shift (from 1821 cm^{-1} and 1746 cm^{-1} at room temperature), with the 'high wavenumber' $Rh(NO)^-$ species making a contribution to the intense peak at 1754 cm^{-1}. The broad peak centred on 1667 cm^{-1} can be assigned to the 'species below 1700 cm^{-1}' as outlined in the previous section (6.3.1).

Figures 6.9 and 6.10 reveal the temporal characteristics of the 5 wt% catalyst as it is exposed to a flow of 5% NO/He at 423 K. The DRIFTS integrals shown in figure 6.9 highlight the rate of evolution for each of the nitrosyl species, as well as the relative amounts that are formed during the exposure. The species below 1700 cm^{-1} and the $Rh(NO)^+$ species are seen to rapidly evolve and stabilise on the Rh surface. As initially indicated by figure 6.8, there is ca. 20% more $Rh(NO)^+$ species being formed at 423 K than at room temperature (assuming perfectly reproducible experiments have been performed and by analysing the DRIFTS absorbance data). Both the $Rh(NO)_2$:ν_{asym} (N-O) / $Rh(NO)^-$ and the $Rh(NO)_2$:ν_{sym} (N-O) integrals display similar adsorption characteristics during the time resolved experiment, a result mirrored in the room temperature case.

Figure 6.10 shows a three dimensional profile of the evolution and stabilisation of the main nitrosyl surface species discussed above.

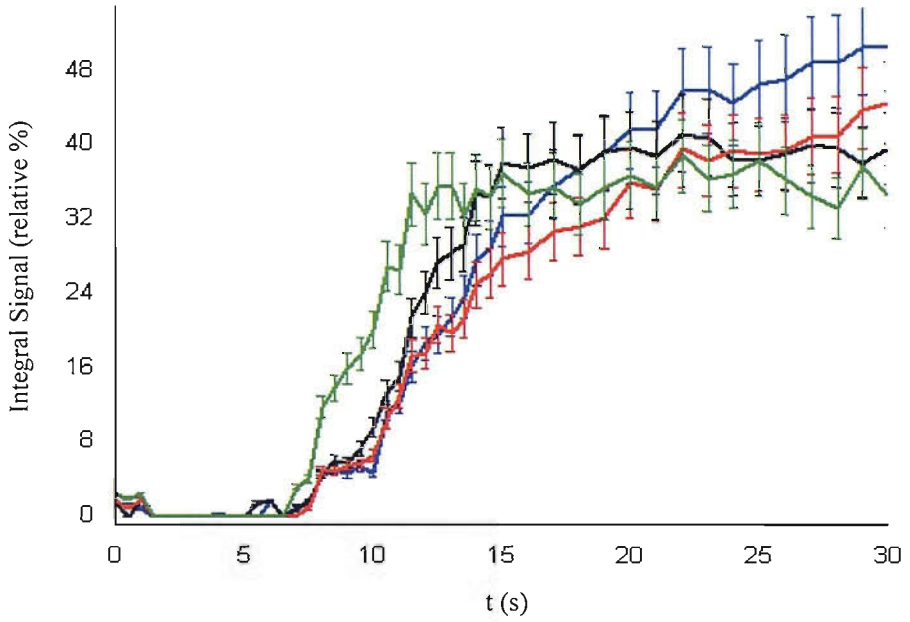

Figure 5.9: Integrals charting the evolution of IR active species on 5 wt% RhCl on exposure to 5% NO/He at 423 K; 'species below 1700 cm^{-1}' (green line), $Rh(NO)_2$ ν_{asym} (N-O) / $Rh(NO)^-$ (blue line), $Rh(NO)_2$ ν_{sym} (N-O) (red line) and $Rh(NO)^+$ (black line). Errors are derived from the corresponding standard deviations.

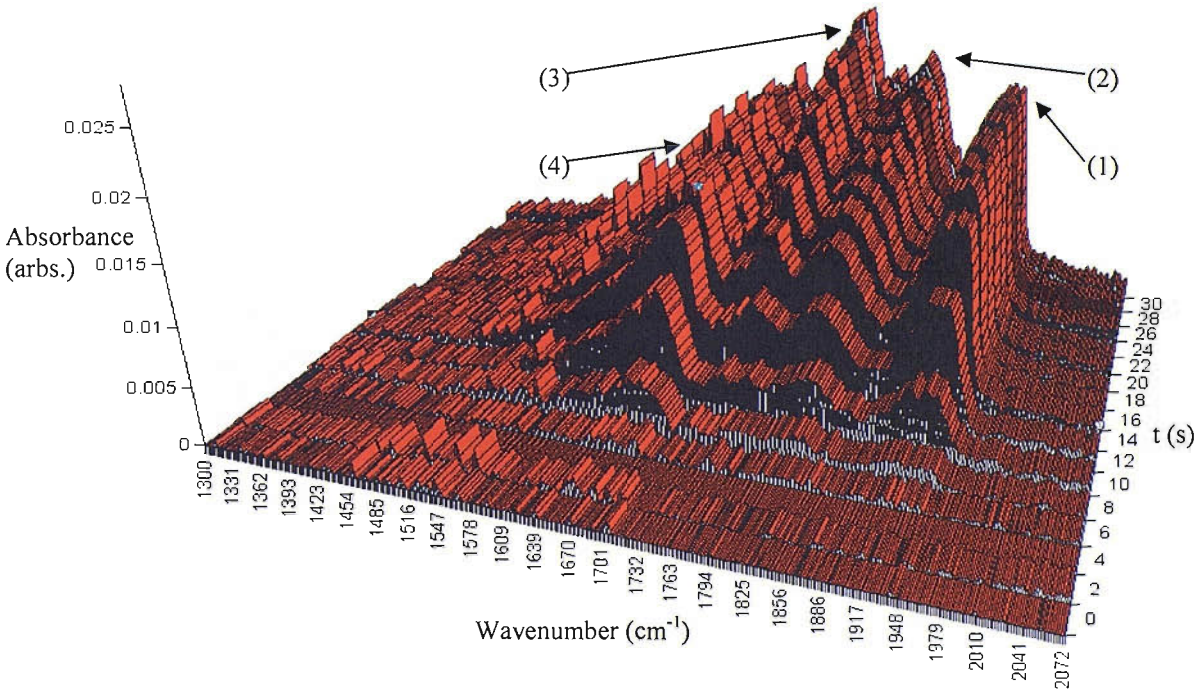

Figure 6.10: DRIFTS spectra (2070-1300 cm^{-1}; 4 cm^{-1} resolution) as a function of time after exposure to 5% NO/He at 423 K showing the; (1) $Rh(NO)^+$; (2) $Rh(NO)_2$ [ν_{sym} (N-O)]; (3) $Rh(NO)^-$/ $Rh(NO)_2$ [ν_{asym} (N-O)] and (4) 'species below 1700 cm^{-1}' peaks for 5 wt% RhCl. For clarity one spectrum every 2 s is shown.

6.3.3 NO exposure at 573 K

Figure 6.11 shows k^3 weighted Rh K-Edge EDE spectra for 5 wt% RhCl before and after exposure to 5% NO/He at 573 K, along with the corresponding Fourier transforms. The structural and statistical information derived from these spectra are given in table 6.3.

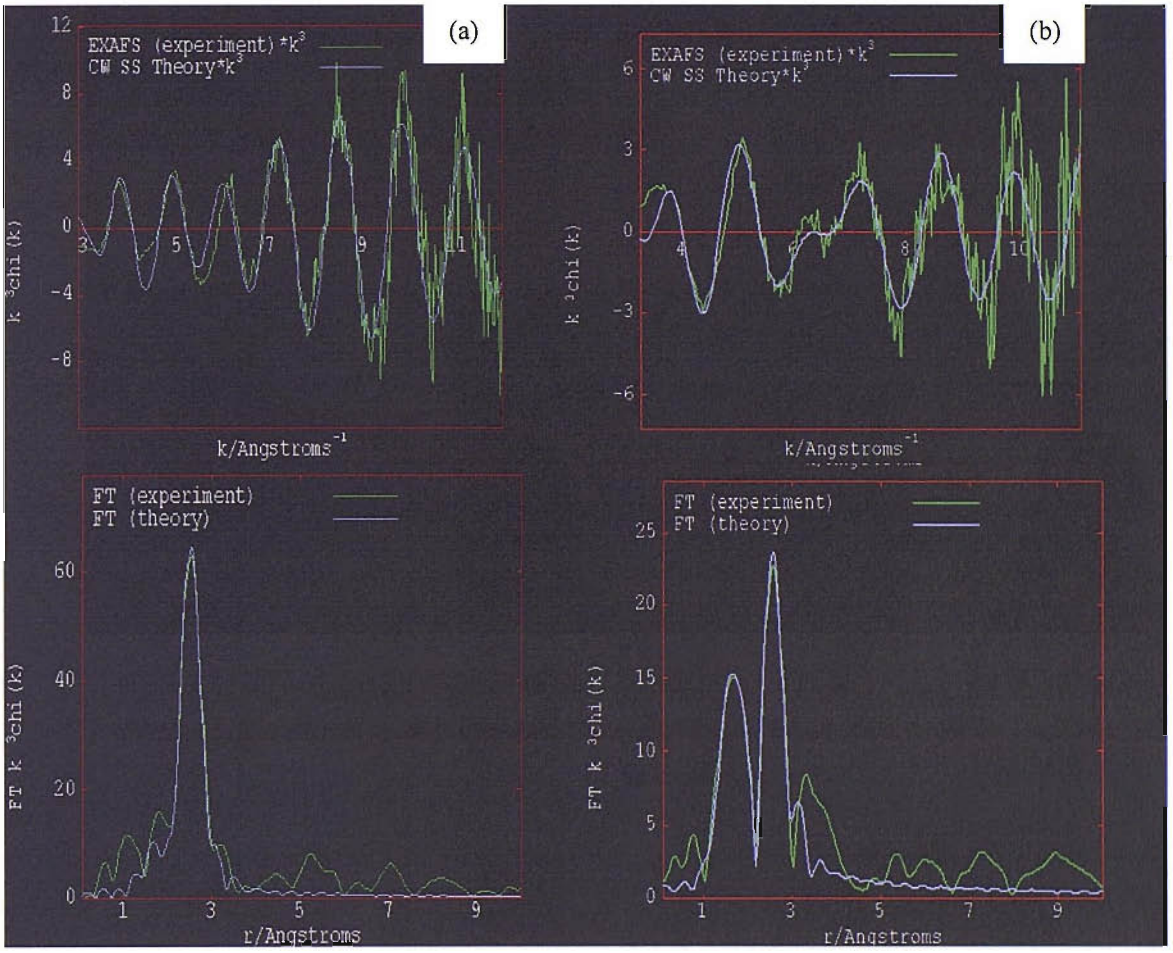

Figure 6.11: k^3 weighted Rh K-Edge EDE data derived from 5 wt% RhCl under; (a) 5% H_2/He and (b) 5% NO/He at 573 K after 30 seconds exposure. The corresponding Fourier transforms are given underneath each spectrum.

Sample/Conditions	Scatterer (s)	CN	r/Å	$2\sigma^2/Å^2$
(a) 5 wt% RhCl in 5% H_2/He at 573 K	Rh	5.9 (±0.5)	2.64 (±0.02)	0.017 (±0.001)
(b) 5 wt% RhCl in 5% NO/He at 573 K after 30 seconds exposure	Rh	2.3 (±0.3)	2.58 (±0.02)	0.017 (±0.001)
	O/N	2.2 (±0.2)	2.03 (±0.01)	0.006 (±0.002)

Table 6.3: Structural and statistical data derived from the analysis of spectra given in figure 6.11. Other parameters; (a) Ef = -0.33 eV, R = 43%, k = 3-12$Å^{-1}$, (b) Ef = -7.00 eV, R = 54%, k = 3-11 $Å^{-1}$.

Figure 6.12 charts the Rh-Rh coordination data during the time resolved exposure of 5 wt% RhCl to 5% NO/He at 573 K, and is plotted alongside the corresponding DRIFTS integral of the $Rh(NO)^+$ species.

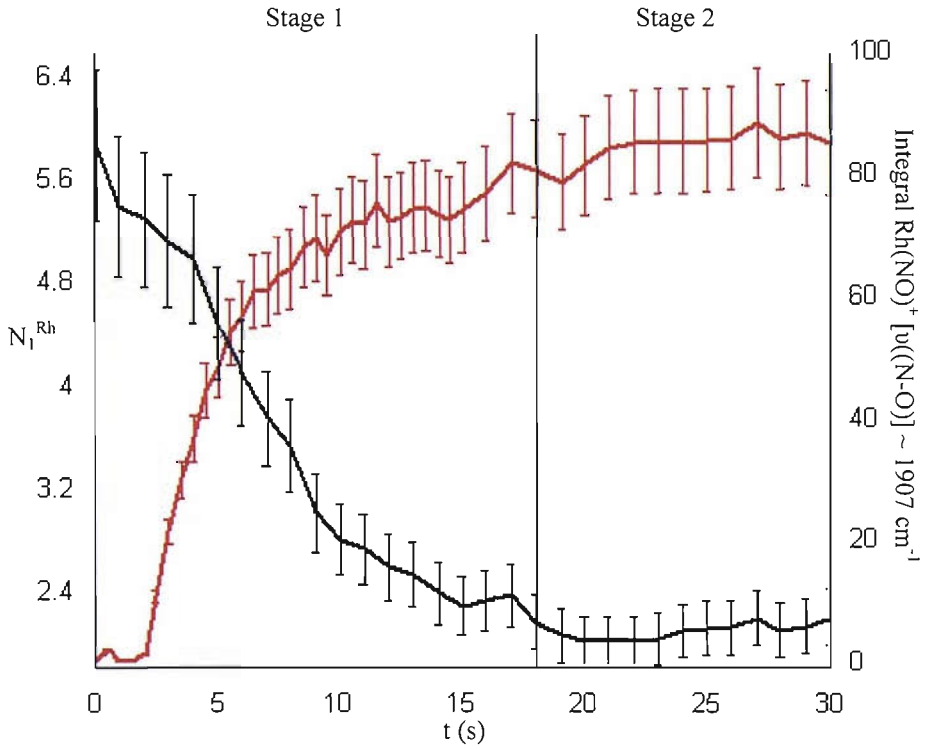

Figure 6.12: Rh-Rh coordination number (black line) and integral of the (N-O) stretch of the $Rh-NO^+$ ligand (v ~ 1907 cm^{-1}) (red line) as a function of time during time resolved 5%NO/He exposure to 5wt% RhCl at 573 K. EDE and DRIFTS data from (at least) every second of the time resolved experiment is plotted. Errors are derived from the corresponding standard deviations.

The EXAFS data shown in figures 6.11 and 6.12 shows the 5 wt% Rh system to exhibit a significantly different structural response to 5% NO/He at 573 K when compared to the analogous experiments performed at lower temperatures. The static EXAFS data in figure 6.11 shows evidence of extensive oxidation of the Rh to have taken place after 30 seconds of $NO_{(g)}$ exposure, with the N_1^{Rh} reporting a value of 2.3. The structural profile depicted by the EDE data reflects this result in figure 6.12. The disruptive adsorption process can again be followed over two distinct stages; however the 'induction' period is reduced to ca. 2 seconds and can be attributed wholly to the dead time of the system. Therefore the onset of the oxidation process appears to be instantaneous to the introduction of $NO_{(g)}$ into the gas stream. After this initial, relatively rapid oxidation of the Rh component (where N_1^{Rh} falls from an initial value of ca. 6 to ca. 2.3 at 18 seconds), no further significant oxidation is observed. However, at t = 60 seconds the N_1^{Rh} indexes a value of 2.12 (±0.3), a value that indicates the Rh component to now exist almost exclusively as an oxide, i.e. (essentially) as Rh_2O_3.

The corresponding DRIFTS absorbance integral charted alongside the EXAFS data shows the evolution of the $Rh(NO)^+$ species to correlate well with the structural changes synchronously obtained by EXAFS. With no apparent 'induction' period seen at lower temperatures, the $Rh(NO)^+$ species rapidly forms and stabilises on the Rh surface: the data directly mirrors the two stage oxidation process occurring over the Rh.

The DRIFTS spectrum and the integral data given in figures 6.13 and 6.14 respectively show that at 573 K the linear $Rh(NO)^+$ species (ν (N-O) = 1907 cm^{-1}) is the only appreciable IR active species present on the catalyst. The weak, broad band centred on 1728 cm^{-1} could be assigned to the high wavenumber $Rh(NO)^-$ species, however the quality of the signal is not sufficient to permit any further analysis. This is also the case for the broad band centred on 1646 cm^{-1}, previously assigned 'species under 1700 cm^{-1}'. Another notable result is the apparent absence of any $Rh(NO)_2$ species, observed at lower temperatures.

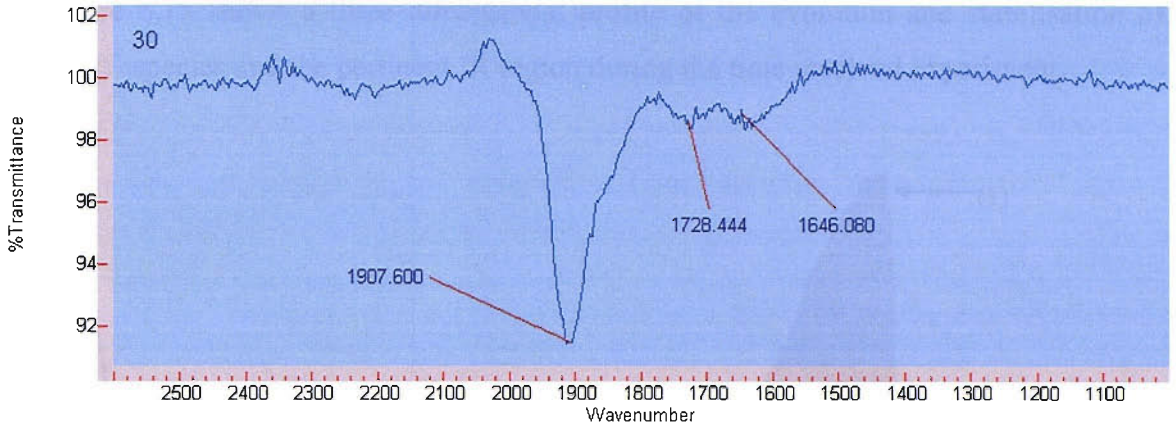

Figure 6.13: DRIFTS spectra taken from 5 wt% RhCl after 30s exposure to 5% NO/He at 573 K. The acquisition time for the spectrum was 64 ms.

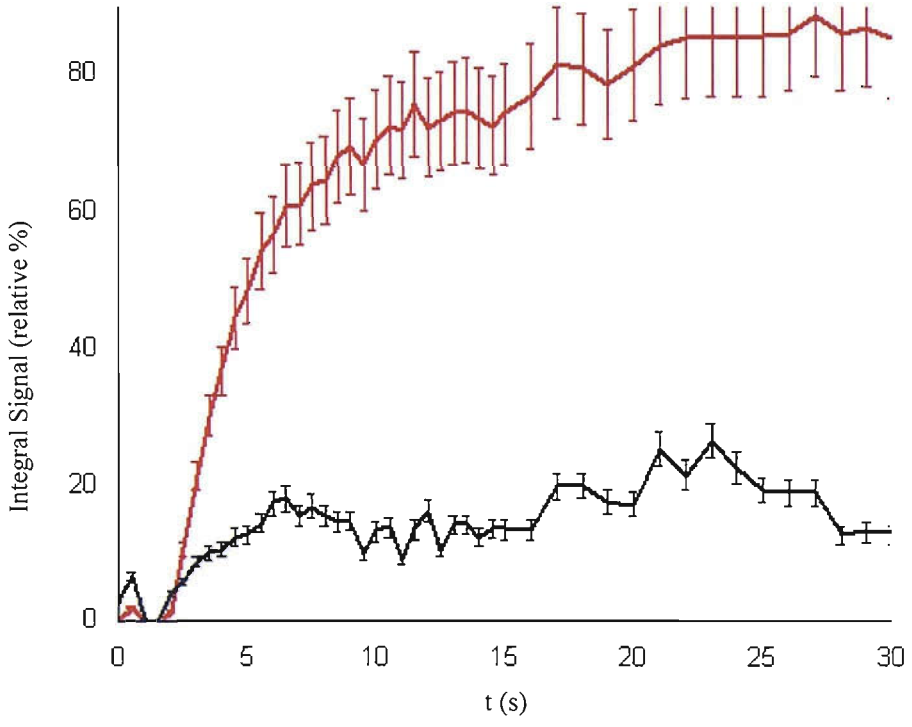

Figure 6.14: Integrals (from absorbance DRIFTS data) charting the evolution of IR active species on 5 wt% RhCl on exposure to 5% NO/He at 573 K; $Rh(NO)^+$ (red line) and $Rh(NO)^-$ (black line-shown only for comparative reasons). Errors are derived from the corresponding standard deviations.

Figure 6.15 shows a three dimensional profile of the evolution and stabilisation of the $Rh(NO)^+$ species and the pertinent IR region during the time resolved experiment.

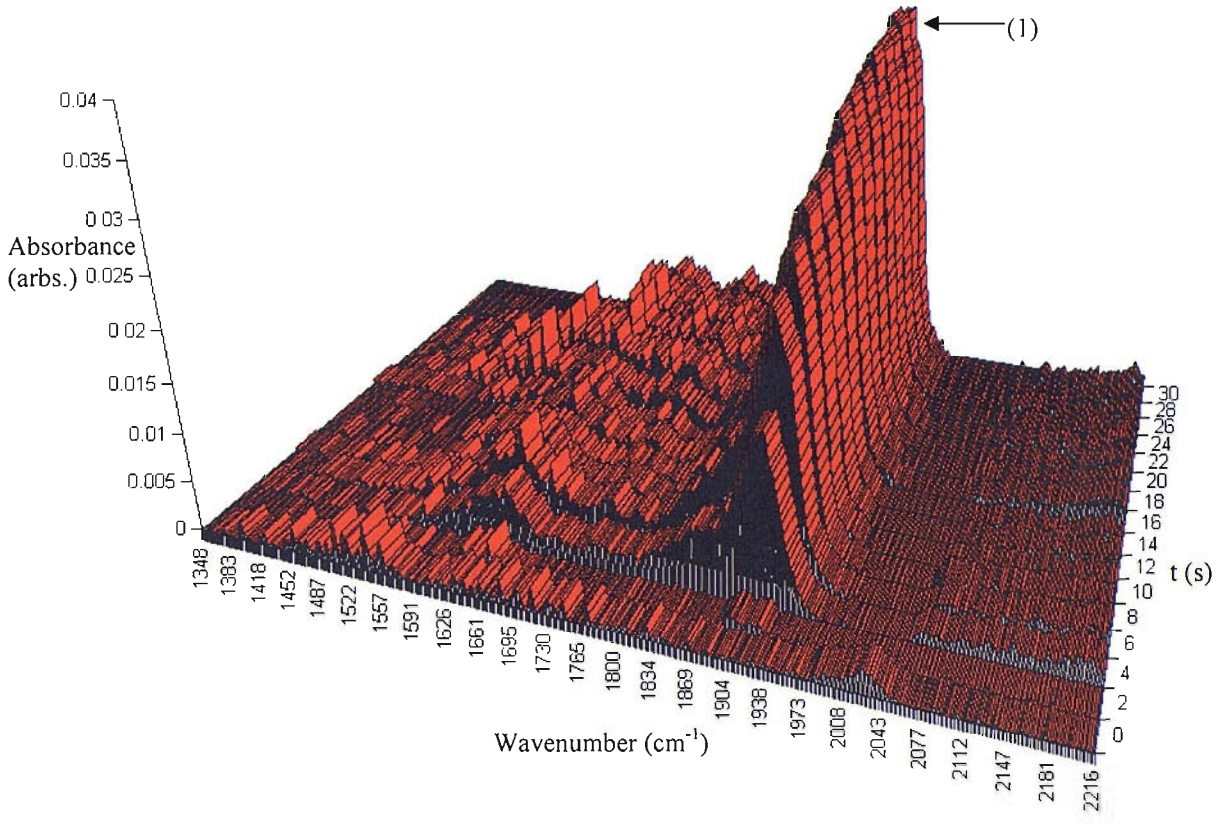

Figure 6.15: DRIFTS spectra (2216-1300cm^{-1}; 4 cm^{-1} resolution) as a function of time after exposure to 5%NO/He at 573 K showing the (1) $Rh(NO)^+$ peak for 5 wt% RhCl. For clarity one spectrum every 2 s is shown.

The coordination data given in figure 6.16 directly compares the structural response of the 5 wt% RhCl system to 5% NO/He at all of the temperatures investigated. It is clear from the data that increasing the temperature employed significantly alters the structural behaviour of the catalyst. Firstly, the effect of the initial particle size (i.e. at t = 60ms) decreasing with increasing temperature can be observed here. The N_1^{Rh} value falls from a value of ca. 7 at RT to just below ca. 6 by 573 K. The observed structural changes are significant even after considering errors associated with the data analysis (the use of DW factors for example), and other factors such as anharmonic effects that could give rise to changes in the coordination

number.[18,19] However, this phenomenon is dealt with elsewhere[20] and does not form part of the discussion here as the focus is on the structural-reactivity behaviour of these catalysts during the time resolved experiments. The figure also clearly shows that the employment of higher temperatures facilitates the disruption of the nanoparticles; both the extent and rate of oxidation are seen to markedly increase with increasing temperature.

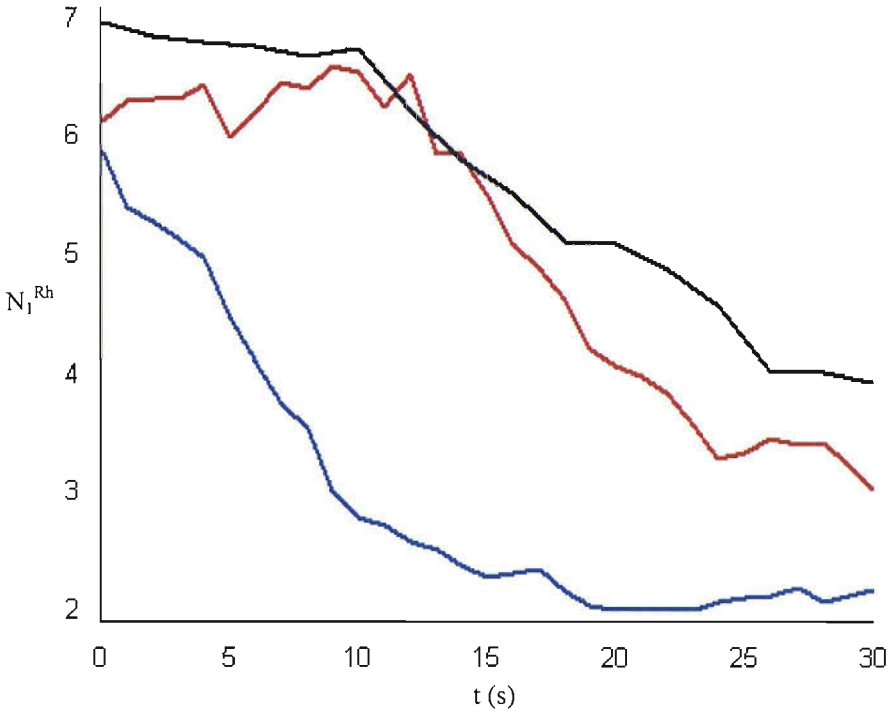

Figure 6.16: Rh-Rh coordination number as a function of time during the time resolved 5% NO/He exposure to 5 wt% RhCl at; room temperature (black line), 423 K (red line) and 573 K (blue line). Data from at least every second of the time resolved experiments are plotted.

6.4 Synchronously obtained mass spectrometric results

Figures 6.17 and 6.18 display the mass spectrometric results obtained during the time resolved experiments. The overall turnover and, more importantly, selectivity of the reactive processes occurring over the Rh catalyst is seen to be a significant function of temperature. Indeed no significant reactive turnover or gas production is observed until 573 K.

Figure 6.17 profiles the mass spectrometric response of $NO_{(g)}$ during the time resolved experiments. The approximate levels of $NO_{(g)}$ uptake may be calculated from this data, and

conveyed in terms of NO/Rh atoms initially present on the catalyst. Results from the mass spectrometer indicate that no significant gas phase product is formed at RT or 423 K, with the respective net $NO_{(g)}$ uptake being ca. 0.47 (±0.15) NO/Rh atom at RT and ca. 0.68 (±0.18) NO/Rh atom at 423 K. As the temperature is increased to 573 K the reactive turnover of $NO_{(g)}$ is observed: the net $NO_{(g)}$ uptake is ca. 1.42 (±0.3) NO/Rh atom with ca. 0.85 NO/Rh atom being converted into a gas phase product.

Figure 6.18 highlights the system to be highly selective towards the production of $N_{2(g)}$ at 573 K (maximal value ca. 70%), with significantly less $N_2O_{(g)}$ being produced (maximal value ca. 10%). The profiles in figures 6.17 and 6.18 reflect the general trend observed in the synchronously obtained EXAFS/DRIFTS data, i.e. the reactive processes occurring over the catalyst can be followed over distinct stages. The mass spectral results indicate an initial 'induction' period of ca. 5 seconds preceding a second stage where $NO_{(g)}$ is rapidly adsorbed by the catalyst system (to produce mainly N_2 at 573 K). A final stage from ca. 12 seconds reports the gradual decrease of the amount of $NO_{(g)}$ adsorbed by the system (and the subsequent decrease the production of gaseous species at 573 K). This is most likely due to the saturation of the Rh surface by various nitrosyls and adsorbed oxygen, making the system inactive towards any further $NO_{(g)}$ uptake.

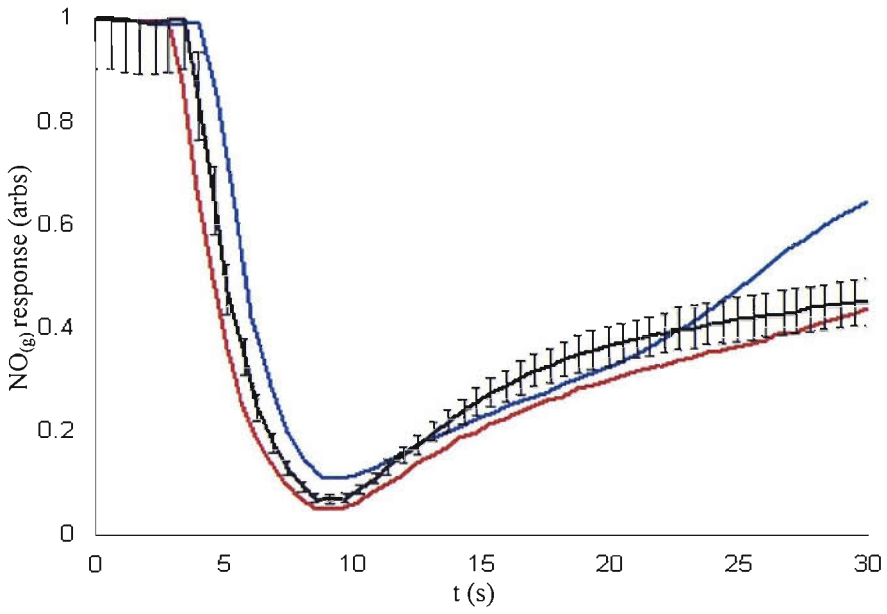

Figure 6.17: Response of $NO_{(g)}$ during the time resolved exposure to 5% NO/He for the 5 wt% RhCl system at; room temperature (blue line), 423 K (black line) and 573 K (red line). Error bars, derived from standard deviation, are only shown for one data set for clarity reasons.

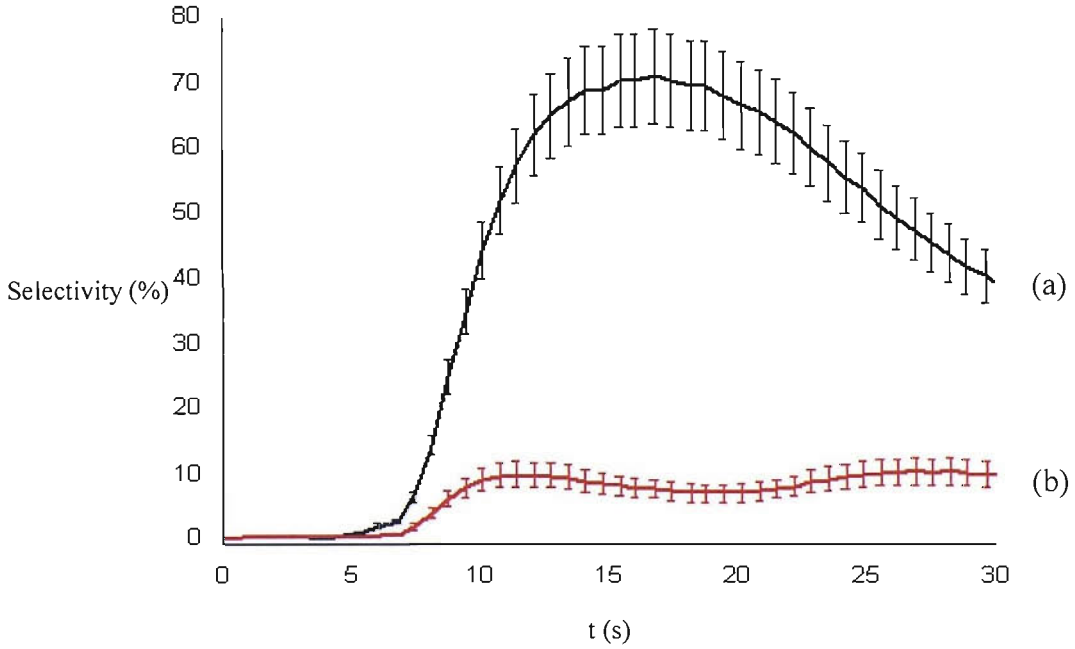

Figure 6.18: Catalyst selectivity for the 5 wt% RhCl system during the time resolved exposure to 5% NO/He at 573 K showing; (a) N_2 and (b) N_2O selectivity. Error bars are derived from the corresponding standard deviations.

6.5 Discussion

The results from the temperature controlled, time resolved and synchronous EXAFS/DRIFTS/MS experiments reveal the Rh nanoparticles under investigation to display a diverse response to the adsorption of $NO_{(g)}$. Indeed the variation of temperature alone induces significant changes in the catalyst composition, in summary the particles become increasingly dispersed at higher temperatures. These results are not formally considered here, but do correlate well to the discussion in chapter 5 of particle sintering at higher temperatures and underline the non-static nature of the system under investigation. Although the effect of temperature on the initial catalyst structure is acknowledged, any further discussion will regard the pre-reduced catalysts to be essentially identical (i.e. existing as wholly metallic, fcc particles) as the focus of this chapter lies with the structural-reactivity response of Rh to $NO_{(g)}$.

In order to analyse the results effectively, the experiments performed at room temperature and 423 K will be designated as 'low temperature' experiments. This grouping is necessary as the catalyst displays strikingly similar behaviour at these two temperatures, and significantly altered behaviour at 573 K.

It is clear from the Rh-Rh coordination data obtained by EXAFS that the adsorption of $NO_{(g)}$ leads to the rapid disruption of the nanoparticles at all the temperatures investigated. The rate and extent of this oxidation of Rh is governed by the temperature at which the exposure is performed.

Similar experiments[4] using the microreactor based EDE/MS apparatus (see chapter 2.5.7) have shown Rh to be rapidly oxidised in the presence of $NO_{(g)}$. The study showed a pre-reduced 4 wt% $RhCl/Al_2O_3$ system to be fully oxidised within 5 seconds of exposure to 5% NO/He at 313 K. The rapid, highly exothermic dissociative chemisorption of $NO_{(g)}$ was found to be the initial step for the phase changes. Although the study did not have the capacity for rapid acquisition of EXAFS spectra, it does reflect the corrosive nature of $NO_{(g)}$ interaction with Rh. However, despite many experimental parameters remaining essentially constant (e.g. gas flow rates, gas exposure times, catalyst charge) the timescales over which Rh oxidation occurs varies significantly between the microreactor based and the current, DRIFTS cell based experimental platform. Even at 573 K the complete oxidation process is

charted over timescales 3 times longer than those in the mentioned study. This serves as an effective example in highlighting that direct comparisons between the EDE/MS and EDE/DRIFTS/MS experiments should be made with caution.

6.5.1 Low temperature NO experiments

Data derived from each of the time resolved techniques at low temperatures reveals the adsorption process to occur over two distinct stages. The initial period, denoted the induction time, the catalyst structure remains unaltered with no obvious response to the introduction of $NO_{(g)}$. Although the 'dead time' of the gas (i.e. the transport time of the gas to impinge on the catalyst at the start of the experiment) of ca. 2 seconds does contribute to this period, it will not be regarded as having a significant bearing upon the results that are recorded on timescales of up to 60 seconds. As $NO_{(g)}$ adsorption is well known to be predominantly molecular within these temperature regimes,[5] the initial adsorption of molecular $NO_{(g)}$ onto Rh defect sites would be the most likely cause of the induction time. After this stage the rapid oxidation of the Rh nanoparticles ensues, a strong indication that $NO_{(g)}$ dissociation is now occurring. These changes are reported by the fall in N_1^{Rh} value by EXAFS, a significant uptake of NO by MS and the evolution of various nitrosyl surface species by DRIFTS. Although no significant reactive NO turnover is observed by MS, the EXAFS/DRIFTS follow an ever changing process until stabilisation occurs where no further changes to the system occur within the time frame of these experiments (i.e. no further particle disruption reported by EXAFS and the stabilisation of the surface nitrosyl species).

The results that are observed in this study are in line with previous experiments performed on similar Rh systems;[1,5] however they are generally not presented in a truly synchronous and time resolved manner as demonstrated here. The unique capacity of these experiments therefore reveals information about the adsorption and subsequent disruption processes that could only be surmised by using the techniques separately.

A simple first inspection reveals each data set to be intrinsically linked, i.e. the uptake of $NO_{(g)}$ correlates to the formation of surface nitrosyls and subsequent disruption of the Rh nanoparticles. However, the high quality and density of available data enables a much more detailed analysis, and hence conclusions, to be drawn about the adsorption of $NO_{(g)}$ upon Rh.

This includes the elucidation of which nitrosyl species are directly linked to the structural changes observed.

A thorough examination of the individual EXAFS/DRIFTS data sets reveals that the species below 1700 cm^{-1} do not bear a significant influence on the structural changes occurring to the Rh. The primary reason for this is that the species form very rapidly upon the surface without affecting any considerable structural changes in the Rh. That the nitrates/nitrites absorbed upon the alumina surface would have no effect on the metal component seems entirely reasonable. Any subsequent NO spillover from this species influencing the behaviour of Rh, although plausible, cannot be quantified by the current data and thus will not be considered further. The postulated 'low wavenumber' $Rh(NO)^-$ species also found in this wavenumber region does not bear any detectable relation to the changes occurring. Since there is no evidence of any metallic Rh forming throughout the oxidative process, the influence of NO bound to metallic Rh sites can also be thought of as being minimal.

The $Rh(NO)^+$ species is most likely a spectator species at low temperatures due to several reasons. The slow formation and relatively insignificant amounts of the species formed at room temperature indicate no direct association between this species and the observed phase changes. This correlates well with existing studies that conclude the formation of $Rh(NO)^+$ requires the presence of oxidised Rh sites; which would in turn suggest that the species is associated with occupying the oxidised sites rather than being involved in the creation of them (see below). The postulation could still be applied at 423 K despite an apparent linear relationship between the formation of $Rh(NO)^+$ and the Rh oxidation; the higher temperature facilitates a faster and more extensive production of oxidised Rh sites. This could explain why a significant amount (ca. 20% more) of the species is observed at 423 K when compared to the room temperature case. As stated previously, for such comparisons to be made the discussion above assumes the experiments to be perfectly reproducible.

The $Rh(NO)_2$ species cannot wholly be discounted as making a contribution to the Rh oxidation, however it is unlikely it does in a significant manner when several key points are considered. Firstly, the relatively slow formation of the species (as indicated by the evolution of the symmetric stretch of $Rh(NO)_2$) bears minimal temporal correlation to the structural changes reported by EXAFS. In fact the $Rh(NO)_2$ is the last species seen to evolve and

stabilise on the Rh surface. Also, on the basis of numerous studies of NO interaction with Rh, the $Rh(NO)_2$ species would be continually decomposing to the $Rh(NO)^+$ species or to N_2O.[9,12,13,14] The following section explains the role of the transient $Rh(NO)_2$ species in the formation of the linear nitrosyl. However, the capacity for the $Rh(NO)_2$ species to oxidise the Rh within this temperature regime cannot be wholly disregarded as the net effect of its decomposition would be to add $O_{(ads)}$ to the system.

The evidence supplied by the complimentary experimental data therefore points to a primary species responsible for the majority of Rh oxidation, the bent $Rh(NO)^-$ nitrosyl at 1745 cm^{-1}. The formation of this species correlates well to the corresponding structural changes reported by EXAFS and NO uptake indicated by MS measurements (hence why the EXAFS data in figures 6.2 and 6.7 are plotted alongside their 'archetypal' $Rh(NO)^-$ integral from DRIFTS). The excellent temporal correlation seen here, combined with previous observations indicating the significant role $Rh(NO)^-$ plays in Rh oxidation,[9,10,13] bolsters this argument.

It should be noted here that the elucidations made above are made largely by correlating the temporal characteristics of the various species during the experiment. As such, they should only be considered as the most likely scenario occurring; the influence of any nitrosyl species making a contribution to the overall oxidative process of Rh cannot be entirely disregarded.

The adsorption and subsequent disruptive processes outlined above continue until stabilisation in the second stage indicates no further changes occurring to the Rh. This suggests some form of coverage limit is reached by this stage. This is most likely due to the saturation of the surface with nitrosyl species and other adsorbed species such as oxygen and nitrogen, inhibiting any further changes to the system. It is possible that longer timescales would induce further changes, for example further oxidation of the particles through oxygen diffusion or even the gaseous production of N_2/N_2O; further, more detailed experimentation employing longer timescales would be needed to test for this.

In summary, the time resolved experiments performed at low temperatures reveal a bent $Rh(NO)^-$ species at 1745 cm^{-1} to be largely responsible for the phase changes that occur when Rh is exposed to 5% NO/He. The predominantly molecular adsorption of $NO_{(g)}$ on Rh results in an induction period at the initial stage of the experiment. It appears that a certain coverage

limit creates the appropriate conditions in which rapid oxidation of Rh ensues, and with it the evolution of the $Rh(NO)^-$ entity. A self propagating oxidation process is observed until a limit is reached where no further oxidation is reported; most likely due to saturation effects.

6.5.2 High temperature NO experiment

The Rh system displays a remarkably different response to 5% NO/He at 573 K when compared to the analogous experiments performed at low temperature. Firstly, the initial inspection of the EXAFS data shows that the employment of higher temperature simply acts to aid the oxidative process seen at lower temperatures. This is seen quantitatively by the absence of any significant induction period at the beginning of the experiment, and in the comparatively rapid and extensive oxidation of the Rh metal. In fact the local Rh-Rh coordination value indexes a value associated with bulk Rh oxide (Rh_2O_3) by the end of the experiment. These observations alone are consistent with previous work involving $NO_{(g)}$ adsorption at high temperatures;[21] where rapid, dissociative adsorption of $NO_{(g)}$ dominates the overall behaviour of Rh.

The unique capacity to acquire DRIFTS and MS data alongside EXAFS allows for a more detailed analysis into the observed structural changes. From the outset these data reveal an entirely different adsorption process to be in effect at this temperature; in short the MS data reports significant reactive NO turnover and DRIFTS shows $Rh(NO)^+$ to be the only appreciable species to exist on the Rh surface.

That $Rh(NO)^+$ is the only stable species is an unexpected result based upon data derived at lower temperatures. The species was deemed to be purely a spectator to the oxidative processes, only forming at oxidised Rh sites created by other nitrosyls (namely $Rh(NO)^-$ and $Rh(NO)_2$). As the $Rh(NO)^+$ species is quite clearly related to the phase changes of Rh, another model must be applied for the chemistry occurring within these temperature regimes.

The results of NO adsorption experiments on Rh by Liang et al. proposed the following two reactions to occur:[13]

$Rh(NO)_2 \rightarrow Rh(NO)^+ + NO_{(g)}$ Equation 1

Equation 1 was proposed to occur in tandem with a unimolecular decomposition pathway, subsequently yielding N_2O:

$Rh(NO)_2 \rightarrow Rh(O) + N_2O_{(g)}$ Equation 2

It is clear from the data that increasing the temperature increases the kinetic domination of the Rh oxidation that is observed. This would result in an increased preference for the net electron donating and thermally stable $Rh(NO)^+$ species to form directly on the oxidised Rh sites once they are formed. However, it is equally likely that the species could form via a transient formation of $Rh(NO)_2$ (as in equation 1, see below).

This highly transient form of $Rh(NO)_2$ is therefore a likely candidate for the structural changes observed. The precursor entity could form upon the Rh and decompose instantly to yield the $Rh(NO)^+$ reported by DRIFTS. It would also act to add more $O_{(ads)}$ to the system, as would be required for the continual oxidation of the metal particles. As such this is the most likely route to the changes that are detected within these conditions, which on simple inspection wrongly denotes the $Rh(NO)^+$ to be the active species.

The mass spectral data reinforces the model proposed above. A significant reactive turnover of NO is observed at 573 K. The data reports that the system is highly selective towards $N_{2(g)}$ production initially. Observations in the past have shown that metallic Rh is associated with the production of $N_{2(g)}$ in the catalytic reduction of $NO_{(g)}$ by $H_{2(g)}$.[22] However, the selectivity is seen to decrease over time as the metal is oxidised as a result of the breakdown of the proposed transient $Rh(NO)_2$ species. Again this is consistent with the numerous existing work detailed in this chapter. It would be reasonable to suggest that N_2 formation would eventually cease and an increase in N_2O production (which is associated with oxidised Rh sites) would be evident if longer timescales were used. Indeed the extensively oxidised, 'Rh_2O_3 like' catalyst structure combined with the decreasing amounts of $N_{2(g)}$ production at the end of the experiment supports this notion. As no actual catalytic chemistry is occurring in these experiments, the saturation of the Rh surface with nitrosyl

species and other adsorbed species would eventually render the system unreactive in terms of N_2/N_2O production.

6.6 Conclusion

The application of the EXAFS/DRIFTS/MS experiment has yielded considerable information on the structural response of Rh to $NO_{(g)}$ adsorption. The time resolved, synchronous experiments were performed over a temperature range from 298-573 K. The increased dispersion of the Rh nanoparticles at increased temperatures (prior to any $NO_{(g)}$ exposure) hinted at the dynamic nature of the system under investigation. However, as these effects are discussed elsewhere, the focus centred upon understanding the complex 'whole' of the processes associated with the adsorption of $NO_{(g)}$ with Rh.

A rapid and extensive oxidation of the pre-reduced, metallic Rh nanoparticles was observed upon exposure to 5% NO/He at all temperatures. The use of higher temperatures had a facilitative effect on this response afforded by the EXAFS data, and by 573 K no induction period was evident (an event that limited the oxidative processes at lower temperatures).

The adsorption of $NO_{(g)}$ at low temperatures was deemed to be molecular, and this was found to be a major contributor to the induction period at the start of the experiments. Despite a range of nitrosyl species being formed at low temperature, the $Rh(NO)^-$ species was found to be responsible for the majority of the oxidation, with $Rh(NO)_2$ also being another contributor.

Markedly different behaviour was observed at 573 K, notably through the significant reactive turnover of $NO_{(g)}$ during the experiment. DRIFTS indicated the linear $Rh(NO)^+$ species to be the only stable species evident at this temperature. However, based on previous findings from this and other studies it was surmised to be a spectator species, a by-product from the decomposition of a highly transient $Rh(NO)_2$ species. This geminal dinitrosyl species contributed to the oxidation of the Rh component; as did the rapid, dissociative adsorption of $NO_{(g)}$. This had the overall effect of lowering the selectivity of the system towards $N_{2(g)}$ production. The continual oxidation and effective poisoning of the system with nitrosyl/adsorbed species would eventually render the Rh system inactive.

The high quality and density of data (with a nominal time resolution of ca. 17 Hz) available from these experiments has shown the adsorption and subsequent oxidation process in unprecedented detail. The information extracted from the synchronously obtained data allows for models to be postulated and evidenced using several techniques, essential in understanding these complex supported systems. From a wider viewpoint, studies such as these serve to highlight the challenges that face the design of catalyst systems: in this case exposure to NO alone effectively poisons the catalyst within a few tens of seconds. They also underline the importance of fully understanding the underlying processes that occur over these responsive and characteristically diverse systems.

6.7 Reduction characteristics of pre-exposed Rh catalysts to NO: A variable temperature study

6.7.1 Introduction

The focus of this chapter thus far has been on the adsorption characteristics of Rh exposed to a flow of $NO_{(g)}$. The study revealed the pre-reduced, metallic Rh system to be rapidly oxidised across the temperature range; at 573 K a fully oxidised, 'Rh_2O_3 like' structure was observed within 20 seconds of 5% NO/He exposure. The adsorption and oxidation processes resulted in the system becoming increasingly inactive towards NO turnover, due to the saturation of the metal with species such as $O_{(ads)}$. The metallic Rh system is therefore rapidly poisoned by exposure to $NO_{(g)}$. This is taken from the viewpoint of reactions that occur over systems such as the TWC where metallic Rh is the core component in converting $NO_{x\,(g)}$ to $N_{2\,(g)}$.

The continual regeneration of active catalyst sites is one of the key considerations in the design of catalytic systems; indeed it is central to the definition of a catalyst. Although no catalytic chemistry has been probed in this chapter, the aims of this thesis include relating the structural-reactivity behaviour of Rh to real, 'working' catalysts such as the TWC. To this end the regeneration of Rh metal from oxidised systems will be probed using the EXAFS/DRIFTS/MS experiment. Systems pre-exposed to 5% NO/He will be subjected to a flow of $H_{2(g)}$ at varying temperatures to chart their behaviour via the array of techniques available. It will endeavour to reveal the characteristics of how, if at all, the catalyst 'recovers' to its metallic state.

6.7.2 Experimental

The EDE/DRIFTS/MS experimental apparatus was used as outlined in chapter 2.5.8.

In a typical experiment, the 5 wt% RhCl catalyst (ca. 45 mg) was pre-treated by heating under a flow of 5% H_2/95%He to 573 K. The system was then subjected to a flow of 5% O_2/95%He for ca. 5 minutes before switching back to the flow of 5% H_2/95%He and held at

the required temperature. Pre-exposure to 5% NO/95%He at 25 $mlmin^{-1}$ was then performed for the duration of ca. 15 minutes.

After purging under a flow of He, 5% H_2/95%He at 25 $mlmin^{-1}$ was introduced synchronously with the start of the EDE/DRIFTS/MS experiment. EXAFS detection was made via the FReLoN CCD camera with a total acquisition time of ca. 60 ms.

6.7.3 Results and discussion

NB: The experiments were performed at a range of temperatures (298-573 K, every 50 K) for both the 2 wt% and 5 wt% RhCl systems, to match the NO adsorption experiments outlined earlier in this chapter. However, the only analysable data to emerge from these experiments was for the 5wt% RhCl system at 373 K, 473 K and 573 K (EXAFS and DRIFTS data only; the mass spectrometric data was corrupted).

Figure 6.19 shows representative DRIFTS spectra of the IR active species present during the time resolved reduction of Rh at 573 K. As expected, the signal taken at 64 ms shows that the linear $Rh(NO)^+$ at 1909 cm^{-1} is the only appreciable species that exists upon the Rh surface initially. The IR signal taken at the end of the experiment (t = 30 seconds) shows there is no detectable IR active species present. This result is observed at all of the temperatures investigated in this section.

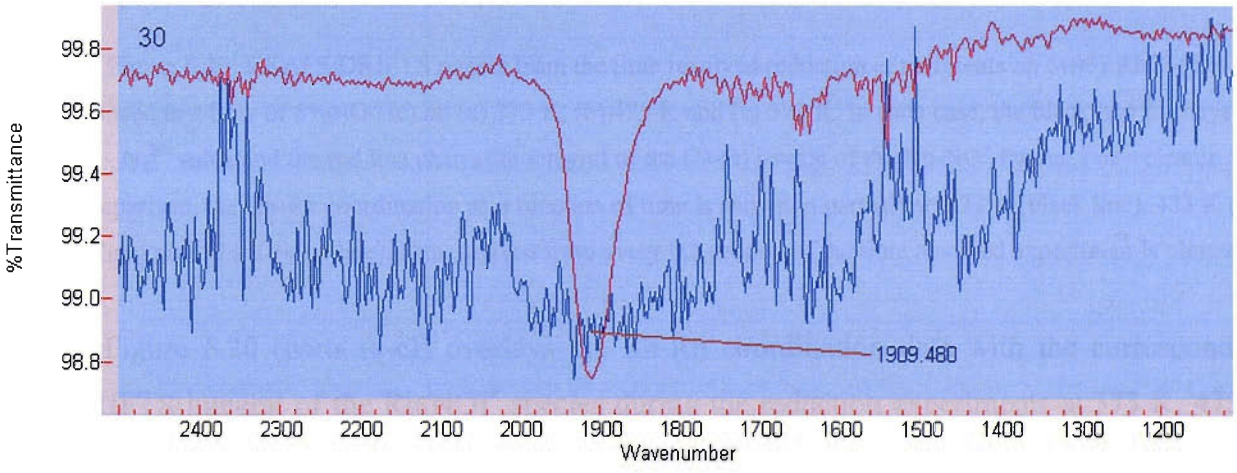

Figure 6.19: DRIFTS spectra taken from 5 wt% RhCl after exposure to 5% H_2/95%He at; t = 64 ms (red line) and t = 30s (blue line) at 573 K. The acquisition time for each spectrum was 64 ms.

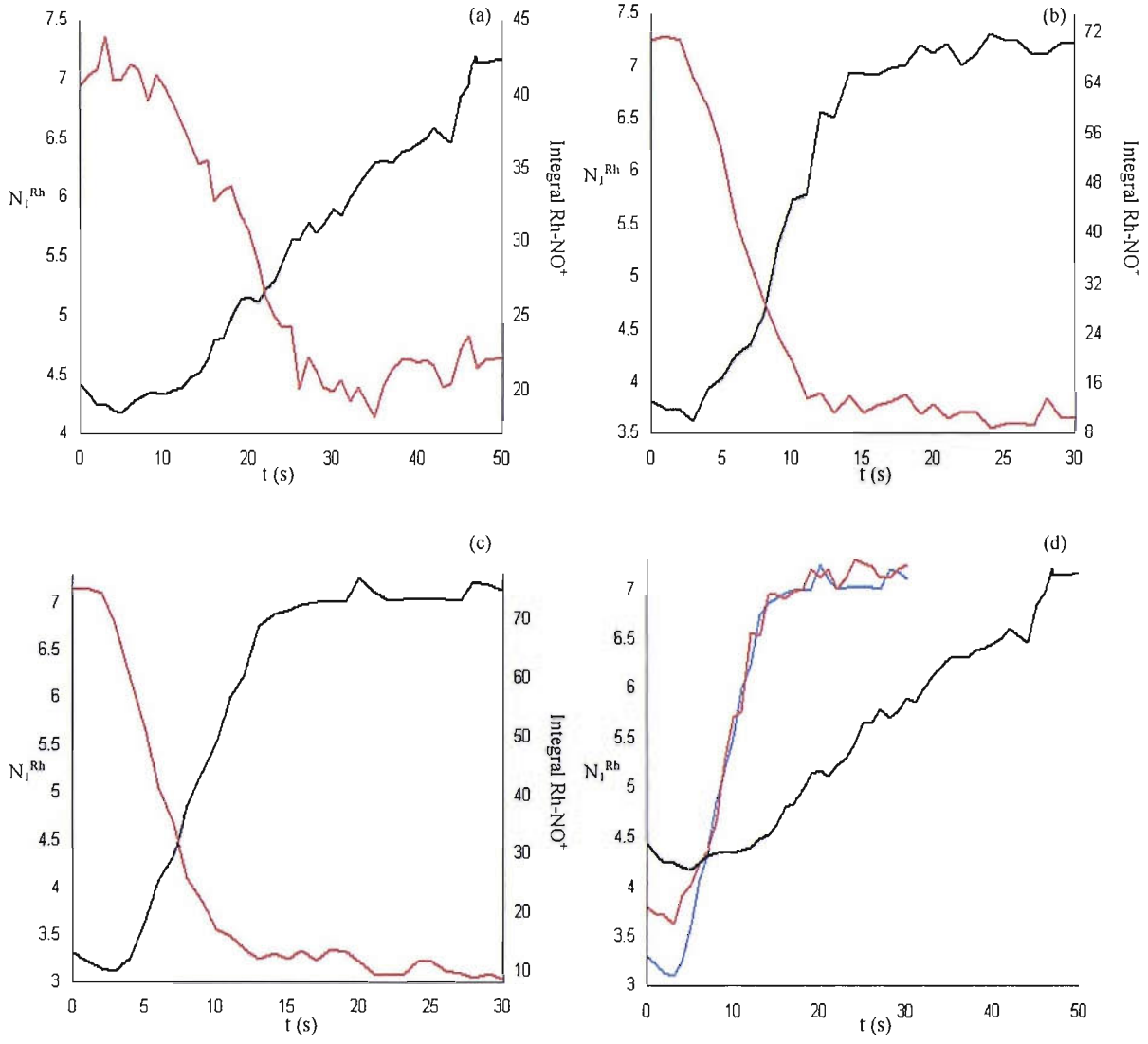

Figure 6.20: EXAFS/DRIFTS results from the time resolved reduction experiments on 5wt% RhCl (pre-exposed to a flow of 5%NO/He) at; (a) 373 K, (b) 473 K and (c) 573 K. In each case, the black line displays the N_1^{Rh} value and the red line charts the integral of the (N-O) stretch of the Rh-NO$^+$ ligand. For a clearer comparison, the Rh-Rh coordination as a function of time is shown in part (d) at; 373 K (black line), 423 K (red line) and 573 K (blue line). Data derived from every 0.5 second of the time resolved experiment is plotted

Figure 6.20 (parts (a-c)) overlays the Rh-Rh coordination data with the corresponding DRIFTS integral of the $Rh(NO)^+$ species during the reduction experiments at 373 K, 473 K and 573 K. The Rh-Rh coordination data from all three temperatures are plotted for a direct comparison in figure 6.20 (part (d)). The figures show a strong temperature dependency on the rate of reduction of the Rh; at 373 K the N_1^{Rh} value stabilises at a value of ca. 7 within

45 s, whereas the same value is indexed within 15 s at 473 K and 573 K. The attenuation of the $Rh(NO)^+$ DRIFTS integral is closely correlated to the subsequent rise in Rh-Rh coordination at each temperature, with no appreciable amount of the species evident on the Rh surface by the end of the experiment (where the N_1^{Rh} value has reached its maximum).

It is evident that the oxidised adduct formed under $NO_{(g)}$ is reduced back to particulate Rh by $H_{2(g)}$ at all of the temperatures investigated. The initial extent of Rh oxidation is dependent upon the experimental temperature, an expected result as the previous section revealed higher temperatures to facilitate a more extensive oxidation of the Rh component. Upon exposure to 5% H_2/He the reduction of the Rh is observed and the corresponding rate is assisted by the temperature employed. An interesting result arises by comparing the relative rates of reduction over the three temperatures. By increasing the reduction temperature by 100 K from 373 K to 473 K a threefold increase in rate is observed. However, another 100K increment reveals no further significant change in the reduction rate, i.e. the experiments at 473 K and 573 K are essentially invariant.

This differential could be due to the variance in average particle size that the different temperature regimes produce. The larger average particle sizes seen at low temperatures would take longer to reduce than the smaller, more corroded analogues exposed to $NO_{(g)}$ at higher temperatures. This also correlates well to the notion that molecular dissociation is dominant at lower temperatures, whereas corrosive, dissociative adsorption is observed at higher temperatures. Observations such as these suggest that the type of dissociation occurring over these systems may directly affect their particle morphology and any subsequent structure-function response.

However, the results also indicate that some form of diffusion limit exists as there is evidence of a point where increasing the temperature no longer serves to facilitate the rate of reduction. Multiple experiments between 373 K and 473 K would be needed to uncover this temperature regime in more detail.

The unfortunate absence of any mass spectrometric data does not reveal the gaseous products formed during the reduction process. However, based upon similar existing studies[22,23] it would be reasonable to suggest that $N_2O_{(g)}$ production would be dominant; as the collapse of the oxidic Rh phase is directly associated with the production of $N_2O_{(g)}$ in the

NO/H_2 reaction. Other products such as $N_{2(g)}$ and $H_2O_{(g)}$ could also be formed during the reduction process.

The results presented in this study are in contrast to the study outlined in ref. (4). The EXAFS results obtained in the study only indicate a collapse in the NO induced oxidised Rh phase and regeneration of the metal above 400 K. This is despite many experimental parameters remaining essentially constant (e.g. gas flow rates, gas exposure times, catalyst charge). A similar discrepancy was observed between the analogous NO adsorption experiments earlier in this chapter; a reiteration that comparisons between experiments performed with the EDE/MS (microreactor) set-up and EDE/DRIFTS/MS (DRIFTS cell) need to be made with caution, as significantly varying results are obtained with seemingly similar experimental parameters.

In summary, the reduction of the $NO_{(g)}$ induced oxidised phase of Rh proceeds at temperatures as low as 373 K, and the rate of the recovery of the metal is facilitated at increased temperatures. Both the reduction temperature and particle morphology seem to directly affect the reduction characteristics of the catalyst system, with larger Rh particles at lower temperatures indexing a significantly longer reduction time. The $Rh(NO)^+$ species was the only stable species evidenced by DRIFTS prior to exposure to $H_{2(g)}$, and the subsequent disappearance of the species is closely correlated to the regeneration of particulate Rh. There is no evidence for any significant particle sintering at any of the temperatures investigated. A more complete study is needed to investigate this process in detail, especially with regard to obtaining mass spectrometric results and performing the experiments over a wider temperature range.

In the context of the chapter as a whole, these experiments effectively show that there is considerable difference in the kinetics of Rh oxidation by $NO_{(g)}$ and the reduction of this oxidised phase back to particulate Rh. The results suggest that under the conditions employed, any dynamic equilibrium between the oxidative and reductive processes would favour the oxidation process. This significant influence exerted by $NO_{(g)}$ on Rh would have to be a key consideration with regards to understanding the structural-reactivity behaviour of the steady state catalyst.

6.8 References

[1] W.A. Brown, D.A. King, *J. Phys. Chem. B.*, 2000, **60**, 17.

[2] For instance: H.S. Gandhi, G.W. Graham, R.W. McCabe, *J. Catal.*, 2003, **216**, 433.

[3] For instance: K.C. Taylor, *Catal. Rev. Sci. Eng.*, 1993, **35**, 457.

[4] T. Campbell, A.J. Dent, S. Diaz-Moreno, J. Evans, S.G. Fiddy, M.A. Newton, S. Turin, *Chem. Commun.*, 2002, 304.

[5] M.A. Newton, A.J. Dent, S. Diaz-Moreno, S.G. Fiddy, J. Evans, *Angew. Chem. Int. Ed.*, 2002, **41**, 2587.

[6] For instance: B. E. Hayden, A. King, M. A. Newton, *Surf. Sci.*, 1998, **397**, 306.

[7] H. Arai, H. Tominaga, , *J. Catal.*, 1976, **43**, 131.

[8] G. Srinivas, S.S.C. Chuang, S. Debnath, *J. Catal.*, 1994, **148**, 748.

[9] J.A. Anderson, G.J. Millar, C.H. Rochester, *J. Chem. Soc. Faraday Trans.*, 1990, **86**, 571.

[10] For instance, B.E. Nieuwenhuys, *Adv. Catal.*, 2000, **44**, 259.

[11] P. Granger, C. Dujardin, J.-F. Paul, G. Leclercq, *J. Mol. Cat. A*, 2005, **228**, 241.

[12] R. Dictor, *J. Catal.*, 1988, **108**, 89.

[13] J. Liang, H.P. Wang., L.D. Spicer, *J. Phys. Chem.*, 1985, **89**, 5840.

[14] E.A. Hyde, R. Rudham, C.H. Rochester, *J. Chem. Soc. Faraday. Trans.*, 1988, **80**, 531.

[15] T.W. Root, G.B. Fisher, L.D. Schmidt, *J. Chem. Phys.*, 1986, **85**, 4679.

[16] D. Loffreda, D. Simon, P. Sautet, *Chem. Phys. Letts.*, 1998, **291**, 15.

[17] M.A. Newton, A.J. Dent, S.G. Fiddy, B. Jyoti, J. Evans, in preparation.

[18] B.S. Clausen., J.K. Norskov., *Topics Catal.*, 2000, **10**, 221.

[19] G. E. van Dorssen, D.C. Koningsberger., *Phys. Chem. Chem. Phys.*, 2003, **5**, 3549.

[20] M.A. Newton, A.J. Dent, S.G. Fiddy, M.Tromp, B. Jyoti, J. Evans, in preparation.

[21] For instance: M.J.P Hopstaken, J.W. Niemantsverdriet, *J. Phys. Chem. B*, 2000, **104**, 3058.

[22] M.A. Newton, B. Jyoti, A.J. Dent, S. Diaz-Moreno, S.G. Fiddy, J. Evans, *Chem. Phys. Chem.*, 2004, **5**, 1056.

[23] B. Jyoti, Mphil Thesis, University of Southampton, 2002.

Chapter 7. The structure-function response of Rh and RhPd systems to CO and NO

7.1 Introduction

The focus of this thesis thus far has been orientated towards investigating the basic properties of Rh/Al_2O_3 systems, and the structural response these systems exhibit when they are exposed to molecules such as CO and O_2. The studies have afforded a great deal of information on these catalysts, especially regarding to their adsorptive properties. However, the performance and behaviour of the systems under realistic, 'working' catalytic conditions has not been probed in detail. This chapter will therefore aim to examine the structure-reactivity behaviour of the supported Rh systems during a temperature controlled catalytic reaction; the exemplar being NO reduction by CO.

The CO/NO reaction over Rh, covered in detail in chapter 1, was chosen as the exemplar reaction because of the considerable attention it has received from the scientific community, mainly due to its connection with environmental protection.[1] Many other subject areas such as surface science and technology could be included here, as surface science based studies widely use the reaction as a testing platform for the ongoing development of catalytic systems such as the TWC. From a purely scientific viewpoint, the reaction is of particular interest as it represents one of the simplest examples of a catalytic reaction that proceeds via the decomposition of an adsorbed species.[2] Moreover, a clearly defined relationship between the structure of the Rh and interacting molecules is still not evident, despite a large number of infra-red based experiments being conducted on similar systems.[3,4,5,6]

The adsorption properties of each molecule has already been covered in detail in this thesis (see chapter 5 for adsorption of CO, chapter 6 for adsorption of NO), and have shown the relative capacities of each molecule to elicit structural changes of the Rh nanoparticles. $NO_{(g)}$ was found to be more destructive towards Rh than $CO_{(g)}$, rapidly oxidising even the largest particles investigated (N_1^{Rh} = 7-8, atomicity 35-75 Rh atoms). These findings will be used to aid the interpretation of the catalysis results in this chapter.

Initially, the combined EDE/DRIFTS/MS experiments compare the RhCl and RhN systems to investigate the influence chlorine exerts on the catalysts under catalytic conditions. The scope of experiments will then be expanded to include a Rh system alloyed with a small amount of an adjunct metal, Pd. Previous studies upon the 4%Rh/1%Pd system have shown that the Pd effectively insulates the Rh component against any facile oxidation under the

temperature controlled reduction of NO by H_2.[7,8] Whether a similar result is obtained under the NO/CO reaction is investigated, and compared to results from the elemental Rh systems.

Lastly, each reactive gas in the feedstock will be periodically alternated at various temperatures to monitor the structural response of the system to such changes in the reactive environment.

7.2 The structure-reactivity behaviour of RhCl and RhN systems during temperature controlled NO reduction by CO

NB: The EXAFS data obtained for the 2wt% Rh systems for use in this chapter was not of sufficient quality to permit accurate analysis, therefore only the 5 wt% Rh systems will be reported upon.

7.2.1 Experimental

NB: This experimental section applies to the experiments performed in sections 7.2 and 7.3.

The EDE/DRIFTS/MS experimental apparatus was used as outlined in chapter 2.5.8.

In a typical experiment the catalyst (ca. 45 mg) was pre-treated by heating under a flow of 5% H_2/He to 573 K. The system was then subjected to a flow of 5% O_2/He for ca. 5 minutes before switching back to the flow of 5% H_2/He and cooled to room temperature. After purging under a flow of He, a 50:50 mixture of 2.5% NO/He and 2.5% CO/He at 25 $mlmin^{-1}$ each was introduced synchronously with the start of the EDE/DRIFTS/MS experiment. Experiments are performed as a function of temperature.

EDE experiments were performed using the Si[111] monochromator in Laue configuration to allow for the simultaneous sampling of Rh and Pd K edges (see section 6.3 for information on the incorporation of Pd into this study). EXAFS detection was made via the Princeton CCD camera, with a total acquisition time of 1.2-1.5 s per EDE spectrum. This matched the experimental heating rate of 10 K min^{-1} to yield ca.1 EDE spectrum K^{-1}.

7.2.2 Results

The initial state of the 5 wt% RhCl and RhN systems to be investigated in this section was firstly probed by EXAFS; the statistical data derived from this is given in table 7.1. The reduced samples returned values that were expected from previous studies and as reported in chapter 3;[8] N_1^{Rh} = ca. 7 and 7.5 for RhCl and RhN respectively. The slightly larger average Rh-Rh coordination number reported from the RhN system can be rationalised from the higher average particle size reported by the TEM studies, also reported in chapter 3.

Sample/Conditions	Scatterer	CN	r/Å	E_F	R (%)
5 wt% RhCl in 5% H_2/He at 298 K	Rh	6.8 (± 0.6)	2.67 (±0.02)	-5.24	34
5 wt% RhN in 5% H_2/He at 298 K	Rh	7.4 (± 0.6)	2.67 (±0.02)	-4.23	31

Table 7.1: Structural and statistical data derived from the analysis of EXAFS for the systems indicated. Other parameters; k = 2 – 12.5 Å, $2\sigma^2/Å^2$ = 0.011(±0.001).

Figure 7.1 shows in situ Rh K-edge EDE data taken from 5wt% RhCl and 5wt% RhN during heating to 573 K under the reactive mixture of 50:50 2.5%NO/2.5%CO/He. Figure 7.2 shows the synchronously obtained DRIFTS data for each system.

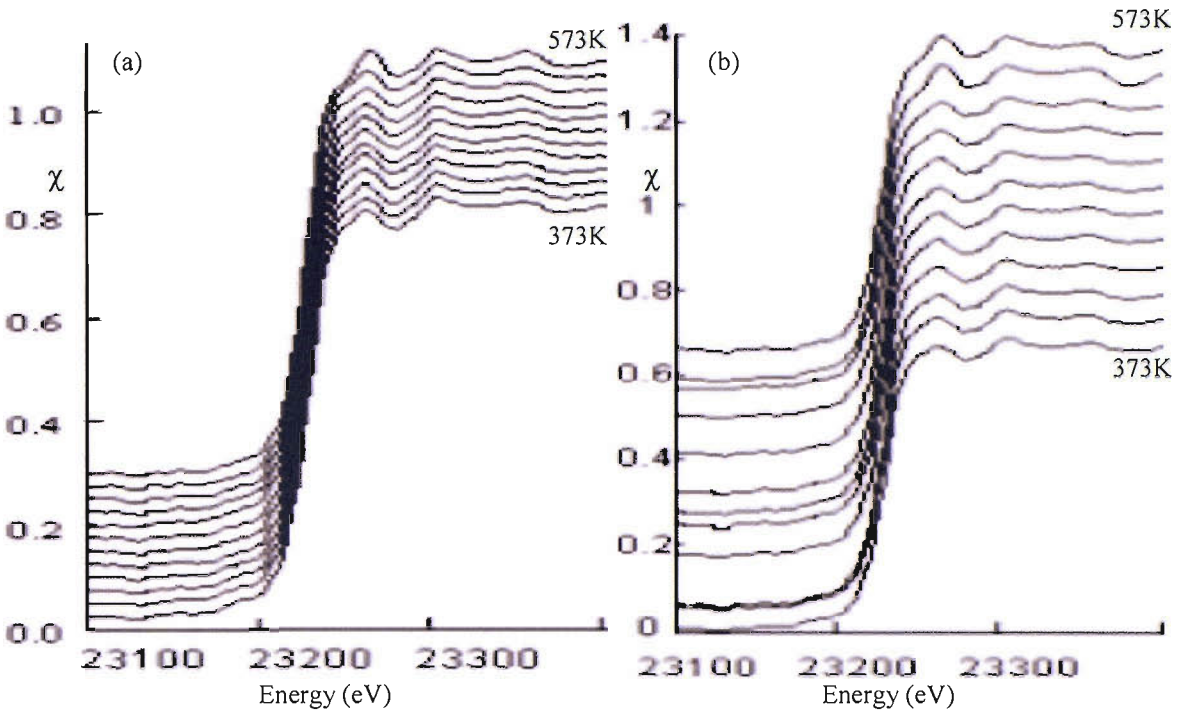

Figure 7.1: Rh K edge EDE spectra derived during $NO_{(g)}$ reduction by $CO_{(g)}$ (under 50:50 2.5%NO/2.5%CO/He) for; (a) 5 wt% RhCl and (b) 5 wt% RhN as a function of temperature. One spectrum every 25 K is shown.

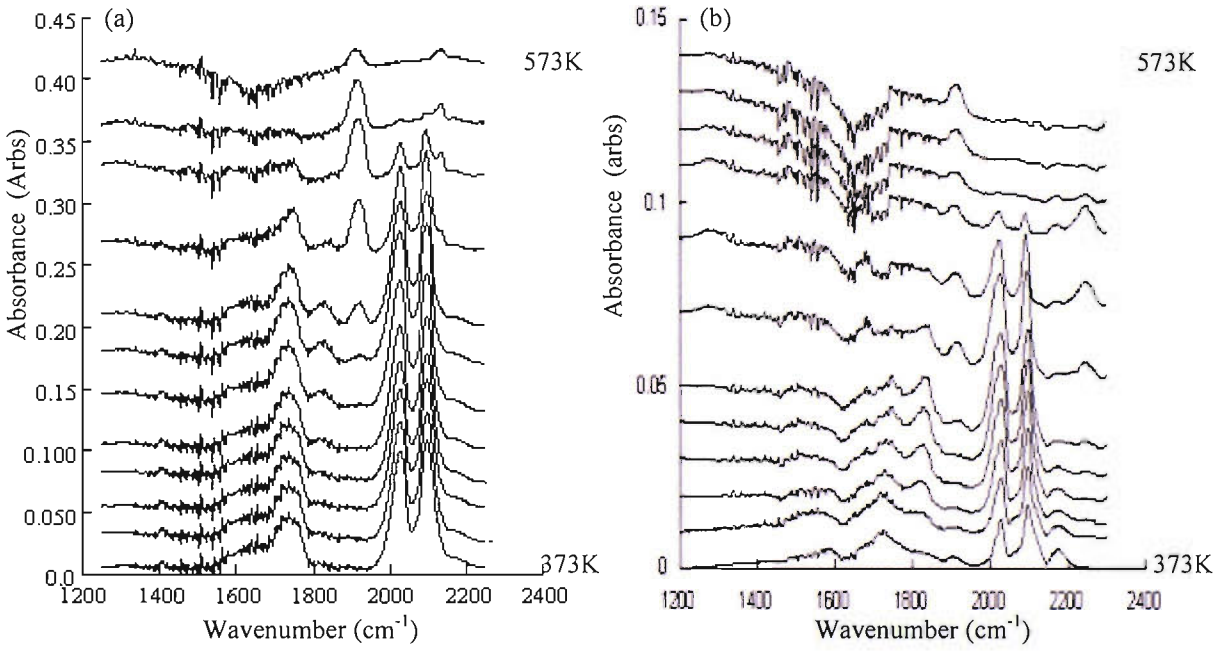

Figure 7.2: Absorbance DRIFTS spectra (1200-2300 cm^{-1}; 4 cm^{-1} resolution) obtained synchronously to the EDE data shown in figure 7.1.

First inspection of the XANES region of the EDE spectra at low temperatures in figure 7.1 shows that exposure to the catalytic mixture has lead to the oxidation of both the 5 wt% Rh systems. Under the current conditions employed, it is only at higher reaction temperatures (ca. 530 K onwards) that the XANES regions begin to evidence signatures associated with metallic Rh. This is an expected result based upon current (chapter 5) and previous findings,[9,10] where exposure to $NO_{(g)}$ alone induces rapid and extensive oxidation of the Rh component. Indeed, the experiments on these systems found the oxidic states to persist and could only be re-reduced by H_2 at temperatures above ca. 400 K.

The corresponding DRIFTS spectra shown in figure 7.2 correlate well to the EDE data in that the IR features strongly support that the Rh component is oxidised at lower temperatures. The spectra below 500 K are dominated by the signal from the $Rh(CO)_2$ species (υ_{sym} ~ 2100 cm^{-1}, υ_{asym} ~ 2025 cm^{-1}). The gem-dicarbonyl species is the only significant carbonyl entity evident on the catalyst surface, with no contribution from species associated with extended Rh surfaces (i.e. linear and bridging CO). This is also the case for adsorbed NO in that the only nitrosyls observed are attributable to oxidised Rh. The spectra do not present evidence of significant amounts of the Rh(CO)(NO) entity forming at ca. 2100 and 1755 cm^{-1} (for υ (CO) and υ(NO) respectively),[11] although they could conceivably be present under the existing, more intense peaks in these regions. However, there are absorptions at ca. 1750 and 1830 cm^{-1} which would correspond to the asymmetric and symmetric stretches of the $Rh(NO)_2$ species. The peak at ca. 1750 cm^{-1} could also be attributed to a monodisperse $Rh(NO)^-$ species.

$Rh(NO)^+$ sites are also seen to evolve on both systems at temperatures above ca. 470 K (~ 1900 cm^{-1}). The presence of this linear nitrosyl species is not unexpected as it was the only stable surface species observed in this temperature regime during similar experiments performed using $NO_{(g)}$ alone (see chapter 6). It is interesting to note that the disappearance of the $Rh(CO)_2$ peaks coincides with the formation of the $Rh(NO)^+$; which in turn closely correlates to the formation of metallic Rh (as observed in the XANES data).

Figure 7.3 shows the variation of the Rh-Rh coordination number during the temperature dependant catalytic experiments alongside the corresponding DRIFTS integrals derived from the asymmetric stretch of the $Rh(CO)_2$ species. Figure 7.4 shows the same N_1^{Rh} data plotted against the net NO residue (%) obtained during the catalytic experiments.

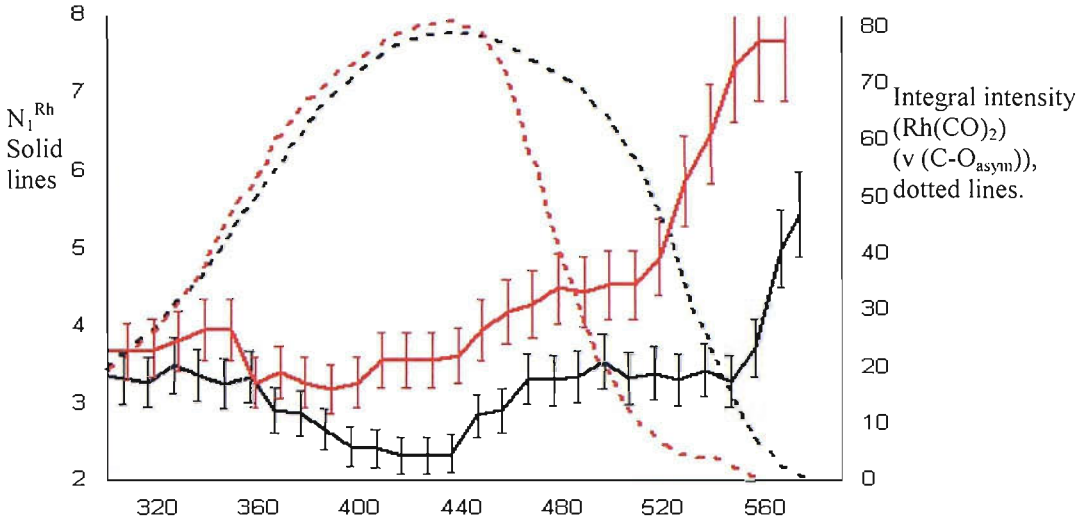

Figure 7.3: Variation in N_1^{Rh} as a function of temperature during NO reduction by CO over 5 wt% RhCl (Solid black line) and 5 wt% RhN (solid red line) catalysts. The corresponding integral intensities of the $Rh(CO)_2$ (ν ($C\text{-}O_{asym}$)) are also plotted (dashed black line for the RhCl system). Error bars given for the coordination data are derived from the corresponding standard deviations.

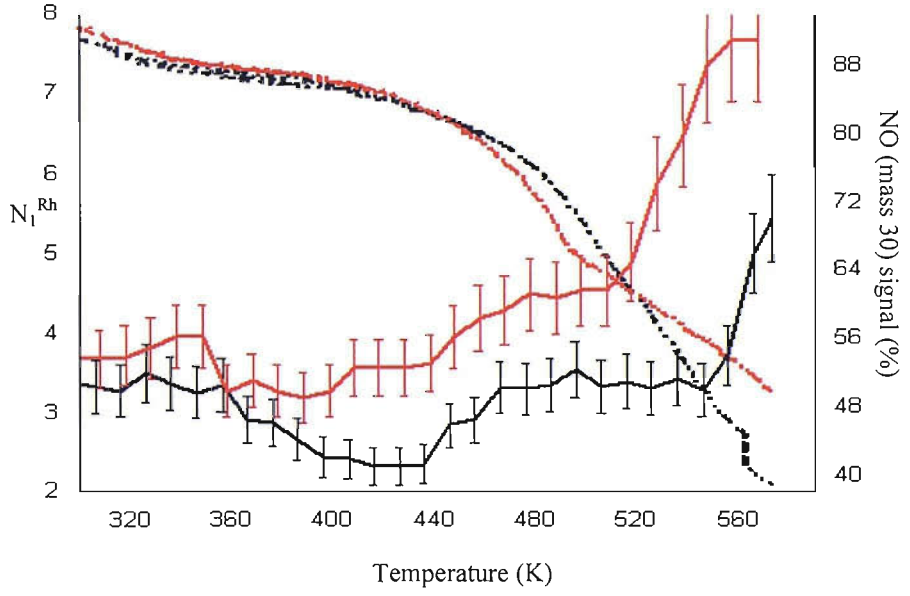

Figure 7.4: Variation in N_1^{Rh} as a function of temperature during NO reduction by CO over 5 wt% RhCl (Solid black line) and 5wt% RhN (solid red line) catalysts. The corresponding net NO signals from downstream feedstock analysis are also plotted (dashed black line for the RhCl system). Error bars given for the coordination data are derived from the corresponding standard deviations.

Table 7.2 shows representative structural and statistical information derived from the analysis of the EDE data given in figures 7.3 and 7.4; data from the beginning (298 K) and end (573 K) of the temperature controlled experiment is given to highlight the mentioned differences between the systems.

Sample/Conditions	Scatterer (s)	CN	r/Å	$2\sigma^2/Å^2$
(a) 5wt% RhCl in 50:50 mix of 2.5%CO/2.5%NO/He at 298 K	Rh	3.4 (±0.4)	2.68 (±0.02)	0.011 (±0.01)
	O (or C/N)	1.3 (±0.1)	1.97 (±0.01)	0.005 (±0.01)
(b) 5wt% RhCl in 50:50 mix of 2.5%CO/2.5%NO/He at 573 K	Rh	5.4 (±0.5)	2.64 (±0.02)	0.017 (±0.01)
(c) 5wt% RhN in 50:50 mix of 2.5%CO/2.5%NO/He at 298 K	Rh	3.7 (±0.4)	2.66 (±0.02)	0.011 (±0.01)
	O (or C/N)	1.0 (±0.1)	1.98 (±0.01)	0.005 (±0.01)
(d) 5wt% RhN in 50:50 mix of 2.5%CO/2.5%NO/He at 573 K	Rh	7.4 (±0.5)	2.63 (±0.02)	0.017 (±0.01)

Table 7.2: Structural and statistical data derived from the analysis of the EDE during the temperature controlled experiment as indicated. Other parameters; (a) Ef = -5.17 eV, R = 50%, k = 2-11.5 $Å^{-1}$, (b) Ef = -4.6 eV, R = 43%, k = 2-12$Å^{-1}$, (c) Ef = -6.39 eV, R = 57%, k = 2-11 $Å^{-1}$, (d) Ef = -3.39 eV, R = 44%, k = 2-12.5 $Å^{-1}$.

These data show that the surface adsorbates and the onset of NO conversion can be correlated to the structure of the Rh phase. Figure 7.3 shows that the collapse of the oxidic Rh phase is initiated at ca. 500 K for the RhN system, with an increase in N_1^{Rh} value from ca. 4.5 to index a 'metallic' Rh value of ca. 7.5 at the end of the experiment. This is in contrast to the behaviour displayed by the RhCl system, the collapse is not observed until temperatures above ca. 550 K. Moreover, the N_1^{Rh} value of ca. 5.5 by the end of the experiment reveals that, under the conditions employed, the RhCl system still retains partial oxidic character throughout the experiment. It must be stated that the increased average particle sizes present on the RhN systems (as reported in chapter 3) would also be a major contributor to the differences in coordination values. The TEM data shows the average particle to be 26 Å for the RhN system; 4.5Å (±1Å) larger than for the RhCl system. As such both the EXAFS and TEM data need to be considered when making these correlations. The figure also shows that the attenuation of the predominant $Rh(CO)_2$ species is linked to the aforementioned change in Rh phase. The relative amount of gem-dicarbonyl surface species is seen to decrease at ca.

450 K for both systems, with further attenuation occurring at a much faster rate for the RhN system.

The mass spectrometric data displayed in figure 7.4 shows that despite the differing structural behaviour between the two systems, the catalytic characteristics are very similar across the temperature range. It is clear from the results of both systems that significant NO conversion is observed in the presence of oxidised Rh phases (and/or 'smaller' Rh particles), an unexpected result as it is generally accepted that a metallic Rh phase is responsible for NO conversion during NO reduction by CO.[2] Again, the mentioned particle size differences between the two systems would also be playing a key role here.

7.2.3 Discussion

The exposure of 5 wt% Rh catalysts made with a chlorinated and non-chlorinated precursor to a 50:50 mix of 2.5%CO/2.5%NO/He results in the extensive oxidation of the Rh metal below 500 K. Simple inspection of the XANES region of the EDE data, and the synchronously obtained DRIFTS data points to $Rh(CO)_2$ centres being the predominant carbonyl species below 500K. However, this result in itself is unexpected based upon experimental findings from this thesis (see chapter 5) and previous studies of similar systems exposed to $CO_{(g)}$ alone.[12,13,14] Results from this thesis found that exposure to flowing 5%CO/95%He does not significantly alter the structure of the 5 wt% catalyst, i.e. the N_1^{Rh} value of ca. 7.5-8 is reported throughout the temperature range employed (up to 423 K). However, the lower loaded 2.5 wt% Rh systems (N_1^{Rh} ca. 3.5) were extensively disrupted within 30 s at temperatures as low as 298 K. The aforementioned similar studies found that $Rh(CO)_2$ only formed in significant amounts upon Rh particles displaying a Rh-Rh coordination of < 4-5, consistent with current results.

It is therefore reasonable to suggest that the addition of $NO_{(g)}$ to the $CO_{(g)}$ feedstock results in the promotion of surface species such as $Rh(CO)_2$. The easily dissociable oxidant NO is well documented to oxidise metallic centres more readily than CO, and findings from this thesis provide direct evidence of this effect (see chapters 4 and 5 respectively). However, above 300 K these oxidised sites are only seen to be converted into $Rh(CO)_2$ sites.

The results do not provide any evidence of the $Rh(CO)_2$ species being actively stabilised by the presence of chlorine in the catalyst make-up, as has been previously proposed.[15] The role of chlorine in similar Rh systems has also been previously reported to actively stabilise the $Rh(NO)_2$ species,[5] and again results from this study show no sign of this being the case under the current conditions employed.

The structural data collected for the two systems does however show that the use of a chlorinated precursor retards the formation of an obviously metallic Rh phase; when compared to the analogous chlorine free system. The removal of the $Rh(CO)_2$ species from the RhN system can be associated with the observed formation of metallic Rh at temperatures above ca. 520 K. Although this decline in the geminal dicarbonyl species is almost identical for the chlorinated system, a significant change in the phase of Rh is not observed until T > 550 K. By this temperature the DRIFTS data shows that the $Rh(CO)_2$ species has attenuated to ca. $1/8^{th}$ of its maximal surface coverage. Therefore these experiments evidence chlorine to stabilise Rh as an oxide, but not for this remaining to be in the form of $Rh^{I}(CO)_2$. This statement can also be applied to the observed $Rh(NO)_2$ species. The above is only one possible scenario; the differences in particles sizes may also be partly, or indeed wholly, taking part in the differing structure-function behaviour of the two catalysts. Other factors such as dispersion of particles on the surface could also affect the obtained coordination values.

The differences in Rh phase at higher temperatures (T > ca. 520 K) between the two systems are further evidenced by the presence of $Rh(NO)^+$. The study of the response of 5 wt% Rh catalysts to 5% NO/He alone (see chapter 6) revealed that the formation of $Rh(NO)^+$ requires the existence of oxidic Rh sites. The study also concluded that the species was most likely to be a highly transient form of $Rh(NO)_2$, which could still be applied in the current case.

In summary, these current experiments show a stoichiometric CO/NO feedstock to corrode relatively large Rh particles into mainly the $Rh(CO)_2$ species under ambient conditions. Catalysis ensues as a direct result of the decomposition of the $Rh(CO)_2$ species, as a function of temperature. The presence of chlorine in the catalyst hinders the formation of a metallic Rh phase at post light off temperatures, with no apparent detriment to overall catalyst efficiency. Further investigation into the influence the differing particle sizes have on

these systems is needed; with specific emphasis on the role of chlorine affecting the catalyst composition and subsequent structure-function behaviour.

7.3 The structural-reactivity behaviour of RhCl and RhPd alloy systems during temperature controlled NO reduction by CO

The previous section dealt with comparing the effect the use of chlorine in the Rh catalyst composition has on the structural-reactivity behaviour in the NO/CO reaction. The experiments also uncovered that the addition of the oxidant NO to the CO feedstock led to the rapid oxidation of the Rh nanoparticles at low temperature.

As previously stated in this chapter, $NO_{(g)}$ is known to be more destructive towards Rh nanoparticles than $CO_{(g)}$, oxidising relatively large particles with an average atomicity up to ca. 80 atoms even at room temperature. This propensity displayed by $NO_{(g)}$ for Rh oxidation was demonstrated by our group in both the plug flow microreactor[6] and DRIFTS cell experiment platforms.[16] Such studies also revealed that the lability displayed by $NO_{(g)}$ was found to be an important factor in determining the catalytic selectivity during the reduction of $NO_{(g)}$ by $H_{2\,(g)}$. The experiments performed using the NO/H_2 reaction also investigated a Rh system alloyed with a small amount of an adjunct metal, Pd. The properties of the 4wt%Rh/1wt%Pd alloy catalyst are reported elsewhere,[7,8] however a brief overview of its main characteristics is given below in section 7.3.1. The principal conclusion to be drawn from this work in terms of this thesis is that the facile oxidation of the Rh component is effectively eliminated by the introduction of Pd to the catalyst composition.

This section will therefore use the EDE/DRIFTS/MS platform (the EDE/MS microreactor platform is used for the overview of the RhPd catalyst) to investigate and compare the behaviour of Rh and RhPd systems during the same temperature programmed NO/CO reaction experiments utilised in the previous section (7.2). Such experiments will endeavour to expand upon the understanding of the complex nature of supported Rh and RhPd nanoparticles under catalytic conditions.

7.3.1 Overview of the 4wt%Rh/1wt%Pd system

7.3.1.1 Experimental

It should be noted that the following overview of the RhPd alloy is given as a basic guide only, as key differences and discrepancies between the data obtained from the microreactor and DRIFTS cell based platforms have been highlighted throughout this thesis. The results can still be viewed as viable when making overall comparisons of the catalyst's characteristics.

TEM and XPS measurements on the alloy system were made as explained in chapter 2 (sections 2.6 and 2.3 respectively).

Briefly, a typical experimental procedure for EDE/MS data acquisition was carried out as follows. The EDE//MS microreactor experimental apparatus was used as outlined fully in chapter 2.5.7. The catalysts used were prepared using chlorinated precursors by the co-impregnation technique as explained in chapter 2.9. The previously calcined and reduced catalyst sample (ca. 20 mg) was loaded into a quartz tube, which was then placed into the microreactor apparatus.

Each catalyst was pre-treated in situ prior to any EDE/MS experiment. This involved exposing the sample to a flow of 5%H_2/95%He at room temperature for ca. 30 minutes, before switching back to a flow of He.

The gases under mass flow control were set to give 25 $mlmin^{-1}$ each over the sample bed. The resultant composition of the gaseous products was continuously monitored via the mass spectrometer sampling 16 mass fragments.

EDE measurements were performed using an asymmetrically cut (6^{o}) Si[111] monochromator in Laue (transmission) configuration. Detection of the EXAFS was made with the phosphor masked, Peltier cooled, CCD camera (Princeton). Air was used as the I_0 for the EDE measurements.

7.3.1.2 Results and discussion

Figure 7.5 shows the particle size distribution derived from the TEM data of the 4wt%Rh/1wt%Pd sample; the corresponding statistical data is given in table 7.3.

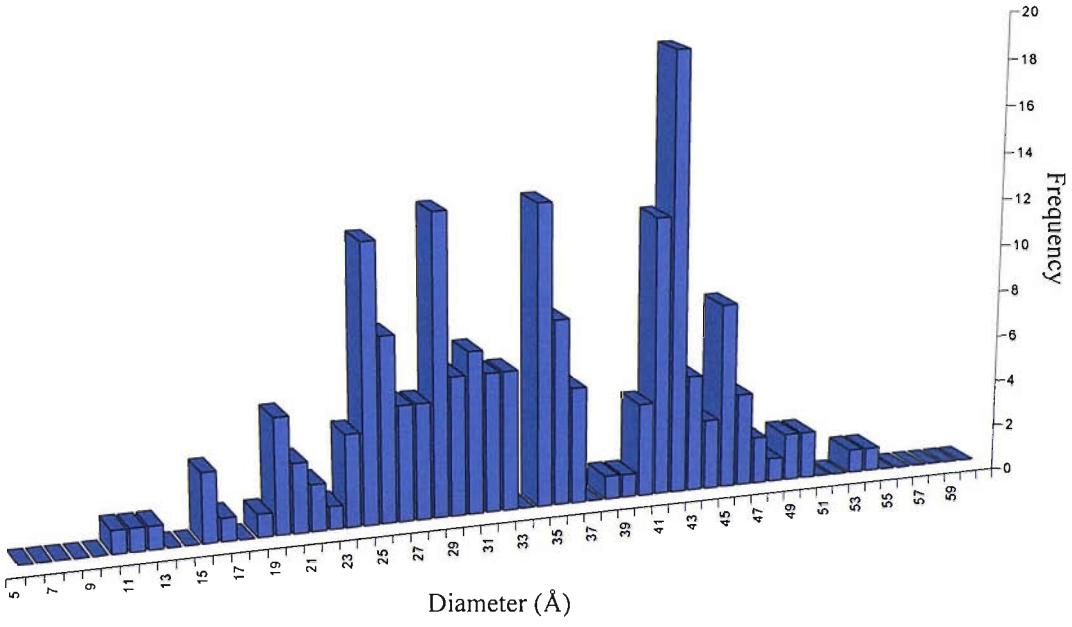

Figure 7.5: Particle size distribution for the 4wt%Rh:1wt%Pd system derived from multiple TEM images.

	4wt%Rh/1wt%Pd
Average particle size (Å)	32.5
Std. Deviation	16.3
Number of atoms in mean particle	989
Mean number of surface atoms	416
Dispersion	0.43

Table 7.3: Statistical data derived from the PSD data in figure 7.5.

The TEM data shows 4wt%Rh/1wt%Pd system to exhibit a bimodal particle size distribution. This could be due to the metal components, and hence particles, no longer existing as discrete entities, i.e. alloying has occurred. This could also occur due to the effect

of phase separation, where 'Rh-like' nucleation sites yield smaller particles, and 'Pd-like' sites yield the larger particles observed. The predominant particle size regime ranges from ca. 24-34 Å and 40-43 Å. This result is consistent with similar studies of supported Rh/Pd systems that report comparable particle sizes for the alloyed particles to be in the regime of 25-35 Å .[17]

Figure 7.6 shows the respective Rh and Pd XPS spectra of the 4wt%Rh/1wt%Pd system.

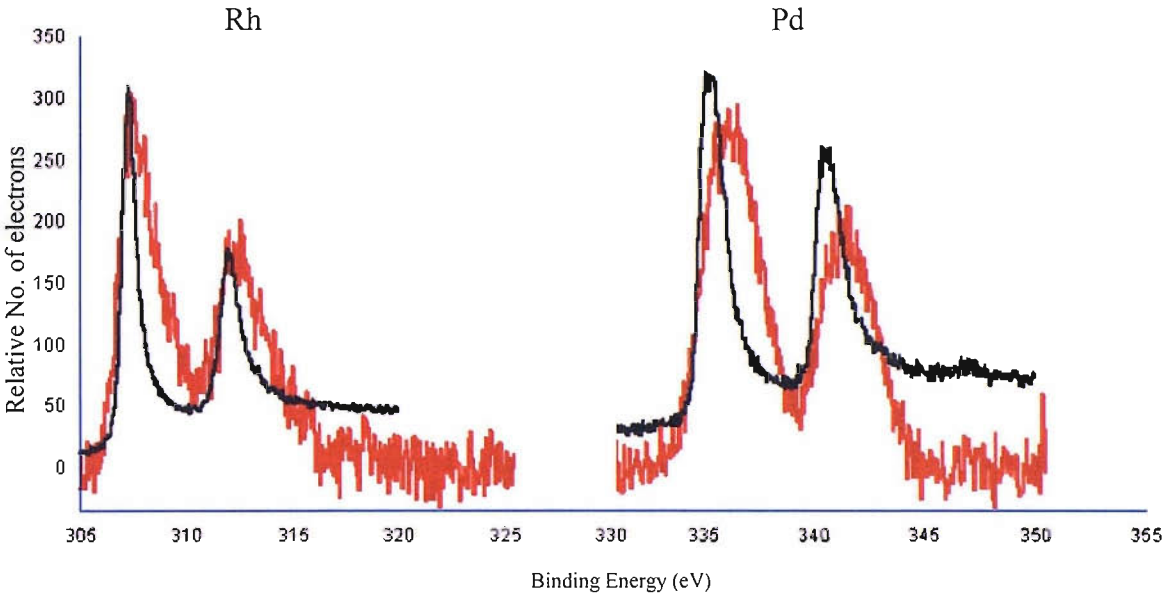

Figure 7.6: XPS spectra taken of the 4wt%Rh/1wt%Pd system, showing both Rh and Pd 3d 5/2 and 3d 3/2 regions; the red line indicates the experimental data; the black line indicates the spectra taken from the respective bulk foil.

The Rh ($3d_{5/2}$) binding energy (BE) of ca. 307 eV correlates closely to that of the BE of bulk metallic Rh, indicating that by introducing Pd to the catalyst make up has effectively insulated the Rh component against any facile oxidation as seen with the elemental 5 wt% RhCl analogue system.[8]

These XPS studies previously performed by our group also included examining a range of alloy samples with varied metal loadings; the results collectively revealed a possible explanation for the insulation of the Rh nanoparticles given by the following.

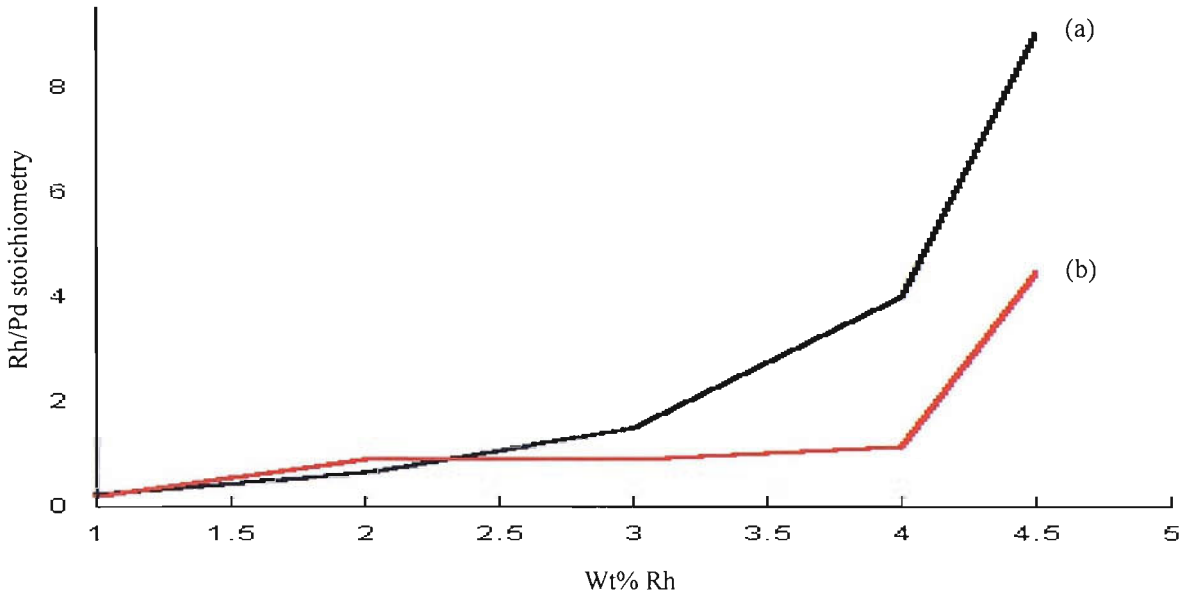

Figure 7.7: Rh/Pd ratio as a function of Rh metal loading in numerous alloy systems; (a) represents the systems in their respective 'homogeneous' states; and (b) represents the experimental values obtained.

Analysis of figure 7.7 reveals that the catalyst systems do not exist as completely homogeneous systems after ca. 2.5 wt% Rh metal loading is surpassed. At the 3 wt% Rh loading level ca. 1.6 times as much Pd is present at the surface compared to the homogeneous case. This effect is seen to increase markedly by a factor of ca. 2 by the 4 wt% Rh level, where there is ca. 3.5 times as much Pd at the surface. The 4.5wt%Rh/0.5wt%Pd system has ca. 2 times as much Pd segregated to the surface. These results were obtained with the use of the XPS equation ($E_{KE} = h\upsilon - E_K - \Phi$), and data set (b) was attained by applying the relevant sensitivity factors to the 'homogeneous' data.

As such, it is most likely that the segregation of the Pd to the surface of the alloyed nanoparticles in question leads to the insulation of the Rh component. Moreover, a comparison of the metal component's binding energies shows that extensive alloying has indeed occurred in the system. Table 7.4 summarises the relevant XPS data for the alloy system and compares it to the analogous elemental systems.

System	Rh $3d_{5/2}$ BE (eV)	Pd $3d_{5/2}$ BE (eV)	Pd_{3d}/Rh_{3d} (experiment)	Pd_{3d}/Rh_{3d} (stoichiometric)
5% Rh/Al_2O_3	308.9	-		
4%Rh/1%Pd/Al_2O_3	307.4	336.2	1.026	0.25
5%Pd/Al_2O_3	-	335.6		

Table 7.4: Rh $3d_{5/2}$ and $Pd_{5/2}$ binding energies from XPS measurements. All of the systems were prepared with chlorinated precursors. The experimentally observed Pd(3d)/Rh(3d) ratio compared to the stoichiometric ratio, which includes the correction for the escape depth, is also given for the alloy system.

Figure 7.8 shows the k^3-weighted EXAFS data (Rh K edge EDE) obtained for a 'fresh' 4wt%Rh/1wt%Pd system alongside a 5wt% RhCl system for comparison. The EXAFS signatures highlight a significant difference in intensity between the two systems; and provide further evidence to the observations made with the TEM and XPS measurements. An inspection of the XANES structure shows that incorporation of Pd at the 1 wt% level results in a metallic Rh signature; this is confirmed by the subsequent structural analysis of the EXAFS data given in table 7.5. As shown previously (see chapter 3), the 5 wt% RhCl system is extensively oxidised in its 'fresh' state, with an N_1^{Rh} value of ca. 3. The subsequent surface morphology can be perceived as being Rh_2O_3. The alloy system however yields an $N_1^{Rh/Pd}$ (Rh) value of just below 8, indicating a metallic particulate structure present and the complete stabilisation of the Rh component to have occurred.

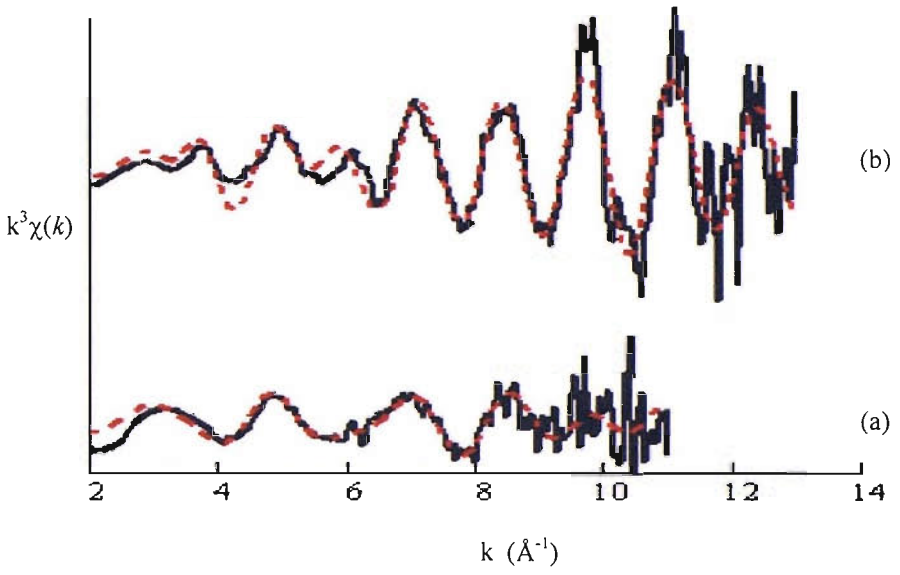

Figure 7.8: k^3-weighted Rh K edge EDE spectra derived from 'fresh' samples; (a) 5 wt% RhCl and (b) 4wt%Rh:1wt%Pd.

Sample	Scatterer (s)	CN	r/Å	$2\sigma^2$/Å^2
(a) 5 wt% RhCl	Rh	2.2 (± 0.2)	2.66 (± 0.03)	0.012 (± 0.002)
	O	3.0 (± 0.3)	1.97 (± 0.01)	0.005 (± 0.001)
(b) 4wt%Rh/1wt%Pd	Rh/Pd	7.7 (± 0.6)	2.67 (± 0.02)	0.012 (± 0.002)

Table 7.5: Structural and statistical data derived from the analysis of spectra given in figure 7.8. Both samples 'fresh' under flowing He at 298 K. Other parameters; (a) Ef = -2.4 eV, R = 57%, k = 2-11 Å^{-1}, (b) Ef = 2.2 eV, R = 56%, k = 2-13 Å^{-1}.

In summary, on the nanoscale Rh and Pd form alloyed particles that are enriched with Pd at the surface. This interaction and surface segregation leads to a curtailment of Rh oxidation which is predominant in the elemental Rh catalyst analogue.

7.3.2 Results: The structural-reactivity behaviour of RhCl and RhPd systems during temperature controlled NO reduction by CO

Figure 7.9 shows in situ Rh K edge EDE data taken from 5wt% RhCl and 4wt%Rh/1wt%Pd during heating to 573K under the reactive mixture of 50:50 2.5%NO/2.5%CO/He. Inspection of the XANES region of both the catalytic systems reveals that, under the current conditions employed, there is no evidence for the formation of oxidic Rh (also see ref. 9). As surveyed in section 7.2, the 5wt% RhCl system evidences an oxidic structure when exposed to the catalytic mixture at low temperatures. However, the 4wt%Rh/1wt% alloy system shows a metallic Rh XANES signature under the same experimental conditions. Based on the properties of the alloy system this is an expected result due to the insulating properties of Pd.

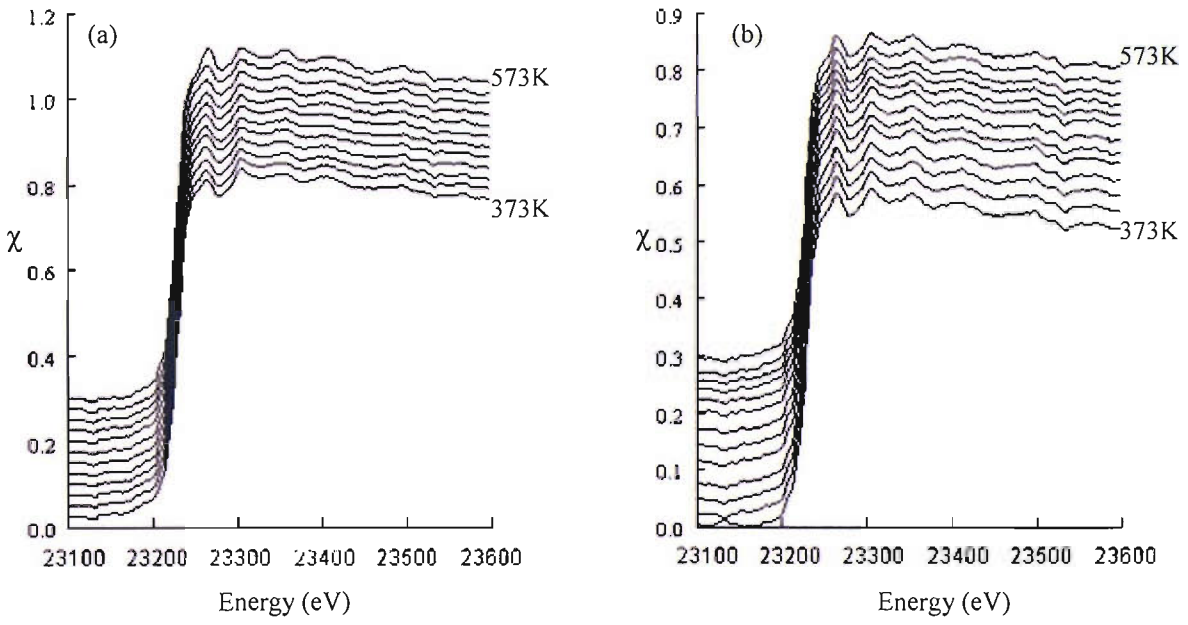

Figure 7.9: Rh K edge EDE spectra derived during NO reduction by CO (under 50:50 2.5%NO/2.5%CO/95%He) for; (a) 5wt% RhCl and (b) 4wt%Rh/1wt%Pd as a function of temperature. One spectrum every 25 K is shown.

Figure 7.10 shows the Pd K edge EDE data simultaneously obtained with the data given above in figure 7.9. Although the data is not of sufficient quality to allow EXAFS analysis, it is worthy of note that the XANES signature is consistent with the Pd particles existing in a metallic environment, rather than an oxide or surrounded by other small scatterers such as carbon or nitrogen. This metallic signature is observed throughout the temperature controlled experiment. Yet again this result is consistent with previous studies, where similar temperature dependent experiments using the NO reduction by H_2 reaction observed a metallic Pd structure existing throughout the temperature regime.[7,8]

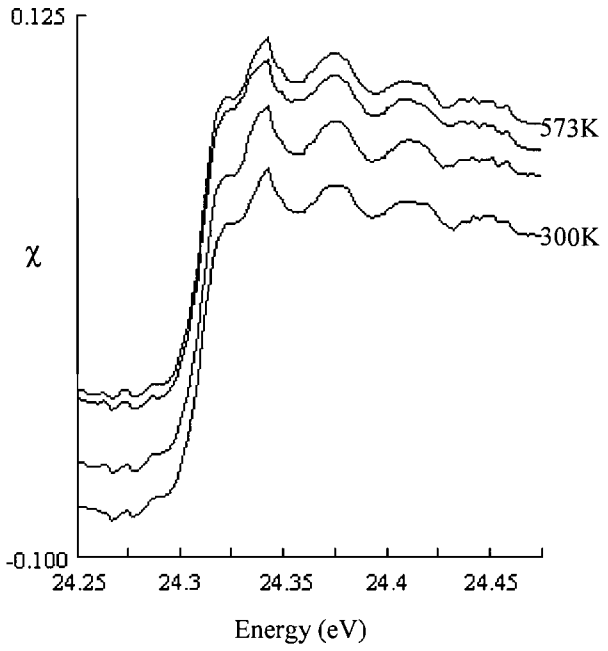

Figure 7.10: Pd K edge EDE spectra derived during NO reduction by CO (under 50:50 2.5%NO/2.5%CO/He) for 4wt%Rh/1wt%Pd. Spectra taken at 300, 373, 473 and 573 K are given.

Figure 7.11 shows the synchronously obtained DRIFTS data for both the systems under investigation. It is clear from the absorbance spectra given that similar IR active species exist upon both of the systems, despite the systems displaying differing EDE spectra. However, by simple inspection it is also apparent that the overall amounts of species are different; with significantly less population of species present upon the alloy system. As with the RhN system studied in section 7.2, most of the IR absorptions are associated with Rh existing in

an oxidation state higher than 0 (as opposed to be being dominated by stretches of CO or NO absorbed upon metallic Rh). Yet again it is the seemingly ubiquitous $Rh^{I}(CO)_2$ (υ_{sym} ~ 2100 cm^{-1}, υ_{asym} ~ 2025 cm^{-1}) on oxidised Rh sites that dominates the IR spectra below ca. 525 K.

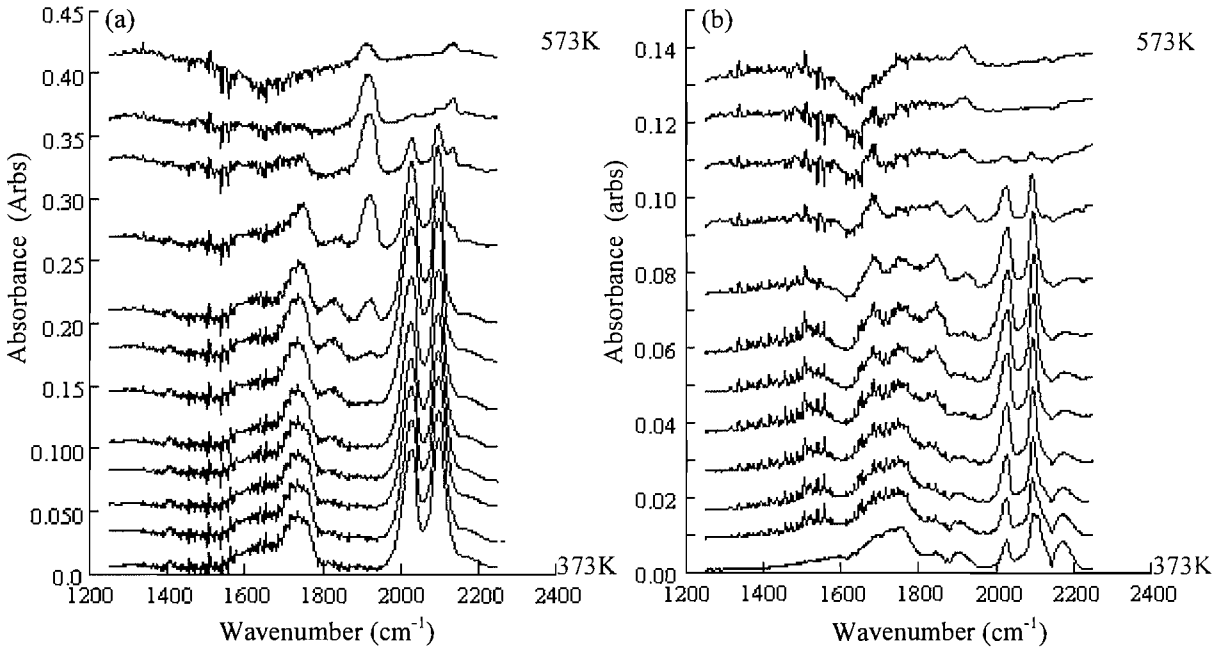

Figure 7.11: Absorbance DRIFTS spectra (1200-2300 cm^{-1}; 4 cm^{-1} resolution) obtained synchronously to the EDE data shown in figure 7.9 for; (a) 5wt% RhCl and (b) 4wt%Rh/1wt%Pd as a function of temperature. One spectrum every 25 K is shown.

There are however some key differences present between the spectra when assigning the peaks below ca. 500 K. Figure 7.11 part (a) is identical to figure 7.1 part (a), which is analysed in section 7.2. Briefly, the peaks at ca. 2100 cm^{-1} and 2025 cm^{-1} are due to the symmetric and asymmetric peaks of the $Rh(CO)_2$ entity, the bands at 1830 and 1750 cm^{-1} are assigned to the symmetric/asymmetric stretches of the $Rh(NO)_2$ species. The peak at 1750 cm^{-1} could also be due to a monodisperse $Rh(NO)^-$ species. The peak at 1910 cm^{-1} (above ca. 525 K) is due to the $Rh(NO)^+$ species (determined to most likely be a highly transient form of $Rh(NO)_2$). Although not present in significant proportions, the presence of the Rh(CO)(NO) species cannot be discounted to appear under the existing, more intense peaks.

Analysis of the alloy system in figure 7.11 part (b) reveals a weak signal peak at ca. 1680 cm^{-1} is observed on the alloy system until ca. 525 K, and may be associated with NO bound

to Rh metal.[18] The differing intensities of the two peaks normally associated with the $Rh(CO)_2$ species (at ca. 2100 cm^{-1} and 2025 cm^{-1}) at lower temperatures suggest that other species apart from the geminal dicarbonyl entity are present on the alloy. This is most likely due to CO or NO bound in some manner upon Pd affecting the overall DRIFTS spectra. Indeed, the broad peak centred at ca. 2175 cm^{-1} is most likely CO bound upon Pd, based on previous similar studies (CO adsorption on metallic Pd supported on TiO_2).[18]

The alloy system also shows evidence for the Rh(CO)(NO) species (υ (CO) ~ 2110 cm^{-1} and υ (NO) ~ 1755 cm^{-1}) forming at low temperatures. The substantial absorptions at 1750 cm^{-1} and 1840 cm^{-1} can be attributed to monodisperse $Rh(NO)^-$ species and/or a $Rh(NO)_2$ site as explained in section 7.2. The presence of the $Rh(NO)^+$ species at ca. 1920 cm^{-1}, another recurring result in these analogous experiments, is seen to increase in signal strength at elevated temperatures (although the proportionate amount of this species is significantly less when compared to the elemental Rh system) .[19] Quantitative assessment of the fraction of Rh that these various species represent could not be carried out due to the insufficient quality of DRIFTS absorbance data.

At temperatures in excess of 525 K, the only appreciable species present on both catalysts is the $Rh(NO)^+$ entity.

Figure 7.12 shows the net NO conversion (derived from mass 30 in the corresponding MS data) occurring over the two catalysts during the catalytic experiments. Alongside this signal the ratio of masses 44 and 22 are plotted for the following reason. The ionisation of N_2O within the mass spectrometer leads to more fragmentation of that for CO_2. This means that the probability of the generation of a doubly charged molecular ion of mass 22 is reduced relative to CO_2. The ratio of mass 44/22 therefore serves as a method to observe the CO_2/N_2O selectivity during reduction; an increased 44/22 ratio means increased selectivity toward N_2O.

It is clear from the figure that both systems display very similar behaviour in the reduction of $NO_{(g)}$ by $CO_{(g)}$. From the viewpoint of N_2O selectivity the two catalysts are essentially identical; it is interesting to note that as N_2O selectivity reaches a maximum at ca. 525 K, $NO_{(g)}$ conversion is seen to decrease steadily. This decrease is from near complete conversion at just below 500 K to index values of ca. 50 and 65% conversion for the 5wt% RhCl and alloy system respectively at 573 K. Moreover, this is the same temperature regime in which

the dominant IR active species (such as $Rh(CO)_2$) are seen to desorb from the catalyst surfaces. The observed phase change by EDE of the 5wt% RhCl system from an oxide to more metallic environment also occurs within this region (see discussion below and also section 7.2).

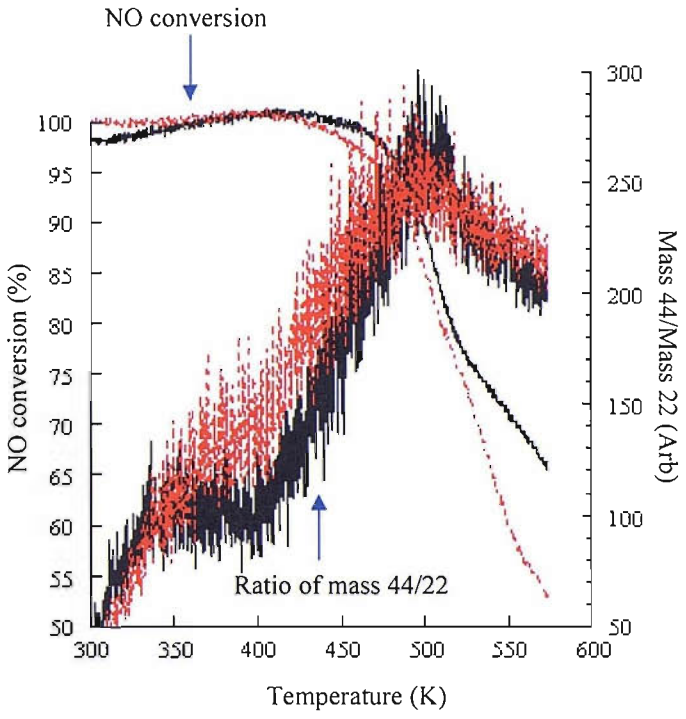

Figure 7.12: NO conversion shown alongside the ratio of mass 44/mass 22 during NO reduction by CO over 5wt% RhCl (given in red) and 4wt%Rh/1wt%Pd (given in black).

Figure 7.13 plots the variation of a number of DRIFTS absorptions during the catalytic experiments, previously assigned in the text above. Combined with figure 7.12, it can be shown that below 500K $NO_{(g)}$ conversion ensues but is associated with increasing levels of N_2O. This can in turn be correlated to the formation and removal of what is most likely the $Rh(NO)_2$ species (evidenced by the band at ca. 1840 cm^{-1} (ν_{sym} NO)). The removal of this species can also be approximately correlated to the formation of the stable $Rh(NO)^+$ species.

At temperatures above ~500 K the selectivity is seen to improve in tandem with the removal of the majority of the surface organometallic species. As noted above, this is the same region in which increases in Rh-Rh coordination number is observed for the 5wt%

RhCl catalyst. The only significant surface species detectable by DRIFTS beyond ca. 525 K is the $Rh(NO)^+$ species.

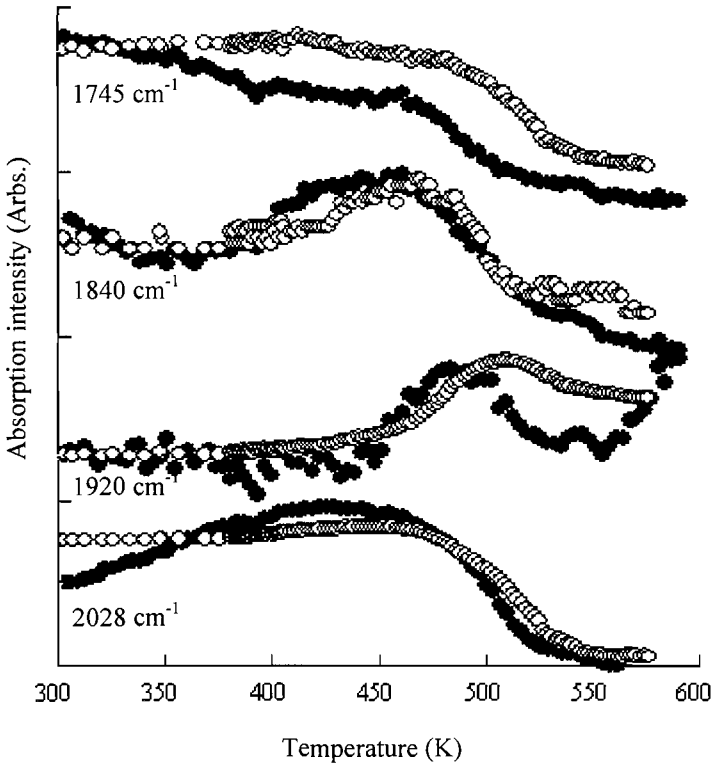

Figure 7.13: The variation of DRIFTS absorptions for a number of surface species observed during the NO reduction by CO as a function of temperature. Open circles display data from the 5wt% RhCl system, filled circles from the 4wt%Rh/1wt%Pd system.

Figure 7.14 shows the Rh-Rh (Pd) N_1^{Rh} values derived from the analysis of the Rh K edge for both the elemental and alloy systems during the temperature dependent experiment. Table 7.6 indexes structural and statistical data from the opposite extremes of the experiment (i.e. at 298 and 573 K) for the two systems in question. The N_1^{Rh} values of the alloy system derived from the analogous NO reduction by H_2 experiment is also given for comparison.

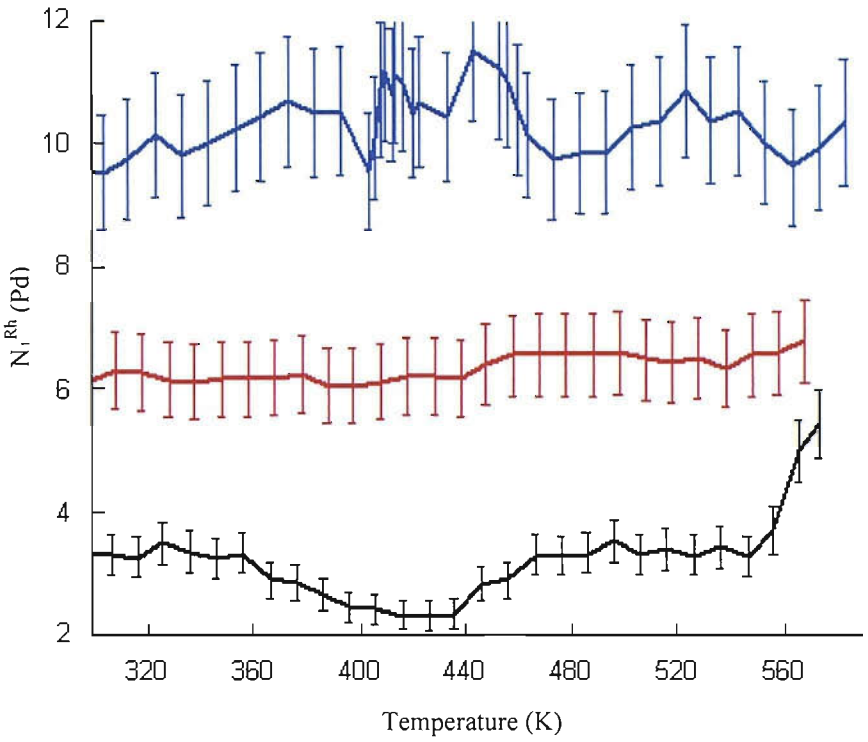

Figure 7.14: Rh-M (M= Rh/Pd) coordination numbers derived from the Rh K edge during NO reduction by CO over; 5 wt% RhCl (black line) and 4wt%Rh/1wt%Pd (Red line). The blue line displays data from 4wt%Rh/1wt%Pd during the analogous NO reduction by H_2 experiment for comparison.[7] Error bars given for the coordination data are derived from the corresponding standard deviations.

Sample/Conditions	Scatterer (s)	CN	r/Å	$2\sigma^2/Å^2$
(a) 5wt% RhCl in 50:50 mix of 5%CO/5%NO/He at 298 K	Rh	3.4 (±0.4)	2.68 (±0.02)	0.011 (±0.01)
	O (or C/N)	1.3 (±0.1)	1.97 (±0.01)	0.005 (±0.01)
(b) 4wt%Rh/1wt%Pd in 50:50 mix of 5%CO/5%NO/He at 298 K	Rh	6.1 (±0.5)	2.68 (±0.02)	0.011 (±0.01)
(c) 5wt% RhCl in 50:50 mix of 5%CO/5%NO/He at 573 K	Rh	5.4 (±0.5)	2.64 (±0.02)	0.017 (±0.01)
(d) 4wt%Rh/1wt%Pd in 50:50 mix of 5%CO/5%NO/He at 573 K	Rh	6.8 (±0.5)	2.66 (±0.02)	0.017 (±0.01)

Table 7.6: Structural and statistical data derived from the analysis of the EDE during the temperature controlled experiment as indicated. Other parameters; (a) Ef = -5.17 eV, R = 50%, k = 2-11.5 $Å^{-1}$, (b) Ef = -7.71 eV, R = 58%, k = 2-12.5 $Å^{-1}$ (c) Ef = -4.6 eV, R = 43%, k = 2-12$Å^{-1}$, (d) Ef = -5.79 eV, R = 59%, k = 2-11.5 $Å^{-1}$.

Although the DRIFTS and MS results indicate that the two systems display similar characteristics (in terms of activity and selectivity), evidence from the Rh EDE data suggest that on a structural level they are significantly different (although the active species may not necessarily be different). The average coordination number for the alloy system is seen to remain constant, within error, between a value of 6 and 6.5 throughout the temperature conditions employed. The extensively oxidised 5wt% RhCl system indexes a coordination value of ca. 3 up to 350 K, which decreases steadily to a value of ca. 2.5 at 425 K. Interestingly, this decrease in N_1^{Rh} occurs synchronously to the observed increase in ν(CO) and ν(NO) IR intensities. Above this temperature the value steadily returns to ca. 3, and it is only above 550 K that the CN is seen to increase to a value of ca. 5.5. Again it is worthy to note that it is within this temperature region where the majority of the carbonyl/nitrosyl bands in the DRIFTS spectra disappear, leaving the persistent $Rh(NO)^+$ species as the only IR active species present on the surface of these catalysts.

The behaviour of the RhPd catalyst during the reduction of NO by H_2 index against a consistent Rh-Rh (Pd) coordination value of between 9 and 10 across the same temperature region. It should be acknowledged that these experiments found the alloy system to be significantly promoted for the NO/H_2 reaction when compared to the overall catalytic performance of the 5wt% RhCl elemental case.

Figure 7.15 displays the relationship of the coordination number of FCC nanoparticles and the average number of atoms within the nanoparticles. This is directly derived from the EXAFS studies of Jentys,[20] which is fully explained in chapter 3. Plotted on the figure is the average coordination numbers derived during the current CO/NO reaction for the two systems under investigation. As with figure 7.14, the average coordination number derived from the NO/H_2 reaction over the alloy system is also given for comparative purposes.

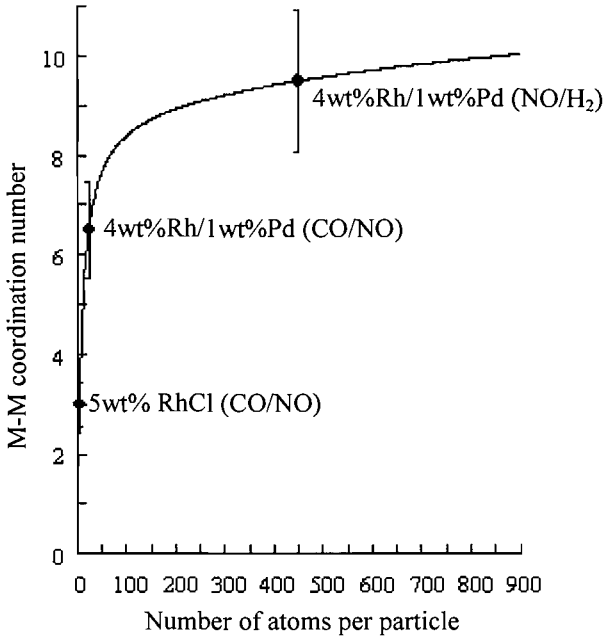

Figure 7.15: Plot of the relationship between average particle atomicity and average Rh-M coordination number for FCC nanoparticles derived from EXAFS measurements. The average N_1^M value for the systems/conditions in question are also displayed (taken at room temperature), with error bars given at the 15% level.

The figure highlights that a coordination number of up to ca. 9 is an effective indicator of the average particle size and the average radius (r_p), based on an FCC hemispherical morphology of the nanoparticles. Assuming that the nanoparticles under current scrutiny do exist as FCC entities, the results would suggest the following. During the analogous NO/H_2 reaction results from Rh EDE data show the average alloyed RhPd nanoparticles to contain between 200 to over a 1000 atoms (equating to an average of ca. 450 atoms). This corresponds to a particle size distribution (PSD) lying between 10Å < r_p > 17Å. Under the CO/NO feedstock currently employed (at room temperature) these values are seen to be significantly reduced for the same RhPd catalyst; the average atomicity now lies between 20-40 atoms. This clear reduction equates to a PSD lying between 4.6Å < r_p > 6 Å.

In this instance the 5wt% RhCl system (and therefore also the RhN system investigated in section 6.2) has to be considered in a different manner as N_1^{Rh} values of 2-3 cannot be indicative of FCC particles. Although unlikely, extended formations of Rh_3 or Rh_4 units could index the low coordination numbers observed; DRIFTS results suggest this not to be the case due to the species forming on the Rh surface. Therefore it is only above ca. 550 K

and the consequent increase of coordination to values resembling metallic Rh ($N_1^{Rh} \approx 7$) can this system be viewed as existing in an fcc, metallic environment.

7.3.3 Discussion and conclusions

The DRIFTS and mass spectrometric results obtained for the 4wt%Rh/1wt%Pd and elemental 5wt% RhCl systems show the catalysts to display strikingly similar behaviour in terms of selectivity and activity during the reduction of NO by CO, an effective example being the essentially invariant selectivity towards N_2O production. The structural data extracted from synchronously obtained EDE presents evidence contrary to these results, with factors such as metal phase changes and particle morphology all playing a key role in the complex make-up of these systems. This viewpoint must however be approached with caution as EXAFS is an averaging technique, the active species forming on the surfaces could conceivably be the same. Also, if the Pd was an active component, then subsequent correlations made between the two systems would not be probed by analysing the Rh K edge alone. As such the following discussion is based on the data that has been formally analysed, and fits into a viable scenario.

The collective, complementary results for both catalysts indicate that below 500 K and under the CO/NO feedstock used the Rh component has been fragmented. This disruption of the initial nanoparticles into what is most likely a mixture of discrete $Rh(CO)_2$ units and small Rh clusters occurs for both systems. These results are unexpected when considering the alloy system, based upon the extensive previous knowledge of these bimetallic systems. The 4wt%Rh/1wt%Pd system has been demonstrated to effectively insulate the Rh component against any facile NO oxidation. Moreover, the alloy system consists of particles that have an average atomicity that is up to 70 times larger than previous studies investigating the disruptive capacity of CO on Rh.[21,22] The 5wt% RhCl system has an average atomicity that is up to ca. 3 times greater than the systems used in the same mentioned studies.

The aforementioned insulation of the Rh component in the alloy catalyst was explained and evidenced by the segregation of Pd to the surface of the particles, preventing the dissociation of NO.[7] Although Rh is well known to dissociate CO, by results from this thesis (see chapter 5) and numerous other studies,[23] the oxidative disruption is generally regarded to

proceed as a molecular adsorption. Contrary to dissociative adsorption, the segregated Pd at the surface of the particles should not significantly affect their capacity to absorb CO (and indeed, NO).[24]

Analysis of all the available data therefore suggests that molecularly adsorbed CO is able to strip Rh with significant efficiency, under the current conditions employed, even from relatively substantial and effectively insulated nanoparticles. This remarkable process occurs to a significant degree until the nanoparticles are 'Pd-rich' enough to resist the disruption. Results also suggest that the Pd component is not significantly affected by the aforementioned process, as it remains in a metallic state throughout the experiments performed.

The argument proposed above also serves to explain the notably similar catalytic behaviour displayed by the elemental Rh and alloyed RhPd catalysts in terms of activity and selectivity. As the majority of the Rh is stripped from its particulate environment, it is reasonable to suggest that it is held on the surface as a relatively unreactive organometallic surface species; thus both species would in essence behave similarly. As the Rh coordination number does not return to values resembling 'fully' metallic Rh nanoparticles (i.e. N_1^{Rh} = 7-10) as most of these surface species are removed also suggests that re-alloying of the Rh with Pd does not occur, essentially resulting in a phase separated system. It is worthy of note that these observations are in contrast to similar studies using NO reduction by H_2,[7,8] where the alloyed nanoparticles significantly promote the catalysis occurring over these structurally interesting and complex systems.

It should be reiterated that the above is only one possible explanation into the processes occurring over these systems. For example, the postulation of a phase separated system may not be accurate due to the averaging nature of the EXAFS technique. The coordination values are observed to decrease from ~7.7 to 6.8 which correspond to a decrease of ~55 to 50 atoms. The EXAFS does not allow for the distinction between Rh and Pd; therefore the overall disruptive process may be wholly, or indeed partly, due to particle size effects.

In summary, the complementary data obtained during the temperature controlled NO reduction by CO highlight the extensive, disruptive oxidation of Rh nanoparticles, the capacity of which exceeds measurements made in previous studies. That these unexpectedly corrosive processes were previously unknown, or at the very least underestimated, would

have a profound impact on the core understanding of their catalytic influence. This in turn would directly affect technological applications such as catalyst design, such as the three-way automotive catalyst for which the NO/CO reaction is a paramount consideration.

This study therefore introduces the need for future projects to consider the fundamental chemistry occurring over the nanoparticulate surfaces, and how structural variances can significantly affect the characteristics of such catalytic systems.

7.4 The structural-reactivity behaviour of RhCl systems during temperature controlled switching experiments between gas flows of CO and NO

Further to the experiments performed within this chapter, a new method employing the continual periodic switching of $CO_{(g)}$ and $NO_{(g)}$ in the gas stream was instigated. The aim of these experiments was two-fold: to expand and test the EDE/DRIFTS/MS experiment's capabilities under such conditions whilst probing the structure-function responses of the catalysts under varying catalytic conditions further. These isothermal experiments were carried out at three relevant temperatures: at 473 K where the onset of catalysis is observed, a temperature above the region where the rise in Rh-Rh coordination is in line with the catalysis (573 K) and finally at a temperature where the catalysis ensues at a rapid rate (623 K). The reasons for choosing these temperatures can be realised on inspection of figure 7.4.

7.4.1 Experimental

The basic experimental parameters such as catalyst pre-treatment and EDE/DRIFTS/MS data acquisition remain unchanged as described above in section 7.2. The switching experiments introduced a flow of 5%NO/95%He in synchrony to the start of the experiment (the catalyst charge was held in a flow of 5%CO/95%He prior to the start of the experiment). The gas flows (set at 25 $mlmin^{-1}$ each) were then alternated at 10 second intervals over a period of 90 seconds.

Although these experiments were performed using the 2.5wt% and 5wt% RhCl systems over a range of temperatures (298 K – 673 K in 50 K steps), only data obtained at 473, 573 and 623K for the 5wt% RhCl system was of sufficient quality to permit full analysis. Also,

the simultaneously obtained MS data was corrupted in parts due to software problems, and therefore will be excluded from any further discussion.

7.4.2 Results

Figure 7.16 plots the Rh-Rh coordination values as a function of time during the CO/NO switching experiments. The initial N_1^{Rh} values of the catalyst of ca. 7 are consistent with the results described in chapter 4; the CO adsorption study on identical Rh systems uncovered similar coordination values regardless of the temperature employed (i.e. no significant particle disruption was observed under the flow of $CO_{(g)}$).

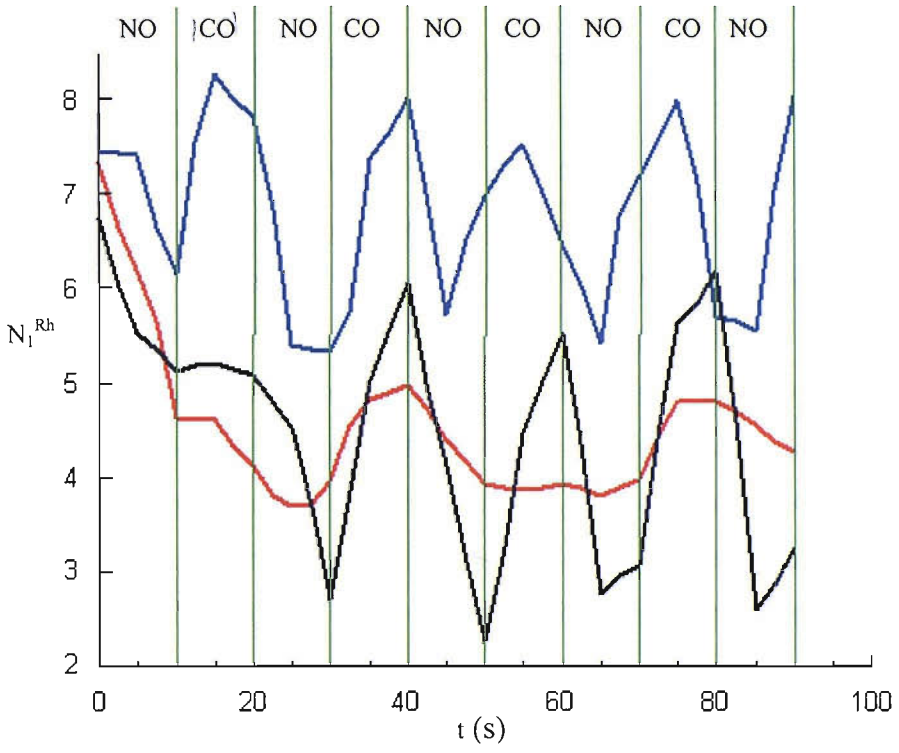

Figure 7.16: Variation of Rh-Rh coordination during the NO/CO switching experiment over 5wt% RhCl at; 473 K (red line), 573 K (black line) and 623 K (blue line). The corresponding gas switching is indicated by the intersecting green lines. One EDE spectrum every 2.5s was analysed.

The initial switch from a flow of $CO_{(g)}$ to $NO_{(g)}$ (i.e. the first 10 seconds of the experiment) instigates another expected result of Rh particle oxidation. By switching to the flow of the easily dissociable oxidant NO, rapid disruption of the Rh component is observed, which is comparable to the time resolved experiments carried out in chapter 6. The extent of this oxidation appears to be directly correlated to the temperature employed; by 10 seconds the N_1^{Rh} values have fallen to ca. 4.5 at 473 K, 5 at 573 K and 6 at 623 K.

After this initial switch, the subsequent periodic alternation of the gas flow yields significantly differing structural-reactive behaviour at the temperatures employed. Extensive oxidation of the nanoparticles takes place during the first 30 s of the experiment at 473 K; the coordination number attenuates to ca. 3.7. An increase to an N_1^{Rh} value of ca. 5 is observed between 30 and 40 s, after which values of ca. 4 are indexed between 50 and 70 s. The pattern of coordination variation during 30 to 70 s appears to repeat itself during the last 20 s of the experiment, although longer experiment times would have to be performed to confirm any consistent periodic pattern.

Increasing the temperature by 100 K to 573 K does not significantly affect the oxidation process seen at 473 K over the period of the first ca. 30 s; in fact the process is more extensive with N_1^{Rh} values as low as ca. 2.7 being indexed. After this time the structural profile differs with more substantial changes; there is an apparent oscillating variation of the Rh-Rh coordination which has a period of ca. 20 s during which the N_1^{Rh} values varies between ca. 2.5 and 6. Moreover, these variances can be correlated to the gas flows they are subjected to; the local coordination value falls as $NO_{(g)}$ oxidises the system, a 'recovery' with the re-reduction of the Rh component is observed when the flow is switched to $CO_{(g)}$.

A similar pattern of behaviour is observed at 623 K but with one main exception; there is a dampened response of the initial oxidation step during the first ca. 30 s that is seen at lower temperatures. The initial switch from $CO_{(g)}$ to $NO_{(g)}$ does partially oxidise the system as expected, the coordination number falls from ca. 7.5 to index a value of 6 at by 10 s. However the switch back to a flow of $CO_{(g)}$ re-reduces the particles within 5 seconds of exposure; the N_1^{Rh} value is ca. 8.2 at 15 s. After this time a similar pattern of oscillatory behaviour is observed as described for the experiment run at 573 K, but with the system indexing significantly higher coordination numbers.

The effect of performing the experiment at 623 K appears to have two ramifications. Firstly, the catalyst does not appear to be extensively oxidised at any stage of the experiment when compared to the experiments performed at lower temperatures, an average N_1^{Rh} value of 6.8 is reported (compared to ca. 4.5 at lower temperatures). Also, the catalyst is seen to respond to the course of the gas switching more closely, i.e. each gas switch invokes a comparatively instantaneous and substantial response shown by the fluctuation in Rh-Rh coordination (see below).

The EDE spectra shown in figure 7.17 details the XANES region from a peak and a trough of a typical 'cycle' explained above for all the temperatures studied; for consistency all data points were taken from between t = 30 and 50 s. Table 7.7 gives the relevant structural and statistical data for the spectra. The persistent oxidic signature of the EXAFS and low coordination ($N_1^{Rh} \approx$ 4-5) at 473 K is expected based upon results shown in figure 7.16. These data become more interesting at 573 K, where the metallic XANES signature (indexing an N_1^{Rh} value of ca. 6) changes to an almost completely oxidic, 'Rh_2O_3-like' environment evidenced by a coordination value minimum of 2.2. The characteristic EXAFS pattern observed at 623 K is consistent with the Rh nanoparticles residing in a metallic environment; the statistics confirm this as coordination values in the range of ca. 6-8 are reported throughout the 'cycle'. Although most likely, the formation of an oxide may not be the only cause for the reduction of the Rh-Rh 1st shell coordination number in these experiments, a notion that is re-iterated throughout this chapter. It may be equally likely that the disruptive processes yielding smaller surface particles may be the cause of the reduction in coordination; further experiments involving XANES and analysis of Rh-O contributions would be needed to assess the overall influence of particle sizes.

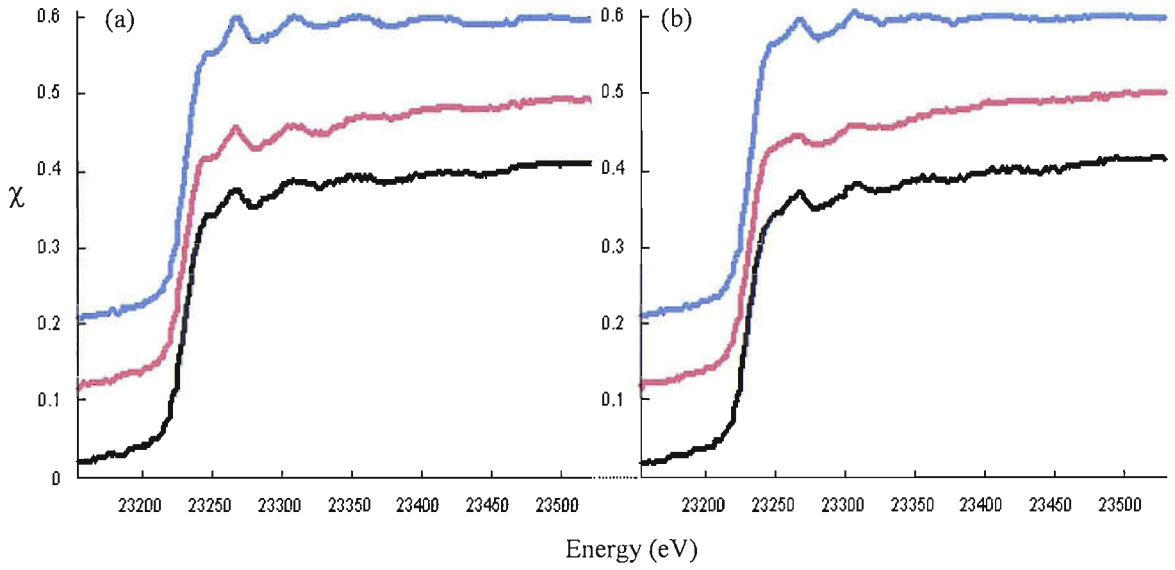

Figure 7.17: EDE spectra detailing the XANES region for a typical 'cycle' observed during the CO/NO switching experiment as shown in figure 7.16; part (a) shows spectra from a 'peak' at t = 40s and part (b) from a 'trough' at t = 50s (except for 623K where t = 45s). Black line = 473 K, red line = 573 K, blue line = 623 K.

Sample/Conditions	Scatterer (s)	CN	r/Å	R/%	Ef/eV	k/ $Å^{-1}$
(a) 5wt% RhCl at t = 40 s and 473K (black line)	Rh	4.9 (±0.5)	2.67 (±0.02)	58	-3.29	3-12
(b) 5wt% RhCl at t = 50 s and 473K (black line)	Rh	3.9 (±0.3)	2.66 (±0.02)	59	-4.10	3-11
(a) 5wt% RhCl at t = 40 s and 573K (red line)	Rh	6.1 (±0.5)	2.63 (±0.02)	56	2.72	3-11
(b) 5wt% RhCl at t = 50 s and 473K (black line)	Rh	3.9 (±0.3)	2.66 (±0.02)	59	-4.10	3-11
(a) 5wt% RhCl at t = 40 s and 623K (blue line)	Rh	7.9 (±0.7)	2.66 (±0.02)	50	0.79	3-13
(b) 5wt% RhCl at t = 45 s and 623K (blue line)	Rh	5.7 (±0.5)	2.67 (±0.02)	56	0.19	3-13

Table 7.6: Structural and statistical data derived from the analysis of the EDE data as shown in figure 7.17. The DW factors ($2\sigma^2/Å^2$) used were: 0.011 at 473 K, 0.016 at 573 K and 0.017 at 623 K.

The significant structural changes that are observed at lower temperatures over the course of the experiment are further evidenced by the information laid out in table 7.7, which indexes the state of the catalyst at the beginning and end of the experiment. The low coordination values of ca. 4 and 3 at 473 K and 573 K (at t = 90 s) respectively clearly show

the predominantly oxidic state of the Rh; it is only by 623 K that the system can respond effectively enough to the gas switching to remain in a metallic state (N_1^{Rh} = 8 at t = 90 s).

Sample/Conditions	Scatterer (s)	CN	*r*/Å	R/%	Ef/eV	k/ Å^{-1}
5wt% RhCl at t = 0 s at 373 K	Rh	7.1 (±0.6)	2.66 (±0.02)	49	0.58	3-12
5wt% RhCl at t = 90 s at 373 K	Rh	4.2 (±0.3)	2.65 (±0.02)	55	3.53	3-11
5wt% RhCl at t = 0 s at 473 K	Rh	6.7 (±0.5)	2.64 (±0.02)	56	3.82	3-12
5wt% RhCl at t = 90 s at 473 K	Rh	3.3 (±0.2)	2.61 (±0.02)	61	-6.09	3-11
5wt% RhCl at t = 0 s at 623 K	Rh	7.3 (±0.5)	2.65 (±0.02)	54	-2.64	3-13
5wt% RhCl at t = 90 s at 623 K	Rh	8.0 (±0.7)	2.65 (±0.02)	56	0.42	3-13

Table 7.7: Structural and statistical information derived from analysis of the EDE data taken at the start and end of the CO/NO switching experiment.

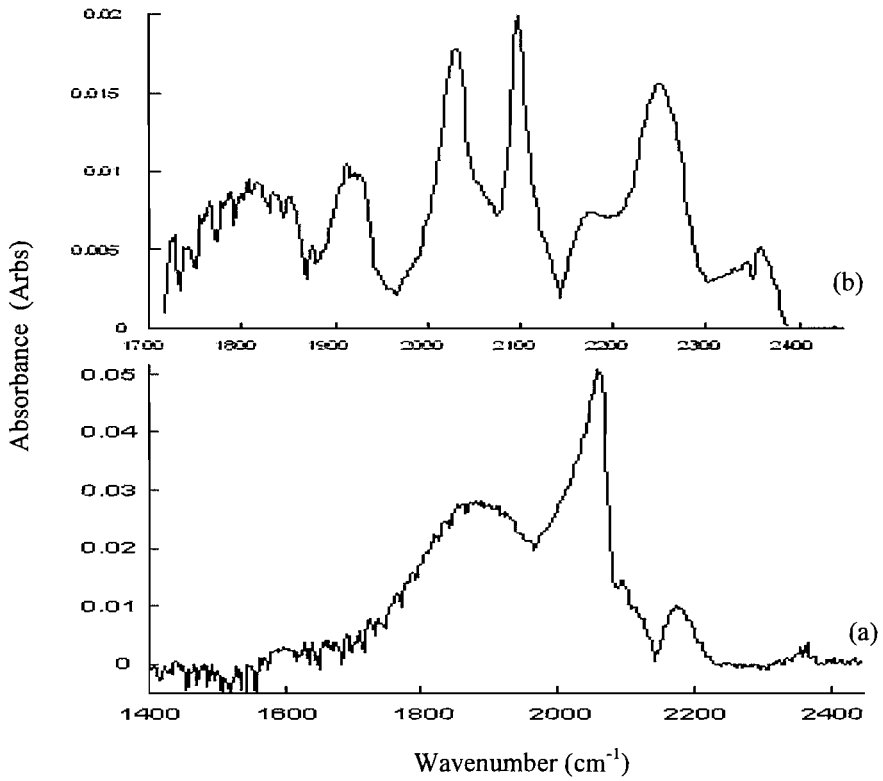

Figure 7.18: Absorbance DRIFTS spectra (4 cm^{-1} resolution) obtained during the CO/NO switching experiments at 473 K for the 5wt% RhCl system; (a) under 5% CO/He t = 0 s and (b) at t = 60 s (catalyst is under $CO_{(g)}$) after continual switching between $CO_{(g)}$ and $NO_{(g)}$.

The static absorbance DRIFTS data shown in figure 7.18 serves to identify the surface species formed during the experiment, and the results reinforce the trends seen in the simultaneously obtained EDE data at 473 K.

The sharp peak in figure 7.18 part (a) at 2059 cm^{-1} can be assigned to the linear CO (CO_L) species, and the broader, less intense peak centred on ca. 1886 cm^{-1} to the bridged CO (CO_B) species. This is consistent with the results obtained in an earlier chapter (see chapter 5), where both carbonyl species were established as being bound to Rh metal. This result combined with the absence of such species as the $Rh(CO)_2$ unit verifies the metallic environment the EDE data reports. The absence of the geminal dicarbonyl unit cannot be wholly discounted, as it may exist in less significant proportions (i.e. the peaks could be present underneath the broad band associated with CO_B).

Figure 7.18 part (b) is given as a prototypical DRIFTS spectrum, selected at t = 60 s to highlight the range of surface species that are observed over the duration of the experiment. As expected, the species that do form are indicative of the Rh species existing in an oxidic state. The $Rh(CO)_2$ species dominates the spectrum with two sharp peaks (υ_{sym} ~ 2096 cm^{-1}, υ_{aym} ~ 2030 cm^{-1}). The broad peak centred at ca. 1805 cm^{-1} can be assigned to a monodispersed $Rh(NO)^-$ species and/or the $Rh(NO)_2$ site. The $Rh(NO)^+$ species is observed to exist on the surface, with a strong signal peak at 1913 cm^{-1}.

As such, after the initial oxidative process over the first ca. 20-25 s of the experiment, the EDE and DRIFTS data are very similar to those obtained using an identical catalyst subjected to a 50:50 flow of 5%CO/5%NO/He at 473 K (see section 7.2).

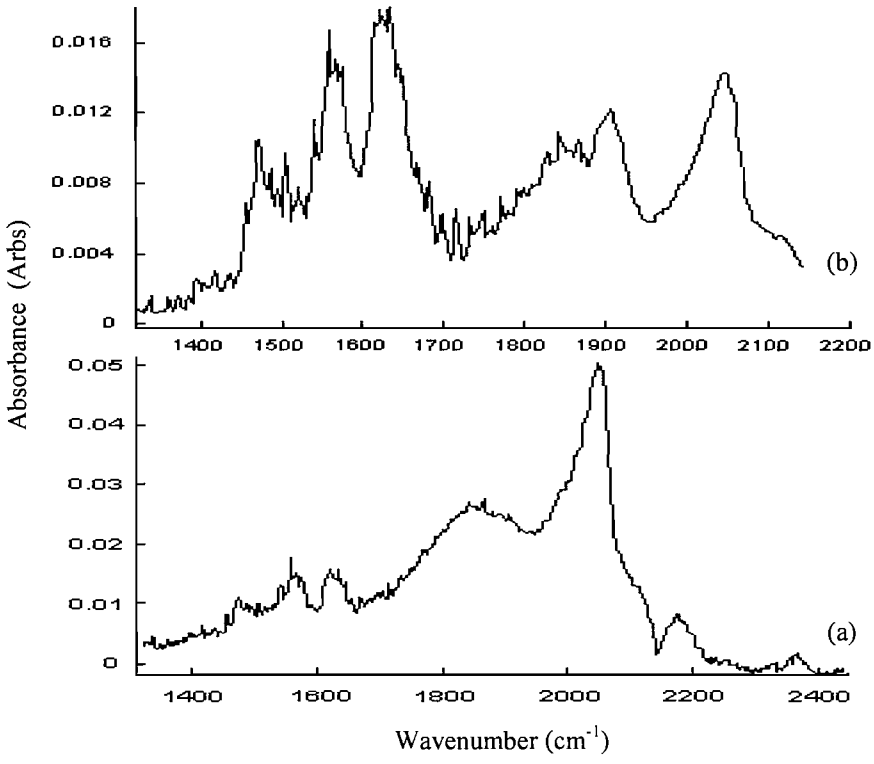

Figure 7.19: Absorbance DRIFTS spectra (4 cm^{-1} resolution) obtained during the CO/NO switching experiments at 573 K for the 5wt% RhCl system; (a) under 5%CO/He t = 0 s and (b) at t = 60 s (catalyst is under $CO_{(g)}$) after continual switching between $CO_{(g)}$ and $NO_{(g)}$.

The DRIFTS data shown in figure 7.19 part (a) again shows evidence of the metallic environment prior to the start of the experiment at 573 K with the CO_L and CO_B species evident, significant surface coverage of the species still exists even at this temperature. Assuming reproducible experiments have been performed, based on the integrals of the absorbance DRIFTS data (a semi-quantitative technique used throughout this thesis) ca. 92% of CO_L and 75% of CO_B are still present on the surface when compared to the case at 473 K. However, the spectrum in part (b), taken at t = 60 s, shows a significant change has occurred with respect to the surface adsorbates present on the surface of the catalyst. The most notable difference is the absence of the characteristic $Rh(CO)_2$ peaks that were present at 473 K; the spectrum above 1700 cm^{-1} is now dominated by the CO_L (υ (C-O) ~ 2043 cm^{-1}) and the linear nitrosyl species (υ (N-O) ~ 1907 cm^{-1}). There is also a shoulder region evident just below the nitrosyl species that can be assigned to the CO_B species. The intense peak at 1622

cm^{-1} could be due to NO bound to metallic Rh, and is quite possible as the EDE reports that the system does retain some metallic character throughout the experiment. Contributions from nitrates and carbonates on the alumina surface are the most likely cause for the peaks at ca. 1570 cm^{-1} and 1472 cm^{-1} respectively.[14]

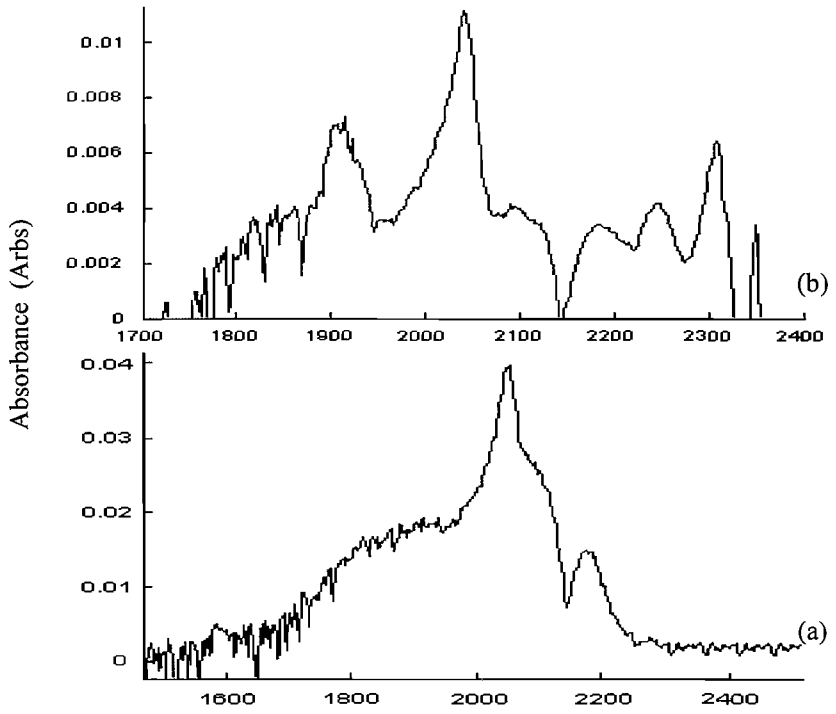

Figure 7.20: Absorbance DRIFTS spectra (4 cm^{-1} resolution) obtained during the CO/NO switching experiments at 623 K for the 5wt% RhCl system; (a) under 5%CO/He t = 0 s and (b) at t = 60 s after continual switching between $CO_{(g)}$ and $NO_{(g)}$.

The CO_L and CO_B species in figure 7.20 part (a) are an expected result, but the spectrum is shown to illustrate that the species are persistent in significant proportions even at 623 K. Again, assuming each experiment is performed in an identical manner, the absorbance DRIFTS integral data reports there to be ca. 78% and 61% of the CO_L and CO_B species respectively remaining on the surface when compared to the case at 473 K.

Figure 7.20 part (b) is similar to the analogous spectrum at 573 K, with the linear nitrosyl and carbonyl peaks at ca. 1914 cm^{-1} and 2041 cm^{-1} respectively. The data taken at t = 60 s reports that ca. 82% of the CO_L and ca. 60% of the linear nitrosyl species remains at this temperature when compared to the species' coverage at 573 K. Another important

comparison at this temperature is the significant attenuation of the shoulder region (due to the CO_B species) just below 1900 cm^{-1}, although contributions from the linear nitrosyl peak do not permit a quantitative assessment of the extent of this coverage depopulation.

Figure 7.21 part (a) follows the pertinent IR active surface species as a function of time at 473 K; and in doing so the time resolved DRIFTS data reveals the system to be far from static. The time frame of 30-50 s was chosen as it effectively portrays a typical 'cycle' of switching and the associated response of the key surface species, i.e. switching from $CO_{(g)}$ → $NO_{(g)}$ → $CO_{(g)}$. The relatively short dead time of a gas switch (as explained in chapter 2.5.8) of just under 2 s, combined with the almost instantaneous responses of the surface species as laid out in figures 7.21-7.23, bolster the validity of the data acquired for the EDE/DRIFTS/MS experiment as a whole.

The 3D plot (figure 7.21(a)) clearly shows the gradual formation of the $Rh(CO)_2$ species as the $CO_{(g)}$ is switched into the feedstock. The subsequent depopulation of this species as $NO_{(g)}$ is introduced over the catalyst is accompanied by the evolution of the linear nitrosyl. It is most likely that the diminution of the $Rh(CO)_2$ species proceeds with the evolution of $CO_{2\,(g)}$, although repetition of the experiment to include mass spectrometric data would need to be performed to validate this. This pattern of response to the gaseous environment by the dominant geminal dicarbonyl and linear nitrosyl species is repeated throughout the experiment in consistent 'cycles'. It is worthy of note that the other surface species explained above in the 'static' DRIFTS spectra do not significantly alter with the gas switching and can therefore be regarded as spectator species.

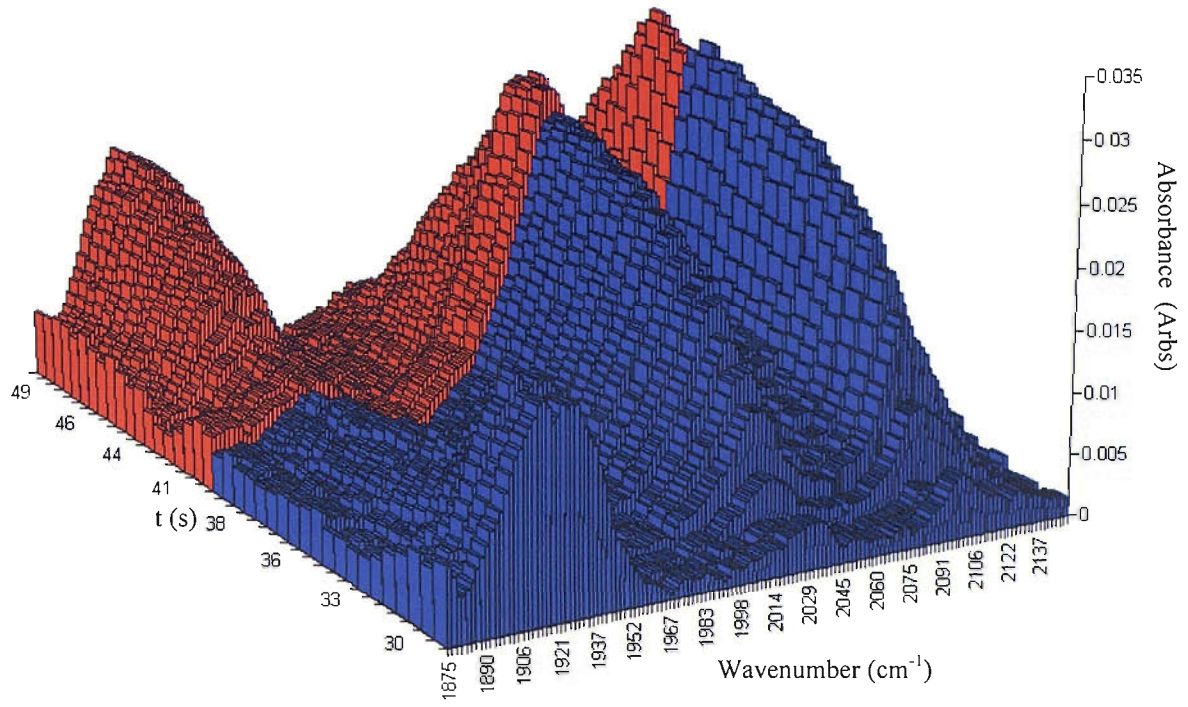

Figure 7.21 (a): Absorbance DRIFTS data (1874 cm^{-1} – 2148 cm^{-1}, 4 cm^{-1} resolution) obtained during the CO/NO switching experiments at t = 30 – 50 s at 473 K. The blue region indicates $CO_{(g)}$ in the feedstock, the red indicates $NO_{(g)}$.

Figure 7.21 part (b) combines the two experimental techniques by indexing the Rh-Rh coordination values and the DRIFTS integrals of the two dominant surface species.

Firstly, the figure shows that the initial switch from $CO_{(g)}$ → $NO_{(g)}$ induces the rapid oxidation (depicted by the EDE data) as explained above, moreover these changes are mirrored in the DRIFTS signal with a sharp decrease in integral intensity for both IR active species. After this time period which approximately spans the first switch (ca. 10 s), the aforementioned 'cycles' can be viewed to proceed with the gas switching; the evolution/depopulation of the geminal dicarbonyl and linear nitrosyl being completely out of phase with each other.

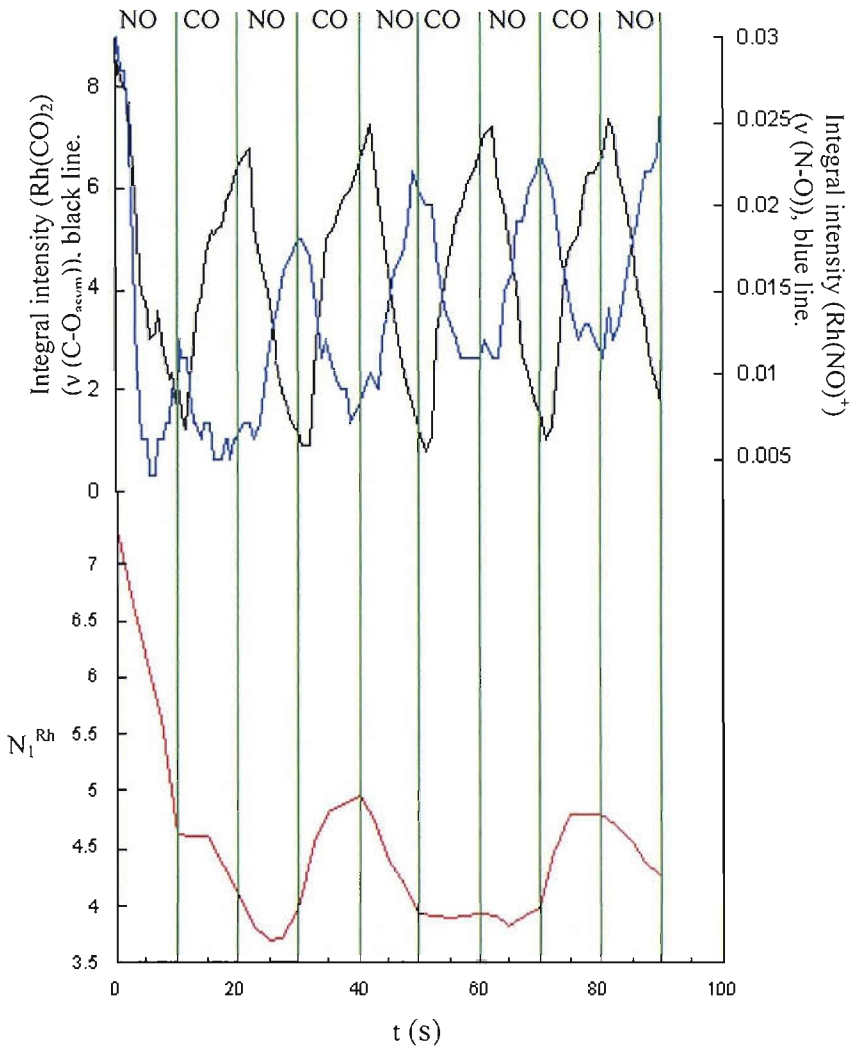

Figure 7.21 (b): Variation of the Rh-Rh coordination value and DRIFTS integrals (as indicated) during the CO/NO switching experiment over 5wt% RhCl at 473 K.

The figure as a whole serves to show that although the surface species respond effectively to the gaseous environment the catalyst is subjected to, this is not the case in a structural sense. At 473 K there is no significant change in the Rh-Rh coordination following the initial, extensive oxidation during the first ca. 10 s. The slight variations in coordination that do occur appear to follow the gas switching with approximately half of the frequency of the overall switching. The significance of this effect would have to be probed further, as the observations may be due to factors such as experimental/data analysis error.

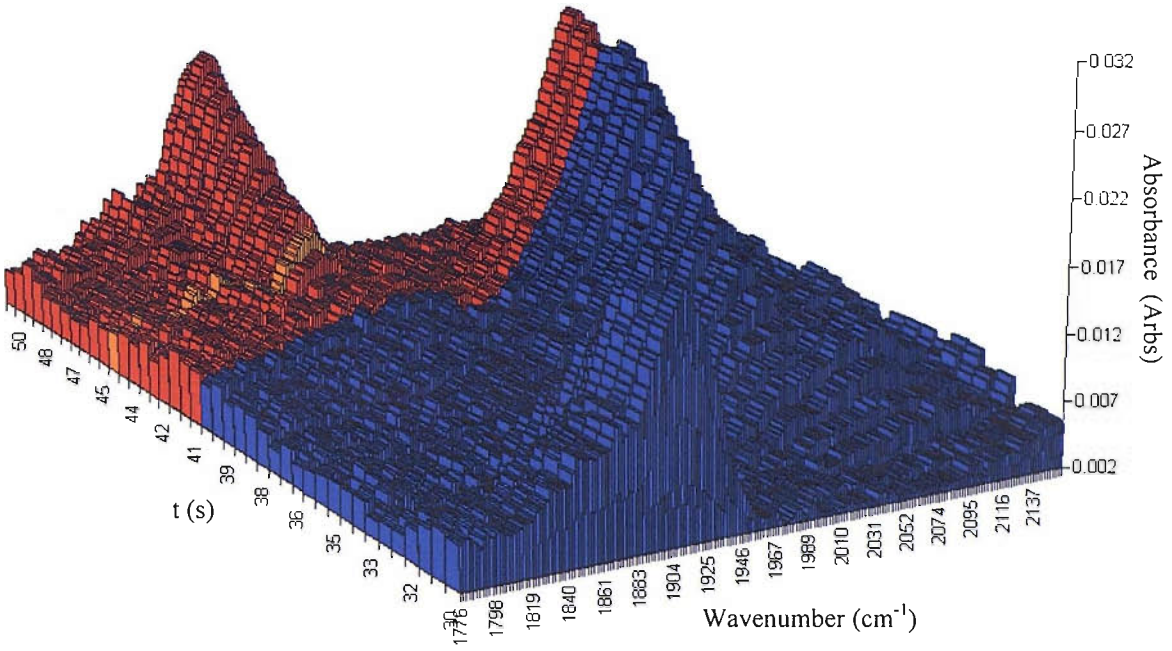

Figure 7.22 (a): Absorbance DRIFTS data (1776 cm^{-1} – 2154 cm^{-1}, 4 cm^{-1} resolution) obtained during the CO/NO switching experiments at t = 30 – 50 s at 573 K. The blue region indicates $CO_{(g)}$ in the feedstock; the red indicates $NO_{(g)}$.

Figure 7.22(a) shows the surface species at 573 K to behave similarly to the gaseous feedstock when compared to the case at 473 K, with the obvious difference of the CO_L/CO_B species now dominating in the cycle in place of the geminal dicarbonyl entity (there is no evidence for $Rh(CO)_2$ forming at this temperature). The presence of the CO_B species occurring as a shoulder to the linear nitrosyl band at just below 1900 cm^{-1} is the most likely cause for the integral data indexing double frequency behaviour (figure 7.22(b)). The figure also effectively shows that after an initial oxidation event, structurally the system closely follows the pattern of gas switching, and such changes are significant when compared to the case at 473 K. This pattern can be summarised as the CO_L/CO_B species forming on metallic Rh (N_1^{Rh} ca. 6) under $CO_{(g)}$ and the $Rh(NO)^+$ entity on oxidised Rh sites (N_1^{Rh} ca. 3) under $NO_{(g)}$.

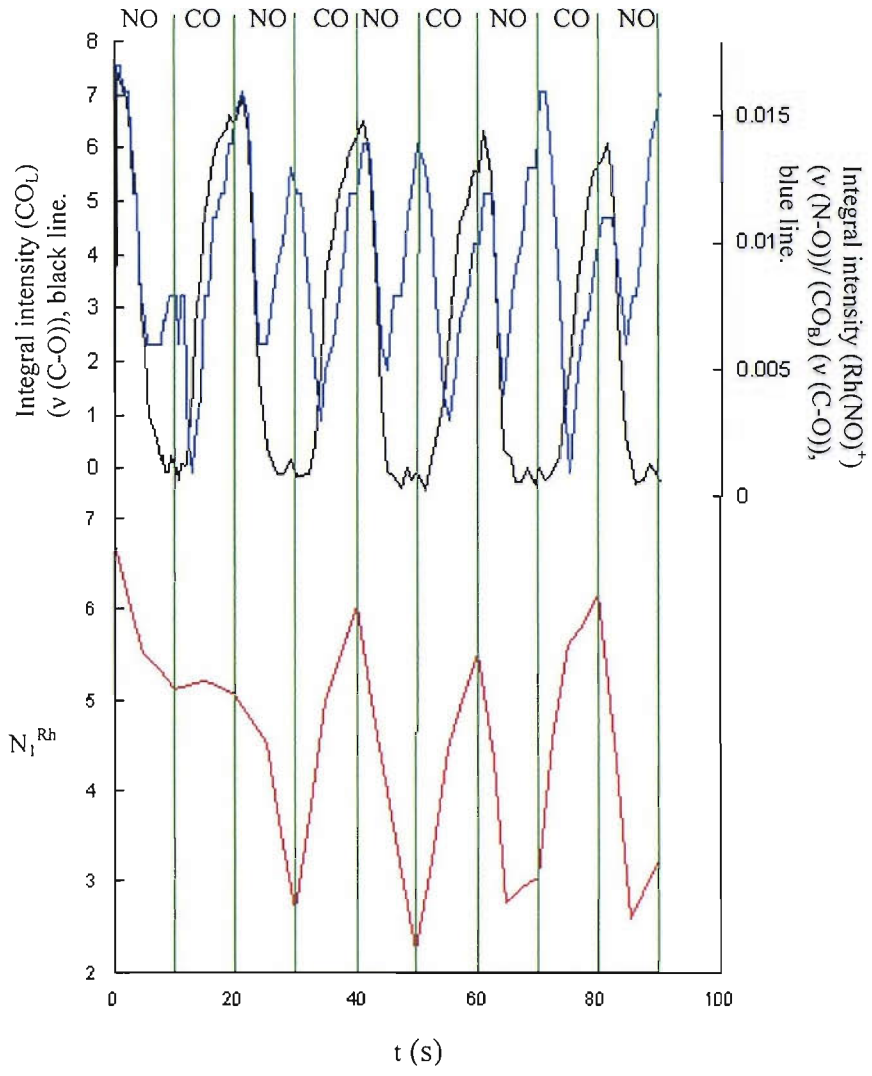

Figure 7.22(b): Variation of the Rh-Rh coordination value and DRIFTS integrals (as indicated) during the CO/NO switching experiment over 5wt% RhCl at 573 K.

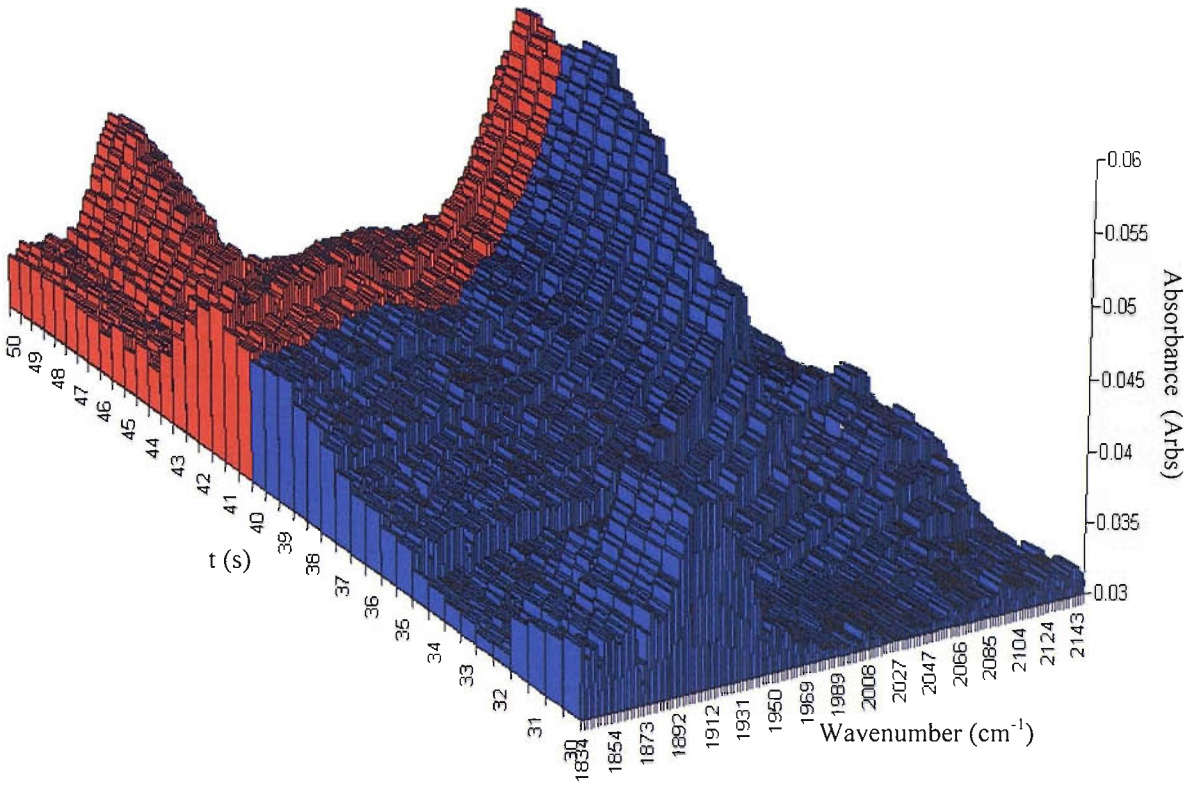

Figure 7.23(a): Absorbance DRIFTS data (1834 cm^{-1} – 2144 cm^{-1}, 4 cm^{-1} resolution) obtained during the CO/NO switching experiments at t = 30 – 50 s at 623 K. The blue region indicates $CO_{(g)}$ in the feedstock; the red indicates $NO_{(g)}$.

The typical cycle of gas switching at 623 K displayed in figure 7.23(a) is almost identical to the behaviour observed at 573 K, with the alternation of the CO_L/CO_B species and linear $Rh(NO)^+$ now being a consistent result at these higher temperatures employed. However, a key difference is exhibited in that the contribution from the CO_B band is significantly less at 623 K (as noted earlier in this section with the corresponding 'static' DRIFTS spectrum). Unfortunately the quantitative assessment of this decrease in surface population is not possible due to the contribution from the overlapping Rh-NO band due to the linear nitrosyl species.

The effect noted above can be counted as significant, as the 'double frequency' of the DRIFTS integral data seen at 573 K is seen to have a more muted effect at 623 K (figure 7.23(b)).

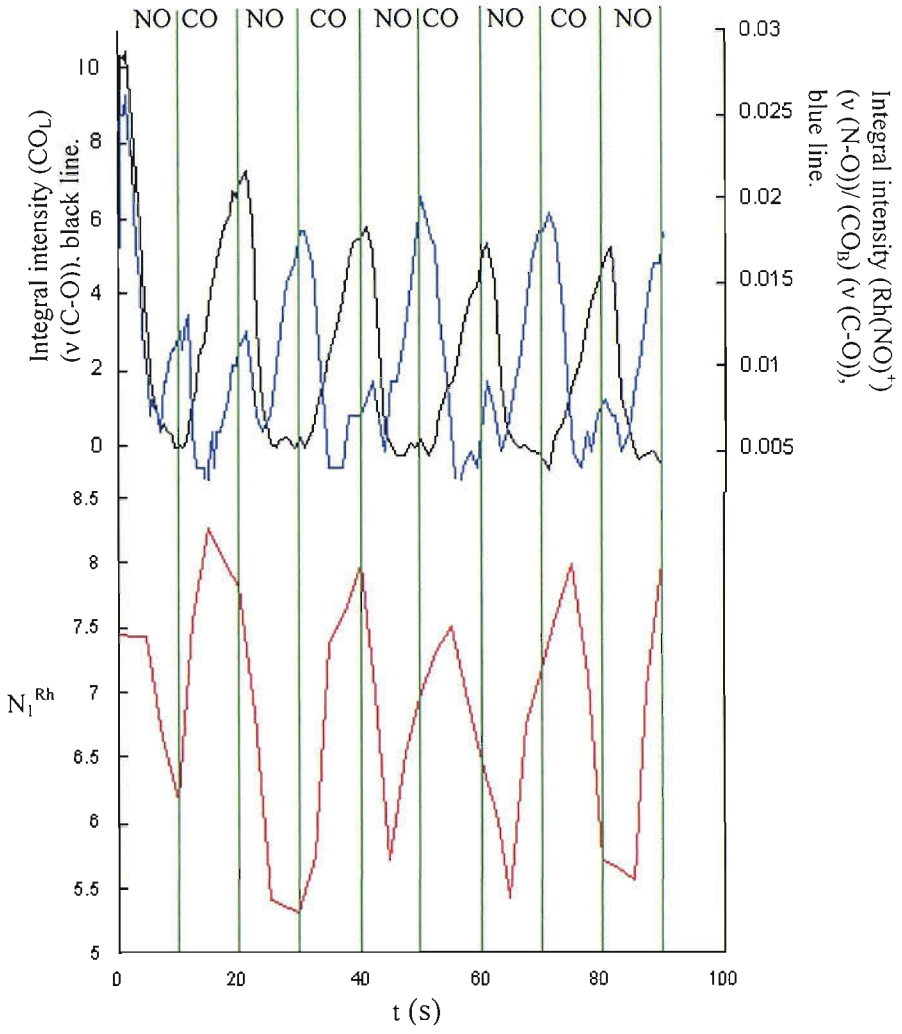

Figure 7.23(b): Variation of the Rh-Rh coordination value and DRIFTS integrals (as indicated) during the CO/NO switching experiment over 5wt% RhCl at 623 K.

The figure also shows the overall effect the absence of the initial, extensive oxidation event has on the behaviour of the catalyst. There is a clear synchrony between the structural response of the nanoparticulate Rh and the gas switching at this elevated temperature; with essentially CO_L forming on wholly metallic fcc Rh (N_1^{Rh} ca. 8) under gaseous CO and $Rh(NO)^+$ on partially oxidised (N_1^{Rh} ca. 5.5) under gaseous NO.

7.4.3 Discussion and conclusions

Firstly, the switching experiments as a whole enabled the testing of the experimental apparatus to temperatures reaching 623 K. This was achieved with no detrimental effect on the quality of the data obtained. They also served to show that the associated deadtimes of the system do not appear to have a significant effect on experiments such as these, i.e. experiments where the gaseous environment is alternated with a fixed, relatively rapid (10 s) frequency.

As such high temperatures (which are within the optimal working regime of many catalyst systems such as the TWC) could be attained, the experiments served another favourable purpose of expanding the studies of $CO_{(g)}$ exposure on Rh systems (see chapter 5), as the systems were held under gaseous CO prior to the start of the experiments. The primary conclusion to be drawn here is the dominant formation of CO_L/CO_B (prior to any gas switching) across the range of temperatures employed; also the species do not invoke any significant disruption of the metallic Rh particles at any temperature (from 298-623 K). Moreover, as the catalyst was held under the gas for extended periods (up to 10 minutes compared to 90 s in the time resolved studies detailed in chapter 5), the disruptive capacity of $CO_{(g)}$ on 5wt% RhCl can be viewed as minimal under the current conditions employed. However, this statement may not be totally accurate when considering that a decrease in N_I^{Rh} of ca. 0.5 (for example) for 'smaller' surface particles may potentially be significant; EXAFS however is an averaging technique and the most likely conclusions are drawn from the analysis of the results.

The initial oxidation event that occurs upon the first gas switch is observed to be a key factor in how the system responds to further changes in the feedstock, as well as its overall structure-function characteristics throughout the course of the experiment.

At lower temperatures (473 K) the nanoparticles are disrupted under $NO_{(g)}$ in a similar manner seen in a previous chapter (see chapter 6) and other previous studies.[9,10] Cleavage of these particles is extensive enough for the Rh to now reside as significantly smaller oxidic particles, and potentially as discrete surface entities. The dispersed Rh has the capacity for the facile formation of the $Rh(CO)_2$ species under $CO_{(g)}$; hence the system remains as a

predominant oxide throughout the experiment with no evidence of the Rh reclustering back into its original particulate form.

At the highest temperature employed (623 K) there is now sufficient energy that can be supplied by the local environment to facilitate the almost instantaneous response of particulate Rh to the gases introduced over the catalyst. As the Rh particles are not extensively corroded at the start of the experiment, there is now an interchange between CO bound on metallic Rh and the omnipresent linear nitrosyl species on partially oxidised Rh particles. Moreover, there is no apparent evidence for any particle fragmentation occurring throughout the experiment as the system efficiently re-reduces to its original coordination environment under $CO_{(g)}$.

An 'intermediary' case is observed at 573 K where the system displays elements from both of the temperature extremes employed. As the Rh retains the majority of its metallic character under $CO_{(g)}$, it is most likely that a mixture of partially corroded particulate and atomic Rh sites exist on the catalyst surface. Another likely surface morphology is 'intact', undisrupted Rh particles consisting of an oxidic outer layer and a metallic inner core (as described in chapter 4); the interchanging processes observed would therefore take place at the fringes of such particles. This concept could also be applied to the case at 623 K.

Although the system is observed to remain structurally stable at higher temperatures (in the sense that metallic Rh is reformed upon exposure to $CO_{(g)}$ in a consistent, cyclic manner), longer timescales and/or higher operating temperatures would be needed to test if the nanoparticles would eventually fragment. More importantly the effect on the characteristics of the processes involved would be of great interest.

The inclusion of the synchronous MS data would be the main aim for future work, as the combination of MS and DRIFTS data taken in parallel has afforded invaluable information on the kinetics and mechanism of various reactions,[25] such as the determination of the active site for CO oxidation on Rh/Al_2O_3.[26] The influence of how varying particle sizes effect the overall processes (and hence data analysis) that occur in such experiments is an recurring aim for future work; which would include more detailed study into the XANES and TEM data obtained for these systems to try and address this issue.

In summary, the structure-function response of the 5wt% RhCl catalyst to the gas switching regime established is heavily influenced by the phase (and experimental

temperature) of the Rh in the early stages of the experiment. At lower temperatures the almost static oxidic Rh phase is evidenced by the predominant, discrete $Rh(CO)_2$ unit under $CO_{(g)}$. Moving to higher temperatures, the changes in structure are more substantial and follow the pattern of the gas switching closely, primarily due to the Rh remaining in particulate form, further evidenced by the presence of carbonyl species bound to metallic Rh.

Such experiments provide a solid foundation for future studies involving catalysts, especially where the reactive feedstock and environmental conditions are varied constantly, the three way automotive catalyst being a primary example.

7.5 References

[1] For instance, K.C. Taylor, *Catal. Rev. Sci. Eng.*, 1993, **36**, 457.

[2] V.P. Zhdanov, B. Kasemo, *Surf. Sci. Rep.*, 1997, **60**, 31.

[3] P. Granger, H. Praliauad, J. Billy, L. Leclercq, G. Leclercq, *Surf. Interface Anal.*, 2002, **34**, 92.

[4] T. Chafik, D.I. Kondarides, X.E. Verykios, *J. Catal.*, 2000, **190**, 446.

[5] K.A. Alumusaiteer, S.S.C. Chuang, C.D. Tan, *J. Catal.*, 2000, **189**, 247.

[6] E. Nóvak, F. Solymosi, *J. Catal.*, 1990, **125**, 112.

[7] M.A. Newton, A. J. Dent, S. Diaz-Moreno, S. G. Fiddy, B. Jyoti, J. Evans, *Chem. Phys. Chem.*, 2004, **5**, 1056.

[8] B. Jyoti, MPhil Thesis, University of Southampton, 2002.

[9] T. Campbell, A. J. Dent, S. Diaz-Moreno, J. Evans, S. G. Fiddy, M. A. Newton, S. Turin, *Chem. Comm.*, 2002, 304.

[10] M.A. Newton, A. J. Dent, S. Diaz-Moreno, S. G. Fiddy, J. Evans, *Angew. Chem. Int. Ed.*, 2002, **41**, 2587.

[11] B.E. Hayden, A. King, M.A. Newton, N. Yoshikawa, *J. Mol. Catal. A*, 2001, **167**, 33.

[12] H. Arai, H. Tominaga, *J. Catal.* 1976, **43**, 131.

[13] M.A. Newton, D.G. Burnaby, A.J. Dent, S. Diaz-Moreno, J. Evans, S.G. Fiddy, T. Neisius, S. Turin, *J. Phys. Chem. B.*, 2002, **106**, 4214.

[14] M.A. Newton, D.G. Burnaby, A.J. Dent, S. Diaz-Moreno, J. Evans, S.G. Fiddy, T. Neisius, S. Pascarelli, S. Turin, *J. Phys. Chem. A.*, 2001, **105**, 5965.

[15] P. Johnston, R.W. Joyner, *J. Chem. Soc. Faraday Trans.*, 1990, **89**, 863.

[16] M.A. Newton, B. Jyoti, A.J. Dent, S.G. Fiddy, J. Evans, *Chem. Commun.*, 2004, 2382.

[17] M. Harada, K. Asakura, Y. Ueki, N. Toshima, *J. Phys. Chem.*, 1993, **97**, 10742.

[18] J. Evans, B.E. Hayden, G. Lu, *Surf. Sci*, 1996, **360**, 61.

[19] J. Liang, H. P Wang, L. D. Spicer, *J. Phys. Chem.*, 1985, **89**, 5840.

[20] A. Jentys, *Phys. Chem. Chem. Phys.*, 1999, **1**, 4059.

[21] H.F.T. Van't Blik, J.B.A.D. Van Zon, T. Huiziinga, J.C. Vis, D.C. Koningsberger, R. Prins, *J. Phys. Chem.* 1983, **87**, 2264.

[22] A. Suzuki, Y. Inada, A. Yamaguchi, T. Chihara, M. Yuasa, M. Nomura, Y. Iwasawa, *Angew. Chem. Intl. Ed.*, 2003, **42**, 4795.

[23] For instance, S. Andersson, M. Frank, A. Sandell, A. Giertz, B. Brena, P.A. Bruwiler, N. Martensson, J. Libuda,, M. Baumer, H.J. Freund, *J. Chem. Phys.*, 1998, **108**, 2967.

[24] M.A. Newton, B. Jyoti, A.J. Dent, S.G. Fiddy, J. Evans, manuscript in preparation.

[25] M. Marwood, R. Doepper, A. Renken, *Can J. Chem. Eng.*, 1996, **74**, 660.

[26] M. Cavers, J.M. Davidson, I.R. Harkness, L.V.C. Rees, G.S. McDougall, *J. Catal.*, 1999, **188**, 426.

Chapter 8. The response of Rh/Al_2O_3 catalysts to H_2S and SO_2; subsequent poisoning of NO reduction by H_2

8 The response of Rh/Al_2O_3 catalysts to H_2S and SO_2; subsequent poisoning of NO reduction by H_2.

8.1 Introduction

One of the main aims of this thesis has been concerned with investigating the catalytic behaviour of supported Rh nanoparticles in terms of both net performance and catalyst structure under various conditions. The poisoning of any catalyst system is an inherent consideration for the overall design process involved in optimising the working life of the system.

Sulfur containing molecules are well known to be extremely efficient poisons in a diverse range of catalytic processes. This includes the reduction of NO by Rh containing catalyst systems.[1,2,3,4] The same reaction has been used to much effect in the past to investigate the structure-function characteristics of Rh systems identical to the catalysts probed by this thesis.[5] Although widely acknowledged as a poison, sulphur can also act to enhance the catalytic selectivity in other systems.[6]

The absorption of sulfur containing molecules on Rh and its subsequent impact on factors such as catalytic structure has generally been the focus of studies utilising extended Rh surfaces.[7,8,9] This is despite that in other cases, model or supported, highly dispersed nanoparticles are known to respond morphologically to sulphur adsorption.[10]

This section will therefore investigate how Rh nanoparticles respond to H_2S and SO_2, gases which have the potential to elicit observable structural changes in the catalyst composition. The subsequent effect these changes have on the net performance of a catalytic reaction will be charted via NO reduction by H_2.

8.2 Experimental

A typical experimental procedure for EDE/MS data acquisition was carried out as follows. The EDE//MS microreactor experimental apparatus was used as outlined fully in chapter 2.5.7. The 5 wt% catalyst studied in this chapter was prepared using the chlorinated precursor

as explained in chapter 2.9. The previously calcined and reduced catalyst sample (ca. 20 mg) was loaded into a quartz tube, which was then placed into the microreactor apparatus.

Each catalyst was pre-treated in situ prior to any EDE/MS experiment. The samples were exposed to a flow of 5 $\%H_2$/He (20 ml min^{-1}) for approximately 30 minutes at room temperature. EDE/MS data was obtained in synchrony to the introduction of the gas (5% H_2S/He or 5% SO_2/He set at 20 ml min^{-1}) to the microreactor system. For the NO/H_2 poisoning experiments the sulphur containing gases were pulsed into a 20 ml min^{-1} flow of NO/H_2/He (H_2 : NO = 1.5) over a period of ca. 20 minutes.

EDE measurements were performed using an asymmetrically cut (6°) Si[111] monochromator in Laue (transmission) configuration. Detection of the EXAFS was made with the phosphor masked, FReLoN CCD camera, which gave a typical total acquisition time of 50 ms. Air was used as the I_0 for the EDE measurements. Downstream analysis of the gas flow was made with a quadropole mass spectrometer (Pfeiffer).

8.3 Results and discussion

NB Elements of the data analysis and subsequent interpretation in this chapter have been jointly carried out with Dr. Mark Newton, a PDRA at the time of performing these experiments.

Figure 8.1 shows the mass spectrometric data [m/z 34 (H_2S) and m/z 64 (SO_2)] taken synchronously with EDE measurements during room temperature exposure of 5 wt% RhCl to 5% H_2S/He and 5% SO_2/He. The inset in figure 8.1 charts the thermal response of the system as a function of time.

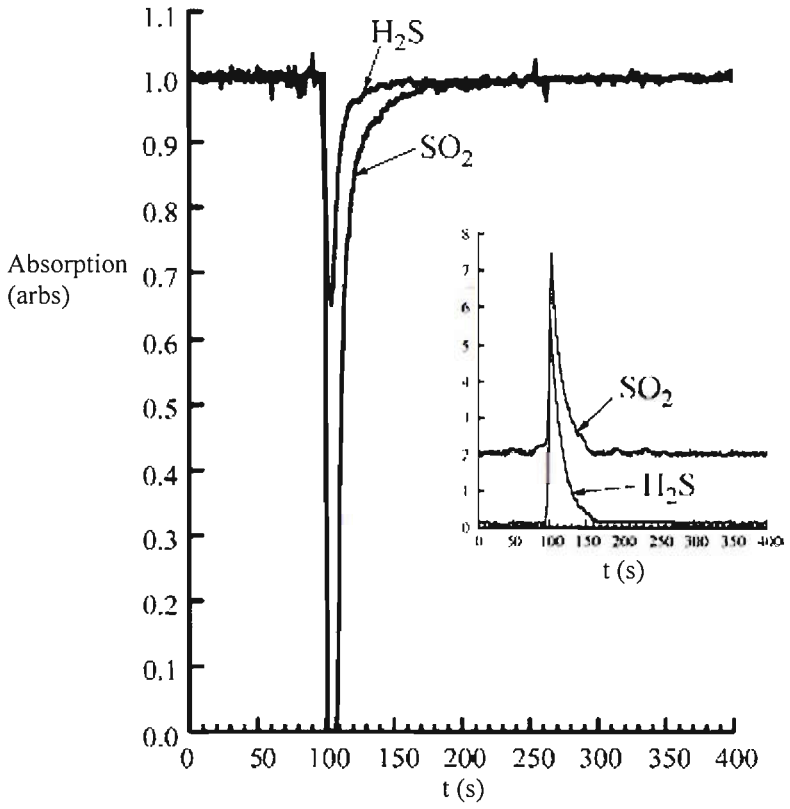

Figure 8.1: Mass spectrometric responses derived from exposure of 5 wt% RhCl to flowing 5% H_2S/He and 5% SO_2/He at room temperature. The inset shows the thermal response to the indicated gases. The gases were introduced to the microreactor system at t = 100 s.

It is clear from the figure that both SO_2 and H_2S are instantly taken up at room temperature. On first inspection, both gases are seen to invoke a similar thermal response from the catalyst bed; the uptake is accompanied by similar exotherms of ca. 6 K. The only desorption event that is observable by MS is a burst of H_2 that accompanies the uptake of H_2S.

Subsequent uptake measurement calculations of the individual gases (expressed as per Rh atom) reveal that significantly less H_2S [0.63 (±0.1) S/Rh] is adsorbed than SO_2 [3.8 (±0.1) SO_2/Rh].

Figure 8.2 shows representative k^3 weighted EDE spectra for the 5 wt% RhCl system, before and after exposure to 5% H_2S/He and 5% SO_2/He at 298 K. Table 8.1 gives the structural and statistical data derived from analysis of the spectra. Analysis of the EDE profile and the subsequent statistics reveal that the two sulfur containing gases invoke

contrasting changes to the composition of the 5 wt%RhCl system under the conditions employed. The reduced sample under 5% H_2/He at room temperature returned a coordination value that was expected from previous studies[11] and as reported in chapter 3; (N_1^{Rh} = ca. 7). Exposure to the flow of 5% H_2S/He for ca. 5 minutes elicits a significant structural change to the system, which can be seen clearly by the significant attenuation of the EXAFS signal in figure 8.2. The local Rh-Rh coordination falls to a value of ca. 2, with a similar value being reported for the Rh-S coordination (ca. 1.8). Elongation of the Rh-Rh bond distance from 2.66 to 2.72 Å is also observed.

In contrast to the vast changes H_2S exposure makes, SO_2 exposure under identical conditions appears to have a much more subtle effect. Firstly, the essentially invariant EXAFS pattern compared to the reduced sample suggests no significant structural changes to have occurred; this is quantified by formal analysis as the local Rh-Rh coordination number returns a value of ca. 5.7. A similar Rh-Rh bondlength of 2.65 Å is also reported; in fact the system does not evidence extensive contributions from scatterers such as sulfur (or indeed oxygen).

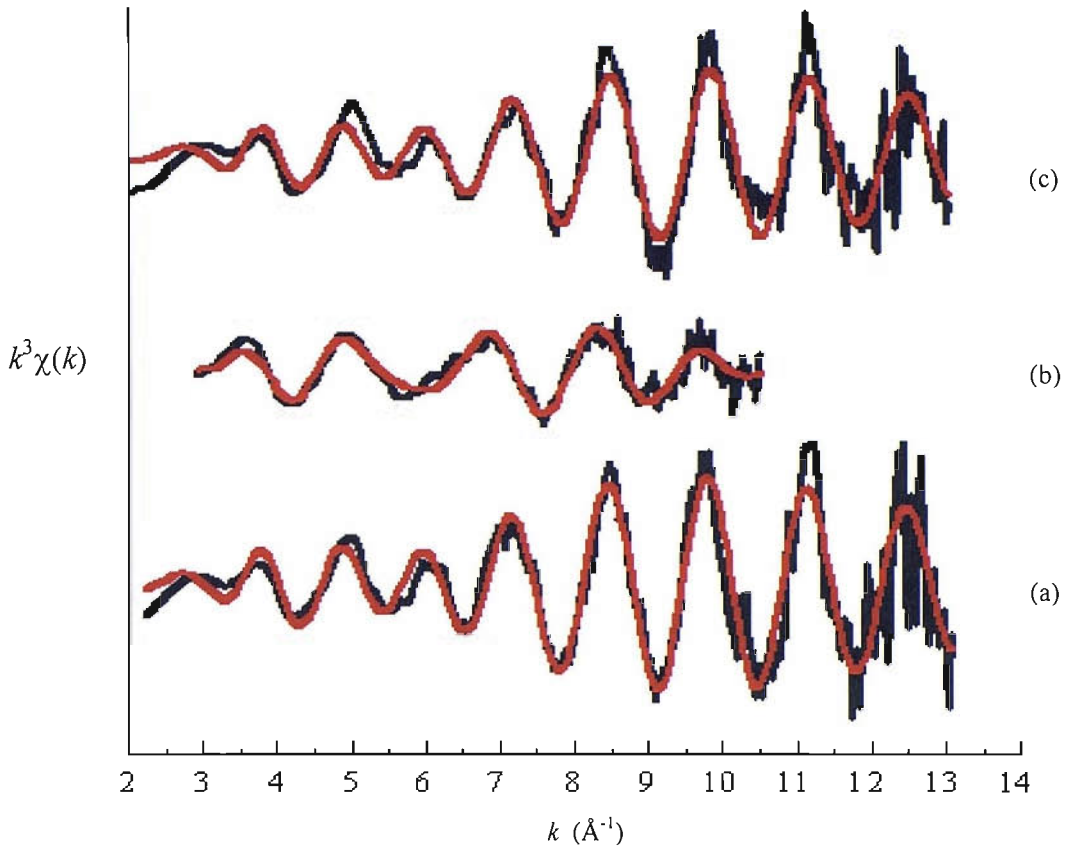

Figure 8.2: EDE spectra derived from (a) reduced Rh nanoparticles (b) after ca. 5 minutes exposure to 5% H_2S/He and (c) after ca. 5 mins exposure to 5% SO_2/He.
All spectra acquired at 298 K with ca. 1.5 seconds acquisition time. Experimental data is given in black, theoretical fits are shown in red.

Spectrum	k_{min} (Å^{-1})	k_{max} (Å^{-1})	Scatterer (s)	CN	r/Å	$2\sigma^2$/Å^2	E_F	R (%)
(a) post 5% H_2/He at 298 K	2	13	Rh	7.0 (±0.7)	2.66 (±0.02)	0.011 (±0.001)	-7.9	51
(b) post 5 mins 5% H_2S/He at 298 K	3	11	Rh	2.0 (±0.2)	2.72 (±0.02)	0.011 (±0.001)	-6.9	43
			S	1.8 (±0.2)	2.29 (±0.02)	0.009 (±0.01)		
(c) post 5 mins 5% SO_2/He at 298 K	2	12	Rh	5.7 (±0.6)	2.65 (±0.02)	0.011 (±0.001)	-6.8	48

Table 8.1: Structural and statistical data derived from the analysis of the EDE spectra given in figure 8.2. The acquisition time used was 1.5 s per spectrum.

Figures 8.3 and 8.4 show the structural response of Rh nanoparticles during a switch from a flow of He to 5% H_2S/He and 5% SO_2/He. Figure 8.3 charts the Rh-Rh and Rh-S coordination numbers; figure 8.4 follows the corresponding Rh-Rh bondlengths as a function of time.

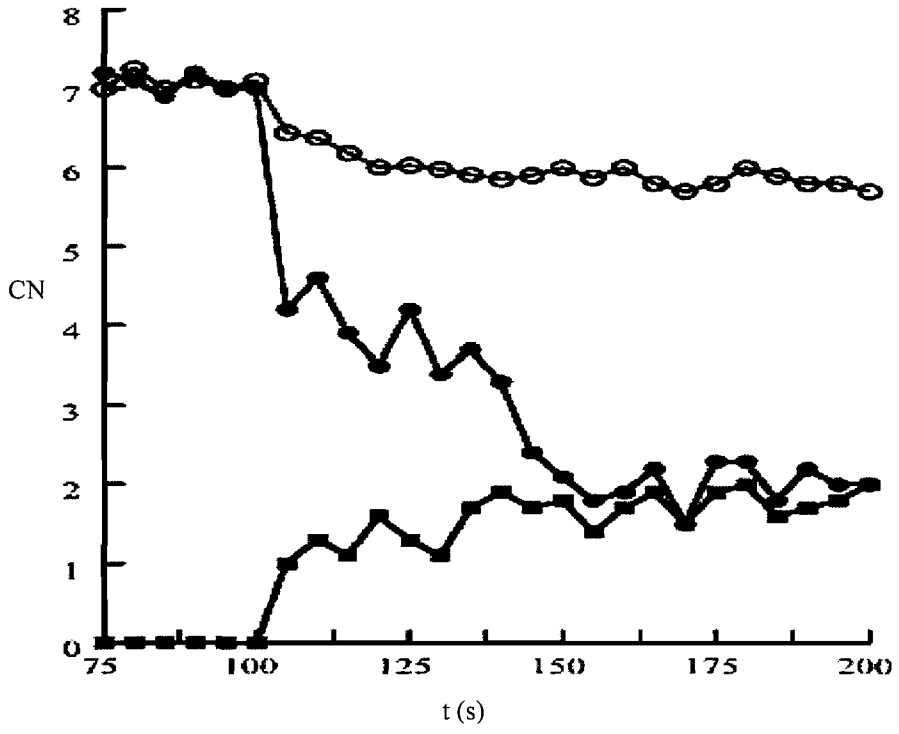

Figure 8.3: Rh-Rh coordination numbers (CN) derived from the EDE data during gas switches from He to 5% H_2S/He and 5% SO_2/He (at room temperature) as a function of time. Filled circles = Rh–Rh (H_2S); open circles = Rh–Rh (SO_2); squares = Rh–S (H_2S).

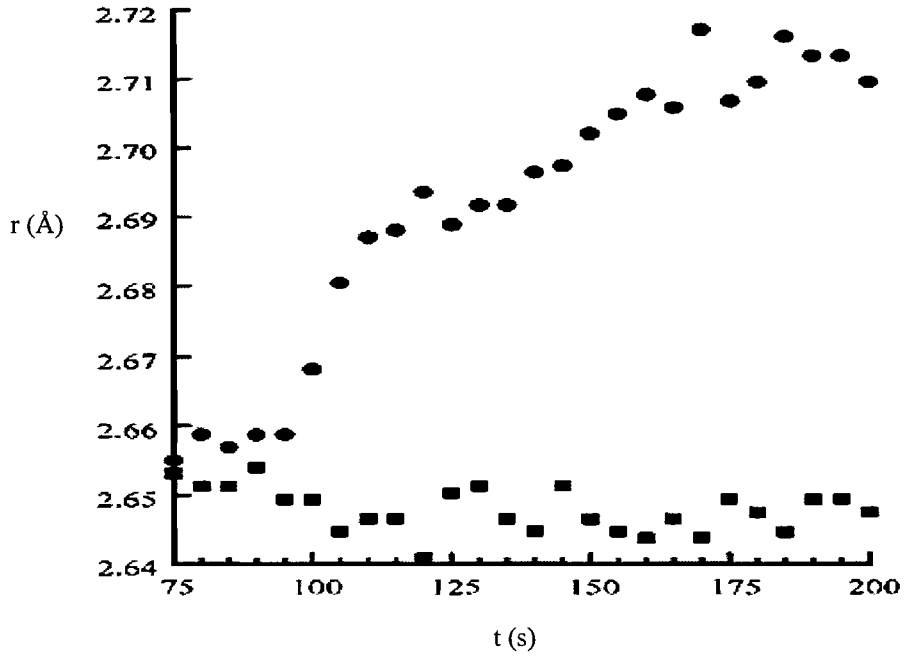

Figure 8.4: Rh–Rh nearest neighbour bond lengths during gas switches from He to 5% H_2S/He (circles) and 5% SO_2/He (squares) as a function of time.

Analysis of these data allows for the rapid structural response of the catalyst system to be followed with sufficient time resolution afforded by the experiment. H_2S initially induces a very rapid sulfidation (<5s), which is followed by a slower process that results the complete sulphidation of the system, i.e. the formation of nanoparticulate Rh-S (2.71 Å < Rh < 2.72 Å, Rh-S = 2.3 Å). This process is observed to occur over the time scale of ca. two minutes.

This behaviour most likely proceeds with the initial sulfidation of the surface Rh particles, which is followed by a slower sulfidation of the remainder of the metallic core. An alternative explanation to this includes the differential rates of sulfidation occurring over differing sized Rh particles present on the catalyst, as particle size effects cannot be ruled out as playing a key role in the observed changes.

Figure 8.4 presents the Rh-S distance to be ca. 2.71 Å, which is consistent with values obtained for bulk Rh sulphides via X-ray diffraction.[12,13,14] However, this Rh-Rh bondlength is significantly shorter than expected for Rh_2S_3,[13] although bondlengths within this regime have been reported for Rh_2S_4[12] and $Rh_{17}S_{15}$[14] (average Rh-S-Rh bond angle of ca. 73°). Therefore, the closest bulk analogue that bears resemblance to this species both

stoichiometrically and structurally is $Rh_{17}S_{15}$.[14] However, there is no apparent bulk analogue for the nano-sulfide formed on the supported Rh systems. It is therefore reasonable to suggest that the shortened Rh-Rh distance and acute Rh-S-Rh bond angle result from a strict constraint of these species to a three dimensional nanoscale domain (based upon the bridging sulfur model).

The surface sulphide that forms is observed to be extremely stable, even at temperatures in excess of 673 K under a flow of 5% H_2/He. The in situ sulfiding of the 5 wt% RhCl system during the NO reduction by H_2 (H_2 : NO = 1.5) at 525 K results in the complete curbing of catalytic activity (from >90% NO conversion with virtually no N_2O production).

Conversely, SO_2 is seen to elicit a different response in the Rh system, despite exhibiting a very similar thermal response to H_2S. There is no direct evidence of any sulfidation or oxidation at 300 K or 573 K. EXAFS measurements confirm this; there are no significant O or S contributions to the EXAFS despite a high level of SO_2 uptake. Indeed the only measurable effect seen is the decrease in Rh-Rh coordination. This subtle change can be viewed in an alternative manner in figure 8.5, which highlights the raw absorption data from EXAFS and the inset follows the 'white line' signal as a function of time (a qualitative method of following changes in XAFS as described in chapter 4).

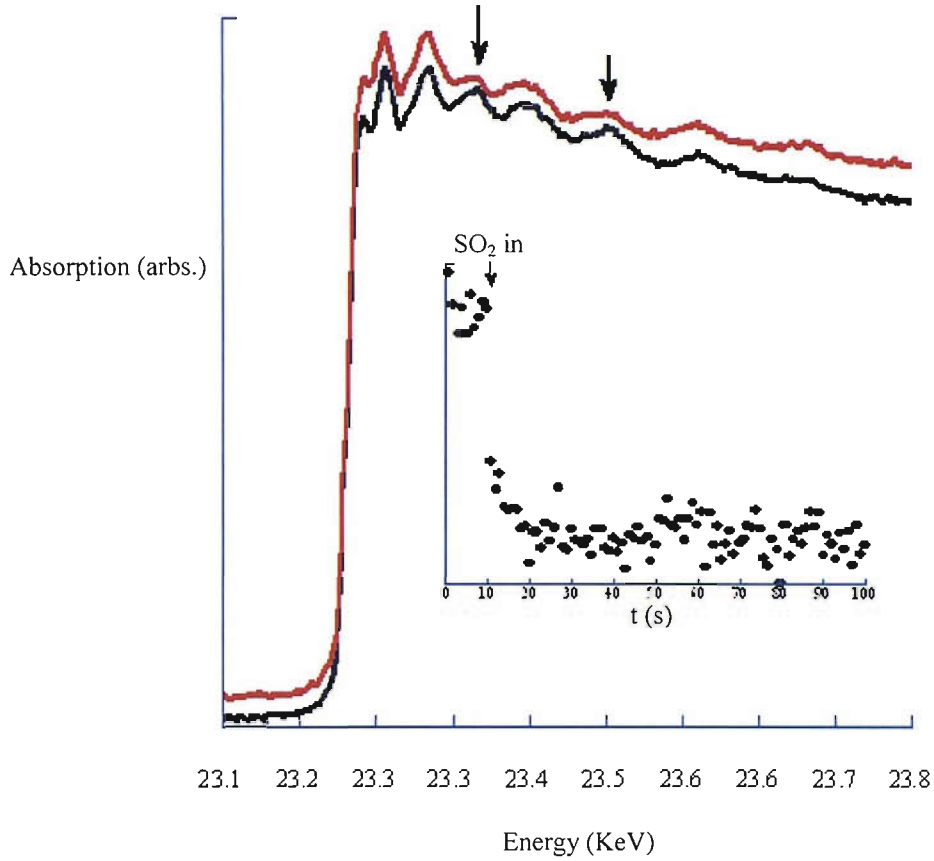

Figure 8.5: Raw EDE adsorption data derived from reduced 5wt%RhCl (black line) and after exposure to flowing 5% SO_2/He (red line) at room temperature. The arrows indicate the regions where EXAFS attenuation is clear. The inset follows the 'white line' during exposure to 5%SO_2/He for the EXAFS feature at 23320 eV.

An initial inspection of the change in the first shell Rh-Rh coordination shows the average particle size to approximately halve from ca. 50 to 25 atoms.[15] However, this assumption is based on hemispherical particles from the average particle size distribution (PSD); the vast range of PSD for this system given in chapter 3 means a more complex morphological change of the Rh particles cannot be ruled out. Interestingly, the decrease in local coordination by exposure to SO_2 (although subtle) is in contrast to the promotion of particle sintering the gas has on similarly loaded Pt/Al_2O_3 catalysts (3 and 9 wt% systems).[16]

Moreover, the repeated pulsing of SO_2 into the catalytic mixture (NO/H_2) at 523 K over a period of ca. 20 minutes does not have a significant effect on the net performance of the system, with NO conversion remaining above the 90% level throughout the experiment. This is in stark contrast to the rapid, highly detrimental effect H_2S has on supported Rh

nanoparticles. The total curtailment of catalytic activity is observable within ca. 2 minutes of pulsing H_2S into the catalytic mixture.

8.4 Conclusion

In conclusion, these results show that although the potential for exothermic dissociation of SO_2 exists, the process is abated on nanoparticulate Rh with a PSD of 10-45Å (data taken from TEM measurements of the 5 wt% RhCl system – see chapter 3.3.1). Any interaction of SO_2 with Rh is therefore primarily molecular and the majority of gaseous uptake occurs with the alumina support (ca. 11 SO_2/nm^{-2} at room temperature). A subtle modification of the structure of Rh is observed, however this imposes very little effect upon the NO/H_2 reaction on the timescales investigated (<30 minutes).

In contrast, exposure of Rh to H_2S results in highly exothermic dissociative adsorption and complete sulphidation of nanosized Rh. The process is rapid, irreversible and completely disrupts NO reduction by H_2 occurring over Rh.

Such experiments serve to give an insight into how highly dispersed, 'working' catalysts would respond to potential poisons both in terms of structure and catalytic performance. The current experiments have a broader viewpoint of the TWC, where sulphur containing gases are an important consideration in areas ranging from catalyst design to overall exhaust emissions.

8.5 References

[1] A. Amberntsson, M. Skoglundh, M. Jonsson, E. Ffridell, *Catal. Today*, 2002, **73**, 279.

[2] E.A. Efthimidis, S.C. Christoforou, A.A. Nikopoulos, I.V. Vasalos, *Appl. Catal. B*, 1999, **22**, 91.

[3] H.N. Rabinowitz, S.J. Tauster, R.M. Heck, *Appl. Catal. A*, 2001, **212**, 215.

[4] J.S. Hepburn, H.G. Stenger, C.E. Lyman, *J. Catal.*, 1991, **128**, 48.

[5] For instance, M.A. Newton, A.J. Dent, S. Diaz-Moreno, S.G. Fiddy, B. Jyoti, J. Evans, *Chem. Phys. Chem.*, 2004, **5**, 1056.

[6] For instance, C.H. Bartholemew, P.K. Agrawal, J.R. Katzer, *Adv. Catal.*, 1982, **31**, 135.

[7] A. Santoni, B.C.C. Cowie, G. Scarel, V.R. Dhanak, *Surf. Sci.*, 1997, **388**, 254.

[8] V.R. Dhanak, S.P. Harte, G. Scarel, B.C.C. Cowie, A. Santoni, *Surf. Sci.*, 1996, **366**, L765.

[9] K.C. Wong, W. Liu, M. Saidy, K.A.R. Mitchell, *Surf. Sci.*,1996, **345**, 101.

[10] P.J.F. Harris, *Nature*, 1986, **323**, 792.

[11] B. Jyoti, MPhil Thesis, University of Southampton, 2002.

[12] J.S. Beck, T. Hilbert, *Z. Anorg. Allg. Chem.*, 2000, **626**, 72.

[13] S. Geller, *Acta Crystallogr.*, 1962, **15**, 1198.

[14] E. Parthe, D. Hohnke, F. Hulliger, *Acta Crystallogr.*, 1967, **23**, 832.

[15] A. Jentys, *PCCP*, 1999, **1**, 4059.

[16] A.F. Lee, K. Wilson, R.M. Lambert, C.P. Hubbard, R.G. Hurley, R.W. McCabe, H.S. Gandhi, *J. Catal.*, 1999, **184**, 491.

Chapter 9. Summary

This thesis has successfully carried out an investigation into the structure-function surface chemistry of selected oxide-supported rhodium catalysts. The specific target of this investigation was to gain a thorough understanding of the nature of Rh nanoparticles, and their subsequent properties under reactive environments; with a broader aim of probing the processes that occur over real, 'working' catalysts such as the three-way automotive catalyst.

The central methodology was based around an experimental platform that would probe such processes in situ and in a truly synchronous, time resolved manner primarily due to the short timescales that they occur over. X-ray absorption fine structure was envisaged as the primary technique to achieve the aims of this thesis as it is a very powerful technique to determine the local structure of compounds; indeed it was the lack of structurally deterministic studies in this field that formed the underlying motivation of the current study. By combining EXAFS with DRIFTS and MS and bringing them to bear on these nanoparticulate systems in a single experiment, a number of important heterogeneous reactions and processes could be studied with unprecedented detail. The further utilisation of complimentary ex situ techniques such as TEM, XPS and EDX served to bolster the 'complete' understanding of the catalysts the current study was charged with achieving.

A detailed characterisation of the γ-Al_2O_3 supported Rh systems with metal loading from 1-10 wt% was carried out in **chapter 3**. As the experiments used a combination of the myriad techniques including TEM, EDX, XPS, and Rh and Cl K-edge XAFS as explained in **chapter 2**, it also served to scrutinise them.

The results indicated that only the in situ techniques applied allowed for the characterisation of wholly metallic Rh particles. It was found that even brief exposure to air at room temperature results in the facile partial oxidation of the samples; an overall particle morphology of a metallic core surrounded by an oxidic layer was proposed. The study also stressed that caution must be applied when comparing the results between techniques applied in situ versus ex situ.

Clear differences were evident in the particle size distribution as depicted by TEM as a function of catalytic precursor, with average particle sizes in the range of 10-60 Å. Un-chlorinated precursors resulted in larger particles which were more difficult to oxidise than their chlorinated precursor analogue systems. For the chlorinated systems, no significant association of chlorine to the rhodium particles was observed with any of the techniques

applied. For all loadings however a similar amount of chlorine was retained on the support after the calcination and reduction processes, suggesting a maximum amount of chlorine attachment/association sites were available on the γ-Al_2O_3 support.

XAFS measurements provided in situ information on the samples under investigation. In addition to EXAFS; the XANES studies on the Rh K-edge has shown to be a reliable technique to characterise the average metal particle sizes for small particles up to 55 atoms. EXAFS and XANES both demonstrated the likely particle shape size to be spherical. Moreover, XANES analysis aided the interpretation of the EXAFS results obtained, and in doing so highlighted one of many advantages the XANES technique has over the (generally) more time demanding EXAFS technique.

The redox characteristics of the 5wt% RhCl catalyst was probed in **chapter 4**. The study not only served as an insight into the rapid phase fluxionality of Rh nanoparticles, but also proved that the current experimental platform could be used to follow these important processes on a time scale of tens of milliseconds. The facile reduction and oxidation processes (performed at varying temperatures) could be charted accurately due to the high time resolution; an area where previous studies had denoted such processes to be 'immeasurably fast'. For example, following an initial 'induction' period, the reduction process occurred in a single kinetically limiting step, which at 573 K was complete within 1 second. Important kinetic data was gleaned from the experiments, as well as the estimation of activation energies, which correlated well to previous studies despite such experiments being performed upon low dispersed Rh systems, an interesting observation in itself.

The adsorption characteristics of CO at various temperatures (298 – 423 K) was studied in **chapter 5**, where the time resolved experiments revealed that exposing a relatively low loaded RhCl catalyst (2.5 wt%) to a flow of gaseous 5% CO/He induces a rapid disruption of the particles and results in the dominant formation of discrete $Rh(CO)_2$ species. The use of higher exposure temperatures facilitated the rate of this disruption. DRIFTS and other evidence suggested that complete disruption did not occur; particulate Rh played a key role throughout the exposure experiments. Several models involving particle sintering/agglomeration and the role of hydroxyl groups from the alumina surface were discussed to try and explain the continual presence of larger particles that are undetectable by techniques such as EXAFS. The postulated idea of an equilibrium between particle

disruption and agglomeration was bolstered when the 5 wt% system was analysed. On simple inspection, the catalyst structure was not significantly affected at any temperature employed. However, the DRIFTS data again reported CO species that are associated with metallic and oxidic Rh; confirming that a range of processes are most likely to be in effect here, and all of the available data needs to be considered when analysing the complex 'whole' of these supported systems.

The structure-function response of the 5 wt% RhCl catalyst at varying temperatures on exposure to another key molecule, NO, was closely followed in **chapter 6**. A rapid and extensive oxidation of the pre-reduced, metallic Rh nanoparticles was observed upon exposure to 5%NO/He at all temperatures employed. The use of higher temperatures had a facilitative effect on this response afforded by the EXAFS data, and by 573 K no 'induction' period was evident (an event that limited the oxidative processes at lower temperatures).

The adsorption of NO at low temperatures (298 and 423 K) was deemed to be molecular, and this was found to be a major contributor to the induction period at the start of the experiments. Despite a range of nitrosyl species being formed at low temperature, the $Rh(NO)^-$ species was found to be responsible for the majority of the oxidation, with $Rh(NO)_2$ also being another contributor.

Markedly different behaviour was observed at 573 K, notably through the significant reactive turnover of $NO_{(g)}$ during the experiment. DRIFTS indicated the linear $Rh(NO)^+$ species to be the only stable species evident at this temperature. However, based on previous findings from this and other studies it was surmised to be a spectator species, a by-product from the decomposition of a highly transient $Rh(NO)_2$ species. This geminal dinitrosyl species contributed to the oxidation of the Rh component; as did the rapid, dissociative adsorption of $NO_{(g)}$. This had the overall effect of lowering the selectivity of the system towards $N_{2(g)}$ production. The continual oxidation and effective poisoning of the system with nitrosyl/adsorbed species would eventually render the Rh system inactive.

The reduction of the $NO_{(g)}$ induced oxidised phase of Rh was found to proceed at temperatures as low as 373 K, and the rate of the recovery of the metal was facilitated at increased temperatures. For example, by increasing the reduction temperature by 100 K from 373 K to 473 K saw a threefold increase in reduction rate. Both the reduction temperature and particle morphology seemed to directly affect the reduction characteristics of the catalyst

system, with larger Rh particles at lower temperatures indexing a significantly longer reduction time. The $Rh(NO)^+$ species was the only stable species evidenced by DRIFTS prior to exposure to $H_{2(g)}$, and the subsequent disappearance of the species was closely correlated to the regeneration of particulate Rh. There was no evidence for any significant particle sintering at any of the temperatures investigated, although further work is needed to understand this process and the structural-reactivity behaviour of the catalysts under steady state conditions.

Progression to observe the behaviour of the 5 wt% RhCl and RhN systems under catalytic conditions and at various temperatures was carried out in **chapter 7**. The CO/NO reaction was chosen due to its relevance to the TWC and the work undertaken in the previous two chapters. The experiments showed that a stoichiometric CO/NO feedstock corroded the relatively large Rh particles into mainly the $Rh(CO)_2$ species under ambient conditions. Catalysis ensued as a direct result of the decomposition of the $Rh(CO)_2$ species, as a function of temperature. The presence of chlorine in the catalyst composition seemed to hinder the formation of a clear metallic Rh phase at post light off temperatures, but with no apparent detriment to overall catalyst efficiency.

Analogous experiments comparing the 5 wt% RhCl system to an alloy catalyst comprising of 4wt%Rh/1wt%Pd produced equally interesting results. The alloy system, extensively analysed by our group in the past, was chosen for these experiments due to the insulating properties the adjunct metal (Pd) had shown; it effectively curtailed the facile oxidation of the Rh component observed under ambient conditions. The alloy system was found to have an average particle atomicity of 20 - >70 times larger than previous studies showing disruption to CO alone, even the average atomicity of 5 wt% RhCl system was 3 times greater. However, the temperature controlled NO reduction by CO highlighted the extensive, disruptive oxidation of Rh nanoparticles, the capacity of which exceeded measurements made in previous studies; it appears that molecularly adsorbed CO can strip Rh extremely efficiently under these reaction conditions, even from the relatively massive and passivated alloy nanoparticles That these unexpectedly corrosive processes were previously unknown, or at the very least underestimated, would have a profound impact on the core understanding of their catalytic influence. This in turn would directly affect technological applications such

as catalyst design, such as the three-way automotive catalyst for which the NO/CO reaction is a paramount consideration.

The final part of **chapter 7** looked at probing these structural changes in a more direct manner; this was done via observing the structure-function response of the 5wt% RhCl catalyst to a gas switching regime that alternated CO and NO in the gas stream in a periodic fashion. The isothermal experiments were carried out in pertinent regions; at the onset of catalysis, a region where structural changes were observed in the EXAFS data (i.e. a rise in Rh-Rh coordination value) and a temperature where catalysis proceeded rapidly. The detailed study found that the response of the catalyst is heavily influenced by the phase (and experimental temperature) of the Rh in the early stages of the experiment. At lower temperatures the almost static oxidic Rh phase is evidenced by the predominant, discrete $Rh(CO)_2$ unit under $CO_{(g)}$. Moving to higher temperatures, the changes in structure are more substantial and follow the pattern of the gas switching closely, primarily due to the Rh remaining in particulate form, further evidenced by the presence of carbonyl species bound to metallic Rh.

The manner in which these highly dispersed, 'working' catalysts would respond to potential poisons both in terms of structure and catalytic performance was studied in **chapter 8**; which used SO_2 and H_2S as the poisons and observed the effect on both the catalyst itself and the subsequent effect they had on the NO reduction by H_2 reaction.

The results showed that although the potential for exothermic dissociation of SO_2 exists, the process is abated on nanoparticulate Rh with a PSD of 10-45Å (i.e. the 5 wt% RhCl catalyst). Any interaction of SO_2 with Rh is therefore primarily molecular and the majority of gaseous uptake occurs with the alumina support. A subtle modification of the structure of Rh was observed, however this imposes very little effect upon the NO/H_2 reaction on the timescales investigated (<30 minutes).

In contrast, exposure of Rh to H_2S resulted in a highly exothermic dissociative adsorption and complete sulfidation of nanosized Rh. This process was found to be rapid, irreversible and completely disrupted NO reduction by H_2 occurring over Rh.

By successfully achieving the original aims of this thesis the future direction of the project has already been envisaged and is currently being implemented. The now proven EDE/DRIFTS/MS experimental platform has now been installed as a permanent facility at beamline ID24, ESRF, France. The initial experiments performed on the developed system have been successful; they have looked at the effect of adding ceria to the catalyst composition. Early results suggest that the Rh component is more extensively oxidised on the ceria systems where compared to similarly loaded Rh/Al_2O_3 catalysts. The myriad of ex situ techniques used in this study will continue to be used in this project extension. Further studies are also planned to answer the many questions this thesis has bought to bear regarding the nanoparticulate Rh systems, for example the role that particle sizes have on the overall behaviour of these systems needs to be addressed in detail.

With regards to future experiments, the possibilities and potential are endless; for instance the structure-function behaviour of palladium and/or platinum, both core components in the TWC would be a natural progression from the current study. The central platform itself could also be developed in many ways; the small focal spot of X-rays the EDE experiment affords could be used to provide a cell with a system dead time many magnitudes shorter than in the current set-up. This would therefore allow for processes to be investigated at even higher time resolutions, the hardware for this (i.e. CCD detectors) are under continual development to meet with such demands. Other examples of modifying the current set-up include using an anisotropic sample holder in order to optimise the IR and XAFS measurements made for a particular system, or indeed to adopt a transmission geometry for the IR measurements.

In summary, the central methodology and indeed motivation for such in situ studies to be carried out has now been proven – it is now the surrounding technologies (for example with experimental software/hardware and data processing) that also need to be considered and developed alongside the project in order to maximise the potential of these experiments.